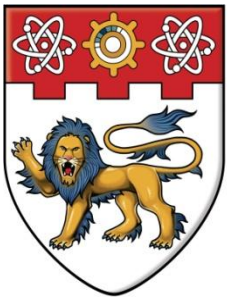

NANYANG TECHNOLOGICAL UNIVERSITY

The role of N157 of A-ATP synthase subunit B in nucleotide binding and expression, production and structural and mechanistic features of subunits α and ε of *Mycobacterium tuberculosis* F-ATP synthase

By
Lavanya Sundararaman
Supervisor: Prof. Gerhard Grüber

School of Biological Sciences
Nanyang Technological University
Singapore

2015

Acknowledgement

At the outset, I thank the Almighty for his many blessings that have manifested through innumerable people and situations. First and foremost, I wish to express my sincere gratitude to my advisor, Professor Gerhard Grüber, for his guidance and warm encouragement. I feel fortunate for to be a part of his lab and shall remain ever grateful to him for providing a conducive environment to grow as a student of science.

I gratefully acknowledge the financial support rendered by the Nanyang Technological University of Singapore in the form of Research Scholarship. This research was supported by the Ministry of Education (MOE), Singapore (MOE2011-T2-2-156; ARC 18/12; G. Grüber) and the Ministry of Health (MOH), Singapore (NMRC, CBRG12nov049; G. Grüber). I am also grateful to the academic and technical staff at the School of Biological Sciences, who have helped me in one way or other in my research work.

I am very thankful to each and every present and past member of Grüber's lab for all the help and support. Special thanks to Malathy for helping me learn crystallography and also for the work related to SAXS. Many special thanks to Goran and Conny for helping me train in the basic techniques of Molecular Biology and I wish to acknowledge the help and assistance offered by Priya and Ankita with regard to the experimental work. I owe a great deal to Saw for all her help.

I am ever indebted to the immense care and support offered by Asha, Sandip, Phat, Dhiren Arvind not only on the work front but also on the emotional side. You have stood as family with your love and I am thankful for all the happy times that we have shared and that are yet to come. My heartfelt gratitude to Wilson and Hendrik for all the interesting enlightening scientific and non-scientific conversations. You are one of the coolest and friendliest scientist I have met and thank you for being such wonderful labmates. Nithin, Prof. Oliver and Dr. Candace have been extremely kind in educating me with their knowledge and I am extremely thankful. My heartfelt gratitude to my dear friend, Ms. Wendy Hanai for patiently help me proofread the entire thesis.

It would not have been possible for me to be pursuing my dream here, if not for beautiful mentoring done by my teachers from my earlier years of education and I wish to take this opportunity to express my most sincere gratitude to my role models, Mrs. Gita Mahalingam, Dr. Denis Mascarenhas, Dr. Sujatha Ramadas, Dr. Mahuya Ghosh, Mr. Prabhakar B. S and Prof. P. Balaram. I owe very special thanks to all my friends at Sri Vidya Mandir, Bangalore, Indian Institute of Science, Bangalore and St. Joseph's College, Bangalore and NTU, Singapore. I consider myself truly blessed to have so many well wishers and I wish to thank each one of them for all their love and encouragement and extend my warm regards for all the memorable times. Pursuing my passion for dance gave me the opportunity to meet some wonderful people, Chitra

Shankar, Murali Shankar, Pallavi Sharma, Jennifer Leong and all my fellow dance buddies. Thank you all for the fun times on the dance floor.

I am truly feel blessed to be friends with Sohoni family and thank them for their love. I shall remain eternally grateful to Dhiren for being the best friend I could have ever asked for. You truly brought this verse to life, *"Teri har ek burayi pe daante who dost, Gam ki ho dhoop to saaye bane tera who dost, naache bhi who teri khushi main, Yaaron dosti badi haseen hai!"*. Thank you Dr. Saab for inspiring me to be a better person and a better scientist. "*Aap to Dhiren ho Yaar*!!" ☺. No extent of words would do justice to the gratitude I feel towards Laxmi, Kaushik, Nishanth. All you 5^{th} borns are the epitome of awesomeness. Thank you for sharing all the happiness and adding so much richness and beauty to my life. Will always treasure you guyz, as most importantly you let me be me ☺. Ramya, you are a wonderful friend who stood by as a pillar of strength and I shall always remain a fan of your composure and kindness. "932 Khiladis"- Jithin Da, Raunaq, Dhiren, Soumya, Ashok and Pravesh- thank you for your warmth and hospitality.

My heartfelt gratitude to my parents, my sister Priya, my brother Arun and my grandparents Vittal thatha and Lakshmi Patti for their undying selfless support, love and understanding and for being the greatest source of inspiration. I thank also my extended family members who have encouraged and supported me.

To,

Vittal Ramamrutham, my Master Oogway and

Gita Mahalingam, my almighty and my secret angel

Table of Contents

Acknowledgement.....i

Table of contents.....iv

List of figures.....viii

List of tables.....viii

Abbreviation.....xii

Abstract.....13

1. Introduction.....16

1.1 Introduction to ATP synthases.....17

1.2 Physiological roles of the rotary ATP synthase.....18

1.3 Subunit composition of F_1F_O and A_1A_O -ATP synthases.....18

1.4 Overview of *Mycobacterium tuberculosis*.....20

1.5 Niches and adaptations of *mycobacteria* to survive harsh conditions in macrophages.....25

1.6 Organisation and Functioning of F_1 and F_O domains.....26

1.7 Subunit α of F_1F_O ATP synthase.....29

1.8 Subunit ε of F_1F_O ATP synthases.....33

1.9 Overview of archaea.....39

1.10 Adaptations of ATP synthases of archaea to their ecological niches.....43

1.11 Organisation of A_1 and A_O domains.....44

1.12 Insights into the structure and functional role of subunit B of A_1A_O ATP synthases.....47

1.13 Aims of this Thesis.....50

2. Materials and methods.....52

2.1 Materials.....53

2.1.1 Chemicals.....54

2.1.2 Molecular biology materials.....55

2.1.3 Chromatography.....55

2.1.4 Other instrumentation.....56

2.1.5 Computer software.....56

2.2 Methods.....57

2.2.1 Construction and mutagenesis of N157T; subunit B mutant of A-ATP synthase from

Methanosarcina mazei Gö1.....58

2.2.2 Data Collection.....58

2.2.3 Structure Determination.....58

2.2.4 Protein Data Bank Accession Code.....58

2.2.5 Cloning of subunit α constructs from *M. tuberculosis* and *Bacillus* PS3 F_1F_O ATP synthase.....59

2.2.6 Electroporation transformation.....61

2.2.7 Production and purification of subunit α constructs: *Mt*α and *Mt*$\alpha_{1\text{-}513}$ of F_1F_O ATP synthase *M. tuberculosis*.....62

2.2.8 Small angle X-ray scattering measurements for subunit α constructs: *Mt*α, PS3α and α^{chi}.....64

2.2.9 Cloning strategy for generating sub complex of $\alpha^{chi}{}_3\beta_3\gamma$ – hybrid protein of thermophilic *Bacillus* PS3 and *M. tuberculosis*.....66

2.2.10 NADH coupled continuous assay to measure ATP hydrolysis activity of the complex PS3$\alpha_3\beta_3\gamma$ and $\alpha^{chi}{}_3\beta_3\gamma$ (PS3 and *Mt*) F_1F_O -ATP synthase.....71

2.2.11 Labeling of PS3$\alpha_3\beta_3\gamma$ and $\alpha^{chi}{}_3\beta_3\gamma$ for Single molecule rotation Experiments.....71

2.2.12 Rotation Assay for biotin labeled complexes of PS3$\alpha_3\beta_3\gamma$ and $\alpha^{chi}{}_3\beta_3\gamma$.....72

2.2.13 Cloning various constructs of subunit ε F_1F_O ATP synthase from *M. tuberculosis*.....73

2.2.14 Production and purification of subunit ε constructs: *Mt*$\varepsilon_{1\text{-}120}$, ε_{121hyb}, *Ec*ε and PS3ε F_1F_O ATP synthase.....76

2.2.15 Quantification of proteins by bicinchoninic acid (BCA) method.....77

2.2.16 Circular Dichroism spectroscopy.....78

2.2.17 Crystallization of *Mt*$\varepsilon_{1\text{-}120}$.....78

2.2.18 Cloning of subunit *Mt*$\varepsilon_{1\text{-}120}$ F_1F_O ATP synthase from *M. tuberculosis* H37rv in the *M. smegmatis* system.....79

2.2.19 Protein expression using *M. smegmatis* as a host.....80

2.2.20 Thermofluor Stability Assay.....80

2.2.21 Nuclear Magnetic Resonance (NMR) Spectroscopy.....82

2.2.22 Isotopic labeling (^{15}N) of proteins.....82

2.2.23 2D -^{15}N NMR spectroscopy.....83

2.2.24 Expression of $\varepsilon_{1\text{-}120}$ *M. tuberculosis* F-ATP synthase in *E. coli* BL21 GroEL-ES strain.....83

2.2.25 Transformation using heat shock.....84

2.2.26 Production and purification of *Mt*ε_{1-120} in *E. coli* BL21 GroEL-ES cell strain.....84

2.2.27 Purification of *Mt*ε_{1-120} in *E. coli* BL21 GroEL-ES cell strain.....84

2.2.28 Non-Uniform Sampling NMR.....85

3. Results.....88

3.1 Role of N157 of subunit B of A-ATP synthase in nucleotide binding.....89

3.1.1 Introduction.....90

3.1.2 Data collection and structure determination of subunit B N157T mutant of *M. mazei* Gö1 A_1A_O ATP synthase.....90

3.1.3 Crystallographic structure of subunit B mutant N157T of *M. mazei* Gö1 A_1A_O ATP synthase.....91

3.1.4 Structural comparison of the mutant N157T with wild type subunit B.....92

3.2 Insight into the structural and mechanistic traits of the C- terminus of subunit α of *M. tuberculosis* F-ATP synthase.....98

3.2.1 Introduction to subunit α of F-ATP synthase in *Mycobacterium tuberculosis*.....99

3.2.2 Cloning, expression and purification of *Mt*α and *Mt*α_{1-513}.....99

3.2.3 Small angle X-ray scattering (SAXS) and data analysis.....102

3.2.4 Subunit α of *Bacillus* PS3 (PS3α) and chimeric α (α^{chi}) of *Bacillus* PS3 and *M. tuberculosis* F_1F_O ATPsynthase.....105

3.2.5 Sub-complex of $\alpha^{chi}{}_3\beta_3\gamma$-hybrid protein of thermophilic *Bacillus* PS3 and *M. tuberculosis*.....109

3.2.6 Biotin labeling and single molecule rotation experiments for PS3$\alpha_3\beta_3\gamma$ and $\alpha^{chi}{}_3\beta_3\gamma$.....111

3.3 Mechanistic and structural characterization of subunit ε F_1F_O ATP synthase of *Mycobacterium tuberculosis*.....114

3.3.1 Introduction to subunit ε F_1F_O ATP synthase from *M. tuberculosis*.....115

3.3.2 Production and purification of subunit *Mt*ε and *Mt*ε_{1-120} constructs from F_1F_O ATP synthase *M. tuberculosis*.....117

3.3.3 Reconstitution of PS3$\alpha_3\beta_3\gamma$ with *Mt*ε and *Mt*ε_{1-120} and ATP hydrolysis analysis using NADH coupled continuous assay.....118

3.3.4 Production and purification of subunit PS3ε and *Ec*ε constructs F_1F_O ATP synthase from *Bacillus* PS3 and *E. coli*.....120

3.3.5 Reconstitution of PS3$\alpha_3\beta_3\gamma$ with PS3ε and *Ec*ε and ATP hydrolysis analysis using NADH coupled continuous assay.....122

3.3.6 Production and purification of subunit ε_{121hyb}, a hybrid construct from F_1F_O ATP synthase of *M. tuberculosis* and *E. coli*.....125

3.3.7 Reconstitution of PS3$\alpha_3\beta_3\gamma$ with ε_{121hyb} and ATP hydrolysis analysis using NADH coupled continuous assay....126

3.3.8 Reconstitution of $\alpha^{chi}{}_3\beta_3\gamma$ with *Mt*ε and PS3ε and ATP hydrolysis analysis using NADH coupled continuous assay....128

3.3.9 ATP hydrolysis analysis using NADH coupled continuous assay for *Mm*A_3B_3D and *Mt*ε....130

3.3.10 Production and Purification of subunit *Mt*ε_{1-120} F_1F_O ATP synthase *M. tuberculosis* for structural characterization....131

3.3.11 Secondary structure content of *Mt*ε_{1-120}....132

3.3.12 Crystallization of *Mt*ε_{1-120} F_1F_O ATP synthase....133

3.3.13 2D NMR Data acquisition of *Mt*ε_{1-120} F_1F_O ATP synthase....134

3.3.14 Thermofluor Stability Assay (TSA), buffer optimization for *Mt*ε_{1-120} . F_1F_O ATP synthase....137

3.3.15 NMR using Non Uniform Sampling for *Mt*ε_{1-120} F_1F_O ATP synthase....139

3.3.16 ^{15}N Single amino acid labeling of *Mt*ε_{1-120} F_1F_O ATP synthase....140

4. Discussion....142

4.1 Relevance of the conserved asparagine residues in the phosphate-binding loop of the nucleotide binding subunit B of A_1A_O ATP synthases....143

4.2 Importance of P-loop residue K175 of *Mt*α F-ATP synthase in Nucleotide binding....146

4.3 Novel insights into the C-terminal extension of *Mt*α....150

4.4 Subunit ε of *Mycobacterium tuberculosis*....156

5. Conclusions....164

5.1 Conclusions....165

6. References....167

6.1 References....168

List of author's publications....180

Conference Attendance....180

Awards....180

List of Figures

Figure 1.1: Assembled model for subunit arrangement of *E. coli* ATP synthase.....19
Figure 1.2: Adapted model for subunit composition for archaeal A_1A_O-ATP synthase.....20
Figure 1.3: Modified representation of pathogenesis of TB.....21
Figure 1.4: Modified schematic Diagram outlining the ETC components and the F-ATP synthase of *Mt* under aerobic and hypoxic conditions.....22
Figure 1.5: Side view of the $\alpha_3\beta_3\gamma$ catalytically active headpiece of the bovine F-ATP synthase showing subunits $\alpha_3\beta_3\gamma$.....27
Figure 1.6: Adapted schematic diagram outlining the pathway of the binding change mechanism.....27
Figure 1.7: Cartoon representation of subunit α from *E. coli* and *Bacillus* PS3.....29
Figure 1.8: Sequence alignment for subunit α F-ATP synthase from different species of mycobacteria, *Bacillus* genera, *B. Taurus* and *E. coli*.....31
Figure 1.9: Cartoon representation of the crystal structures available for subunit ε of *E. coli* (*Ec*ε) in the compact and the extended state.....34
Figure 1.10: Sequence alignment for subunit ε F-ATP synthase from different species of mycobacteria, *Bacillus* PS3 and *E. coli*.....35
Figure 1.11: Subunits β, ε and γ of *E. coli*.....36
Figure 1.12: Cartoon representation of the inhibitor proteins of F_1F_O- ATP synthase in *P. denitrificans* and mitochondria, IF1.....38
Figure 1.13: Superposition of SAXS structure with the peptide of the C-terminus of *Mt*ε and the N-terminal domain of the *Ec*ε.....39
Figure 1.14: Modified figure illustrating methanogenesis coupled to ATP synthesis in cytochrome free methanogens.....41
Figure 1.15: Modified representation of Methanogenesis coupled to ATP synthesis in cytochrome containing methanogen 42
Figure 1.16: Side view of the A_3B_3D represents the hexameric headpiece of the A-ATP synthase with the centrally located subunit D.....45
Figure 1.17: Subunit B of *M. mazei* Gö1.....47
Figure 1.18: Modified structure of subunit B of A-ATP synthase of *M. mazei* Gö1 showing entry of the nucleotide along with the transient I, transient II and final binding pockett.....48
Figure 1.19: Representation of the P-loop of subunit β bound to ADP and magnesium ion using Ligplot$^+$.....49
Figure 2.1: Modified pET-9d (+) vector map.....61
Figure 2.2: Guinier Plot illustrating the relation between the non-linearity of the curve and aggregation of the sample.....65

Figure 2.3: Modified figure depicting theoretical p(r) values of multi-domain proteins.....65
Figure 2.4: Kratky plots ideally observed for globular, unfolded and multi-domain proteins with linkers.....66
Figure 2.5: Illustration of working principle of Overlap Extension PCR used to generate desired product via insertion mutagenesis.....67
Figure 2.6: pET-24b vector showing full map and unique MCS used for ligation with $\alpha^{chi}\gamma\beta$.....69
Figure 2.7: Scheme for the reaction of NADH coupled continuous assay to measure ATP hydrolysis, showing the conversion of PEP to lactate through pyruvate with the generation of ATP and the oxidation of NADH.....71
Figure 2.8: Schematic representation of the Overlap Extension PCR strategy used to clone *Ec*ε Construct…….....75
Figure 2.9: Modified pET-9d (+) vector showing full map and unique multiple cloning sites (MCS) that has been used to clone various genes.....76
Figure 2.10: Schematic representation of the process of increasing fluorescence with binding of the flurophore dye to the unfolding protein with increasing temperature…….....81
Figure 2.11: 3D NMR experiments for backbone assignment showing the magnetization transfer through NMR active nuclei.....86
Figure 2.12: Pictorial illustration of the working principle of Iterative soft threshold used for reconstruction of non-uniform sampling NMR data sets.....87
Figure 3.1.1: Crystal structure of N157T of subunit B of the *M. mazei* Gö1 A_1A_O ATP synthase….....91
Figure 3.1.2: The 2Fo-Fc electron density map contoured at 1.0σ (dark blue) showing the mutation at N157T in subunit B of the *M. mazei* Gö1 A_1A_O ATP synthase.....92
Figure 3.1.3: The superposition of chain A of N157T mutant with chain A of subunit B-WT……..93
Figure 3.1.4: Structural overlap of subunit B –WT with subunit B mutant N157T of the *M. mazei* Gö1 A_1A_O ATP synthase.....94
Figure 3.1.5: The P-loop region overlap of WT-B with the N157T mutant protein and with subunit α of the bovine F-ATP synthase.....95
Figure 3.2.1: Agarose gels showing the PCR reaction products for *Mt*α and $Mt\alpha_{1\text{-}513}$.....100
Figure 3.2.2: SDS-PAGE gel showing solubility test for *Mt*α and $Mt\alpha_{1\text{-}513}$…….....100
Figure 3.2.3: Purification of recombinant *Mt*α protein using.....101
Figure 3.2.4: Purification of recombinant $Mt\alpha_{1\text{-}513}$ protein.....102
Figure 3.2.5: Forward scattering curve for *Mt*α, Guinier plot of the protein displaying linearity at low angles.....103
Figure 3.2.6: Distance distribution curve, Kratky plot and Normalized Kratky plot for *Mt*α.....103
Figure 3.2.7: Superimposition of model generated for *Mt*α on the SAXS model for subunit α, *E. coli*...104
Figure 3.2.8: Purification of recombinant PS3α.....105

Figure 3.2.9: Purification of recombinant α^{chi} protein using Ni^{2+}-NTA affinity.....106
Figure 3.2.10: Forward scattering curve and Guinier plot for PS3α.....107
Figure 3.2.11: Distance distribution curve and Normalized Kratky plot for PS3α and α^{chi}.....107
Figure 3.2.12: Superimposition of SAXS shapes PS3α with the crystal structure of PS3α.....108
Figure 3.2.13: PCR products for $\alpha^{chi}\gamma\beta$ via Overlap extension PCR.....110
Figure 3.2.14: Purification of recombinant protein $\alpha^{chi}{}_3\beta_3\gamma$.....111
Figure 3.2.15: Purification of recombinant protein $PS3\alpha_3\beta_3\gamma$.....111
Figure 3.2.16: ATP hydrolysis measurement of $PS3\alpha_3\beta_3\gamma$ and $\alpha^{chi}{}_3\beta_3\gamma$.....112
Figure 3.2.17: Visualization of laser excited quantum dots attached to the protein-bead complex under the inverted fluorescence microscope.....112
Figure 3.3.1: Cartoon representation of the subunits α and ε *Ec* (left) and *Mt* (right).....115
Figure 3.3.2: SDS-PAGE showing the expression of recombinant subunit $Mt\varepsilon_{1\text{-}120}$.....117
Figure 3.3.3: Purification of recombinant protein *Mt*ε and $Mt\varepsilon_{1\text{-}120}$.....118
Figure 3.3.4: S200 gel filtration Chromatography profile of reconstituted protein complexes of $\alpha_3\beta_3\gamma$ + *Mt*ε; $\alpha_3\beta_3\gamma$ + $Mt\varepsilon_{1\text{-}120}$.....119
Figure 3.3.5: ATP hydrolysis specific activity calculated on performing the NADH coupled hydrolytic assay of $\alpha_3\beta_3\gamma$ of *Bacillus* PS3 with the recombinant protein, *Mt*ε and $Mt\varepsilon_{1\text{-}120}$.....120
Figure 3.3.6: SDS-PAGE showing the expression of recombinant subunit *Ec*ε and PS3ε proteins.....120
Figure 3.3.7: SDS-PAGE gel showing the solubility test for PS3ε, and *Ec*ε.....121
Figure 3.3.8: Purification of recombinant protein PS3ε and *Ec*ε.....121
Figure 3.3.9: S200 gel filtration Chromatography profile of reconstituted protein complexes of $\alpha_3\beta_3\gamma$ + *Ec*ε and $\alpha_3\beta_3\gamma$ + PS3ε.....122
Figure 3.3.10: ATP hydrolysis specific activity calculated on performing the NADH coupled hydrolytic assay of $\alpha_3\beta_3\gamma$ of *Bacillus* PS3 with the recombinant protein, *Ec*ε and PS3ε.....123
Figure 3.3.11: ATP hydrolysis specific activity calculated on performing the NADH coupled hydrolytic assay of $\alpha_3\beta_3\gamma$ of *Bacillus* PS3 with the recombinant protein PS3ε at different ATP concentrations.....124
Figure 3.3.12: Sequence alignment of subunit epsilon from *E. coli* and *M. tuberculosis*.....125
Figure 3.3.13: Induction and Solubility test for protein expression of ε_{121hyb}.....125
Figure 3.3.14: Purification of recombinant protein ε_{121hyb}.....126
Figure 3.3.15: S200 gel filtration Chromatography profile of reconstituted protein complexes of $\alpha_3\beta_3\gamma$ + ε_{121hyb}.....126
Figure 3.3.16: Specific ATPase activity calculated on performing the NADH coupled hydrolytic assay for $PS3\alpha_3\beta_3\gamma$ with the recombinant protein ε_{121hyb}.....127
Figure 3.3.17: Cartoon representation of the protein complexes with α^{chi}, β and γ in the $\alpha^{chi}{}_3\beta_3\gamma$ complex.....128
Figure 3.3.18: S200 gel filtration Chromatography profile of reconstituted protein complexes of $\alpha^{chi}{}_3\beta_3\gamma$ +

*Mt*ε and $\alpha^{chi}{}_3\beta_3\gamma$ + PS3ε. 128

Figure 3.3.19: Specific activity calculated on performing the NADH coupled hydrolytic assay of $\alpha^{chi}{}_3\beta_3\gamma$ of with the recombinant protein, *Mt*ε and PS3ε.....129

Figure 3.3.20: S200 gel filtration Chromatography profile of reconstituted protein complexes of *Mm* A_3B_3D + *Mt*ε.....130

Figure 3.3.21: Purification of recombinant *Mt*$\varepsilon_{1\text{-}120}$.....131

Figure 3.3.22: CD spectrum of *Mt*$\varepsilon_{1\text{-}120}$.....132

Figure 3.3.23: ^{15}N-^{1}H HSQC spectrum of the protein *Mt*$\varepsilon_{1\text{-}120}$.....134

Figure 3.3.24: ^{15}N-^{1}H HSQC spectrum of the protein *Mt*$\varepsilon_{1\text{-}120}$.....135

Figure 3.3.25: Plots to show the Thermofluor Stability assay shifts for *Mt*$\varepsilon_{1\text{-}120}$ in different Buffers.....137

Figure 3.3.26: ^{15}N-^{1}H HSQC spectrum of the protein *Mt*$\varepsilon_{1\text{-}120}$ in Glycine buffer.....138

Figure 3.3.27: ^{15}N-^{1}H HSQC spectrum of the protein *Mt*$\varepsilon_{1\text{-}120}$ in phosphate buffer.....139

Figure 3.3.28: ^{15}N-^{1}H HSQC spectrum of single amino acid ^{15}N isotope labeled *Mt*$\varepsilon_{1120...}$.....140

Figure 4.1: Overlap of the P-loop for WT-B and mutants H156A, N157A and N157T.....143

Figure 4.2: Cartoon representation of the P-loop highlighting the site of mutation and orientation of other important residues in the vicinity.....144

Figure 4.3: Superposition of structures for subunit α from *E. coli*, *Bacillus* PS3 and bovine mitochondria.....146

Figure 4.4: Sequence alignment of P-loop of subunit α F-ATP synthase from *E. coli*, *Bacillus* PS3, *Bacillus* TA_2A_1, Bovine mitochondria, *E. faecalis* with different species of *Mycobacterium* genus.....147

Figure 4.5: Superposition of P-loop structures for subunit α from *E. coli* and *Bacillus* TA2A1……...148

Figure 4.6: SAXS structure of the *Mt*α with fitting of model obtained from I-TASSER and C-terminal peptide structure obtained from NMR.....149

Figure 4.7: Structure for *Ec*F_1.....151

Figure 4.8: Assembled model for *Mt*F_1.....152

Figure 4.9: Specific interactions in the assembled model for *Mt*F_1.....153

Figure 4.10: Angular velocity vs. rotational position plot between 2 catalytic dwells for $\alpha_3\beta_3\gamma$, $\alpha^{chi}{}_3\beta_3\gamma$ and $\alpha^{chi}{}_3\beta_3\gamma$+ *Mt*ε.....154

Figure 4.11: Schematic representation of the proposed ATP binding and catalysis events during the 120° rotation of subunit γ in $\alpha^{chi}{}_3\beta_3\gamma$ complex.....155

Figure 4.12: Surface charge representation of the *Mt* γ-ε interface.....159

List of Tables

Table 3.1.1: Crystallographic and refinement statistics of the N157T mutant of subunit B of *M. mazei* Gö1 A_1A_O ATP synthase.....96

Table 3.1.2: Hydrogen bonding interactions for the P-loop residues in WT-B and N157T mutant of subunit B of *M. mazei* Gö1 A_1A_O ATP synthase.....97

Table 3.2.1: Data collection and scattering derived parameters for subunit *Mt*α, PS3α and α^{chi} using SAXS.....108

Table 4.1.1: Binding of Mg-ATP ATTO-647N and Mg-ADP ATTO-647N to subunit B-WT and mutants H156A, N157A, N157T.....143

Table 4.1.2: Interaction of residues of subunit ε with subunits α, β and γ in TF1, EF1 and *Mt*F1.....160

Abbreviations

1D	One-dimensional
2D	Two-dimensional
3D	Three-dimensional
Å	Angstrom
ADP	Adenosine diphosphate
ATP	Adenosine triphosphate
BSA	Bovine Serum Albumin
CD	Circular Dichroism
DTT	Dithiothreitol
Mm	*Methanosarcina mazei* Gö1
Ec	*Escherichia coli*
Mt	*Mycobacterium tuberculosis*
PS3	*Bacillus* PS3
MF_1	F_1 ATPase from Mitochondria
EF_1	F_1 ATPase from *E. coli*
EDTA	Ethylenediaminetetraacetic acid
FPLC	Fast Protein Liquid Chromatography
HSQC	Heteronuclear Single Quantum Correlation
Hz	Hertz
IPTG	Isopropyl-β-D-thiogalactoside
kDa	kilo-Dalton
NMR	Nuclear Magnetic Resonance
FCS	Fluorescence Correlation Spectroscopy
NTA	Nitrilotriacetic acid
PAGE	Polyacrylamide Gel Electrophoresis
PCR	Polymerase Chain Reaction
PDB	Protein Data Bank
PPM	Parts per million
r.m.s.d	Root mean square deviation
SDS	Sodium Dodecyl Sulphate
Tris	Tris-(hydroxymethyl) aminomethane

Abstract

The ATP synthases/ATPases arose from a common ancestor and, therefore, A_1A_O ATP synthases share properties with the F_1F_O ATP synthase as present in bacteria, chloroplasts and mitochondria. Although the overall subunit composition and the primary sequence of the major subunits A and B of A_1A_O ATP synthases is fairly different to F_1F_O ATP synthases, their function similar to F_1F_O ATP synthase is to synthesize ATP. The proposed subunit stoichiometry of A_1 is A_3:B_3:C:D:F:$(EG)_2$. The integral A_O domain contains subunits *a* and *c*. Subunit B is a nucleotide binding regulatory subunit. In the present study, the crystal structure for N157T mutant of P-loop of subunit B has been solved to investigate the role of N157 in nucleotide binding. FCS studies of N157T along with the other mutants H156A, N157A and WT-B revealed that the binding affinities of H156A and N156A for ATP are stronger than those of N157T and WT-B. This feature could be attributed to the fact that the size of the binding cavity has increased on substitution with a residue containing a smaller side chain. Similar binding studies with ADP showed that in comparison to the WT-B, the mutants lost the ability to distinguish between the nucleotides, validating the importance of the histidine and asparagine in the P-loop of subunit B.

Subunit α of F-ATP synthase, the homologous subunit of subunit B, in spite of being considered as a non-catalytic subunit does bind nucleotides. Interestingly, subunit α of *Mycobacterium tuberculosis* (*Mt*α) contains a unique stretch of polar residues in its C-terminus and this is exclusive only to the species belonging to the *Mycobacterium* genus. Focus has been directed towards obtaining structural information on *Mt*α. To understand the role of its C-terminus, a chimeric subunit of α from *M. tuberculosis* and *Bacillus* PS3 (PS3) has been generated with residues 1-502 of *Bacillus* PS3 and residues 515-549 of *M. tuberculosis*. The same chimeric protein of subunit α is generated in a complex of PS3$\alpha_3\beta_3\gamma$ to give $\alpha^{chi}{}_3\beta_3\gamma$ and is studied to understand the role of the fused C-terminus of *Mt*α in the ATP hydrolysing activity. The elongated shape and length of *Mt*α led to the speculation that this is an adaptation to compensate for the shorter length of subunit ε in Mycobacteria.

Subunit ε of the F-ATP synthases is essential for the coupling of F_1 and F_O domains. This subunit exists in two conformations, compact and extended. In the extended state subunit ε functions as the intrinsic inhibitor for ATP hydrolysis and hence importantly, prevents wasteful hydrolysis to conserve cellular ATP levels. The same is observed for the F-ATP synthase of *M. tuberculosis*, where ATP hydrolysis is reduced during the latent phase in the course of infection of the pathogen. Encouraging ATP hydrolysis to occur will eventually result in cell death and

therefore, subunit ε presents an interesting drug target for TB. The disease is difficult to tackle, given the emergence of multi drug resistant strains and hence there is an urgent need for new drug leads and targets. Currently, no information is available on the high resolution structure of subunit ε of *M. tuberculosis* and much in regard to its mechanistic role needs to be explored. In the present study, I have worked towards obtaining structural information about the subunit ε and have generated constructs with C-terminal truncation to yield a stable protein. For the construct *Mt*ε_{1-120}, a well resolved 2D ^{15}N-^{1}H HSQC spectrum was recorded. Various new age methodologies such as Non- Uniform Sampling and ^{15}N Single amino acid labelling have been employed for 3D NMR and attempts have been invested with crystallisation techniques to garner data to elucidate the structure of this protein. To explore the mechanistic features, chimeric proteins of *M. tuberculosis* and *E. coli* (*Ec*) were generated and have been studied parallel to *Ec*ε and PSε to gain insight into the functioning of *Mt*ε. *Mt*ε on reconstitution with PS3$\alpha_3\beta_3\gamma$ had no effect on the ATPase activity of the PS3$\alpha_3\beta_3\gamma$ complex. *Ec*ε also similarly did not alter the activity of the complex PS3$\alpha_3\beta_3\gamma$. In contrast, PS3ε on reconstitution increased the ATPase activity of PS3$\alpha_3\beta_3\gamma$, highlighting the specific interaction required between the subunits α and ε. This observation was further validated by reconstituting $\alpha^{chi}{}_3\beta_3\gamma$ with *Mt*ε that showed increased ATPase activity. Taken together, these studies demonstrate that the shorter length of *Mt*ε is compensated with the longer *Mt*α.

1. Introduction

1.1 Introduction to ATP synthases

Most cellular activities, inclusive of metabolism, motility and active transport of essential molecules across membranes require the energy currency, ATP (Adenosine Triphosphate). ATP synthase, a nanoscale enzyme present in all forms of life couples ATP synthesis/hydrolysis to usage/generation of electrochemical membrane potential. The catalytic activity is achieved by the rotation and cooperation of the individual subunits, which is not commonly observed in biological systems. Hence, endowing them with the name of rotary enzyme, a term that is used only otherwise in case of bacterial flagella [1][1][1] .

Currently accepted nomenclature, classifies this rotary enzyme in 3 major classes on the basis of their location and function. It is believed that the 3 distinct classes of this enzyme arose from a common ancestor [1, 2]. Evolution in terms of structural and functional changes allowed for the development of this enzyme in the three domains of life [3, 4]. F_1F_O ATP synthase present in mitochondria, bacteria and chloroplasts use transmembrane movement of ions, driven by the electrochemical gradient to drive the endothermic phosphorylation of ADP to ATP [5]. The function of this enzyme as a nano-scale motor has been intensively studied and demonstrated by single molecule rotation studies. The second class of enzymes are the V_1V_O ATPases that operate as ATP driven ion pumps in eukaryotic membranes [6]. A_1A_O ATP synthases have been identified as the third class in Archaea, which are believed to be the closest to the origin in the tree of life and hence are believed to serve as the most suitable models to study the energy convertors as in the primitive organism [2]. A_1A_O synthases predominantly function in the ATP synthesis mode, with the unique ability to use both H^+ and Na^+-gradients [7]. However some species such as *Pyrococcus* have been shown to possess fermentation activity, hence allowing it to function in both synthase and ion pump mode [8].

The name for each of the ATP synthases have been assigned as described below. Phosphorylation factor, is where F_1F_O is derived from, with '1' standing for the first factor to be identified and 'O' stands for the oligomycin binding site present [9]. A_1A_O denotes the similar components of the enzyme in Archaea and V_1V_O stands for the enzyme initially identified to be located in the Vacuoles.

ATP synthases work at very high efficiency in terms of energy transformation. and their importance is illustrated from the fact that a person can produce enough ATP per day that equals one's own body weight [10].

1.2 Physiological roles of the rotary ATP synthases

F_1F_O ATP synthases predominantly work towards the synthesis of ATP with the expenditure of the electrochemical gradient. However, in the case of mitochondrial F_1F_O ATP synthases, under hypoxic conditions, where the proton motive force (pmf) declines, the enzyme starts to work in reverse to hydrolyse ATP and re-establish the electrochemical membrane potential [11-13]. The wasteful hydrolysis is controlled by Inhibitory factor protein (IF_1) that binds to block the catalytic cycle [14-17]. Similar reversibility of function of ATP synthases is seen in anaerobic bacteria and in chloroplast, with the inhibition being strongest in chloroplast during the dark cycles [5, 18]. Na^+-powered bacterial F-ATP synthases are seen in *Propiogenium modestum, Ilyobacter tartaricus* [19-21].

V- ATPases function mainly to maintain a steady pmf to acidify the vacuoles and also energise secondary active transport, although their ability to synthesise ATP has been demonstrated, *in vitro*. [22, 23]. In Archaea, ATP synthases are endowed with the ability to utilise H^+ (*Sulfobolus* and *Methanosarcina*), Na^+-(*Pyrococcus*) or both H^+-and Na^+-(*M. ruminatium*) ion gradients to channelize the driving force needed to function [24-32].

With reference to the relevant work in this field, some of the bacterial A-ATP synthases have been referred to as the V-ATPases as in *E. hirae* and *T. thermophilus* [4]. A-ATP synthases share high sequence similarity with V-ATPases and high functional similarity with F-ATP synthases. However, the accepted classification of the three classes is largely justified on the basis of the subunit composition, allowing all bacterial A-ATP synthases to be classified as A-ATP synthases and eukaryotic vacuolar ATPases as V-ATPases [24, 33]. Hence bringing more clarity to the distinction of the three classes.

1.3 Subunit composition of F_1F_O and A_1A_O-ATP synthases

In simple terms, F-ATP synthases consists of two functional domains: a hydrophilic sector, F_1 and an intramembranous, hydrophobic sector called F_O. Ions (H^+/Na^+) cascade down their concentration gradient to the mitochondrial inner membrane or bacterial plasma membrane or thylakoid membrane of chloroplasts through the specific channels localised in the F_O sector of the ATP synthase complex. The energy required by the F_1 for the catalysis to generate ATP is provided by this process. [34]. The F-ATP synthase of *Escherichia coli*, a ~530 kDa protein complex is considered as a model organism and figure 1.1 shows the complete assembled structural model from the available high resolution data of single subunits or domains for the F_1F_O ATP synthase complex which comprises of eight subunits (Figure 1.1).

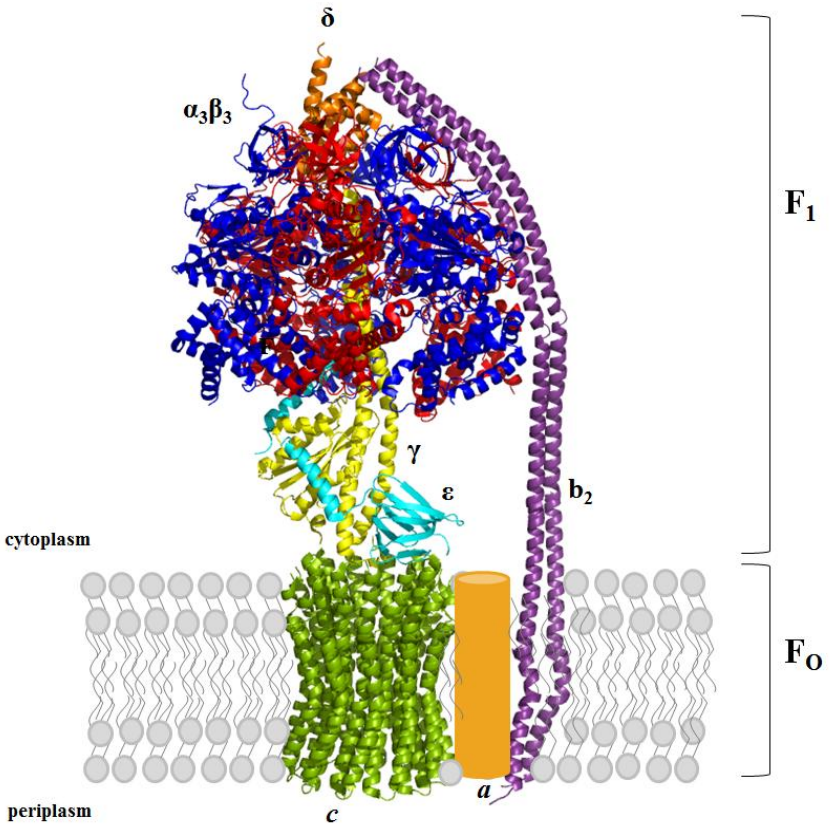

Figure 1.1: Assembled model for subunit arrangement of *E. coli* ATP synthase structure using PyMOL [35]. The model has two broad domains, F_1 and F_O. F_1 corresponds to $\alpha_3\beta_3\gamma\delta\varepsilon$ and F_O to $ab_2c_{10\text{-}14}$ [19]. The structures for the individual subunits were taken from RCSB Protein Data Bank [36]. The structures used were from the *c*-ring of *Ilyobacter tartaricus* (IYCE), F_1 complex of *E. coli* (3OAA), the δ- subunit of *E. coli* (2A7U), the peripheral stalk from bovine mitochondria (2CLY), the tether domain of subunit b from *E. coli* (2KHK) and the membranous part of subunit b of *E. coli* (1B9U) [18, 21, 37-40].

The F_1 domain is composed of five subunits, α, β, γ, δ, and ε, with a definite proportion of $\alpha_3\beta_3\gamma\delta\varepsilon$ and this nomenclature is assigned to subunits in decreasing order of their molecular weights. The F_O sector of bacterial ATP synthases comprise of subunits, *a*, *b* and *c*, with the proposed stoichiometry of $a{:}b{:}c_{9\text{-}14}$ [41]. However, species of mycobacteria have *b* and *b'* subunits with the latter fused with subunit δ [42].

The equivalent structure in A_1A_O-ATP synthases is $(AB)_3$:D:F:$(EH)_2$:C:a:c_x, with the A_1 composed of a A_3B_3 headpiece, two peripheral stalks and a central stalk, a membrane-embedded ion-translocating part A_O (Figure 1.2) [43, 44]. The central stalk is formed from Subunits F, D and C and subunits E and H heterodimer are the two peripheral asymmetric stalks which are elastic [45]. ATP is synthesized in the A_3:B_3 hexamer and the energy provided for or released during that process is transferred to the A_O domain, of subunit *a* and subunit *c*, and the two active domains are energetically coupled via the stalk part.

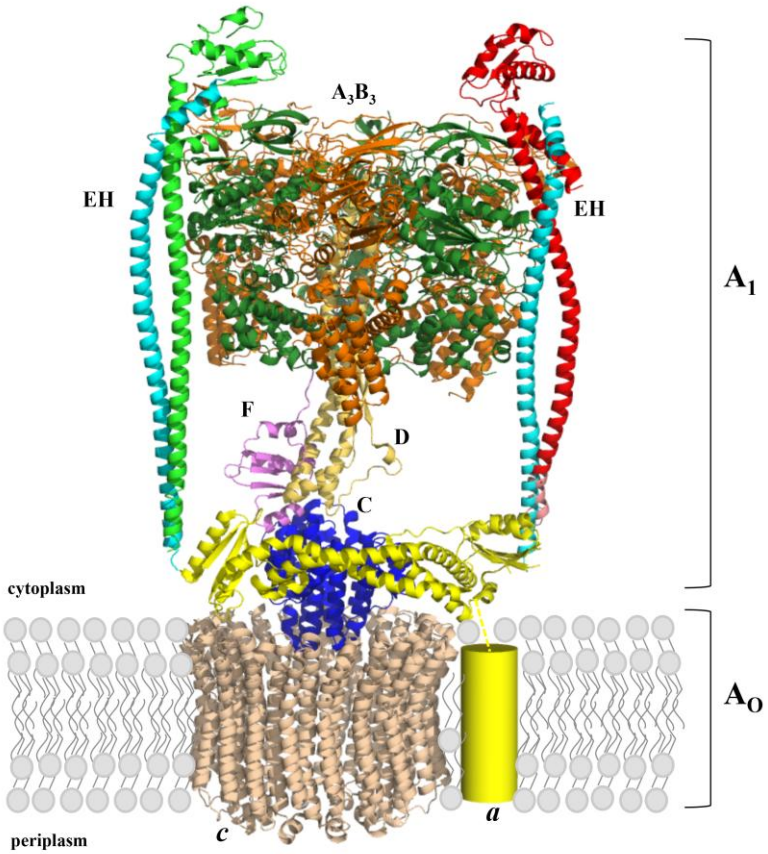

Figure 1.2: Adapted model for subunit composition for archaeal A_1A_O-ATP synthase[45][45]. The structures for the individual subunits were taken from RCSB Protein Data Bank [36]. The PDB accession code for the structures used are as follows; subunit A of *P. horikoshii* (3I4L), subunit B (2C61), *c*-ring (2BL2), subunit F of *M. mazei* Gö1 (2OV6), subunit C of *T. thermophilus* (1R5Z), subunit D of *E. hirae* (3AON), subunit H of *T. thermophilus* (3K5B), subunit E of *P. horikoshii* (4DT0) and subunit *a* of *M. ruber* (3RRK) [45-52].

The ATP synthases considered for study in this thesis are the A-ATP synthase of *Methanosarcina mazei* Gö1 (*Mm*) and F-ATP synthase of *Mycobacterium tuberculosis* (*Mt*). Both these species spike great interest with respect to their bioenergetics given their great adaptability to extreme environmental conditions that they encounter. The unique features of both these organisms and their ATP synthases are detailed in the following sections.

1.4 Overview of *Mycobacterium tuberculosis*

The genera mycobacteria are classified under Actinobacteria and species belonging to the *Mycobacterium* genus are mostly free living saprophytes, well adapted to soil and aquatic habitats [53]. Most important pathogenic forms are *M. bovis* causing cattle tuberculosis, *M. leprae* causing leprosy and *M. tuberculosis* responsible for tuberculosis (TB) in humans primarily with pulmonary infection but also capable of affecting other organs such as the spine.

Mycobacterium tuberculosis unlike any other pathogen has an unparalleled spread given its prototrophic and flexible metabolic feature. *Mycobacterium tuberculosis* (*Mt*), the aetiological agent of TB remains one of the world's top infectious killers with new cases accounting to about 9 million being reported of the actively spreading TB disease. Apart from the two million deaths that have been reported per year, TB is also the leading killer of people living with HIV [54]. Its unusual cell wall is rich in lipids (mycolic acid), which is responsible for resistance and is a key virulence factor. The composition of the cell wall of the bacteria contains a remarkable mixture of polyketoids, lipoglycans, lipids and glycolipids [55]. The bacteria is also endowed with genes to code for enzymes involved in alternative lipid metabolism, in which exogenous lipids are metabolised by the breakdown of host cell membranes [56]. The ability of *Mt* to maintain the chronicity of the infection is attributed to its ability to switch to cholesterol metabolism by drawing lipid sources from the host [57].

The success of *Mt* as a pathogen can be attributed to its extraordinary sleuth and capacity to combat the environmental changes throughout the course of infection. The changes include: nutrient deprivation, hypoxia, various exogenous stress conditions and the intraphagosomal environment [58]. Currently available antimycobacterial agents are not capable of killing the bacteria leading to a state of drug unresponsiveness and hence allowing *Mt* to enter a latent or persistent phase in the course of infection. In the lungs, *Mt* is confined and thrives within a hypoxic microenvironment [59]. In theory the capacity of dormant bacilli to survive chemotherapy is justified by the existence of both aerobic and anaerobic microenvironments (Figure 1.3).

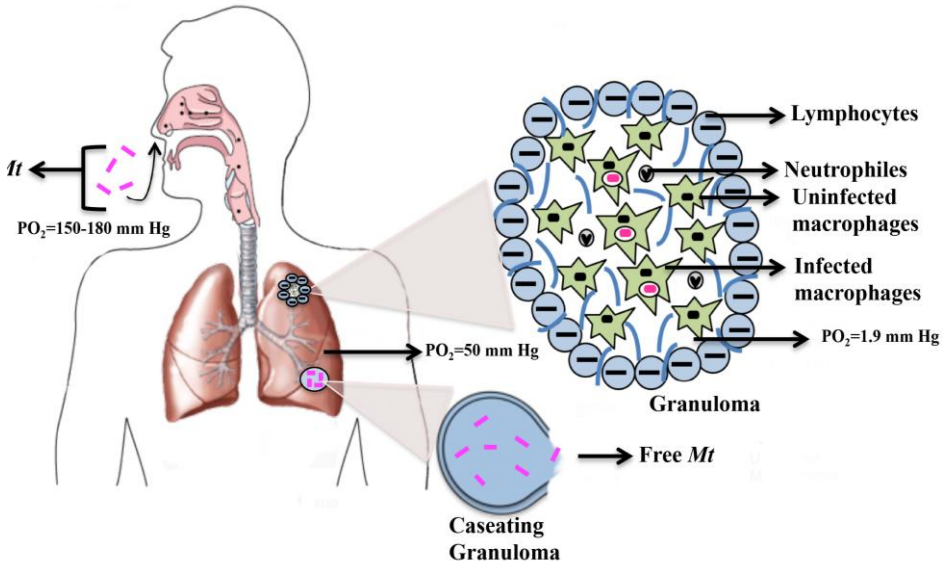

Figure 1.3: Modified representation of pathogenesis of TB [60]. The alveolar macrophages that engulf the pathogen are transformed into the caseous granuloma, where the bacterium survives in the hypoxic state by shifting to the dormant phase [61].

The destruction of the orderly state (life) of a cell eventually leading to its death is caused by the lack of O_2 that in turn causes a loss of energy. Interestingly, *Mt* manages to remain viable with its extraordinary capacity to decrease respiration to a low, albeit not zero level. In vitro demonstrations have shown Nitrate (NO_3^-) to prolong the survival of *Mt* under anaerobic growth conditions [62], but active replication was not promoted. ATP is decreased to 25% of aerobic levels during hypoxic growth of *Mt*, agreeing with the expected consequences of respiratory inhibition [63]. In order to preserve ATP-homeostasis during hypoxia, *Mt* is shown to maintain a fully energised cytoplasmic membrane. This is achieved without involving alternate terminal electron acceptors (NO_3^-, fumarate, etc.) for respiration [64]. These studies indicate that to maintain an energised membrane even in the absence of respiration during hypoxic persistence, *Mt* adopts low levels of metabolic activity (Figure 1.4).

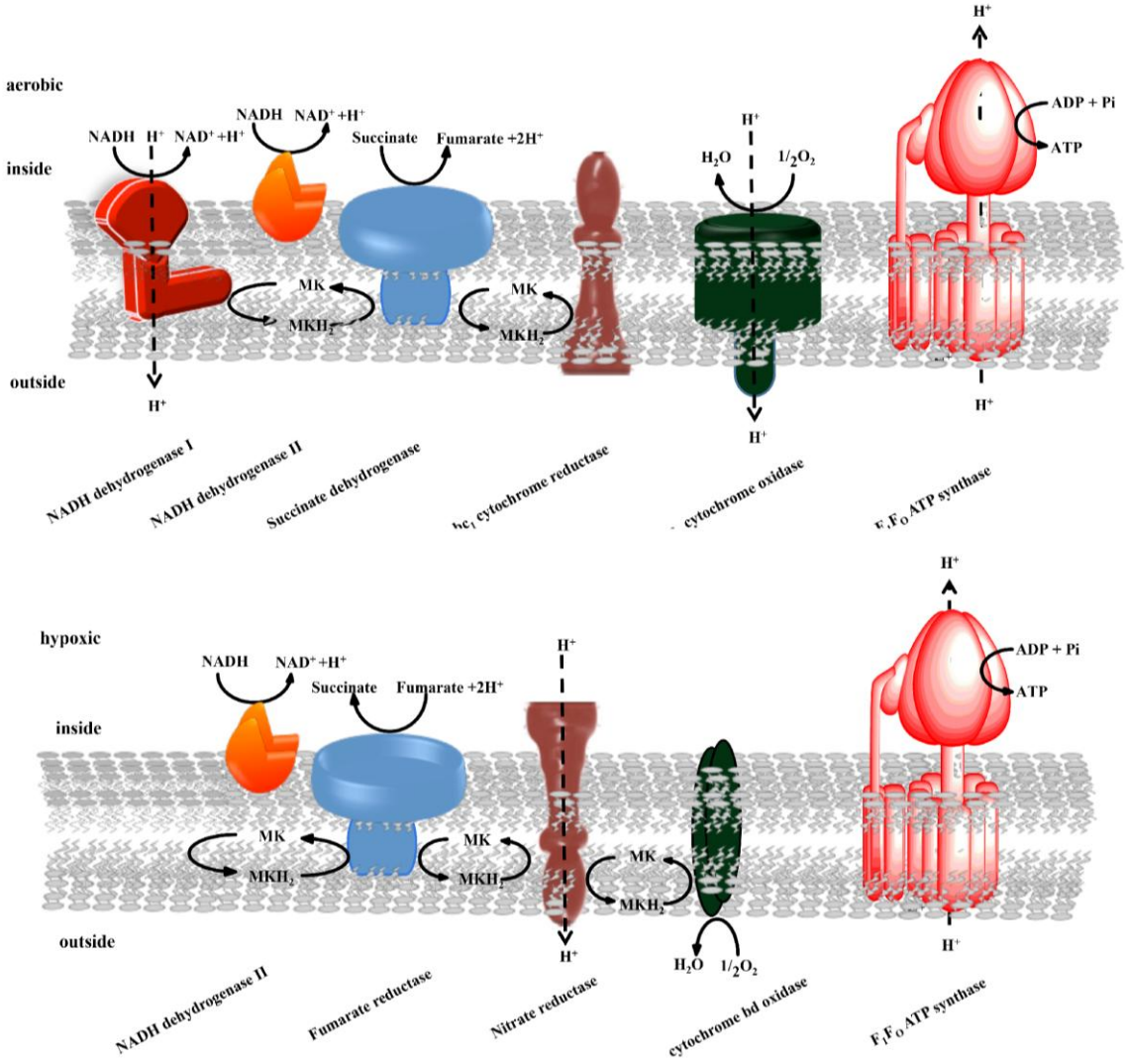

Figure 1.4: Modified schematic Diagram outlining the Electron Transport Chain (ETC) components and the F-ATP synthase of *Mt* under aerobic and hypoxic conditions [58]. In the hypoxic state, only the NADH dehydrogenase II functions, the Nitrate reductase acts as the terminal electron acceptor and the cytochrome *bd* oxidase is up regulated.

NDH-2, type II NADH dehydrogenase, upregulated during dormant phase, plays an essential role and its inhibition proves to be bactericidal for *Mt* [64]. Also to be noted is the down regulation of NDH-1, cytochrome bc_1 and cytochrome aa_3 complexes [65, 66]. Over expression of cytochrome *bd*-type oxidase allows for redox balance in the dormant state [66]. The role of the terminal acceptor is adopted by nitrate reductase, which is over expressed and adds viability to the dormant state [62, 67, 68]. As seen in mouse models, the ATP synthase is also down regulated given the low O_2-availability in the growth hindered state [66, 69]. Additionally, in the latent phase, cellular ATP levels are ~10 fold lower when compared with actively replicating tubercule bacilli [62, 64, 67, 68]. Although an energised membrane is maintained, in comparison to other bacteria a lower pmf of -110 mV is maintained [64]. Uncouplers and ionophores that target the pmf can prove to be detrimental for the bacterium [64]. Both nitrate reductase and succinate dehydrogenase can be considered as suitable candidates to affect the pmf, while NDH-II does not qualify given that it is not involved in H^+ translocation [64, 70-72]. The succinate dehydrogenase functions in reverse as fumarate reductase and this is considered as an important link for the oxidative flux between the Kreb's cycle and electron transport chain. Interrupting the functioning of this enzyme has been proven to regulate aerobic respiration, as most ATP in mycobacteria is generated via oxidative phosphorylation [73].

Overcoming the available first line antibiotics for treating TB, emergence of multi drug resistant strains of *Mt* have been declared as a threat to global health. Expensive treatment and unresponsiveness to standard drugs are the difficulties faced with multidrug-resistant TB (MDR-TB). Inappropriate or improper usage of anti-TB drugs are the root cause of multi-drug resistance. Rarely reported are cases that are deadlier than multi-drug resistant TB that may develop with bad treatment and these respond to even fewer available medicines and are referred to as extensively drug-resistant TB (XDR-TB). Hence, there is a dire need for new drugs and F-ATP synthase is a strongly verified drug target for the treating tuberculosis [69]. Diarylquinones have been identified to target the *M. tuberculosis* F-ATP synthase in both dormant and actively replicating state of mycobacteria [69]. Bedaquiline that belongs to the class of diarylquinones differs from the other first line antibiotics like rifampicin and isoniazide, as it is effective against both the active and latent phase of mycobacteria [64, 67, 73]. Residues essential for binding Bedaquiline are present in the subunit *c* of the mycobacterial ATP synthase [41, 74-77]. Various biochemical and binding studies have provided insight into the binding site for Bedaquiline [78]. Modelling studies have suggested the binding site at the interface of subunit *a* and *c* [79, 80]. However, binding studies conducted with the subunit ε of *Mt* and the drug lead to the proposal that the drug binds like a wedge at the interface of the subunits ε and *c* [81]. A recent study on

the sequence alignment of the ATP synthase from *M. tuberculosis* reveals a unique drug target in subunit γ [78]. Subunit γ is a major component of the central stalk of the ATP synthase enzyme and in mycobacteria it has been shown to house a sequence of 13 amino acid residues that are unique to them and absent in other prokaryotic or eukaryotic homologues [78]. This stretch γG165-D178, consisting of acidic and polar residues has been analysed using NMR analysis and the peptide structure has been modelled into the available high resolution structure of the F ATP synthases structure of *E. coli* [82]. The proximity of this highly charged loop to the subunit *c* opens up the possibility of interaction with specific residues to function in gating proton flow and also modulate elastic properties of γ and *c* subunit to improve the enzyme efficiency [83]. Given the combined role in activity and stability, γG165-D178 may serve as a valid drug target for enzyme activity regulation [82].

Benzothiazinones are another class of mycobacterial drugs that target the mycobacterial epimerase enzyme [84, 85]. Combination treatment of pyrazinamide and diarylquinones has been shown to shorten the treatment duration [86, 87]. A recent study has been made to decipher the mechanism of action and Bedaquiline is believed to bind at the subunit *a* and *c* interface and affect the proton cycling, which proves to be lethal to *Mycobacterium* and this offers an explanation to the delayed onset and the bactericidal action of Bedaquiline [88].

Bedaquiline is marketed as Sirutro on approval by U.S Food and Drug Administration (FDA) and is proven to be effective against MDR and XDR-TB. Adverse effects of affecting the heart, nausea, joint and chest pain and headaches have been reported, compelling the need for a more effective drug lacking potential side effects to treat TB [85]. With the newly emerging TDR (totally drug resistant) –TB, the need to further explore the possibility of a new effective drug has been pursued by recent research work [89]. Quinoline, a class of aryl-sulfonamide has been identified to target the F-ATP synthase and is active against both replicating and non-replicating *M. tuberculosis* H37rv. This lead compound is considered as a promising candidate for further preclinical evaluation to pave path for more effective TB therapeutics [89].

M. tuberculosis H37rv genome consists of a 4.41 Mega basepair circular chromosome coding for 3,924 proteins, of which only a small fraction have been expressed and high resolution structures have been obtained for [90]. This presents an exciting challenge of expressing a soluble protein from *Mt* to study the high resolution structures and hence decipher the protein-protein interactions to further our knowledge about the pathogen that has been a serious disease threat. From being discovered in Egyptian mummies from 2000 BC, it has stood the test of time and has survived under various names (consumption, lupus vulgaris, white plague, Phthisis) and

today is commonly referred to as the XRD-TB. Detailed meticulous research to unravel the bioenergetics of this organism holds the key to the development of drugs to eradicate this disease.

1.5 Niches and adaptations of mycobacteria to survive harsh conditions in macrophages

Within the human body, tubercle bacilli encounter reactive O_2 intermediates (Reactive Oxygen species-ROS), acidity within phagosomes of macrophages, low O_2 tension and toxic lipases and proteases released by dead immune cells. Infected individuals transmit the bacilli via cough. The expelled droplet carries the *Mt* bacterium that is suspended in air. On inhalation, the bacteria reach the lungs, wherein they are engulfed by the alveolar macrophages, which are incapable of destroying the bacterial invasion. Bacilli replicate actively until the human immune system recruits INF-γ to activate the macrophages. INF-γ activated macrophages attempt to limit pathogen growth through tryptophan starvation [91]. *Mt* responds to this by making its own tryptophan [92]. Based on various host responses, *Mt* combats these effects by differently regulating its genes, as highlighted below. Efficiency of killing mycobacteria is enhanced along with production of ROS and acidic stress by the host. In response, *Mt* rescues itself from this oxidative insult by upregulating anti-oxidant enzymes such as superoxide dismutase (SodA and SodC), catalase (KatG), etc [60]. Also *Mt* shifts to lipid metabolism given its availability in the phagosomes, which lack carbohydrates. This is supported by the upregulation of the *icl* (isocitrate lyase), the key enzyme in the glyoxylate shunt allowing utilization of fatty acids as energy source. Other genes responsible in cell wall component production, anaerobic respiration and stress responses are also upregulated [9, 17, 65].

Mt in its dormant state is mainly focussed on maintaining membrane potential, cell wall integrity and guarding its DNA [68]. ROS are encountered by the activated macrophages containing the tubercule bacilli. Additionally, nutrient limitation along with oxidative stress causes the mycobacteria to shift to stationary growth phase [68]. Mycothiol is a unique component in mycobacteria that is used to combat oxidative stress. Glutathione is the equivalent oxidative stress neutraliser in other bacterial systems. The cysteine residues of Mycothiol are oxidised to form Mycothione thus preventing the oxidation of other molecules in the mycobacterial cell.

Activated macrophages by INF-γ with virulent mycobacteria have lowered intraphagosomal pH which is toxic to bacilli [74, 75, 93]. Mycobacteria are endowed with a thick waxy cell wall that enables them to resist acidic stress. Genes responsible for cell wall ultra-structure are

upregulated immediately on imposition of acidic stress [94]. Longer exposure to acidic stress stimulates production of triacylglycerol that serves as an energy source not only to combat the stress and survive in dormancy but also to come out of dormancy state.

The response to the low O_2-tension faced in the granulomas is offered by a two component system DosS/ DosT-DosR that as part of Dormancy regulon upregulates genes. DosR plays the role of transcriptional regulator and DosT and DosS are sensor kinases acknowledging low O_2 tension and Nitric oxide levels [95, 96]. DosR in turn upregulates *hspx* that handles refolding of proteins that were damaged by low O_2 tension [97, 98].

The caseating granuloma breakdown during the later stages of infection and their liquefaction releases host lipases and proteases that damage host tissues. This effect is further enhanced by the lytic enzymes released by dead macrophages. The liquid sputum carrying the free *Mt* is expelled from the lung cavities through coughing. Studies have revealed that the high lipid levels in the sputum induced by DosR regulon allow for mycobacterial persistence even *ex-vivo*, until they meet a new host [67, 68]. *Mt* possess 88 toxin-antitoxin systems within their genomes that enable them to alter growth rate when responding to environmental stress. Also, this system enhances their innate antibiotic resistance, allowing them to survive stress [68].

Mycobacteria on entering a human host have to deal with a plethora of stress for which their waxy cell wall offers great protection. However, the host continues to adopt various mechanisms to further eliminate the bacterial invasion, to which the mycobacteria respond by upregulating certain genes to reinforce their defence against the varied toxic insults of the host. These adaptations allow them to thrive in the host system in latent or active phase [68].

1.6 Organisation and Functioning of F_1 and F_O domains

No complete high resolution structure for an active F-ATP synthase complex has been solved to date. However, the F_1 domain being more amenable to crystallography has been solved to 1.9 Å from the F-ATP synthase of the bovine mitochondria [99]. The F_1 $(\alpha\beta)_3$ complex has pseudo-6-fold symmetry, with each α–β interface forming an active site [100] (Figure 1.5). The three α–β units are rendered non-equivalent due to the asymmetrical interaction with the γ subunit axle hence adopting different active site conformations. In the F_1-ATPase, two catalytic sites have similar conformations (termed β_{TP} and β_{DP}) and bind Mg^{2+} and AMP-PNP (equivalent to Mg^{2+}-ATP) and Mg^{2+}-ADP, respectively [100]. In the ground state of F_1-ATP synthase crystal structures, the third site has a much more open configuration and is empty (β_E) [99].

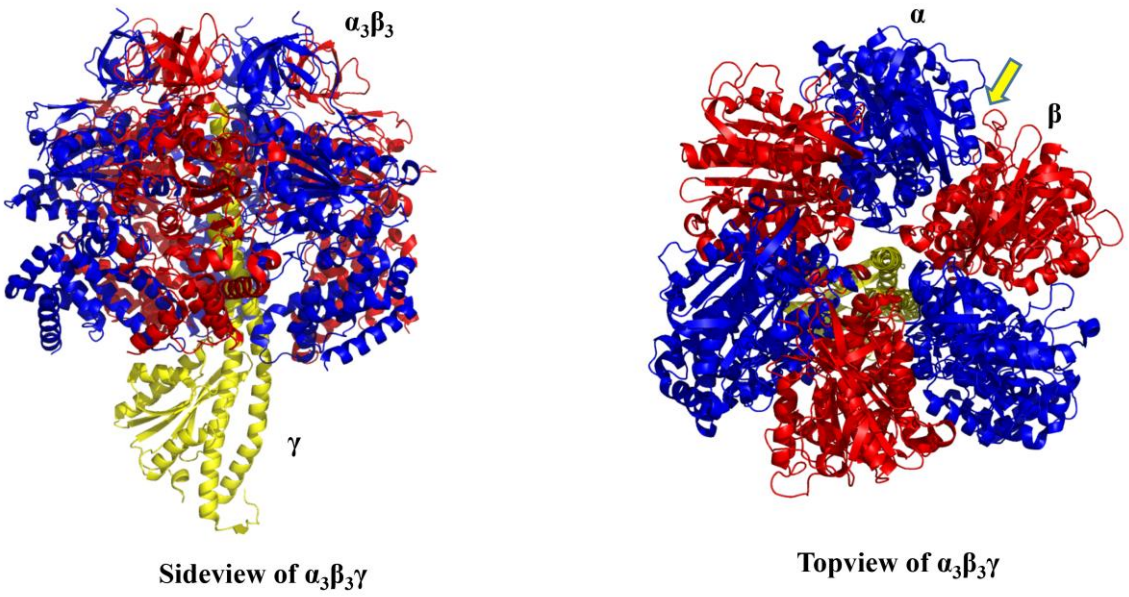

Figure 1.5: Side view of the $\alpha_3\beta_3\gamma$ catalytically active headpiece of the bovine F-ATP synthase showing subunits $\alpha_3\beta_3\gamma$. The top view of the subunits $\alpha_3\beta_3\gamma$ shows the hexameric arrangements of the alternating subunits of subunits α and β with γ situated at the centre. The interface for nucleotide binding is highlighted with a yellow arrow. (PDB ID: 3OAA) [18].

During ATP hydrolysis, each site cycles sequentially through E → TP → DP→E states, where E, TP and DP stand for Empty, ATP occupied and ADP occupied sites, respectively. The transition to the closed β_{TP} state is driven by ATP binding to one site having knock-on effects on the conformations of the other two (Figure 1.6) [10]. These changes are mediated primarily by the stepped rotation of the axle γ subunit and also include effects transmitted through adjoining α subunits.

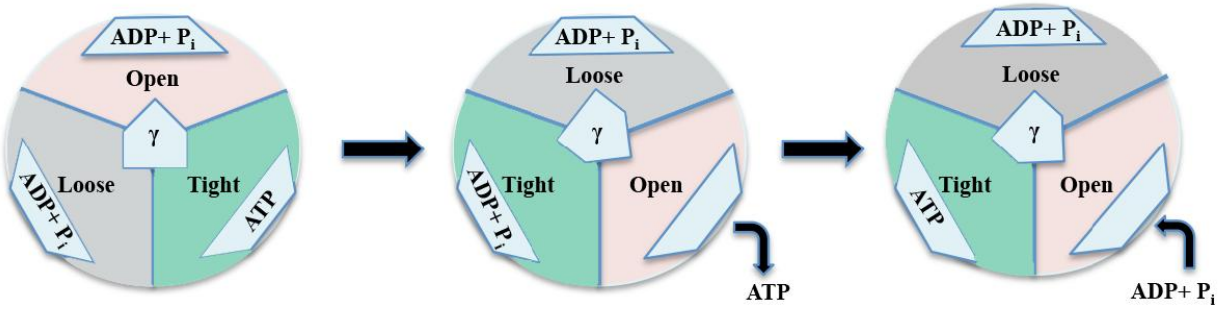

Figure 1.6: Adapted schematic diagram outlining the pathway of the binding change mechanism. The sequential changes occur in the three subunit β sites as result of the interaction with subunit γ during catalysis. [10]

In a transition state, analogue crystal structure (F_1-TS) in which β_{TP} and β_{DP} are occupied by ADP-AlF_4^-, β_E is actually in a 'half-closed' conformation bound by ADP and sulphate (mimicking phosphate), and is presumed to reflect the active site state post-hydrolysis but

preceding product release [101]. ADP binding to β_{DP} is stabilised by azide that also mimics the binding of inorganic phosphate [102]. In the absence of azide, this site can be occupied by AMP-PNP, suggesting that it represents the 'live' site poised to hydrolyse ATP [99]. The active sites show differences even in the absence of bound Mg^{2+} and nucleotides, underlining the influence of interactions with the axle [103]. In an effort to define the order of substrate release, another intermediate in the catalytic cycle has been captured. This structure of F_1-ATPase from bovine heart mitochondria is termed F_1-PH as the crystals were grown by diminishing magnesium ion concentration and by including phosphonate in the mother liquor. In this structure, the β_E is occupied by ADP without magnesium or phosphate, thus illustrating that the nucleotide is the last of the products to be released during ATP hydrolysis [104].

The three conformers equate to the 'open', 'loose' and 'tight' states described by Boyer's binding change mechanism, which reconciles the strong negative cooperativity for substrate binding shown by the three catalytic sites with the observed positive cooperativity of catalysis [10].

Connected to the centre of the $(\alpha\beta)_3$ head complex is the central stalk consisting of one γ and one ε subunit (Figure 1.1). The two α-helices are arranged in a coiled-coil configuration in the γ subunit. The peripheral stalk is attached to the side of the head for stabilization and is capped by a δ subunit on top of two *b* subunits (Figure 1.1).

Subunit *a* is positioned adjacent to a circular ring of subunits *c* in the membrane-embedded region of the F_O domain that surrounds and interacts with the central stalk. In between the subunits *a* and *c* are the ion channels in the F_O domain [34]. In F_O, with protons flowing down their concentration gradient across the proton channel, rotation in 120° increments of subunits *c* and the F_1 central stalk occurs [34].

Each subunit *c* carries a glutamate residue that is exposed on the external surface of the *c*-ring at the centre of the membrane. The protonation and the successive deprotonation of each glutamate generates rotation. On protonation the ionised carboxylate of the glutamate residue is moved by Brownian motion to an increased hydrophobic environment causing rotation of the *c*-ring. Each carboxylate is neutralised on reaching an environment in subunit *a* allowing the release of the proton into the mitochondrial matrix [105].

Across species, an intramembranous, positively-charged arginine residue (R210) in the F_O domain is highly conserved and mutation on this residue is shown to disable the *E. coli* ATP synthase enzyme. It is believed that the positive charge of arginine aides in repelling the positively-charged H^+-ions, promoting their discharge to the N-side of the mitochondrial inner membrane from their *c*-ring binding site [106].

1.7 Subunit α of F_1F_O ATP synthase

The catalytic core of F_1 comprising the $\alpha_3\beta_3$ pseudo-hexamer is capable of high rates of ATP hydrolysis or synthesis and its central cavity space is filled in by the γ-ε central stalk. The elongated portion fills the cavity, while the rest of the γ-subunit extends towards the membrane domain F_O part.

The cleft at the α-β interface localizes six nucleotide binding sites, with only three involved in catalysis. The residues responsible for binding and stabilising the nucleotide are contributed by both the subunits α and β, with the major contribution coming from subunit β for the catalytic sites and from subunit α for the non-catalytic ones. The Phosphate binding loop responsible for nucleotide binding is referred to as P-loop or the Walker-A motif and is present in both subunits α and β despite their difference in catalytic potential. Figure 1.7 shows the crystal structures available for subunit α of *E. coli* and *Bacillus* PS3 with the overall architecture conserved with the N-terminal β-sheets domain, a central α-β domain and a C-terminal α helical domain.

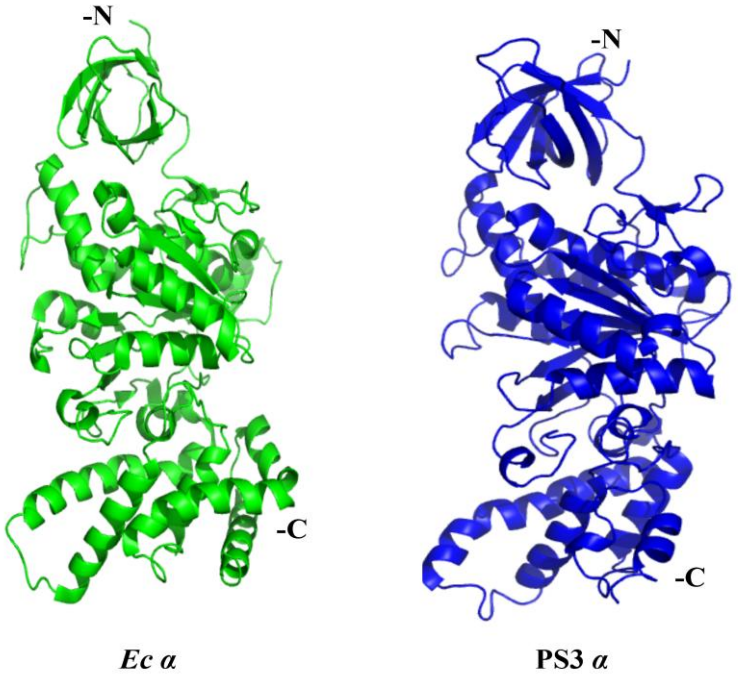

Figure 1.7: Cartoon representation of subunit α from *E. coli* and *Bacillus* PS3 displaying similar overall architecture. (PDB ID: 3OAA and 1SKY) [18, 107].

A positively charged lysine residue (αK175) interacts with the negatively charged terminal phosphate of the nucleotide. αT176 binds the Mg^{2+}-ion, which in turn stabilises the polyphosphate tail of ATP/ADP. βY368 is responsible for the hydrophobic interaction with the adenine part of the nucleotide. The *E. coli* F_1 sites show very similar selectivity for ATP and ADP, K_d=20 μM, unlike the mitochondria and chloroplast enzyme [108, 109]. Genetic

modifications of these sites are shown to cause inactivation, with αD261N mutation causing a decreased ATP binding. αK175A/αT176A/αD261A/αD262N mutant completely lacked the ability to bind ATP and ADP to the non-catalytic sites [110-113]. But as illustrated in MF_1, CF_1 and *Bacillus* PS3, binding of ATP is essential for stimulation of ATPase activity of the enzyme. In the course of multiple turnover of ATP hydrolysis, Mg-ADP is prone to be entrapped in the catalytic sites leading to enzyme inactivation. ATP-binding to the non-catalytic sites brings about a stimulation that is due to the attenuation of ADP inhibition. The release of the inhibitory ADP from the high affinity catalytic sites is facilitated by ATP-binding to the non-catalytic sites. Binding of pyrophosphate to the non-catalytic site has shown a similar effect. However, binding of ADP to these sites can cause hysteretic inhibition as seen for MF_1. This is presumed to block the binding of ATP to these sites thus not allowing the above described activation from happening [114].

Cross-linking studies performed in the F_1 of *E. coli* show interactions between the ε and α subunits in the presence of Mg^{2+}-ADP, indicating a significant movement, which would allow for the mechanism of cooperative ATP hydrolysis/synthesis [115]. The catalytic β and non-catalytic α are fairly similar in the region of the N-terminus and with respect to the residues in the nucleotide binding domain. The major difference arises in the C-terminus, which is responsible for selective and sequential interaction of subunit γ with subunit β to bring about catalysis. With the help of cross linking studies, the C-terminal interactions of the subunits α and β across the non-catalytic site interfaces has been shown to inhibit ATP hydrolysis activity [116].

A recent study was performed on the catalytic subunit A of the A-ATP synthase of *Thermus thermophilus* (*Tth*), which is sensitive to ADP inhibition and subunit A of *Enterococcus hirae (Eh)* is not. Chimeric proteins were generated for *Tth*, fusing its own N-terminal domain with Nucleotide binding (NB) and C-terminal (CT) binding domains from the *Eh*, to ascertain the domain responsible for Mg-ADP inhibition sensitivity [117]. The results strongly indicated that the interaction between NB and CT of *Eh* prevents subunit A from adopting a conformation similar to that of ADP-bound form during turnover, leading to insensitivity to ADP-inhibition of A-ATP synthases. This insensitivity to ADP-inhibition results due to the increased affinity for Pi, without an associated decrease in binding affinity for nucleotide [117].

These data highlight the importance of the C-terminus of subunit α which along with being able to interact with subunit γ also interacts with subunit ε through the DELSEED sequence, present in the alpha helix of the C-terminus of the subunit β and its equivalent in subunit α [108]. Moving more specifically towards the C-terminus of subunit α, it is evident from the amino acid sequence alignment from figure 1.8 that unlike *E. coli*, bovine mitochondria and *Bacillus* PS3

(PS3), *Mt* and other species from *Mycobacterium* genera possess a unique stretch of amino acids, which could play an important regulatory role in catalysis and provide an interesting platform for introspection.

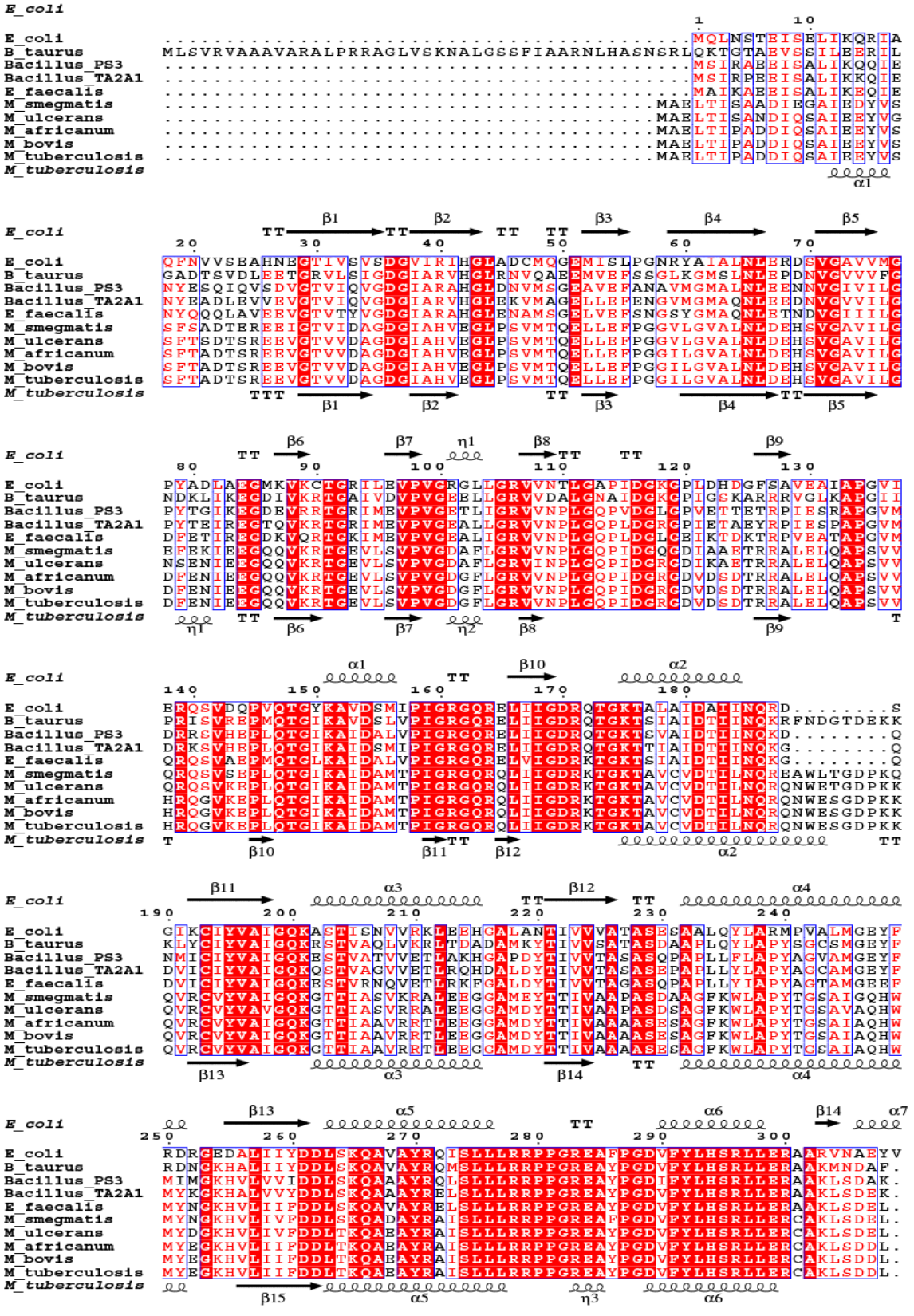

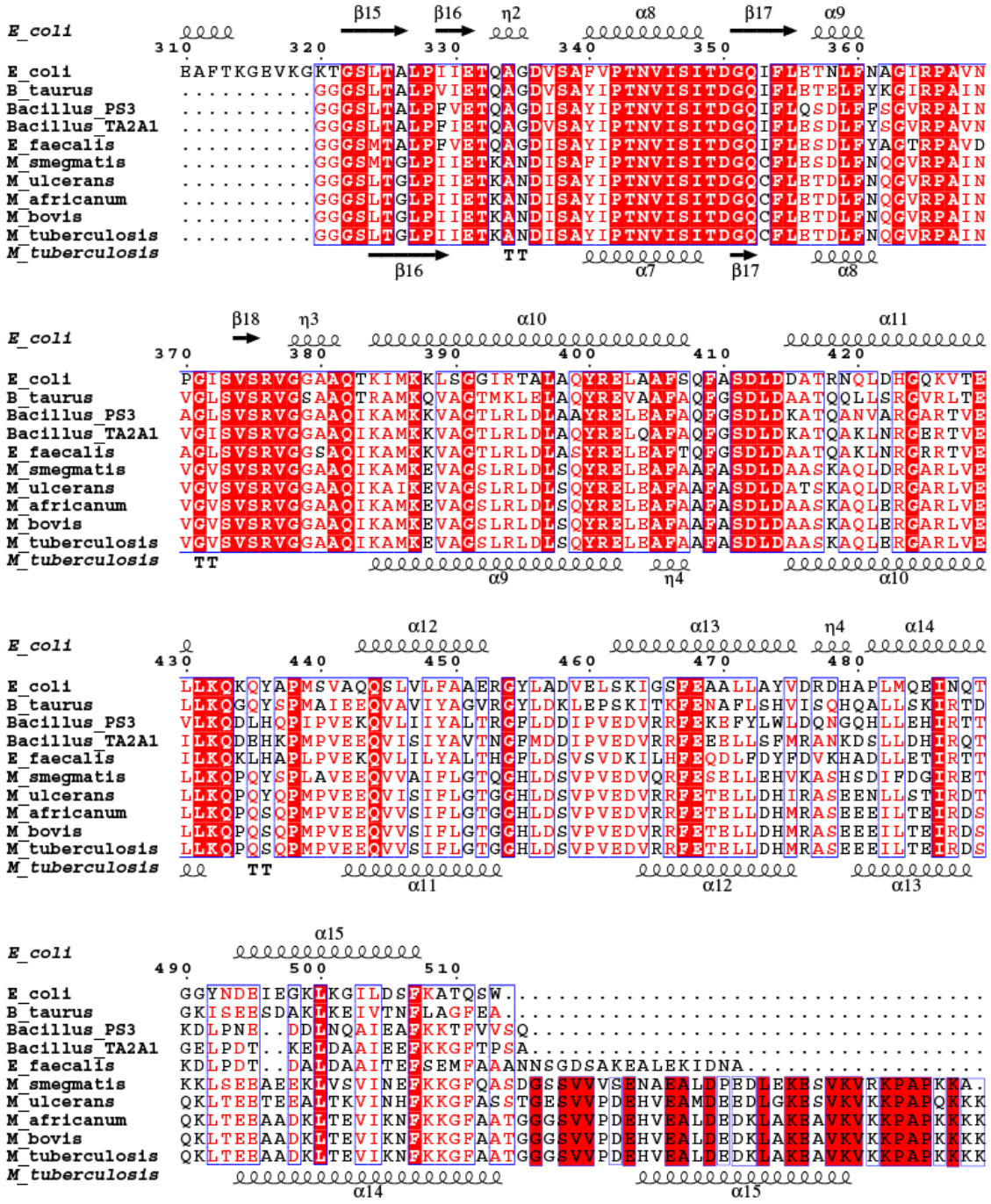

Figure 1.8: Sequence alignment for subunit α F-ATP synthase from different species of mycobacteria, *Bacillus* genera, *B. Taurus* and *E. coli* displaying the unique stretch of amino acids in the C-terminus. Identical residues conserved across the species are shaded in red and residues with comparable polarities are boxed in blue. Alignment was performed using ESPRIPT program [118].

Tentoxin, a tetrapeptide secreted by phytopathogenic fungi is shown to regulate the functioning of the chloroplast F-ATP synthase [119-121]. Detailed studies performed on the residues involved, revealed the involvement of the N-terminus of subunit α along with the conserved residue D83 in subunit β [122]. The importance of β D83 residue was corroborated by substitution studies in *Chamydomonas reinhardtii*, where the mutation of E83D caused a shift

from tentoxin resistance to tentoxin sensitivity [123, 124]. Chloroplast and bacteria (*R. rubrum*) showed a distinct stretch of residues in their N-termini of subunit α and various native and chimeric $\alpha_3\beta_3\gamma$ complexes were produced. With the chimeric complexes incorporating chimeric α into the photosynthetic hybrid F_1, the structural requirements required for binding and inhibition of tentoxin have been identified.

Chimeric protein complexes play an important role in providing a tool to investigate the role played by certain domains in a protein. As described earlier, the C-terminus of *Mt*α, could be of prime importance in regulating the activity of the enzyme and it would be an extremely productive approach to prepare chimeric complexes fusing the C-terminus of *Mt*α in the $\alpha_3\beta_3\gamma$ of a well-studied complex of *Bacillus* PS3 F-ATP synthases. $\alpha^{chi}{}_3\beta_3\gamma$ is the chimeric complex generated with 35 amino acids of the C-terminus of *Mt*α that was included at the end of the subunit α of *Bacillus* PS3 in the complex of PS3$\alpha_3\beta_3\gamma$ to generate a chimeric protein. Given the difficulty of expressing and structurally characterising proteins from *Mt*, this approach will be helpful in better understanding of the important and unique domains.

Moving along this line of thought, it is deemed important to focus on the subunit α from *Mt (Mt*α) and also chimeric protein of subunit α of *Mt* and *Bacillus* PS3 (α^{chi}) as in individual subunits and in catalytically active complex, ($\alpha^{chi}{}_3\beta_3\gamma$). These have been described in detail in section 2.2.9.

1.8 Subunit ε of F_1F_O ATP synthases

Apart from γ, ε (δ in MF_1) is the other subunit of F_1's rotor shaft. Subunit ε plays a dual function in the F-ATP synthase: it is necessary for coupling of catalysis and ion-transport and for regulating the catalytic activity. Subunit ε comprises of two distinct domains, a N-terminal β–sandwich domain (NTD) and an α-helical C-terminal domain (CTD). These features are validated from the available crystal structures of isolated *E. coli* ε (2.3 Å), *Bacillus* PS3 (1.9 Å), the auto inhibited state of subunit ε in F_1 of *E. coli* (3.26 Å) and the NMR solution structures for isolated subunit *E. coli* ε and chloroplast thermophilic cyanobacterium *thermosynechococcus elongates* BP-1 [18, 125-128]. Figure 1.9 shows the crystal structure available for the *E. coli* ε, in both the compact state and the extended state [18, 125].

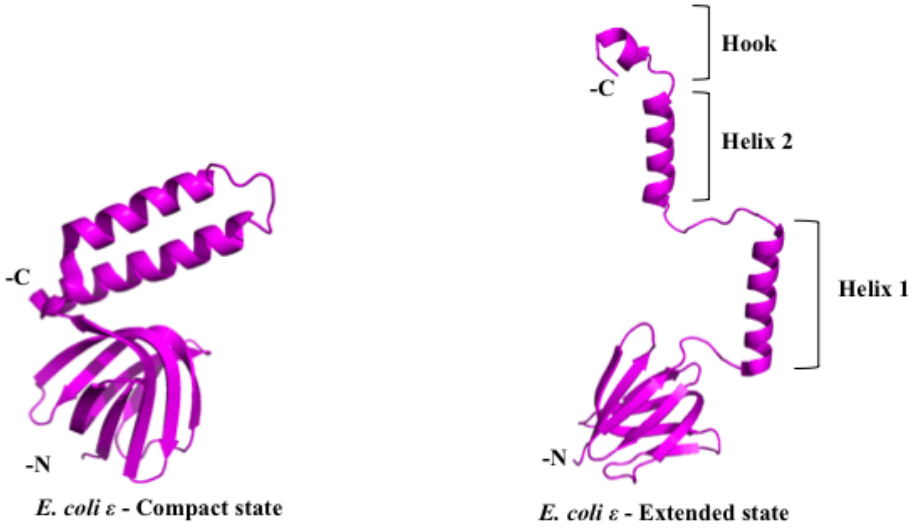

Figure 1.9: Cartoon representation of the crystal structures available for subunit ε of *E. coli* (*Ec*ε) in the compact and the extended state (PDB ID: 1AQT and 3OAA) [18, 125]. The *E. coli* ε in its extended state reveals the helix 1 followed by helix 2 and the terminal hook region.

The NTD of subunit ε has a role to interconnect the *c*-oligomer with subunit γ, and is indispensable for coupling. F-ATP synthases from chloroplasts, mitochondria and bacteria are highly conserved with regard to both their spatial structure and amino acid sequence. The α-helical C-terminal domain of subunit ε functions as a mobile regulatory element that can change conformation in response to nucleotide conditions, or pmf, or both [129]. It is responsible for inhibition of ATPase activity of both the F_1-portion and the whole F_1F_O-ATP synthase in chloroplast and bacterial enzymes [119]. Figure 1.10 shows the sequence alignment of the various species of subunit ε, to highlight the shorter length of those of the *Mycobacterium* species in comparison with *E. coli*, *Bacillus* PS3 and other species for which high resolution structures are available. Spanning only a length of 121 residues, the N-terminus of subunit ε is fairly conserved. The comparatively shorter C-terminus of the *Mycobacterium* species also carries positively charged residues, which could open up the possibility of important polar interactions within the enzyme.

Electrostatic interactions between the positively charged amino acid residues in the C-terminal domain of subunit ε and the negatively charged acid residues of the β-DELSEED segment of subunit β cause the inhibition of ATPase activity [115]. Residues εS108 and βE381 of the *E. coli* enzyme readily cross-link *in vitro*, and this interaction is modulated by nucleotide conditions (Figure 1.11) [115]. A prerequisite for this interaction is the extended state of the C-terminus of subunit ε which is otherwise in a contracted state that lies close to the *c*-oligomer. This conformational change allows the C-terminus of subunit ε to reach the $\alpha_3\beta_3$ hexamer.

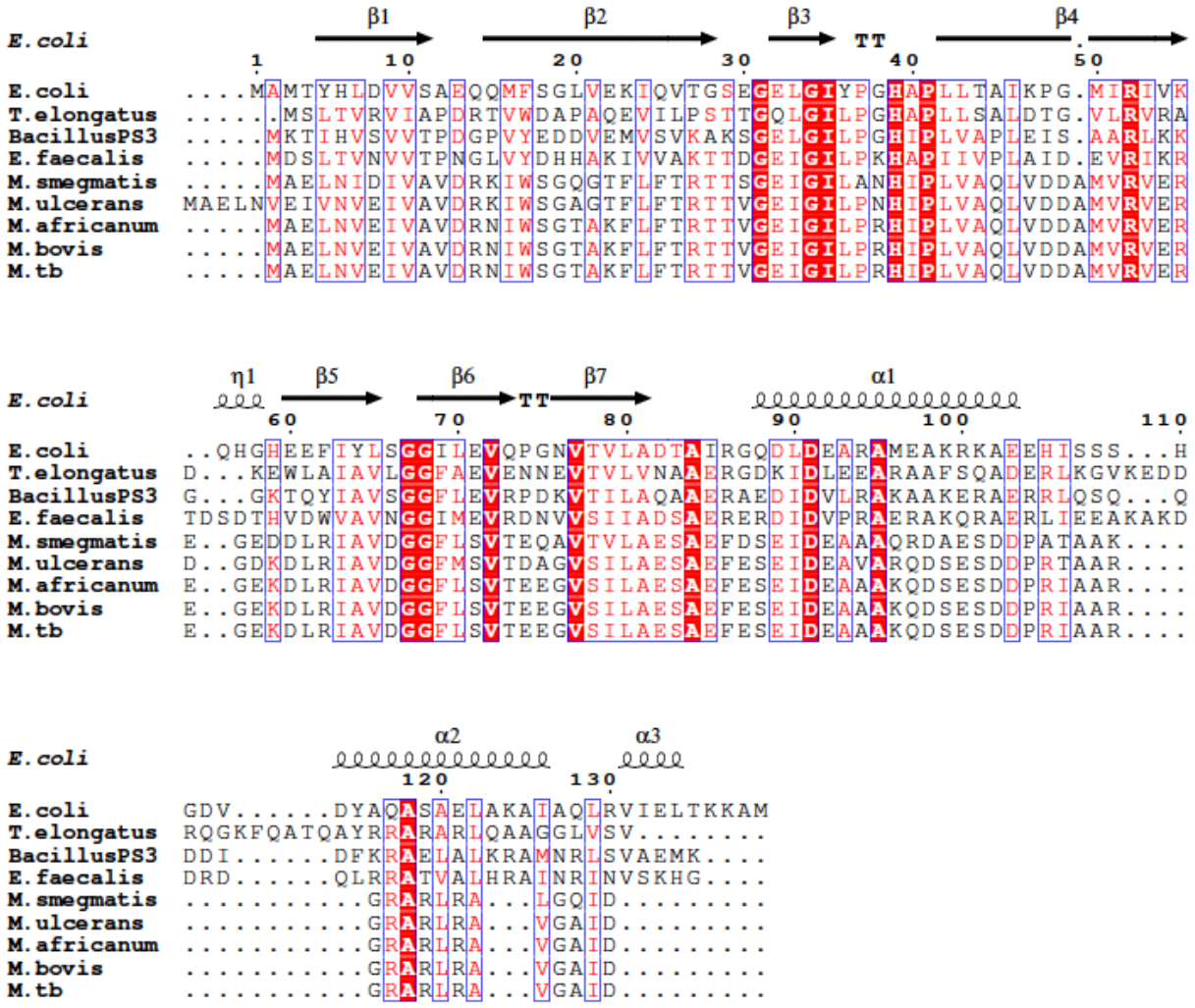

Figure 1.10: Sequence alignment for subunit ε F-ATP synthase from different species of mycobacteria, *Bacillus* PS3 and *E. coli*. ESPRIPT program was used for alignment analysis [118].

Recent findings clearly demonstrate that the Loop2/helix2 of the C-terminal domain plays a pivotal role in inhibiting activity through decreased rotation by extending duration of the inhibited state [130]. Residues εS108 in loop2 and εY114 have been identified as being important for inhibition [130]. Sequential deletion of each of these loops or helices in the C-terminus has shed some light on the role played by the C-terminus of ε, which is believed to interact with other subunits α and β as it moves along with γ in its extended conformation. This traps the subunit γ in a rotary position close to the dwell and subunit ε is believed to increase the duration of catalytic dwell hence reducing the rate of rotation [130].

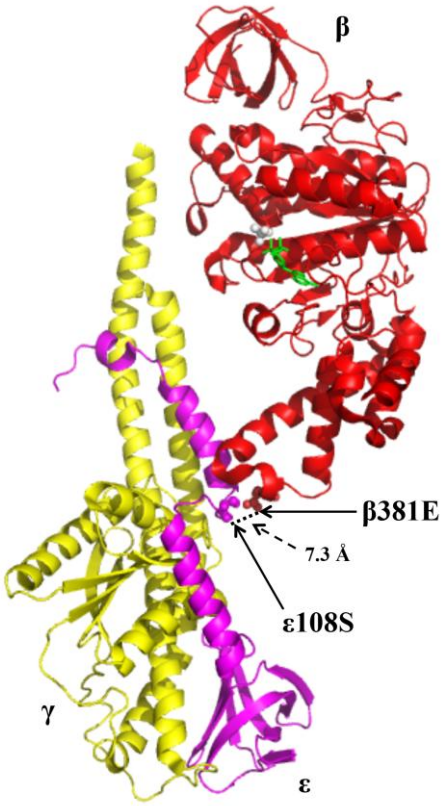

Figure 1.11: Subunits β (red), ε (magenta) and γ (yellow) of *E. coli*. ADP is shown with stick representation and bound SO_4^{2-} is represented with spheres on β_1. Cα of εS108 and β_1E381 that are 7.3 Å apart are shown in spheres [18].

Studies have been performed to show that the ATPase activity of F_1 *Bacillus subtilis* is strongly suppressed by Mg-ADP inhibition and not by the subunit ε [117]. Surprisingly, in this case subunit ε goes on to relieve the inhibition caused by ADP-inhibition. Contrary to all other cases, subunit ε does not act as an inhibitor, but helps attenuate Mg-ADP inhibition displaying this as its primary role in the regulation, especially in systems such as these in *B. subtilis*, where the F-ATP synthase is primarily used to synthesize ATP and not hydrolyse it [131].

A recent study tested the effect on rotation of F-ATP synthase when subunit ε was connected to a globular protein $Cytb_{562}$ (ε-cyt) or to flavodoxin reductase (ε-FlavR), which is believed to span the length between the central and peripheral stalks [118]. Continuous rotation was observed for both ε-cyt and ε-FlavR at the rates of 185 and 148 rps, respectively, which compared well with that of the WT which is 172 rps. However, a significant drop in the proton transport for the enzymes ε-cyt and ε-FlavR lead to the conclusion that the intra-molecular rotation is elastic, but stressing the need for specific interaction within the subunits for H^+ transport [132].

The potential of subunit ε to act as an ATP sensor is based on its ability to bind ATP to the C-terminal domain as observed in some bacteria of *Bacillus* genera [133]. In different organisms, it is probable that the high variation seen in the amino acid composition in the C-terminus of subunit ε is a deciding factor determining different regulation patterns of ATP synthases. Inhibitory role of subunit ε at the physiological level might help in preventing futile ATP hydrolysis by F_1 unbound to F_O, or by F_1F_O upon membrane de-energization [134]. High affinity of Thermophilic ε (Tε) to ATP is attributed to the accumulation of positive charges in the binding site, mainly arginine residues. Thus Tε functions as a intracellular ATP level sensors and a recent study showed that this subunit ε undergoes major conformational changes after addition of ATP, which is not restricted only to subunit ε transiting from the extended form to the compact form [114]. Tools such as NMR spectroscopy and Hydrogen/Deuterium exchange Mass Spectroscopy were used to confirm the major conformational changes leading to stable helical formation and the pronounced stabilisation occurring in the vicinity of the ATP-binding pocket accompanying this transition [120]. A high propensity for dimerization of subunit ε has been revealed through Analytical Ultra centrifugation (AUC) [120]. The same has been confirmed by X-ray crystallographic studies, where the crystal structure was obtained as a dimer with bound ATP at each site. Dimerization propensity can be exploited for designing antibiotic target, as intracellular sequestration of bacterial ε in dimeric form in the presence of a high affinity ATP-analogue could limit the supply of free ε needed for assembly of F_1F_O [135].

In the closely related *Bacillus* PS3, subunit ε is the seventh ATP-binding site that has been described for the F_1 enzyme. ^{88}I(L)DXXRA^{93} is the ATP binding motif with the side chains of R100, R121 believed to coordinate the phosphate group of ATP with εE85 involved in formation of the adenine binding pocket [114]. *Mt*ε however lacks this ATP binding site, with ^{90}IDEAAA^{95} which impedes the binding [81]. Lack of the ATP level sensor could indicate the inability of the subunit ε in *Mt* to switch between the extended and compact forms as in *E. coli* ε, chloroplast ε and PS3ε, reasoning as to why it holds its extended form constantly to inhibit hydrolysis [127].

Along with the inhibition of ATPase activity caused by subunit ε, Mg-ADP inhibition or a role played by additional effectors such as subunit ζ in *P. denitrificans* and subunit δ in *M. luteus* have also been speculated [136, 137]. The catalytic core is also strongly suspected to have a role [136, 137]. Activation of latent ATP hydrolysis serves as an exciting approach for new drug targets to deplete cellular ATP pools particularly when the bacteria is residing in metabolic states with low cellular energy levels [138]. There is no evidence for the regulatory role by the homolog of ε in mitochondrial ATP synthases, and residues analogous to *E. coli* εS108 and

βE381 are more than 50 Å apart in the structure of MF_1 [18]. However, a unique mitochondrial subunit, subunit δ is responsible for the stability of ε's homolog in a compact conformation that makes no contact with $\alpha_3\beta_3$. Also, a distinct inhibitor protein, IF1 has evolved for regulation of the mitochondrial enzyme. Figure 1.12 compares the inhibitory protein of the F_1F_O ATP synthase IF_1 as seen in mitochondria and subunit ζ in *P. denitrificans* [139].

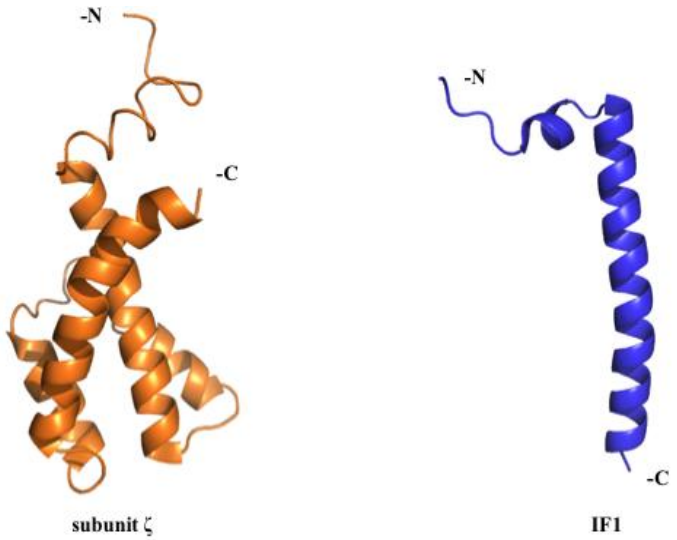

Figure 1.12: Cartoon representation of the inhibitor proteins of F_1F_O- ATP synthase in *P. denitrificans* and mitochondria, IF_1 (PDB: 2V7Q) and subunit ζ (PDB: 2LL0) [17, 139].

Studies on the structure of the ε's inhibitory conformation within the F_1 complex has shed light on a regulatory feature that is unique to ATP synthases of bacteria and chloroplast and not seen in mitochondria. This information is extremely valuable for the development of new anti-microbials that target bacterial but not mitochondrial F-ATP synthases. A promising antituberculosis drug has been discovered that targets the bacterial F-ATP synthase and that is not toxic to its mitochondrial counterpart.

However so far, the only information on the high resolution structural details for the F_1F_O ATP synthase of *Mycobacterium tuberculosis* is of the crystal structure of the *c-ring* [41]. An earnest effort towards the better understanding of structural information has been made by obtaining the solution structures of *Mtε* and the peptide structure of the C-terminus of the same by using solution X-ray scattering and NMR, respectively [81]. The interaction of the drug TMC207/Bedaquiline with the subunit ε has been studied and a model has been proposed to explain the wedge-like interaction of the drug at the interface of subunits ε and *c*. Figure 1.13 shows the model obtained from low resolution structure of *Mtε* [77]. The structure obtained has been superimposed with the peptide structure obtained for the C-terminus of *Mtε* and the N-

terminal domain of the crystal structure of *E. coli* ε (*Ec*ε). This shows the well fitted peptide in the extended domain and crystal structure of the beta sandwich N-terminal domain in the globular part of the solution structure for *Mt*ε [81]. This fitting in comparison to the *Ec*ε-inhibited extended state of the *Ec*ε that blocks ATP synthesis and hydrolysis, shows that the *Mt*ε is shorter and will not be able to reach deep into the catalytic core [18]. However, the C-terminus is laden with positively charged arginine residues that could possibly play an important role in interacting with the C-terminus of the subunits of the catalytic core to regulate catalysis [77]. As shown recently, the C-terminus of subunit ε is highly capable of blocking ATP hydrolysis to avoid excess ATP consumption in mycobacteria and more so in slow growing species, wherein low hydrolytic activity is measured [140]. This situation is encountered in the cell under hypoxic conditions indicating an adaptation of the organism towards the conditions met in TB lesions in lungs [141].

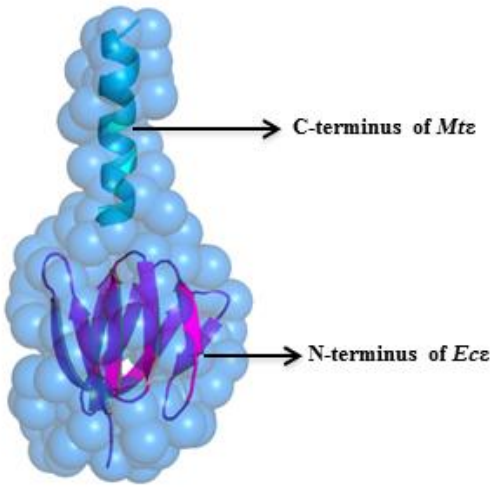

Figure 1.13: Superposition of SAXS structure (blue spheres) with the peptide of the C-terminus of *Mt*ε (cyan; PDB ID: 2LX5 and the N-terminal domain of the *Ec*ε (magenta; PDB ID: 3OAA) [18].

Also, NMR titration experiments have been performed to demonstrate the interaction of the drug TMC207 and *Mt*ε. These experiments clearly showed the W15 of *Mt*ε to be interacting with the drug. A binding constant of 19.1 μM was determined and also weak interactions were detected for *Mt*ε-T19A and *Mt*ε-R37G. These confirm the specific interaction of the drug with the *Mt*ε [77]. So far, these interactions have been proposed based on the study on isolated subunits.

1.9 Overview of Archaea

Archaea have held a distinct position given their unique lifestyle and their occurrence in extreme conditions with respect to temperature, salinity etc. Also accountable are some species

that do inhabit non-extreme environments such as the gastrointestinal tract of human rumen, anoxic zone of freshwater lakes [142-144]. Of the various classes of Archaea are the methanogens that couple methanogenesis to ATP synthesis, extremophiles that survive in extreme saline conditions with salt concentrations up to 5 M or at pHs ranging from 1 to 12 and hyper thermophiles that thrive at temperatures above 100°C. The proteins of hyperthermophiles are highly stable at higher temperatures and also the optimal cellular growth temperature is 80°C or more [145]. The record for highest growth temperatures are for *P. furiosus* at 100°C, *P. occultum* at 98-105°C, *H. butylicus* at 108°C and *M. kandeleri* at 113°C and *P. fumarii* at 113°C [146-150]. Geographically, these have been isolated from hot springs, hot marine sediments and other geothermaly heated environments [44].

Methanogens are the distinct class of Archaea that drive their metabolism via the path of methanogenesis and possess the ability to couple this to ATP synthesis using H_2+CO_2, methyl groups in methanol, acetate and trimethylamine as methanogenic substrates. Methanogenesis at the expense of such substrates produces about 2 mol ATP from H_2+CO_2 under standard conditions [151]. In comparison, aerobic respiration of sugars yield higher number of ~ 30 ATP, while anaerobic fermentation of sugars provide ~ 4 mol of ATP [7]. Methanogens have devised their systems to feed on the available substrates and have beautifully evolved to overcome the energy-limiting conditions to survive and thrive in their environments.

This is achieved by the presence of various unique enzymes. Interestingly, this entire process is observed to be different in methanogens that have evolved with cytochromes and those without cytochromes. Species such as *M. mazei* Gö1, *M. acetivorans* and *M. barkeri* have been evolutionarily equipped with cytochromes, while *M. thermautotrophicus* and *M. jannaschii* are the cytochrome free species.

In all methanogens, the Mtr complex, which is the membrane bound methyl tetrahydromethanopterin-coenzyme M methyl transferase, is responsible to establish a Na^+-gradient across the membrane [152, 153]. As seen in figures 1.14 and 1.15, this complex is responsible for the transfer of the methyl group from methyl-tetrahydromethanopterin to coenzyme M. This exergonic reaction with a $\Delta G°$ of -30 KJ mol^{-1}, drives ~2 Na^+ across the membrane [154, 155].The reduction of methyl-S-CoM with Coenzyme B leads to the formation of a heterodisulphide, CoM-S-SCoB, along with the release of CH_4. The ultimate step of reduction of this heterodisulphide allows for the generation of the H^+ gradient.

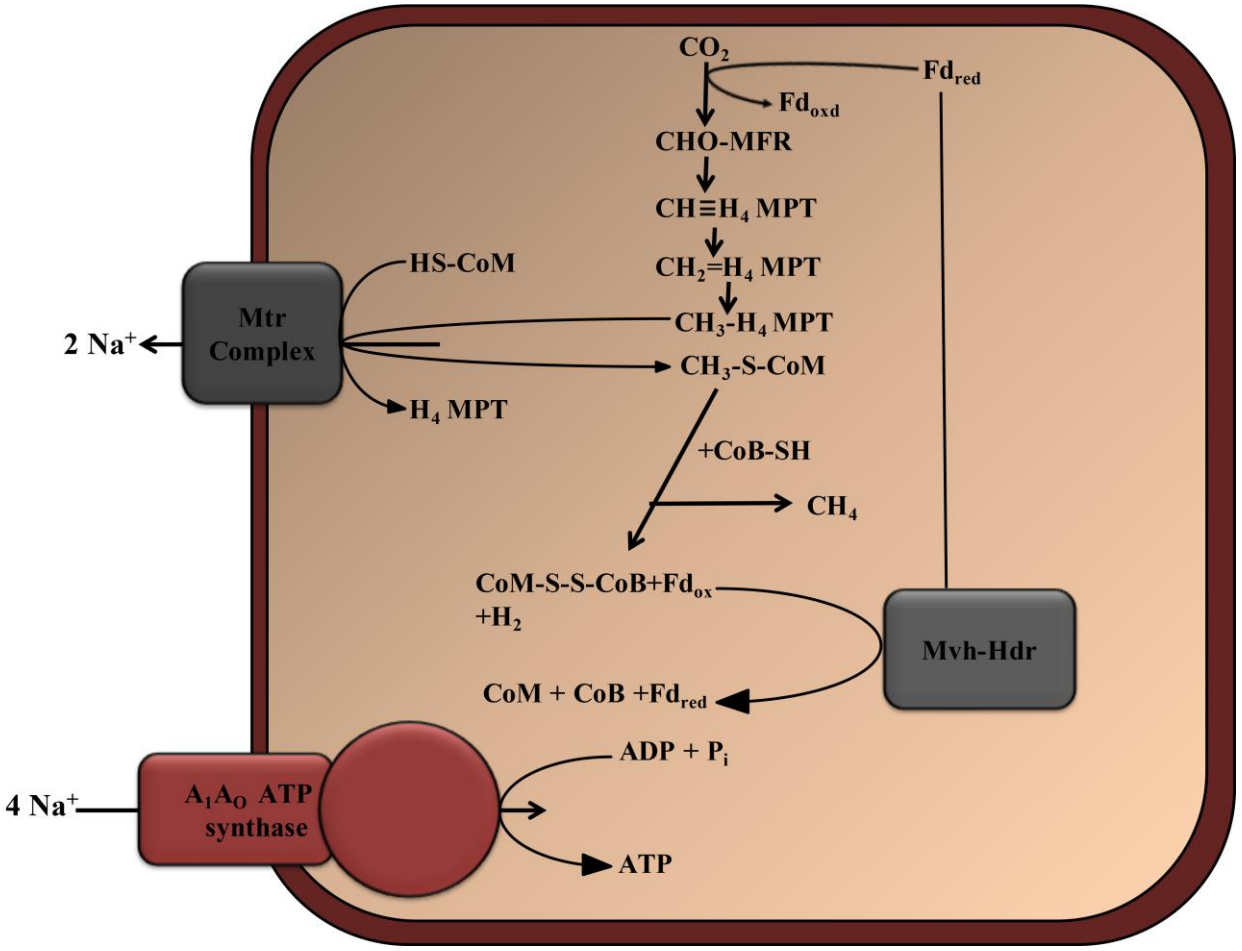

Figure 1.14: Modified figure illustrating methanogenesis coupled to ATP synthesis in cytochrome free methanogens [32]. Methyltetrahydromethanopterin-Coenzyme M Methyltransferase (Mtr) is responsible for the generation of a Na^+-gradient for the ATP synthase to use. Heterodisulphide of Coenzyme M and Coenzyme B is brought about by the Mvh- Hdr complex [7, 32, 155].

However, the mode of the heterosulphide reduction is different in the methanogens with and without cytochromes [155]. In the case of the cytochrome free methanogens, Mvh-Hdr is a soluble complex of methyl viologen-reducing hydrogenase and heterodisulphide reductase that causes the heterosulphide reduction. The energy released is used to transfer electron from H_2 to ferrodoxin. The reduced ferrodoxin acts as the electron donor to the formyl methanofuran dehydrogenase reaction which is the Ist step of methanogenesis. Given that these species have only one coupling site from Na^+, their ATP synthases are also Na^+ selective. This has been confirmed by both sequence and experimental analysis [24, 31, 156].

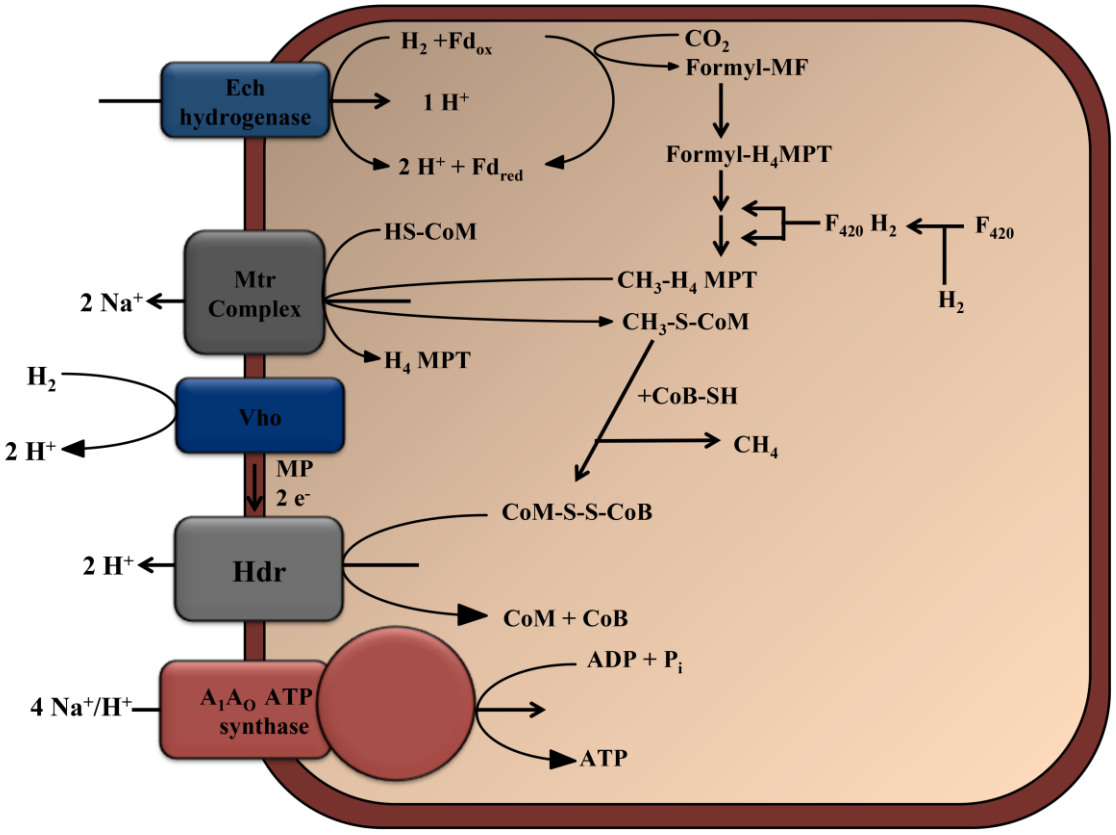

Figure 1.15: Modified representation of Methanogenesis coupled to ATP synthesis in cytochrome containing methanogen [32]. Methyltetrahydromethanopterin-Coenzyme M Methyltransferase (Mtr) establishes the Na^+-gradient and the Vho-Hdr complex generates a H^+-gradient for ATP synthesis. The membrane bound Vho-Hdr complex along with the electron carrier methanophenazine catalyses the reduction of heterodisulphide of Coenzyme M and Coenzyme [7, 32].

An evolutionarily more advanced scenario is encountered with the cytochrome enriched methanogens that also possess the electron carrier methanophenazine [157]. Studies have shown these species to be capable of generating and coupling both Na^+- and H^+-gradients to ATP synthesis in the course of methanogenesis [32]. A membrane-bound heterosulphide reductase (Hdr) anchored by cytochrome *b* is responsible for the proton-motive electron transport.

Methanophenazine-dependent hydrogenase (Vho) is another membrane bound F_{420} non-reducing hydrogenase that activates hydrogen and serves as an electron input model as the Vho-Hdr complex. Thus, a total of four protons are generated, of which two are scalar and two are vectorial (pumped) or the outside of the membrane. This is in case when H_2+CO_2 act as a methanogenic substrate. Wherein, the CO_2 binds to methylfuran to be reduced to a formyl group. This formyl group is transferred to tetrahydromethanopterin (H_4MPT) and is reduced to a methyl group that is further transferred to the Cofactor M (CoM-SH) as described earlier. In case of methyl substrates and acetate substrates, F_{420} and Ferrodoxin, respectively, provide the electrons necessary for the heterosulphide [32].

The ferrodoxin dependent hydrogenase (Ech)-type hydrogenases in *M. mazei* Gö1 is a membrane-bound, iron sulphur centre containing enzyme that caters as electron carrier for the transfer of electron from Ferrodoxin to protons to produce H_2. Further, this small electron transport chain couples the electron transfer to proton export to aid in the establishment of the gradient across the membrane [158]. Ech has also been identified in anaerobic bacteria and are believed to be predecessors to complex I of the respiratory chain [159]. Methanogenic species belonging to *Methanosarcina* hold the unique distinction to generate two ion gradients of H^+ and Na^+ and use these to drive their A-ATP synthases that is essential for ATP synthesis [24, 32, 151].

1.10 Adaptations of ATP synthases of archaea to their ecological niches

Archaea thrive on conditions that are thermodynamically challenged. Hence the organisms are compelled to develop adaptations that allow for tight coupling mechanism and reduce ion leakage for better functioning of the enzyme A_1A_O ATP synthase. The overall architecture of the enzyme reveals that subunit *a* forms the stator onto which the peripheral stalks are mounted. This arrangement is believed to be favourable to hold the entire enzyme in place. The rotation of the central stalk, which is essential to induce conformational changes in the headpiece, is achieved by ion translocation. As depicted in recent studies, the peripheral stalks are essential to hold the entire enzyme assembly [30]. The X-ray crystallographic structure of subunit E from *P. horikoshii* shows a S- shaped structure that would allow for elastic energy to be stored [45]. If the enzyme is viewed as an isolated complex, away from the membrane, the assembly will undergo eccentric movement i.e. precession relative to the two domains. This is avoided *in vivo* given the ion-translocation part is membrane bound. Although the A_3B_3-assembly wobbles as a consequence of the asymmetrical placement of the headpiece on the rotating central stalk, the peripheral stalks comprising of the heterodimer stabilise the wobbling head and also counteract the torque generated during catalysis [76].

The second difference noted in terms of the structure is seen in the composition of the subunit *c*. There is a clear increase in the length of the subunit *c* that is noted with increasing temperatures. As seen in some species of methanogens the number of hairpins increases with increase in optimal growth temperatures (T_{opt}). *M. Mazei*, as most methanogens with T_{opt} of 35°C has one hairpin, *M. thermautotrophicus* of 70°C has two hairpins, *M. jannaschii* of 85°C has three hairpins and 13 hairpins for *M. kandleri* of 98°C [41]. The higher number of covalent linkages are believed to stabilise the rotating *c* ring [24, 160]. Both these aspects seen in the

peripheral stalks and *c*-ring are believed to contribute to additional stability of the nanomachine [44].

The next adaptation seen is with terms of the choice of the coupling ion. Methanogens function at the thermodynamic limit of energy. The Mtr-complex is the only coupling site that allows for the generation of 2 Na^+-ions per mol of CH_4, which in turn relates to 0.5 mol of ATP per mol of CH_4 [155]. Ion-leakage in such a tight situation can prove to be detrimental and in biological systems ion leakage in the case of protons is more prominent than Na^+ [161]. Hence Na^+ would be the preferred choice and cytochrome-free methanogens are believed to have adapted to this primary path of ion flow during methanogenesis. Na^+ specificity is strongly seen in the case of cytochrome-free methanogens. With cytochrome enriched methanogens, both Na^+ and H^+ are used for ion translocation as seen in *Methanosarcinales* [32, 155]. Although H^+ has a preferred binding, both Na^+ and H^+ are used in physiological conditions of pH 7.5 and 400 mM NaCl (sea water) [32].

1.11 Organisation of A_1 and A_O domains

The headpiece of the A_1A_O complex consists of the subunits A and B, alternating around the periphery of a central cavity. Located in $A_{1,}$ the A_3:B_3 headpiece are a total of six nucleotide-binding sites. The three sites of subunit A possess catalytic function and they carry the conserved sequence GXXGXGKTV, referred to as the phosphate-binding loop (P-loop) or Walker A motif, and GER loop, also known as Walker-B motif [162]. In comparison, subunit B is shown to lack the conserved loops formed from GXXGXGKTV- and GER-sequences. Interestingly, nucleotides bind to subunit B as shown by photo-affinity labeling and fluorescence correlation spectroscopy (FCS) and this subunit is believed to play the role of a regulatory subunit [44, 52].

The protuberance at the top of the subunit A contributes to structural difference of the alternating A and B subunits, as shown initially via electron microscopy studies and later verified by the crystallographic structure of the *Pyrococcus horikoshii* A-ATP synthase subunit A [28, 60, 163, 164]. An insert comprising of 80–90 amino acids referred to as the nonhomologous region (NHR) creates this protuberance and no homologue of the NHR is present in the related β or α subunits of F-ATP synthases (Figure 1.16).

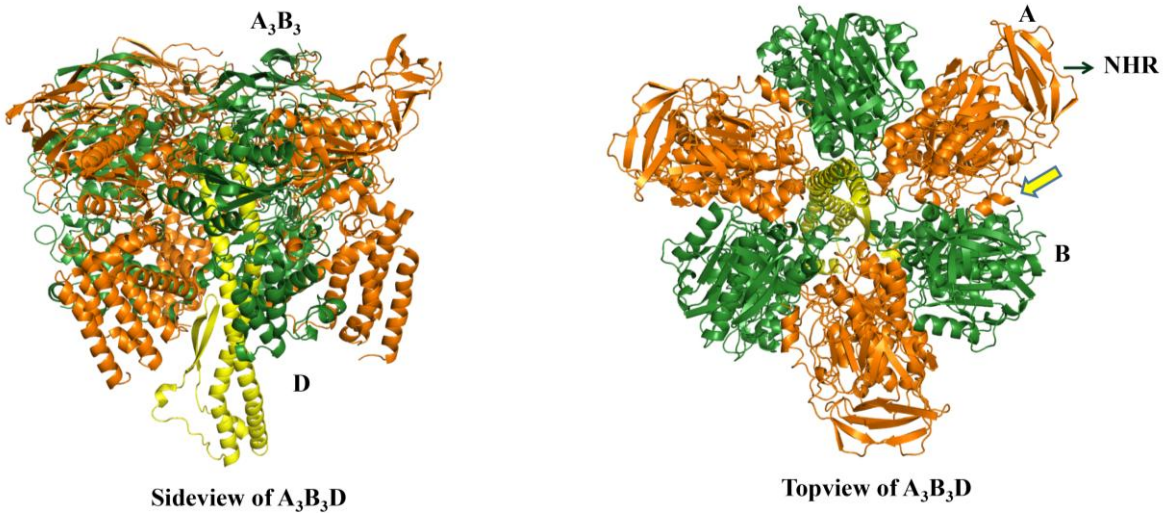

Figure 1.16: Side view of the A_3B_3D represents the hexameric headpiece of the A-ATP synthase with the centrally located subunit D. In the top view NHR indicates the Non-homologous region that is unique to the subunit A with 80-90 extra residues at N-terminus in comparison to subunit B. The interface between the two subunits for nucleotide binding is highlighted with a yellow arrow (PDB ID: 3VR4) [165].

With the recently available sulphate-, vanadate-, ADP- and (AMP-PNP)- bound crystal structures for the subunit A from *P. horikoshii*, the importance of the P-loop residues and their specific interactions have been demonstrated [46, 166]. The P-loop sequence in subunit A, GPFGSGKT, is shown to adopt an arched conformation hence allowing mode of nucleotide binding to be different, when compared to that for subunit β of the F-ATP synthases. This unique conformation leads to weaker and different interactions of the nucleotide with the P-loop residues, causing the nucleotide to be more solvent exposed [167]. This attribute could explain the ability of the A-ATP synthases to also hydrolyse GTP and UTP with activities of 86% and 54%, respectively [30, 166]. Of the residues of the P-loop, serine and phenylalanine are the critical residues, wherein the former interacts with the nucleotide and the phosphate and the latter stabilises the arched conformation of the phosphate binding loop. Of all the residues of the P-loop, serine plays a critical role by interacting with the sulphate via a water molecule and vanadate through hydrogen bonding interaction as seen in their respective bound structures [46, 166]. Comparing the sulphate (A_s), vanadate (A_v) and AMP-PNP (A_{PNP}) bound crystal structures, it has been deciphered from the position and interactions of these bound molecules with the P-loop that the AMP-PNP bound structure relates to the product-bound state, sulphate resembles the substrate like position and vanadate depicts the transition state [44]. This understanding has been drawn from the other vanadate-bound structures available for myosin and F_1F_O ATP synthase [168, 169].

The overall shape of the A_1A_O ATP synthase reveals that the A_3B_3 hexamer and the A_O sector are separated by a 80 Å long central stalk, consisting of the subunits C, D and F, with subunit C placed at the bottom of the central stalk [163, 170]. Subunit D is a part of the stalk penetrating inside this cavity and is in close proximity to an A–B–A triplet [28, 50, 165, 171]. The subunit D can be cross-linked to subunit A in a nucleotide dependent manner and is regarded as a structural and functional homologue of subunit γ of F-ATP synthases [28, 172]. Both subunits D and A interact via their C- and N-terminal helices and in γ (the homologous subunit of D in F_1) intercalation is observed into the cavity of the $\alpha_3\beta_3$ assembly, allowing the linking of β_{TP} and $\beta_{DP,}$ two differently occupied catalytic subunits [100]. In solution, subunit F displays a distinct dual-domain structure with an N-terminal globular domain and the flexible C-terminal part [48, 173]. Up and down movements relative to subunit B, bringing both termini in close proximity is facilitated by the flexible, C-terminal tail of subunit F [103]. Subunit F of the A-ATP synthase has been suggested to be in close contact to the rotating subunit D as per biochemical evidence [104]. Subunit C has a funnel shaped structure, which appears as the collar shaped structure along with subunit *a* [49]. In the related F-ATP synthases subunit C lacks a counterpart, whereas subunit *a* of F-ATP synthases of size ~ 28 kDa is functionally homologous in part to subunit *a* in A-ATP synthases (~ 100 kDa). The latter's N-terminal domain faces the cytoplasmic side and its C-terminal is membrane integrated along with the ion-translocating part. In the recently determined crystallographic structure of the barbell-shaped N-terminal domain of the A-ATP synthase, subunit *a* has been assigned to the collar and orients with the cytoplasmic surface of the membrane in a parallel manner and also shares close proximity to the N-termini of the heterodimers of the peripheral stalk subunits E and H. The middle and helical bundle of subunit *a* faces the wedge-like subunit C, which forms the socket of the elongated central stalk, to attach to the rotating ring of subunit *c* [174].

Adding confidence to the proposed models for the stator subunits with conformational flexibility, the two peripheral stalks in A-ATP synthases in the intact enzyme density are visualised to be in different conformations [30]. The crystallographic structure of subunit E of *P. horikoshii* OT3 shows an extended S-shaped N-terminal α-helix followed by a globular head group [30]. The mechanism proposed is, that the straight conformation switches to an S-shaped conformation of subunit E in the two peripheral stalks facilitating elastic power transmission between the A_1 and A_O sectors [175]. This is essential for facilitating the cooperation of the A_1 and A_O motors and to increase the kinetic efficiency of the A_1A_O ATP synthase engine.

1.12 Insights into the structure and functional role of subunit B of A_1A_O ATP synthases

The highest degree of sequence similarity amounting to 25% overall identity is seen for the major nucleotide-binding subunits of A_1, B and A and the corresponding subunits α and β of the F_1 domain [24]. The high resolution X-ray crystallographic structure of the non-catalytic subunit B was determined at 1.5 Å [52]. The dimensions for subunit B are 50 Å across and 80 Å in length. The subunit has three domains comprising at its termini an N-terminal β barrel with six-strands (residues 13–76) and a C-terminal α-helical bundle with four helices (residues 359–460) and centrally an intermediate α-β domain (residues 77–358) (Figure 1.17).

The α-β domain encompasses seven α helices surrounding the nine-stranded β sheet. The α-β fold relates well with the nucleotide-binding fold found in the nucleotide-binding domains present in the β and α subunits of F-ATP synthases, with a divergent P-loop motif in the analogous position of the subunit B of A-ATP synthases. The overall structure of subunit B compares well with that of the related non-catalytic α subunits of the bovine F_1 ATPase. An r.m.s. deviation of 1.83 Å is measured on the superimposition of both subunits [52]. Comparison of specific regions of both subunits revealed intermediate domains of approximately the same size but with shorter N and C-terminal domains of subunit B when compared to subunit α, causing subunit B to have a more compact appearance.

Figure 1.17: Subunit B of *M. mazei* Gö1. Residues $_{150}$SASGLPHN$_{157}$ that occupy the equivalent position of the P-loop are shown in red and GIT loop that is the equivalent of the Walker-B motif is also highlighted in red. (PDB ID: 2C61) [52].

Subunit B of the *M. mazei* Gö1 A_1A_O ATP synthase binds Mg-ATP and -ADP [52, 176]. As seen in the crystal structures of the subunit B mutant R416W, entrapment of nucleotides in transition-states has allowed the visualization of the path traversed by the nucleotide to the actual binding pocket [177, 178]. These crystal structures of subunit B A_1A_O ATP synthase show the path traversed by the nucleotide which includes the transient stages of binding before reaching the final binding pocket [176-178]. The transient I position is observed on the entry of the nucleotide at the C-terminus of the subunit B, which in turn causes the subunit D to move slightly allowing the nucleotide to interact. Transient II binding position is related to the efrapeptin C binding site and lies close to the P-loop which forms the final binding site (Figure 1.18) [179-181]. These are accompanied by isochronous rearrangements in both the nucleotide binding and the C-terminal region of subunit B. The site of entry for the nucleotide is in proximity to the C-terminal domain and the neighbouring subunit D paves way for the nucleotide to reach transient position I by moving away slightly. Also observed is the movement of the C-terminal by 6° to accommodate the nucleotide in transient position II, closer into the A_3B_3 headpiece close to the P-loop [29]. The final binding pocket can be reached by the rotation of the central stalk subunit D [178].

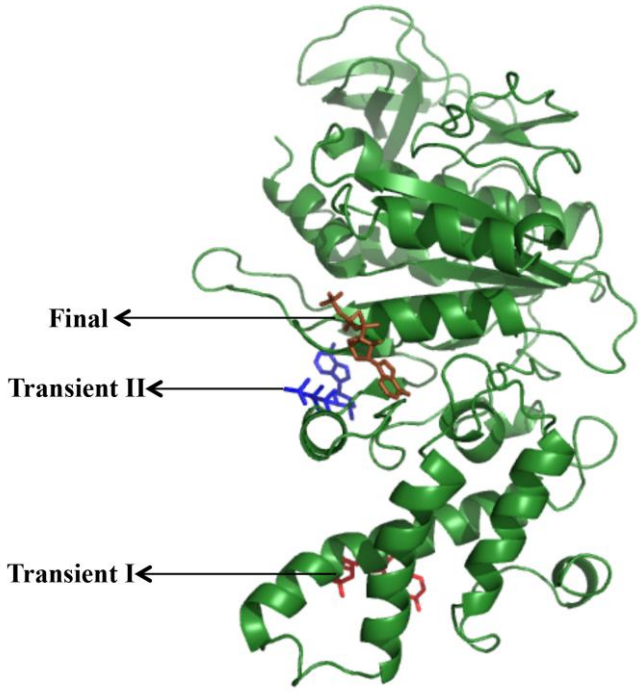

Figure 1.18: Modified structure of subunit B of A-ATP synthase of *M. mazei* Gö1 showing entry of the nucleotide along with the transient I, transient II and final binding pockets [176-178].

Substantial information for nucleotide binding ability of subunit B of A-ATP synthases is provided by the nucleotide binding to WT-B, demonstrated in the presence of reported inhibitors such as NBD-Cl [179]. Interestingly, the nucleotide-binding subunits α of F-ATP synthases has similar binding constants for Mg-ATP and Mg-ADP. Subunit B of A-ATP synthases binds Mg-ATP with a higher preference (K_d = 22 μM) than Mg-ADP (K_d = 50 μM), as demonstrated for the *M. mazei* Gö1 A-ATP synthase subunit B [176]. The proposal for subunit B to function as a regulatory subunit is based on these experimental demonstrations taken together with its inhibitory traits [179].

As mentioned earlier, the nucleotide binding subunit B of the A-ATP synthases do not have the conserved sequence of the P-loop which is otherwise intact in the catalytic A subunit of A_1 and α and β subunits of F-ATP synthases, but is substituted with the peptide SASGLPHN [52, 180-183]. In the conserved Glycine-rich sequence of the P-loop, GXXXXGKT, both lysine and threonine interact with the γ-phosphate and magnesium ion via their side chains as seen in the subunit β [100]. The lysine residue is responsible for the stabilisation of the negative charge in the transition state and the threonine essentially coordinates with the magnesium ion (Figure 1.19) [101].

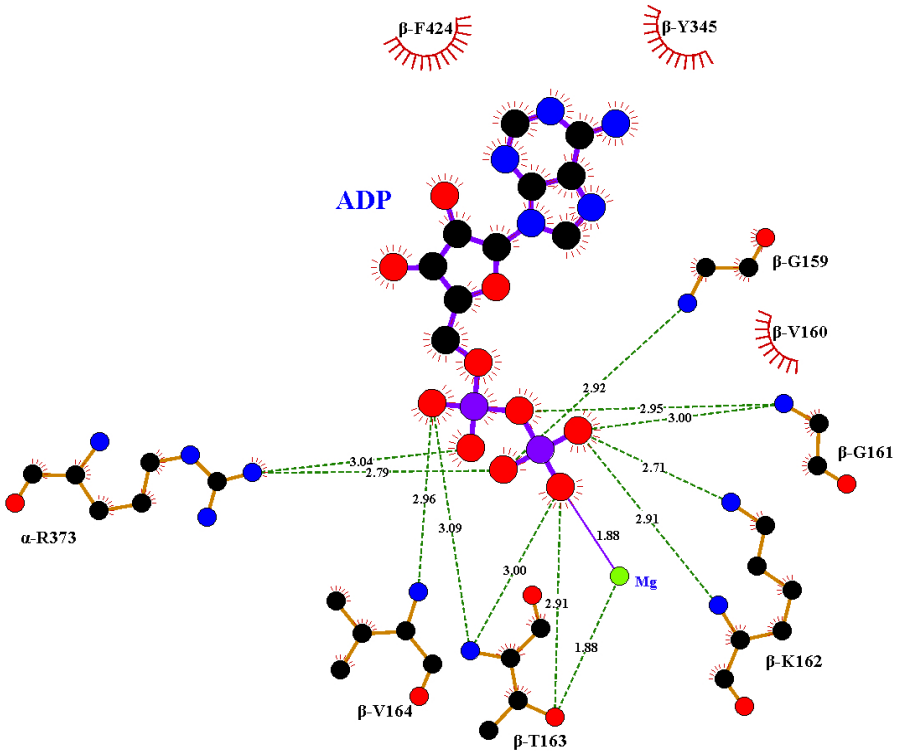

Figure 1.19: Representation of the P-loop of subunit β bound to ADP and magnesium ion using Ligplot$^+$ [184]. Various interactions of the nucleotide with the backbone and side chains of the P-loop residues to stabilise the binding (PDB ID: 4ASU) [104].

This mode of stabilisation of the negative charge is not seen in the case of subunit α and hence is not considered mandatory for catalysis. The position equivalent to that of lysine and threonine is occupied by histidine and asparagine in the P-loop of subunit B of both V_1 and A-ATPases. Mutation of the H180 and N181 of the P-loop ($_{174}$SASGLPHN$_{181}$) in the yeast V-ATPases have shown to cause reduction in their hydrolytic activities by 30-50% [185].

To explore the important roles played by these critical P-loop residues it is important to mutate these residues and study the changes with respect to structural features and nucleotide binding affinities [187].

1.13 Aims of this thesis

i) The A_1A_O ATP synthase is responsible for the production of ATP in archaea. Subunits A and B are the major nucleotide binding subunits of this enzyme, with the catalytic core present in subunit A and with subunit B playing the regulatory role. The P-loop (phosphate binding loop) with the consensus sequence GXXXXGKT is present in subunit A. Such P-loop sequence is not conserved at the equivalent position in subunit B. The structure of subunit B from *M. mazei* Gö1 reveals a unique P-loop $_{150}$SASGLPHN$_{157}$, which is different to the P-loop sequence in the related α subunits ($_{169}$GDRQTGKT$_{176}$) of the F-ATP synthases. The K175 and T176 residues play an important role in nucleotide binding, with specific interactions with Mg^{2+} and the γ-phosphate of the nucleotide through their side chains. The corresponding residues in the A-ATP subunit B are occupied by histidine and asparagine, which are proposed to play similar roles. To investigate the role of P-loop residue in subunit B of *M. mazei* Gö1 A-ATP synthase in nucleotide binding, N157 was mutated to threonine, as it is the corresponding amino acid in the P-loop sequence of the related α subunit of F-ATP synthases from *E. coli* and its equivalent residue (T241) in subunit A of A-ATP synthase, which showed a nucleotide bound conformational variation. The aim of this work was to determine the structure of the N157T mutant to get a better understanding of the relevance of the conserved asparagine residue in the phosphate–binding loop of non-catalytic nucleotide binding subunit B of A_1A_O ATP synthase.

ii) Subunit α is the homologous catalytically silent, nucleotide binding subunit of F-ATP synthase. Particularly, subunit α of *M. tuberculosis* spikes great interest, given that it possesses a unique tail of polar residues in its C-terminus. Interestingly, it shares this feature only with the other species of its own *Mycobacterium* genus. In this work, efforts have been directed towards understanding the role played by C-terminal tail of *Mt*α. To achieve this the individual subunit of native protein for *Mt*α, and α^{chi} (chimeric protein of PS3α and *Mt*α) were generated and structural

studies were performed using solution angle X-ray scattering experiments. To explore the influence of the same in ATP hydrolysis activity, a chimeric complex of $\alpha^{chi}{}_3\beta_3\gamma$ was generated to be compared with the mechanistically well studied native complex of $\alpha_3\beta_3\gamma$ of *Bacillus* PS3. Single molecule rotation studies were performed to strengthen the understanding of the catalytic functioning of the enzyme.

iii) F_1F_O ATP synthase is an essential enzyme in the energy metabolism of *M. tuberculosis*. To conserve the cellular ATP levels during the latent phase, *M. tuberculosis* does not undergo ATP hydrolysis. Subunit ε of F-ATP synthase is an intrinsic inhibitor of ATP hydrolysis. This subunit, which is a part of the central rotary stalk, exists in two conformations, a compact and an extended conformation, where the extended conformation is responsible for inhibiting ATP hydrolysis. Encouraging ATP hydrolysis in the pathogen will lead to wasteful hydrolysis eventually resulting in cell death. Apart from the recently published structure for *c*-ring from *M. phlei*, no structural details have been reported for mycobacterial F-ATP synthase yet. I seek to gain insight into the structural details of subunit ε**,** which will provide the basis for identifying drugs that would work as ATP hydrolysis activators, targeting this intrinsic inhibitory subunit, which is unique to the bacterial F-ATP synthases without affecting the mitochondrial counterpart. Sequence comparison reveals a shortened C-terminal for *Mt*ε and to gain insight on the effect of the shorter *Mt*ε on ATP hydrolysis, various constructs of different lengths of this protein were generated. Full length *Mt*ε, truncated *Mt*ε and extended construct ε_{121hyb} (chimera of *Mt*ε and *Ec*ε) were produced and reconstituted with PS3$\alpha_3\beta_3\gamma$ to study the ATP hydrolytic activity. PS3$\alpha_3\beta_3\gamma$ was also reconstituted with PS3ε and *Ec*ε for comparative studies.

2. Materials and methods

2.1 Materials

2.1.1 Chemicals

All the chemicals used in the current study were of at least analytical grade. Chemicals were purchased from the following companies:

Buffers and salts	Sigma (St. Louis, MO, USA) USB (Sampscott,MA) Calbiochem (Darmstadt, Germany), Fluka (Sigma, Buchs Germany) Roth (Karlsruhe, Germany) Serva (Heidelberg, Germany)
PMSF	Sigma (St. Louis, MO, USA)
Pefabloc ^{SC}	BIOMOL
DTT	Hoefer (San Francisco, CA, USA)
Ni^{2+}-NTA Beads	QIAGEN (Hilden)
LB Media	BD (Sparks, MD, USA)
Electrophoresis Chemicals	
(Agarose, SDS, Glycine, APS etc.)	Bio-Rad (Hercules, CA, USA)
Antibiotics	Calbiochem, Sigma and Gibco (Invitrogen)
IPTG	Fermentas
BSA	GERBU (Heidelberg, Germany)
ATP / ADP / AMPPNP	Sigma (St. Louis, MO, USA)
EDA-ATP ATTO-647N	ATTO-TEC (Siegen, Germany)
EDA-ADP ATTO-647N	ATTO-TEC (Siegen, Germany)
Gelatin	Amresco (Ohio, USA)
Pyruvate Kinase	Sigma (St. Louis, MO, USA)
Lactate Dehydrogenase	Calbiochem (San Diego, USA)
Phospho enol pyruvate	Sigma-Aldrich (St. Louis, MO, USA)
NADH	Sigma (St. Louis, MO, USA)
NMR material	
D_2O	Cambridge Isotope Laboratories (USA)
Biotin-$PEAC_5$-maleimide	(Dojindo, Japan)
Ni^{2+}-NTA-horseradish peroxidase conjugate	(Qiagen, Germany)
Steptavidin coated beads	(Millice)
Biotinylated Quantum-dots 655 nm	(Invitrogen, Germany)

2.1.2 Molecular biology materials

plasmid DNA	
Mycobacterium tuberculosis	H37rv
Primers	1st Base and AIT Biotech (Singapore)
Pfu and T4 DNA Polymerase	Fermentas (Glen Burnie, MD, USA)
KAPA polymerase	KAPA Biosystems (UK)
*Nco*I, *Sac*I, *Kpn*I, *Xba*I, *Bgl* II,	
BamHI, HindIII	Fermentas and New England Biolabs
T4 DNA Ligase	Fermentas and NEB
T4 Quick Ligase	Promega
CIAP Fermentas (Glen Burnie, MD, USA)	
Miniprep Plasmid Kit	Qiagen (Hilden, Germany)
Nucleobond AX midiprep Kit	MN & Co (Düren, Germany)
Escherichia coli expression strains	DH5α, BL21 (DE3), DK8
pET-9d(+)	GRÜBER *et al.*, 2002

2.1.3 Chromatography

Ion exchange

RESOURCE™ Q (6 ml)	Amersham Biosciences (New York City, USA)
Ni^{2+}-NTA resin	Qiagen (Hilden, Germany)

Gel filtration

Superdex 75 HR (10/30)	GE Healthcare (Uppsala, Sweden)
Superdex 200 HR (10/30)	GE Healthcare (Uppsala, Sweden)

Instruments and accessories

Akta FPLC, Akta Prime	GE Healthcare (Uppsala, Sweden)
Millex Filters (0.45 μM)	Millipore (Bradford, USA)
Syringe, needles and accessories	BD Biosciences

Protein concentration devices and estimation

Centriprep YM10	Millipore (Co-cork, Ireland)
Amicon ulta (3 and 30 kDa)	Millipore (Co-cork, Ireland)
BCA Assay Kit	Pierce (Rockford, IL, USA)
Nanodrop	

2.1.4 Other instrumentation

PCR Thermocycler:	
Biometra T personal	Biometra
Biometra T gradient	Biometra
Sonoplus Sonicator	Bendelin
Micropulser Electroporator	Bio-Rad
Ultraspec 2100 Pro Spectrophotometer	Amersham Biosciences
Microcal ITC 200	Microcal (Northampton, UK)

2.1.5 Computer software

Vector NTI 10.3.0	Invitrogen
Quantity One	Bio-Rad
PyMOL v0.99	DeLano Scientific LLC, USA
HKL2000 package	OTWINOWSKI AND MINOR, 1997
Refmac5	CCP4 package (MURSHUDOV *et al.*, 1997)
PHASER	MCCOY *et al.*, 2007
Coot	EMSLEY AND COWTAN, 2004
Ramachandran plot	RAMACHANDRAN *et al.*, 1963
PROCHECK	LASKOWSKI *et al.*, 1993
CCP4	1994
SWIFT II	GE Healthcare Life sciences
Topspin 1.3 & 1.5	Bruker Biospin

2.2. Methods

2.2.1 Construction and mutagenesis of N157T; subunit B mutant of A-ATP synthase from *Methanosarcina mazei* Gö1

The N157T Mutant of subunit B mutant of A-ATP synthase was generated and protein crystals were obtained by Dr. Vikram Tadwal from our laboratory (PhD thesis: Crystallographic details of the nucleotide-binding pocket of subunit A and B of A-ATP synthases and insight into the nucleotide-binding subunit α of the *Escherichia coli* F-ATP synthases).

2.2.2 Data Collection

X-ray Data collection was done by Dr. M.M.S. Sony and Dr. Asha Balakrishnan at 140 K on Beamline 13B1 at (NSRRC, Hsinchu, Taiwan) using the ADSC Quantum 315 CCD detector. The diffraction data was indexed, integrated and scaled using the *HKL 2000* suite of programs [186]. The crystal belongs to orthorhombic space group $P_{212121.}$

2.2.3 Structure Determination

The wild type subunit B (PDB ID: 2C61) was used as a model for the structure determination by molecular replacement method using the programs PHASER and MOLREP [52, 187, 188]. Rigid body refinement was carried out followed by difference Fourier syntheses calculations. The mutant clearly showed electron density corresponding to the mutation. Iterative cycles of model building and refinement was carried out using the programs COOT and REFMAC of the CCP4 suite [188, 189]. The geometry of the final model was checked with PROCHECK and the figures are drawn using the program PyMOL [35, 190]. Structural comparison analysis have been carried out using the SUPERPOSE program as included in the CCP4 suite [191].

2.2.4 Protein Data Bank Accession Code

Atomic coordinates and structure factors for the subunit B mutant N157T are deposited in the RSCB Protein Data Bank under the accession code 3SSA [192].

2.2.5 Cloning of subunit α constructs from *M. tuberculosis* and *Bacillus* PS3 F_1F_O ATP synthase

To amplify the *atp*A coding region of F-ATP synthases of *M. tuberculosis* and *Bacillus* PS3, oligonucleotide primers incorporated with *Nco*I & *BamH*I restriction site (underlined), were designed. Of the constructs mentioned below and in the rest of this thesis *Mtα and* $Mt\alpha_{1\text{-}513}$ refer to the wild type and C-terminal truncated protein of subunit *α from M. tuberculosis,* respectively. PS3α is the wild type protein of subunit *α* from *Bacillus* PS3 and α^{chi} is the chimeric protein of subunit *α* designed to contain the entire PS α+ the C-terminus of *Mtα.*

Construct		Oligonucleotide sequence 5'-3'
Mtα	Forward	5'-CATCATGCCATGGCTGAGTTGACAATCCCC -3'
	Reverse	5'-CATGGATCCTTATTTCTTCTTCTTCGGCGC-3'
$\boldsymbol{Mt\alpha_{1\text{-}513}}$	Forward	5'-CATCATGCCATGGCTGAGTTGACAATCCCC-3'
	Reverse	5'-AGCGGGATCCTTAGGCCGCGAAGCCCTTCTT-3

In the polymerase chain reaction, *M. tuberculosis* plasmid DNA, encoding for sub complex $Mt\alpha_3\beta_3\gamma$ was used as template for *Mtα* and $Mt\alpha_{1\text{-}513}$. For all constructs, PCR was set up in a total volume of 50 µl on ice with the appropriate concentration of constituents as mentioned below.

Reagents	Amount
Pfu buffer (10x)	5 µl
DNTP's (2 mM)	1.5 µl
Primers (100 µM)	2 x 0.5 µl
Template (plasmid DNA)	1 µl
MilliQ water	40.5 µl
Pfu DNA polymerase	1 µl

All reagents were pipetted into a PCR tube kept on ice all the time, mixing of the reagents was done by short centrifugation. PCR Thermocycler (Biometra T personal) was preheated to 99ºC before reaction tubes were placed inside the machine. The following PCR Thermocycler program was used for amplification:

Cycle steps	Temperature	Time	
Lid	99 ºC		
Initial denaturation	96 ºC	2 min	
Cycle denaturation	96 ºC	30 sec	
Annealing	*Mt*α-62 ºC	45 sec	30 cycles
	Mt$\alpha_{1\text{-}513}$-66 ºC		
Extension	72 ºC	1 min	
Final extension	72 ºC	5 min	
End	4 ºC		

Cycle denaturation, annealing and extension steps were repeated for another 29 cycles. Total time taken for the PCR program was 1 h 11 min 30 s. To check the quality, 5 µl of each the PCR product was applied on a 1.2% agarose gel. The gel was then placed in Ethidium bromide (EtBr) solution for 20 min and observed under UV light on destaining. The sizes of the products were confirmed by comparing it with the appropriate DNA marker. For each of the constructs, the remaining reaction mixture (45 µl) was applied on a 1.2% preparative agarose gel and the portions corresponding to the correct PCR product were cut out immediately and purified by gel extraction kit (QIAGEN) as per the manufacturers protocol. The product was finally eluted in 50 µl volume of Tris-HCl buffer of pH 8.0. 1 µl of gel extracted PCR product was applied onto 1.2% analytical agarose gel for estimating the purity of the sample.

Overnight double digestion of all the purified DNA was done using appropriate amounts of *Nco*I and *BamH*I restriction enzymes. After overnight digestion, the reaction mixture was purified by enzyme reaction purification kit from QIAGEN. Subsequently, ligation reaction between vector and amplified PCR products were set up at room temperature (Figure 2.4). pET 9-d(+) vector used for ligation was also double digested with *Nco*I and *BamH*I restriction enzymes and treated with CIAP to prevent self-ligation of the vector [98]. The reagents used were as follows:

Ligase buffer (10x)	1 µl
Vector (V)	100 ng
Insert (I)	3 and 5 times of vector
T4 Ligase	0.35 µl
MilliQ water	Variable
Total	10 µl

The ligation mixture was kept at room temperature for 2 hrs and the reaction was terminated by adding 90 µl of MilliQ water to make a final volume of 100 µl. 1 ml of butanol was added into the mixture and mixed thoroughly. Then the mixture was centrifuged at 13,000 x *g* (using Eppendorf Mini-centrifuge) for 10 min. and the supernatant was discarded gently. The pellet was resuspended in 500 µl of 70% ethanol and centrifuged again for 10 min. Supernatant was again removed and the pellet was re-dissolved in 7 µl of MilliQ water. 7 µl of ligation mixture was used for the transformation into *E. coli* DH5α cells. Single colonies were picked from the transformation plate on the next day and were incubated at 37°C. The plasmid DNA was isolated using standard protocol (QIAGEN mini-prep kit) and subsequently double digested and applied onto 1.2 % agarose gel, in order to confirm the presence of ligated insert. Size of insert and vector were compared with appropriate controls and markers. Verified plasmid was finally transformed into *E. coli* BL21 (DE3) cells for protein production and they were grown on 30 µg/ml Kanamycin-containing Luria-Bertoni (LB) agar plates. *E. coli* BL21 expression strains were purchased from Novagene (Darmstadt, Germany).

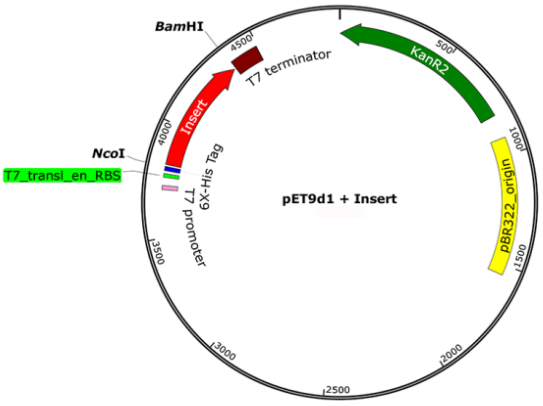

Figure 2.1: Modified pET-9d (+) vector showing full map and unique multiple cloning sites (MCS) that has been used to clone various genes **[193].**

2.2.6 Electroporation transformation

Reagents used: *Luria Bertoni media:* 10 g/l Tryptone
5 g/l Yeast Extract
5 g/l NaCl

Electroporation was done to achieve the transformation of plasmid into electro-competent cells. Electro-competent cells were prepared as per the protocol from Current Protocols in Molecular Biology (Wiley InterScience) manual. 1.5 µl (concentration: 100 ng/µl) of plasmid was added to 100 µl of competent cells and incubated on ice for 5 – 10 min. Electroporation was done at constant voltage of 2500 V (Micropulser Electroporator, Bio-Rad). The cuvette was then immediately placed back on ice for 1 min., following addition of LB media to a total volume of 1 ml. The mixture was incubated at 37°C for 1 h and appropriate dilutions were prepared before plating the cells on antibiotic selection plates.

2.2.7 Production and purification of subunit α constructs: *Mtα* and *Mtα*$_{1\text{-}513}$ of F_1F_O ATP synthase *M. tuberculosis*

Induction test

Reagents for 4 x Lysis buffer: 250 mM Tris-HCl, pH 6.8
9.2 % SDS
40 % Glycerol
0.2 % Bromophenol Blue

At least 3-4 single colonies were randomly picked for each construct and were grown to OD_{600} of 0.6 - 0.7 at 37°C with shaking of 180 rpm (Infors HT Minitron shaker). Final concentration of 1 mM IPTG was then added to start induction. Mixture was kept at 37°C for 2.5 h. Respective controls were left uninduced under identical conditions. Cells were pelleted down and resuspended with 30 µl of 2x Lysis buffer in presence of 1 mM DTT. Resuspended cell mass was heated at 95ºC for 5 min and 15 – 20 µl of each sample was loaded onto a 17 % SDS Polyacrylamide gel. The expression was more in the induced cultures ((+) supplemented with IPTG) than uninduced cultures ((-) not supplemented with IPTG).

Solubility test for recombinant proteins

Following the successful induction of proteins with appropriate concentration of IPTG at the optimized temperature and shaking conditions, solubility of the produced proteins was tested in various buffers as shown below.

I. 50mM Tris-HCl, pH 8.5, 200 mM NaCl

II. 50mM Tris-HCl, pH 7.5, 200 mM NaCl

III. 25mM Hepes, pH 7.5, 200 mM NaCl

IV. 25mM MES, pH 7.0 200 mM NaCl

V. 25 mM Phosphate, pH 6.8 200 mM NaCl

50 ml of culture was grown and induced with IPTG. Cells were pelleted down into five equal fractions by centrifuging at 10,000 x g for 7 min. Freshly prepared protease inhibitor Pefabloc^{SC} in water was added to a final concentration (8 mM). Reducing agent such as DTT (1 mM) was used in the preparation. Resuspension was sonicated at 10% power with KE 76 tip of sonicator (Bandelin Sonoplus) three times for one min each, with a cooling interval of two min between each cycle. Supernatant was then separated from the pellet by centrifugation at 10,000 x g and

transferred to a fresh tube. Pellets were resuspended in the respective buffers. All the steps were carried out on ice. 25 µl of pellet and supernatant were loaded onto a 17% SDS gel.

Purification of subunit *α* constructs: *Mtα, Mtα*$_{1\text{-}513}$, PS3α and α^{chi}

The protein for *Mt*α, *Mt*α$_{1\text{-}513}$ proved to be soluble when cell cultures were incubated at 15°C on induction with IPTG. His$_6$- *Mt*α and His$_6$- *Mt*α$_{1\text{-}513}$ were produced in large scale for purification purposes. Large scale liquid cultures of His$_6$-*Mt*α and His$_6$-*Mt*α$_{1\text{-}513}$ were incubated in Kanamycin –positive (30mg/ml) LB medium at 37°C until OD_{600} of 0.6 was achieved. The His$_6$-tagged proteins were expressed on addition of IPTG (Final concentration: 1 mM) and these cultures were incubated at 15°C O/N. The cells were harvested by centrifugation on a Beckman Coulter Avanti J26X at 8500 g for 13 minutes, 6°C and were stored in -80°C on freezing with liquid nitrogen.

Preceding the purification, the cells were lysed by sonication for 3*1 min in Buffer A (50 mM Tris-HCl, pH 8.5, 200 mM NaCl, 2 mM PMSF and 2 mM Pefabloc^{SC} (BIOMOL) and 10% glycerol). Centrifugation at 10,000 x g for 35 min was employed to allow the cell debris to settle down. The filtered supernatant was incubated with 2 ml Ni^{2+}-NTA agarose beads for 1.5 hours at 4°C to bind the His$_6$-tagged proteins, which were later eluted with a linear imidazole gradient (0-400 mM) in Buffer A. The eluted fractions were applied on SDS-PAGE to check for the presence of the desired protein. The appropriate fractions were pooled together and applied on an Ion- exchange Resource Q column and the fractions containing the His-tagged *Mt*α and *Mt*α$_{1\text{-}513}$ were pooled and concentrated as required using Centricon YM-30 (30 kDa molecular mass cut off) spin concentrators (Millipore). As a final step of purification, gel filtration chromatography using a Superdex 75 HR 10/30 column (GE Healthcare) was performed with buffer 50 mM Tris-HCl (pH 8.5), 200 mM NaCl, 10% glycerol, 5 mM EDTA.

For PS3α and α^{chi}, the appropriate fractions from the Ni^{2+} NTA affinity chromatography step were pooled together and applied on an Ion- exchange Mono Q column and the fractions containing the His-tagged PS3α and α^{chi} were pooled and concentrated as required using Centricon YM-30 (30 kDa molecular mass cut off) spin concentrators (Millipore). Gel filtration chromatography using a Superdex 200 HR 10/30 column (GE Healthcare) was performed with buffer 50 mM Tris-HCl (pH 8.5), 200 mM NaCl, 10% glycerol, 5mM EDTA to obtain the pure protein.

2.2.8 Small angle X-ray scattering measurements for subunit α constructs: *Mtα*, PS3α and α^{chi}

SAXS and X-ray are fundamentally very similar techniques using collimated, intense beam of X-rays to obtain structural information about the sample. The medium of measurement differs with the target molecules found in solution for SAXS, or embedded in well-defined crystals for X-ray Diffraction (XRD). XRD yields high- resolution data as the crystal acts as an amplifier of scattering intensity sampled at discrete points. For proteins that are hard to crystallize, SAXS analysis can be performed to gain insight on the molecular shape and dimensions with very low amounts of sample and in shorter time frames. SAXS in combination with X-ray crystallographic data form a powerful tool for analysis of large multi-component system.

The X-ray scattering data was collected using the Nanostar instrument (Bruker) equipped with a metal-jet X-ray source and Vantec 2000-detector system at SBS, NTU. SAXS experiments were performed with the concentrations 2 and 2.4 mg/ml for *Mtα and* $Mt\alpha_{1\text{-}513}$ respectively in buffer 50 mM Tris-HCl pH 7.5, 200 mM NaCl, 10% glycerol. Sample volume of 40 µl was used for each measurement. A total of 6 datasets, each recorded for a period of 5 minutes were compared to check for radiation damage. The scattering contributed by the buffer was eliminated by subtracting the data for the buffer from that of the sample. Data processing was performed using PRIMUS program package [194].

Guinier plot of logI vs. q^2 (sometimes also referred as S^2), is generated using the Guinier approximation and extrapolated intensity at zero scattering angle (I_0) allows the evaluation of radius of gyration (Rg) [195]. Rg indicates the compactness of protein structure and is calculated as the root mean square distance between its centre of gravity and its end. Extrapolation of the forward scattering curve to zero scattering angle allows one to understand the presence of repulsive or attractive interaction and helps detect aggregation (Figure 2.2). A linear Guinier plot indicates a well behaved sample, while aggregation will cause non-linearity. The molecular weight of the protein can also be estimated from the graph. $I_{(0)}$ is coincident with the direct beam and does not allow for direct measurement. Hence it is determined by the extrapolation of the scattering curve. $I_{(0)}$, the lowest resolution scattering measured at zero angle (S/q=0) and placed on an absolute scale is equal to the square of the number of electrons which is proportional to mass.

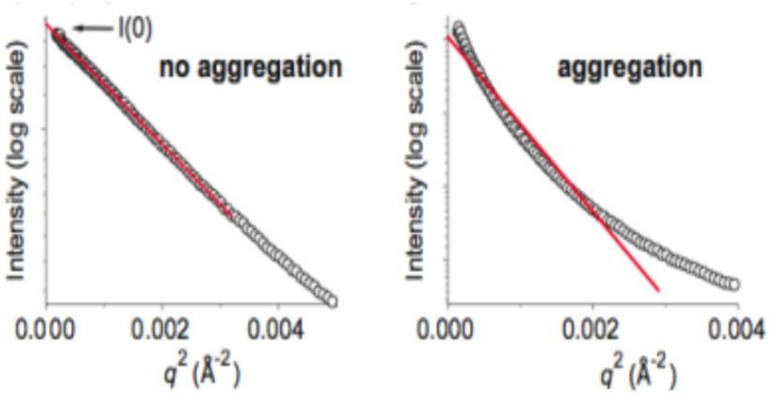

Figure 2.2: Guinier Plot illustrating the relation between the non-linearity of the curve and aggregation of the sample.

p(r), distance distribution function was computed using indirect transform package, GNOM [194]. p(r) is directly related to the shape of the particle and tells how often a distance appears within the particle. With the plot for p(r) versus radius, r(Å), D_{max} the maximum length in the particle is the position where the p(r) returns to zero at large value of r. Figure 2.3 gives an indicative picture.

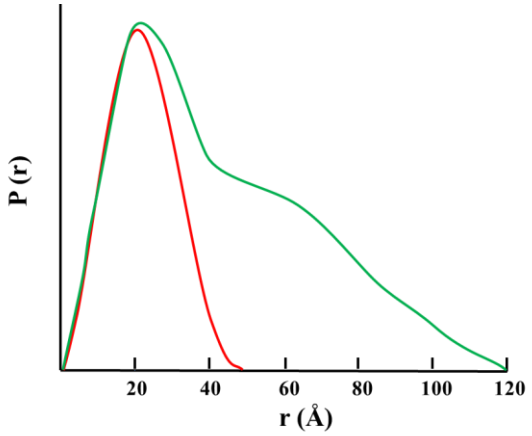

Figure 2.3: Modified figure depicting theoretical p(r) values of multidomain proteins. Peak in red is observed for compact globular proteins while the peak in green is indicative of presence of linker domains and an extended form.

In Kratky plot, $I(q).q^2$ is used to identify disordered states and distinguish them from globular particles. Globular macromolecules follow Porod's law and have a bell-shaped curve. Contrarily, this is not obeyed by unfolded or partially folded proteins wherein only a plateau or increasing trend in the larger *s* value is observed as referred in figure 2.4.

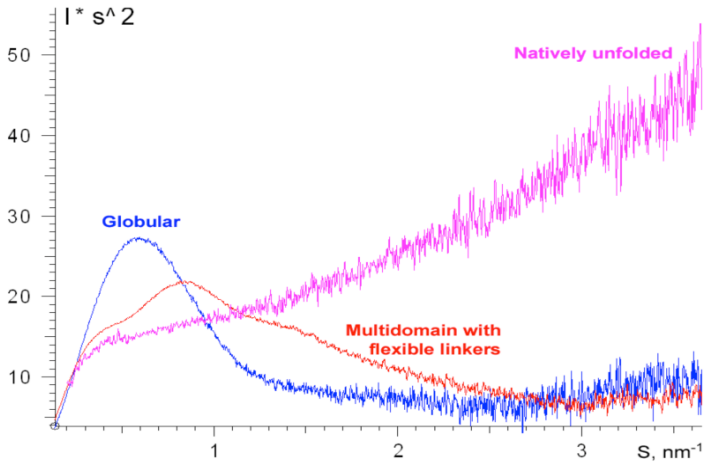

Figure 2.4: Kratky plots ideally observed for globular, unfolded and multidomain proteins with linkers.

After extracting information on these experimental parameters, Denovo calculation of the structural model for the protein was attempted using the program DAMMIN. Superposition of ten highly credible and independent models gave the *ab initio* shape using the program SUBCOMP and the averaged model was generated using DAMAVER program [195, 196].

2.2.9 Cloning strategy for generating sub complex of $\alpha^{chi}{}_3\beta_3\gamma$ – hybrid protein of thermophilic *Bacillus* PS3 and *M. tuberculosis*

To extend the study on unique features and attributes of the C-terminus of *Mt*α, this stretch of 35 amino acids was included at the end of the subunit α of *Bacillus* PS3 in the complex of $PS3\alpha_3\beta_3\gamma$ to generate a hybrid protein, $\alpha^{chi}{}_3\beta_3\gamma$. $\alpha\text{-}PS3_{(1\text{-}502)}$ + $\alpha\text{-}Mt_{(514\text{-}549)}$ constitute the chimeric portion of α^{chi} in $\alpha^{chi}{}_3\beta_3\gamma$ and was engineered through mutagenesis, wherein the extra residues were inserted using PCR via Overlap extension. Insertion of nucleotides in a gene sequence can be achieved via oligonucleotide synthesis also. However, insertion of nucleotide stretches longer than 100 bp gets very challenging with this method.

The arrangement of genes encoding for subunits α, β and γ in F_1F_O ATP synthase is as shown below.

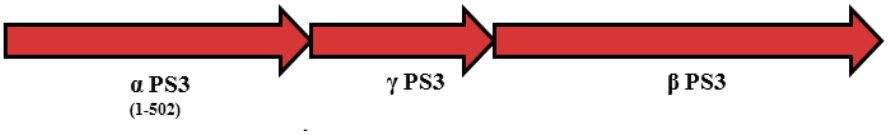

The nucleotide sequence needed to be generated to produce the protein $\alpha^{chi}{}_3\beta_3\gamma$, required insertion of genes encoding for the C-terminus of *Mt*α in the fashion as illustrated below.

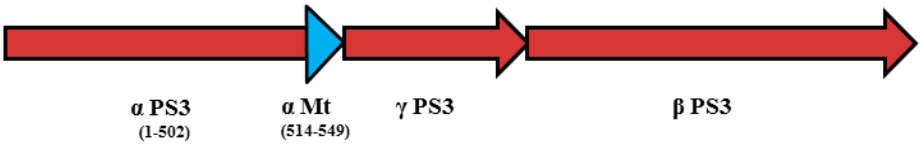

This was achieved by using different templates of plasmid DNA for PS3αγβ and *Mt*α. The plasmid DNA of PS3αγβ encodes for $\alpha_3\beta_3\gamma$ protein complex with mutations included in αC193S, γS107C. This allowed for only one cysteine to be present in the complex, for specific biotinylation for further single molecule rotation studies [197].

At the region of overlap, 4 chimeric primers were generated which contained nucleotides from the template and the overlap region. The primers were 27 nucleotides in length, with 18 coming from the template, forming the annealing segment and 9 from the overlap region, the anchor segment. The anchor segment is derived from adjacent regions in the final desired product. Primers b, c, d and e served as chimeric primers, while a and f served as flanking primers.

Following is a figure illustrating the working principle of Overlap Extension PCR used in this study.

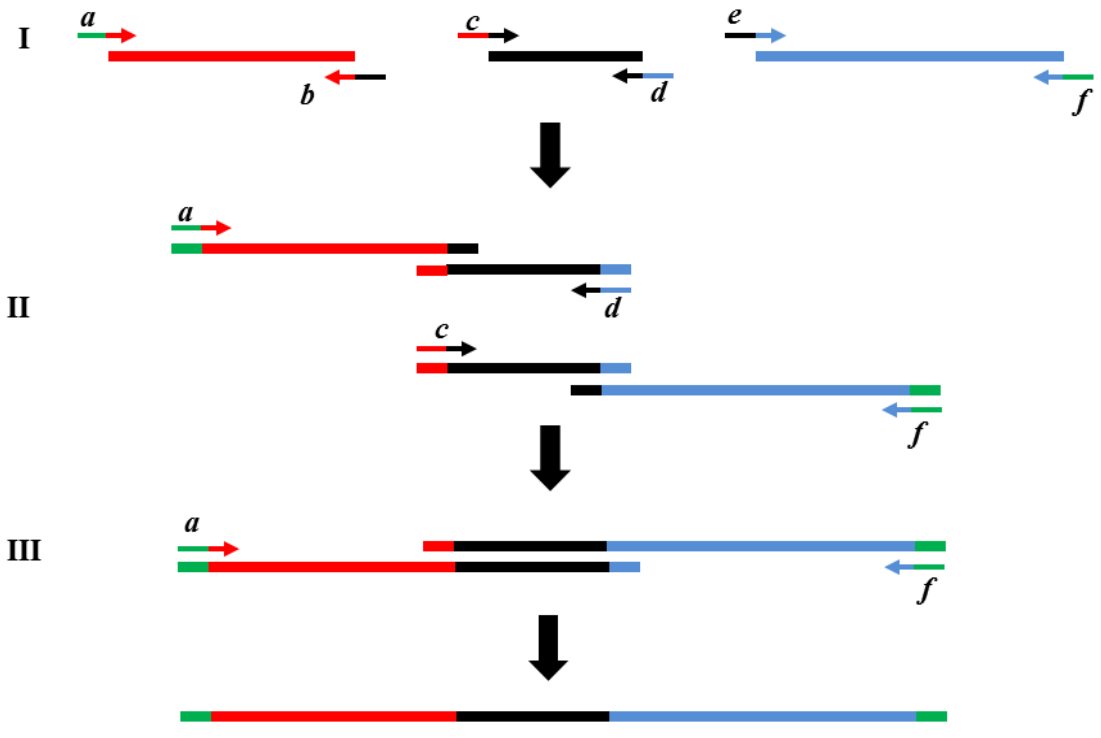

Figure 2.5: Illustration of working principle of Overlap Extension PCR used to generate desired product via insertion mutagenesis.

The Ist set of PCR reactions involved the generation of individual fragments (a+b), (c+d) and (e+f). The fragments are named by the forward and reverse primers used to generate them. The primers and template used are listed below.

Fragment	Forward primer	Reverse primer	Template
a +b	A	b	αγβ (PS3) plasmid DNA
c +d	C	d	*Mt*α plasmid DNA
e +f	E	f	αγβ (PS3) plasmid DNA

Primer	Oligonucleotide sequence 5'-3'
a	5'-AGATGGATCCAATGAGCATTCGAGCGGA-3'
b	5'-AGAGCCGCCTTGAGAAACGACAAACGT-3'
c	5'-GTTTCTCAAGGCGGCTCTGTGGTGCCC-3'
d	5'-CCGCCGGCCTTATTTCTTCTTCTTCGG-3'
e	5'-AAGAAATAAGGCCGGCGGGGGCATATC-3'
f	5'-GAATAAGCTTTCACACTTCGACACCCATCGC-3'

Of the mentioned, (c+d) is the insert fragment and (a+b) and (e+f) form the adjacent flanking fragments. The insert fragment shares terminal complementarities on its either ends with the adjacent fragments.

In the IInd round, Overlap extension PCR was performed to generate two fragments using the primers and template in equimolar ratio as listed below.

Fragment	Forward primer	Reverse primer	Template
a +d	a	d	(a+b) & (c+d)
c +f	c	f	(c+d) & (e+f)

This allowed the formation of each of the flanking regions with the insertion cassette fused to it, with the help of one chimeric and non-chimeric primer. Thus the resulting product form the extended DNA product by forming duplexes during the PCR.

The final round of PCR to incorporate the insertion cassette with the two adjacent terminal complementary segments is achieved by using the terminal flanking primers a and f. This final PCR resulted in the formation of the final desired product wherein the insertion cassette (C-terminus of *Mt*α) is fused in between the terminal flanking region I (PS3α) and terminal flanking region II (PS3γβ) with restriction sites *BamH*I and *Hind*III at 5' and 3' ends respectively.

Following is the reaction mixture set to a volume of 50 µl for all the Polymerase Chain Reactions mentioned, using High fidelity KAPA polymerase.

Reagents	**Amount**
KAPA buffer (5x)	10 µl
dNTP's (2 mM)	1.5 µl
Primers (100 µM)	2 x 0.3 µl
Template (plasmid DNA)	X µl
Deionized water	Y µl
KAPA HiFi DNA polymerase	1 µl

The generated fragment with the desired gene sequence was digested with restriction enzymes *BamH*I and *Hind*III and ligated into similarly double digested and CIAP treated pET 24(b) vector, using the protocol described in section 2.2.2.1 (Figure 2.6). The ligated product was transformed into *E. coli* DH5α cells via Electroporation. 1ml of LB was added and the cells were revived for 1 hour and appropriate amounts were plated on Kanamycin-LB agar plates.

Colonies were screened for positive clone and the plasmid carrying the right clone was shaken in large scale Kanamycin enriched (30 µg/ml), 2YT liquid cultures at 37°C, until OD_{600} of 0.6 was achieved. The His_{10}- tagged proteins were expressed on addition of IPTG (Final concentration: 1 mM) and these cultures were incubated at 37°C for 4 hours. The cells were harvested by centrifugation on a Beckman Coulter Avanti J26X at 8500 g for 13 minutes, 6°C and were stored in -80°C on freezing with liquid nitrogen.

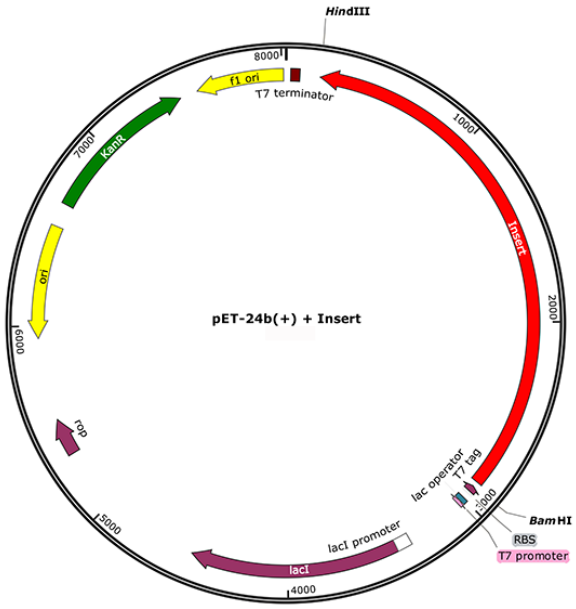

Figure 2.6: pET 24b vector showing full map and unique MCS used for ligation with $\alpha^{chi}\gamma\beta$.

2YT medium is a comparatively more nutrient enriched medium than LB medium, with the following composition.

2YT media: 16 g/l Tryptone
10 g/l Yeast Extract
5 g/l NaCl

2YT medium was used as the growth medium to reach a healthy log phase for bacterial growth, as this was not possible with LB media. To serve as control, the protein for PS3$\alpha_3\beta_3\gamma$ was also purified. As described for the protein purification of subunit α, the steps including cell lysis, centrifugation and incubation with Ni^{2+}-NTA agarose beads were identical. The buffer used was 50 mM Tris-HCl, pH 7.5, 200 mM NaCl, 2 mM Pefabloc^{SC} (BIOMOL) and 1 mM DTT. The His_{10}-tagged proteins of $\alpha^{chi}{}_3\beta_3\gamma$ and $\alpha_3\beta_3\gamma$ were eluted using a linear imidazole gradient (0-600 mM NaCl) and the fractions were checked on a SDS-PAGE. On verification, the fractions containing the protein of interest and pooled together and applied on an Ion- exchange Resource Q column and the fractions containing the His-tagged $\alpha^{chi}{}_3\beta_3\gamma$ and $\alpha_3\beta_3\gamma$ were pooled and concentrated as required using Centricon YM-30 (100 kDa molecular mass cut off) spin concentrators (Millipore).

2.2.10 NADH coupled continuous assay to measure ATP hydrolysis activity of the complex PS3$\alpha_3\beta_3\gamma$ and $\alpha^{chi}{}_3\beta_3\gamma$ (PS3 and *Mt*) F_1F_O-ATP synthase.

ATPase activity of the complex $\alpha^{chi}{}_3\beta_3\gamma$ and PS3$\alpha_3\beta_3\gamma$ was measured using the NADH-coupled continuous assay. This assay is based on the fact that NAD^+ and NADH have different absorbance at 340 nm. Both NAD^+ and NADH show strong absorbance at 259 nm owing to the presence of the adenine moiety. However, NADH, the reduced form shows an additional strong absorbance peak at 340 nm, while the oxidised form does not. Spectrophotometric measurement of the decreasing population of NADH at 340 nm, which is the consequence of its oxidation in this continuous assay, allows monitoring the rate of steady state hydrolysis of ATP in real time. This ATP regenerating system is driven by pyruvate kinase (PK) which catalyses the conversion of a phosphoenol pyruvate (PEP) to a pyruvate, by transferring the phosphate to an ADP to generate an ATP molecule. In the process the resulting pyruvate is converted to lactate by the Lactate dehydrogenase (LDH) at the expense of NADH which gets oxidised to NAD^+. The measurements were done over a period of 250s with an interval of 2 seconds on addition of the ATPase to the enzymatic solution containing 2 mM ATP in 25 mM HEPES, 25 mM KCl, 5 mM $MgCl_2$, 5 mM KCN, 2 mM PEP, 0.5 mM β-NADH, 30 units each of LDH and PK enzymes. The activity of the enzyme was calculated by accounting for the slope of the linear part of the curve.

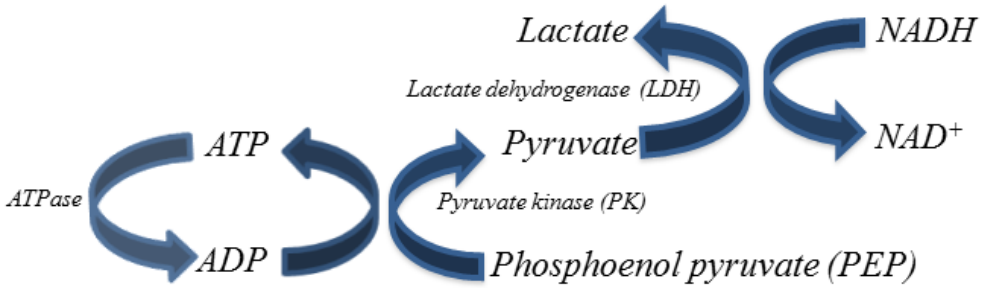

Figure 2.7: Scheme for the reaction of NADH coupled continuous assay to measure ATP hydrolysis, showing the conversion of PEP to lactate through pyruvate with the generation of ATP and the oxidation of NADH.

2.2.11 Labeling of PS3α3β3γ and $\alpha^{chi}{}_3\beta_3\gamma$ for Single molecule rotation Experiments

The following method served to biotinylate Cys107 of subunit γ in PS3$\alpha_3\beta_3\gamma$ and $\alpha^{chi}{}_3\beta_3\gamma$ for the specific attachment of biotin-malemide. A protein concentration of 6.5 μM was used in buffer 50 mM Tris-HCl, 250 mM NaCl, pH 7.5 and incubated with 1.2- fold molar excess of biotin-PEAC5-maleimide (Dojindo, Japan) for 1 min at 4°C. This reaction was terminated using 2 mM N-acetyl cysteine and the unbound biotin was removed by repeated washing with excess buffer (50 mM Tris-HCl, 250 mM NaCl, pH 7.5) in centricon with a molecular cut-off of 100

kDa (Millipore). 25% glycerol was added followed by quick freezing in liquid nitrogen and the protein samples were stored in 5 µl aliquots at -80°C until further use for the rotation experiments.

2.2.12 Rotation Assay for biotin labeled complexes of PS3$\alpha_3\beta_3\gamma$ and $\alpha^{chi}{}_3\beta_3\gamma$

Flow cell chamber was constructed using two cover slips separated by double sided adhesive tape. The bottom cover slip, bigger of the two was initially cleaned by sonication in 1% Hellamanex III, 2 M Sulphuric acid and H_2O for 30 min followed by rigorous washing with H_2O.

For the rotation experiment, the cover slips with the protein sample were prepared as described below. Each of the solutions, in the order stated below were infused into the flow chamber with a volume of 25 µl followed by a incubation period of 4 min and with 7 min incubation for step 5 alone. Washing step with buffer 50 mM Tris-HCl, 250 mM NaCl, pH 7.5 (Buffer A) was included between each step. Components of steps 2-6 were prepared in buffer A.

1. Ni^{2+}-NTA-horseradish peroxidase conjugate (Qiagen, Germany) in deionised water
2. 10 mg/ml Bovine serum albumin
3. 1 nM of Biotinylated protein
4. Steptavidin coated beads, 1:50 (Millice)
5. Biotinylated Quantum-dots 655 nm, 1:20000 (Invitrogen, Germany)
6. 2 mM ATP.

The cover slip with the protein was immediately studied under an inverted fluorescence microscope (IX83, Olympus, Japan) with an oil immersion objective (Plan Apo 100x/1.40 oil). The instrument was equipped with an Ocra Flash-4.0 CMOS camera (Hamamatsu, Japan) to record moving protein-bead complex. A 491 nm diode laser in TIRF mode was used to excite the quantum dots. On a connected computer system, videos were recorded with a frame rate of 100 frames/s and a resulting magnification of 65 nm/pixel. To obtain the angular orientation of the bead in each frame, self-customised Matlab software was used to evaluate the recorded videos by Dr. Hendrik Seilaff.

2.2.13 Cloning various constructs of subunit ε F_1F_O ATP synthase from *M. tuberculosis*.

To amplify the various construct for subunit epsilon *Mt*ε, with Δ*atpC as* coding region, oligonucleotide primers incorporated with *NcoI* & *SacI* restriction site (underlined) were designed.

Construct	Primer	Oligonucleotide sequence 5'-3'
$Mt\varepsilon_{1-120}$	Forward	5'-GAGTTGTCCCATGGCCGAATTGAAC-3'
	Reverse	5'-GATCCGAGCTCTTAGATCGCGCCG -3'
ε_{121hyb}	Forward	5'-GAGTTGTCCCATGGCCGAATTGAACGTTGAGATCGTCGCCGT -3'
	Reverse	5'-TCCGAGCTCTTACATCGCTTTGTCGATCGCGCCGAC-3'
*Ec*ε	Flanking Forward (*a*)	5'TAATCGGACCCATGGCAATGACTTACCACC-3'
	Flanking Reverse (*b*)	5'-GCTTTTCAAGGAGCTCTTACATCGCTTTTTTGGTC-3'
	Internal Forward (*c*)	5'-GACGAAGCGCGAGCAATGGAAGCGAAA-3'
	Internal Reverse (*d*)	5'-TTTCGCTTCCATTGCTCGCGCTTCGTC-3'

The hybrid construct for subunit epsilon for *M. tuberculosis (Mt)* and *E. coli (Ec)* were designed by fusing residues from both the species to amplify the gene and produce the chimeric protein. To generate ε_{121hyb}, residues 1-121 were involved from *Mt*ε and 125-128 from *Ec*ε.

Reagents	Amount
Pfu buffer (10x)	5 µl
DNTP's (2 mM)	1.5 µl
Primers (100 µM)	2 x 0.5 µl
Template (plasmid DNA)	1 µl
MilliQ water	40.5 µl
Pfu DNA polymerase	1 µl

For $Mt\varepsilon_{1-120}$ and ε_{121hyb}, *M. tuberculosis* plasmid DNA was used as template for polymerase chain reaction (PCR). PCR was set up in a total volume of 50 µl on ice with the appropriate concentration of constituents as mentioned below.

All reagents were pipetted into a PCR tube kept on ice all the time, mixing of the reagents was done by short centrifugation. PCR Thermocycler (Biometra T personal) was preheated to 99ºC before reaction tubes were placed inside the machine. The following PCR Thermocycler program was used for amplification:

Cycle steps	Temperature	Time	
Lid	99 ºC		
Initial denaturation	96 ºC	2 min	
Cycle denaturation	96 ºC	30 sec	30 cycles
Annealing	Variable	45 sec	
Extension	72 ºC	1 min	
Final extension	72 ºC	5 min	
End	4 ºC		

Construct	Annealing temperature
$\varepsilon_{1\text{-}120}$	58°C
ε_{121hyb}	59°C
*Ec*ε	PCR I-55°C PCR II-62°C

Cycle denaturation, annealing and extension steps were repeated for another 29 cycles. Total time taken for the PCR program was 1 h 11 min 30 s.

Protocol for quality check and gel extraction for the PCR products was performed identical to that for the *Mt*α constructs. The *Ec*ε was generated and amplified by Overlap extension PCR method. The working principle of this strategy is illustrated in figure 2.8 [198]. The two fragments of subunit ε corresponding to residues from *Ec* were amplified in separate PCRs. The flanking forward primer (*a*) tagged with restriction site *Nco*I and internal reverse primer (b) was used for fragment I. For fragment II, the combination of flanking reverse primer (*d*) tagged with *Sac*I restriction site and internal forward primer (*c*) with overlapping nucleotides was used. These fragments were applied on a 1.2% agarose gel to ensure high purity levels. The amplified fragments coding for the N- and C-termini of the chimeric protein were fused together through a second PCR using primers (*a*) and (*d*). The overlap allowed one strand from each purified fragment to act as a primer on the other and the extension of this overlap by flanking primers (*a* and *d*) in second PCR reaction resulted in the desired product.

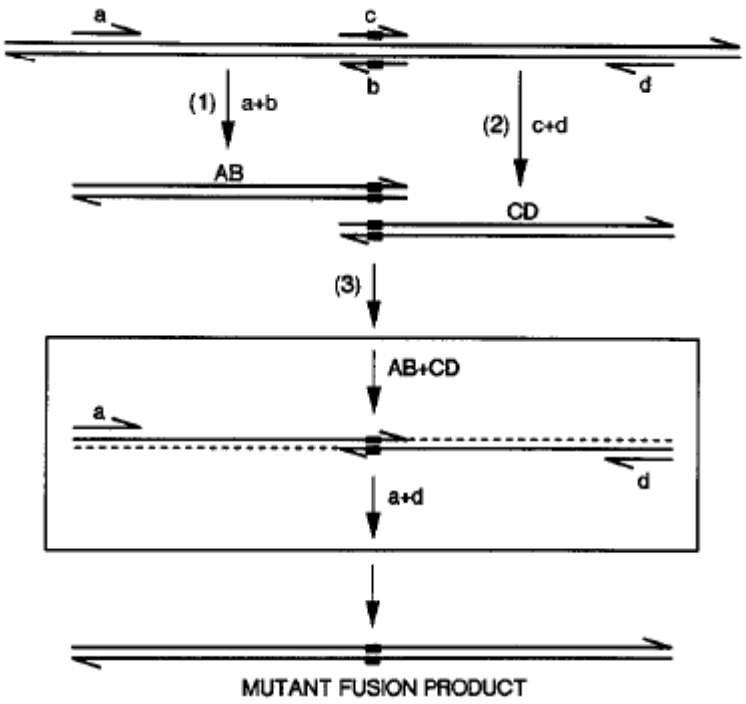

Figure 2.8: Schematic representation of the Overlap Extension PCR strategy used to clone *Ec*ε construct [198].

The protocol followed for cloning the PCR product into the pET-9d vector is identical to that described in section 2.2.5 with a few changes as listed below. The gel extracted PCR product was double digested with *Nco*I and *Sac*I and ligated with similarly double digested and CIAP treated pET9d vector. On sequence verification, the plasmid containing the desired gene of interest was transformed into *E. coli* BL21 DE3 cells for protein expression following which Induction and solubility tests were performed as per the steps described in section 2.2.2.3.

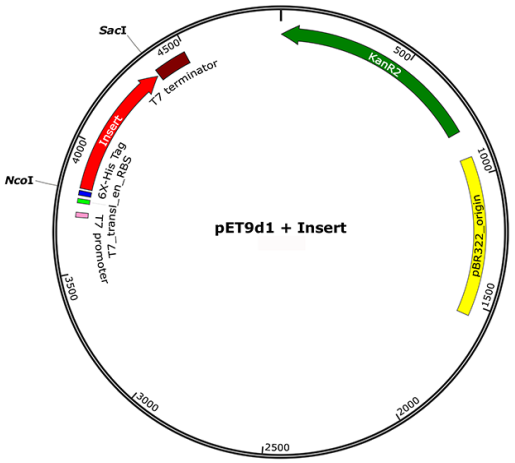

Figure 2.9: Modified pET-9d (+) vector showing full map and unique multiple cloning sites (MCS) that has been used to clone various genes [193].

2.2.14 Production and purification of subunit ε constructs: *Mt*ε$_{1\text{-}120}$, ε$_{121hyb}$, *Ec*ε and PS3ε

F_1F_O ATP synthase

Induction test

The protocol followed for the induction test is exactly as described in section 2.2.7.

Solubility test for recombinant proteins

The steps followed to verify for the right solubility buffer and conditions can be referred under section 2.2.7.

Purification of subunit *ε* constructs: *Mt*ε$_{1\text{-}120}$, ε$_{121hyb}$, *Ec*ε and PS3ε

After successful solubility test, proteins were then purified in large scale. To produce His$_6$- *Mt*ε$_{1\text{-}120}$,ε$_{121hyb}$, *Ec*ε and PS3ε liquid cultures were incubated in Kanamycin-positive (30 mg/ml) LB medium at 37°C with shaking of 180 rpm, until an optical density OD_{600} of 0.6 - 0.7 was achieved. Expression of His$_6$- *Mt*ε$_{1\text{-}120}$ and ε$_{121hyb}$ were obtained by adding of isopropyl (thio)-β-D-galactopyranoside (IPTG) to a final concentration of 1 mM. Following overnight incubation at 15°C for four hours, the cells were harvested at 8500 x *g* for 13 min, 6°C. Subsequently, they were lysed on ice by sonication for 3 x 1 min in buffer A (50 mM Tris-HCl, pH 8.5, 200 mM NaCl, 2 mM PMSF and 2 mM Pefabloc^{SC} (BIOMOL) and 10% glycerol. Precipitated material was separated by centrifugation at 10 000 x *g* for 35 min. Supernatant was filtered (0.45 µm; Millipore). This was passed over a 1.5 ml Ni^{2+}-NTA resin column to isolate

subunit ε. His-tagged protein was allowed to bind to the matrix for 1.5 h at 4°C and eluted with an imidazole-gradient (0 - 400 mM) in buffer A. Fractions containing His-tagged *Mt*$\varepsilon_{1\text{-}120}$ and ε_{121hyb} were pooled and concentrated as required using Centricon YM-3 (3 kDa molecular mass cut off) spin concentrators (Millipore). Imidazole was removed by gel filtration chromatography using a Superdex 75 HR 10/30 column (GE Healthcare) and a buffer of 50 mM Tris-HCl (pH 8.5), 200 mM NaCl.

The cultivation conditions for *Ec*ε and PS3ε were slightly altered as the soluble protein was obtained with liquid cultures grown at 37°C, 4 hours induction with IPTG. The cells were harvested as described earlier and the two step purification protocol including Ni^{2+}-NTA affinity chromatography and ion exchange chromatography were performed to produce the protein for NADH coupled ATP hydrolysis study. ATP hydrolysis assay was performed using NADH coupled continuous assay as described in section 2.2.2.8.

To obtain protein of very high homogeneity and purity for crystallization and NMR studies *Mt*$\varepsilon_{1\text{-}120}$ was subjected to a three step purification protocol including Ni^{2+}-NTA affinity chromatography, ion exchange and gel filtration chromatography. The pooled fractions from the Imidazole gradient were applied on ion-exchange chromatography using Resource™ Q column (GE Healthcare). The buffers used are A: 50 mM Tris-HCl (pH 8.5) and 10 % glycerol and B: 50 mM Tris-HCl (pH 8.5), 1 M NaCl and 10% glycerol. The flow through collected was concentrated as required using Centricon YM-3 (3 kDa molecular mass cut off) spin concentrators (Millipore) and then applied on gel filtration chromatography column using a Superdex 75 HR 10/30 column (GE Healthcare) using buffer of 50 mM Tris-HCl (pH 8.5), 200 mM NaCl and 10% glycerol.

The purity and homogeneity of all the samples were analysed by SDS-PAGE, SDS-gels were stained with Coomassie Brilliant Blue G250. Protein concentrations were determined by bicinchoninic acid assay (BCA; Pierce, Rockford, IL., USA) [199].

2.2.15 Quantification of proteins by bicinchoninic acid (BCA) method

BSA is used as a standard for protein quantification by BCA method. BCA reagent is available in kit form from Pierce (Rockford, IL, USA.) and instruction for measuring protein concentration was followed. In general, two dilutions of protein samples were taken and each of them was measured in triplicate to avoid any error in the measurement. Optical density was measured at 562 nm against blank. Standard curve with 50 µg/ml, 125 µg/ml, 200 µg/ml and 250

μg/ml of BSA was then drawn from the OD_{562} and fitting equation was derived. The same equation was used to calculate protein concentration.

2.2.16 Circular Dichroism spectroscopy

Circular dichroism spectroscopy measures the difference between the absorption of right- and left handed circularly polarized light, arising due to the asymmetry of particular molecule under consideration. Circular dichroism can be used to determine the secondary structure contents of protein in far UV range, where peptide bond acts as active chromophore. Steady state CD spectra were measured in 0.1 mm quartz Hellma cell (60 μl volume) at 18°C on CHIRASCAN spectropolarimeter (Applied Photophysics) instrument at a step resolution of 1 nm from 180 – 260 nm far UV range, of spectrum under continuous purging of N_2 gas. Protein samples were buffer exchanged, reduced or oxidized by appropriate protocols before measurements. Each protein sample was measured in triplicates at a concentration of 1 mg/ml, with the buffer reading taken before and after protein sample. Averaged buffer base line was subtracted from average protein values using in built Chirascan software. Initial degree cm^2 $dmol^{-1}$ units were converted into mean molar residue ellipticity (Θ) with the help of Chirascan software by giving appropriate cell path length, molecular weight, number of amino acid residues and protein concentration values. Final plotting was done in MS Excel (2010). In order to analyze the CD spectrum, the following algorithms were used: Varselec [200], Selcon [201], Contin [202], K2D [203] (all methods as incorporated into the program Dicroprot [204] and Neural Net [205].

2.2.17 Crystallization of *Mt*$\varepsilon_{1\text{-}120}$

Crystallization of *Mt*$\varepsilon_{1\text{-}120}$ attempted using vapour diffusion method at 18°C with two different concentrations of 5 mg/ml and 10 mg/ml. Various commercially available crystallization kits were used as listed in the following table and in total about 800 conditions were tried. These contain a number of previously made conditions of buffer with additives, precipitants and cryoprotectants which have been tried and tested to produce crystals. Hanging drops were set up by mixing 1 μl of the purified *Mt*$\varepsilon_{1\text{-}120}$ in buffer 50 mM Tris-HCl, pH 8.5, 200 mM NaCl and 10% glycerol with 1 μl of the reservoir solution and equilibrated against 200 μl reservoir solution.

Crystallization Kits used

- **Hampton Crystal Screen I**
- **Hampton Crystal Screen II**
- **Wizard I**
- **Wizard II**
- **Wizard III**
- **Wizard IV**
- **Precipitant Synergy I**
- **Precipitant Synergy II**
- **PEG/ION I**
- **PEG/ION II**
- **MORPHEUS I**
- **MORPHEUS II**
- **INDEX I**
- **CRYO I**
- **CRYO II**
- **Grid Screen Ammonium sulphate**
- **Grid Screen MPD**
- **Grid Screen PEG 6000**

2.2.18 Cloning of subunit *Mt*$\varepsilon_{1\text{-}120}$ F_1F_O ATP synthase from *M. tuberculosis* H37rv in the *M. smegmatis* system

To generate *Mt*$\varepsilon_{1\text{-}120}$ in pYUB1049, an *E. coli- Mycobacterium* shuttle vector, the ΔatpC from *Mt* H37rv was amplified using the following primers containing *Nde*I and *Hind*III sites in the forward and reverse primers respectively as described in section 2.2.3.1. The amplified PCR products were then digested with *Nde*I and *Hind*III restriction enzymes. The digested product was purified using the gel extraction kit (QIAGEN) and subsequently ligated into the similarly digested pYUB1049 vector to allow the inclusion of a His-tag at the N-terminal.

As described in section 2.2.3.2, the construct was transformed into *E. coli* TOP10 cells and plated on Hygromycin B (50 μg/ml) enriched LB-agar plates. Positive clones were amplified using QIAPrep Spin miniprep Kit (QIAGEN). The sequence verified plasmid was electroporated into electro competent *M. smegmatis* mc2 4517 cells.

To tackle the high lipid content of the mycobacterial cell wall, a slightly optimized protocol for transformation was used as compared to the one previously described. Plasmid DNA was added to 40 µl of freshly thawed electro competent *M. smegmatis* cells with 260 µl sterile 10% (v/v) glycerol. The mixture was transferred to a 2 mm electroporation cuvette and electroporated at 2.5 kV. On addition of 1 ml of 7H9/ADC media, the electroporated cells were incubated at 37°C for 3 hours. 200 µl of this cell culture was plated on 7H10/ADC +0.05% (v/v) tween80 agar plates with the appropriate antibiotics (Hygromycin and Kanamycin) and were incubated at 37°C for 3 days.

2.2.19 Protein expression using *M. smegmatis* as a host

Small-scale expression test was performed to check for protein expression in the auto-induction medium (ZYP-5052).

Reagents for auto-induction medium (ZYP-5052): 1% N-Z-Amine AS
0.5% Yeast Extract
50 mM Na_2HPO_4
50 mM KH_2PO_4
25 mM $(NH)_4SO_4$
2 mM $MgSO_4$
0.5% glycerol
0.05% Glucose
0.2% α-lactose
Antibiotics (Hygromycin B +Kanamycin)

A seeder culture was started by inoculating the LB/Tween 80 medium with a single transformed colony, which was grown at 37°C for 48 hours. This was used in 1:100 dilution to inoculate the ZYP-5052/ Tween 80 expression culture, which was grown at 20°C and small aliquots of 30 ml were tested every 2 days for protein expression. The cell cultures were centrifuged at 7,500 x g for 20 minutes to harvest the cells. The pellet was resuspended in buffer 50 mM Tris, 200 mM NaCl, 10% glycerol and lysed by sonication on ice for 4* 2 mins. The cell lysate was centrifuged at 40,000 x g to separate the soluble protein in the supernatant from the pellet. 200 µl of the supernatant was incubated for 15 minutes at 4°C with 100 µl of Ni^{2+}-sepharose beads that were pre-incubated with the buffer used for lysis. The sample was spun down at 1,500 X g for 30 seconds to allow the Ni-sepharose beads with the bound protein to settle down. On removal of the supernatant, the beads were washed with the same buffer and centrifuged again. This wash cycle was repeated twice and finally 25 µl aliquot of the Ni-sepharose bead sample was drawn and loaded on a SDS-PAGE gel after the addition of 5 x SDS loading buffer, to check for the presence of the desired protein.

2.2.20 Thermofluor Stability Assay

Reagents and materials used: JBScreen Solubility HTS
Microamp Optical 96-well Reaction plate
Sypro Orange Dye (5000X)
BIORAD Microseal B seal
BIORAD iQ5-Multicolour RT-PCR detection system
Thermoscientific Finnpipette 5-50 µl

Thermofluor stability assay measures the fluorescence emitted by the flurophore dye as a result of change in the protein folding with increase in temperature (Figure 2.14).

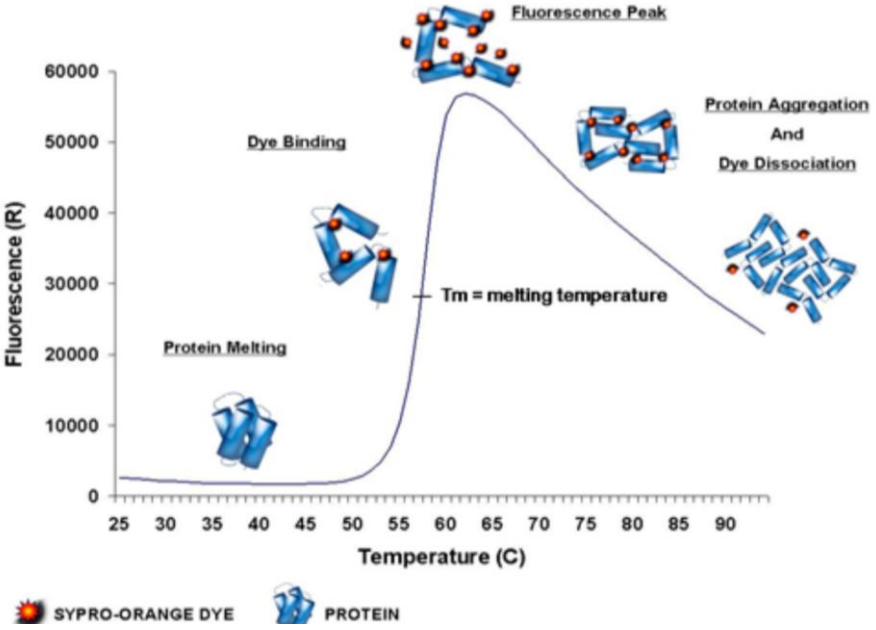

Figure 2.10: Schematic representation of the process of increasing fluorescence with binding of the flurophore dye to the unfolding protein with increasing temperature.

In this experiment, the JBScreen Solubility HTScreen used contains buffer conditions with varying pH, salt and cryoprotectant concentrations to select the optimal buffer condition with additives for the protein of interest. Each well of the 96 welled plate was loaded with the protein (2 mg/ml) and the SYPRO orange dye (1X) with Buffer A (50 mM Tris-HCl, 200 mM NaCl, 10% glycerol) to a total reaction volume of 25 µl. Subsequently, as per the chart provided, the different buffers are added in sequence to each of the wells, using the multichannel Finnpipette. The plates were centrifuged for 5 min at 300 rpm to homogenise the sample. An IQ5 Bio-Rad iCycler iQ5 Multicolor Real-Time PCR Detection System was used for monitoring the melting curve of the proteins with thermal melt program from 20ºC to 95ºC with 1ºC/1 min dwell time was used to record the values. RT-PCR machine has a LED/photodiode set to match the excitation and emission wavelengths of SYPRO orange

dye. The measurements were performed in triplicates to obtain concomitant values. On averaging the values, the curves were plotted for the fluorescence intensity against temperature. The melting temperature (Tm) was determined by the inflection point of the curve. Plots were generated to compare the protein in varying conditions of additives and cryoprotectants.

2.2.21 Nuclear Magnetic Resonance (NMR) Spectroscopy

Nuclear Magnetic Resonance spectroscopy is a versatile technique that helps understand the molecular function of bio molecules such as proteins from a structural and dynamic perspective. Studying various NMR parameters such as chemical shifts, spin-spin splitting, linewidths, relaxation, the nuclear Overhauser effect and chemical exchange, not only allows structure determination, but also provides a deep insight into the interactions such as those of protein ligand to demonstrate new binding partners as well as to map the binding regions. All the NMR experiments were performed on Bruker Avance 600 MHz and 700 MHz at NTU, NMR core facility.

2.2.22 Isotopic labeling (^{15}N) of proteins

Reagents for Minimal media (M9): 42 mM Na_2HPO_4
22 mM KH_2PO_4
8.5mM NaCl
1 g/L $^{15}NH_4Cl$
0.1 mM $CaCl_2$
2 mM $MgSO_4$
10 g Glucose
30 µM $FeCl_3$
5 ng/lThiamine
Antibiotic
LB medium

For the production of uniformly labelled ^{15}N recombinant proteins in *E. coli* BL21 (DE3), M9 minimal medium was used. All unlabelled reagents were of standard laboratory reagents grade. All solutions were prepared using MilliQ water (Millipore, Billerica, MA). 50 ml of overnight culture was grown. The cells were pelleted down by centrifugation at 5000 g at room temperature. The supernatant LB was decanted and the pellet was resuspended and washed in M9 media. An appropriate volume of this was used to inoculate 500 ml of minimal medium to 0.1 OD. Cells were shaken at 37˚C till an OD_{600} of 0.6 was reached. The culture was then induced with 1mM IPTG at 15˚C overnight. The cells were harvested and frozen in liquid nitrogen and stored at -80˚C until purification.

2.2.23 2D -^{15}N NMR spectroscopy

For 2D -^{15}N HSQC (Hetero Nuclear Single Quantum Coherence), ^{15}N labelled protein samples were prepared in three different buffers as listed below.

A: 50 mM phosphate buffer, (pH 6.8, 200 mM NaCl, 10% glycerol)

B: 50 mM Tris-HCl buffer, (pH 7.2, 200 mM NaCl, 10% glycerol)

C: 50 mM Tris-HCl buffer, (pH 7.5, 200 mM NaCl, 10% glycerol).

10% D_2O (v/v) was added to all these samples before recording the spectrum. The experiment was performed on the core facility Avance 600 MHz instrument (Bruker, Billerica, MA) at 298K.

2.2.24 Expression of $\varepsilon_{1\text{-}120}$ *M. tuberculosis* F-ATP synthase in *E. coli* BL21 GroEL-ES strain

To ensure proper folding of protein, chaperones can be used which assist the nascent polypeptide to achieve the right folding pattern to form a properly folded protein. The GroEL-ES class of chaperones in *E. coli* aid folding of synthesized proteins on ATP consumption. GroEL-ES complex system forms a cage encapsulating the substrate protein, which might be a partially folded intermediate. Using ATP the folding is achieved and the folded protein is released with the disassembly of the GroEL-ES complex and making available the cavity for binding another substrate protein.

This system was employed for folding the over expressed *Mt*$\boldsymbol{\varepsilon_{1\text{-}120}}$ in *E. coli* BL21 cells. The cell strain of *E. coli* BL21 GroEL-ES containing pBAD vector was used which codes for GroEL-ES and over expresses this to allow sufficient population of the chaperone to be present to facilitate the folding of the recombinant protein. The promoter present in this vector is induced using Arabinose.

Heat shock competent cells were kindly provided and further prepared according to the following protocol as given by Prof. Oliver Mueller-Cajar's lab (SBS, NTU).

Materials required: Luria Bertoni media: *10 g/l Tryptone*
5 g/l Yeast Extract
5 g/l NaCl
0.1 M $CaCl_2$
15% glycerol

O/N culture was set up using the plasmid provided, in Chloramphenicol enriched LB and shaken at 180 rpm at 37°C. Next morning, this was scaled up to 1 L in Chloramphenicol enriched LB to a starting OD_{600} of 0.1 and allowed to grow at 37°C. On reaching, OD_{600} of 0.6, the culture was removed and placed on ice for 30 minutes. This culture was centrifuged on a

Beckman coulter Avanti J-26XP centrifuge at 4200 rpm for 20 mins at 4°C. Supernatant LB was decanted and the pellet was resuspended in previously autoclaved and chilled mixture of 8 ml of 0.1 M $CaCl_2$ + 15% glycerol. This resuspension was allowed to chill on ice for 30 minutes and aliquots of 50 µl were drawn into each tube and frozen.

2.2.25 Transformation using heat shock

A tube of frozen competent cells was equilibrated on ice for 20 min with the plasmid (pET9d with $\varepsilon_{1\text{-}120}$). Heat shock was performed by placing this mixture on a water bath set to 42°C for 90 seconds and immediately returning this to ice for 2 minutes. This was resuspended in 200 µl of LB and allowed to revive for 30 minutes at 37°C in a shaking incubator. The resuspended cells were plated on Kanamycin-Chloramphenicol LB plates and placed at 37°C O/N. Single colonies obtained the next day, were picked and checked for expression of the desired protein.

2.2.26 Production and purification of *Mt*$\varepsilon_{1\text{-}120}$ in *E. coli* BL21 GroEL-ES cell strain

Overnight inoculum of the transformed plasmid (pET9d with $\boldsymbol{\varepsilon_{1\text{-}120}}$) in *E. coli* BL21 GroEL-ES was setup in Kanamycin-Chloramphenicol enriched LB at 37°C. This was used to scale up the large culture next morning, to a starting OD_{600} of 0.1. The liquid culture in 5 L flasks were placed in the shaking incubator at 37°C and were allowed to grow until the OD_{600} reached 0.5 and were then shifted to an incubator set at 23°C for equilibration. Arabinose (Final concentration: 0.2%) was added to induce the pBAD vector to express GroEL-ES at 23°C for 30 minutes. This was followed with the addition of IPTG (Final concentration: 1 mM) to induce the pET9d vector to express *Mt*$\boldsymbol{\varepsilon_{1\text{-}120}}$. The culture was allowed to shake at 180 rpm at 23°C O/N, after which the cells from the liquid culture were harvested at 8,500 g for 12 minutes at 4°C on Beckman Coulter Avanti J26X centrifuge. The cells were frozen in liquid Nitrogen and stored in -80°C until further use.

2.2.27 Purification of *Mt*$\varepsilon_{1\text{-}120}$ in *E. coli* BL21 GroEL-ES cell strain

The cells for double labeled purified protein was cultivated as per the composition mentioned in section 2.2.3.6.1 with the exception that ^{13}C labeled glucose was used in the cultivation media to obtain ^{15}N and ^{13}C labeled protein. The conditions and antibiotic selection is as defined in the previous paragraph. The purification strategy adopted is as elaborated in section 2.2.3.3.3, with final step of gel filtration performed in 50 mM Phosphate, 200 mM NaCl, 5 mM

EDTA, 10% glycerol. On setting to the appropriate concentration, 3D NMR studies were initiated to acquire 3D Data sets using the Non-Uniform Sampling technique with help of Dr. Sandip Basak and Wilson Nartey and the guidance and support offered by Dr. Scott from Prof. Gerhard Wagner's Lab (Harvard Medical School, USA).

2.2.28 Non-uniform sampling NMR

Although NMR spectroscopy is a versatile technique, a well-known limitation is the difficulty to obtain high-resolution spectrum from short data records. This limitation arises from the fact the time required to complete experiments depends on the number of datasets that need to be acquired and this is problematic in the case of multidimensional NMR experiments. Additionally, extended acquisition time is a constraint but also the instability of the sample under study can add as a woe. Hence the pressing need for designing newer techniques to allow completion of multidimensional NMR experiment in shorter time span.

Non uniform sampling is one such technique, which involves acquiring data sets with random sampling, which is a small percentage of the actual dataset. This is followed with reconstruction and processing of the NMR signal to recover all the required information.

*Mt*ε$_{1\text{-}120}$ provided a good 2D-^{15}N HSQC NMR spectrum. The sample prepared for *Mt*ε$_{1\text{-}120}$ proved to be not stable for a long period of time, propelling efforts to be taken in direction to salvage the best out of the vulnerable sample.

Synergistic efforts were undertaken to express this challenging protein with a better expression system such as BL21 with GroEL-ES and focusing on employing the Non-uniform sampling approach. This technique helped in reducing the acquisition time and experiments were performed to assign the backbone of *Mt*ε$_{1\text{-}120}$.

Experiments performed so far include the 2D ^{1}H-^{15}N HSQC, 3D HNCA, 3D HN(CO)CA, CBCACONH using NUS and 3D HNCACB using traditional NMR. Figure 2.11 gives an idea of the magnetization transfer occurring between the NMR active nuclei for the different experiments, which have been designed to walk through the protein's backbone. These experiments are the workhorse for backbone experiments throwing light on the inter-residue and intra-residue connections.

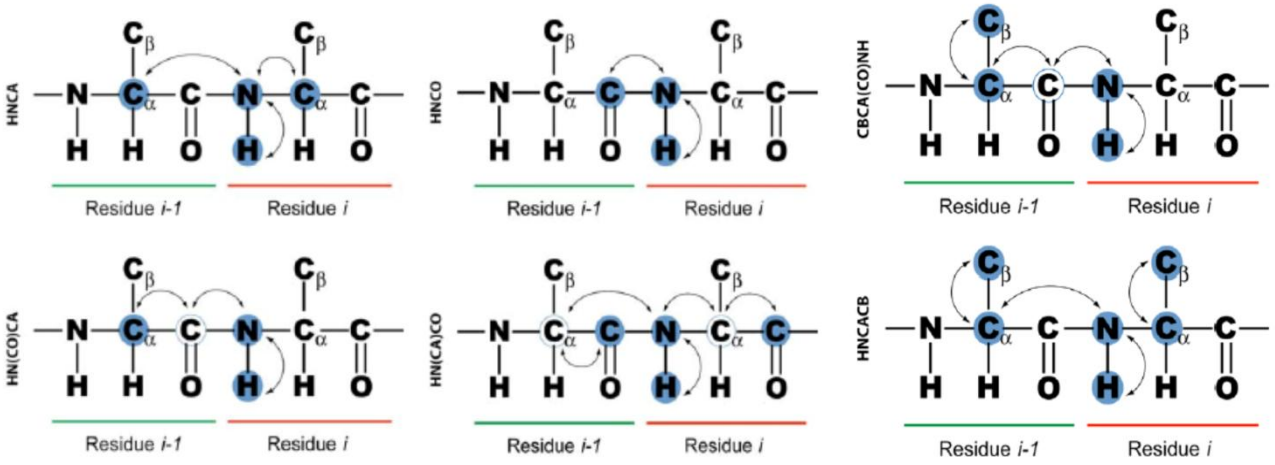

Figure 2.11: 3D NMR experiments for backbone assignment showing the magnetization transfer through NMR active nuclei.

The data acquired for the 3D HNCACB was processed and analyzed using NMRpipe and SPARKY respectively. For NUS, the macros nusPGSv3 designed by Prof. Gerhard Wagner was used to generate the schedule for each of the pulse programs. Ten percent of the actual data points were collected for the NUS data sets. Poisson distribution was enforced on gap sizes to help obtain better reconstruction results as it dictates how the gaps are distributed. Poisson distribution indicates the degree of spread around a known average rate of occurrence. Given that the 10% of the data acquired in NUS is in a random fashion, it is important to apply the Poisson distribution as it specifies the number of successes in a specified region.

Iterative soft threshold (IST) was employed for reconstruction of the non-uniformly acquired data. The principle for IST is illustrated in the following figure 2.16, wherein with the Fourier transformed signal of the Non-uniform signal, a threshold cutoff is applied and this part of the data is stored in a separate file. This part of the signal is now reverse Fourier transformed and subtracted from the original non-uniform signal. In the second iteration, this subtracted signal is forward Fourier transformed and again a new soft threshold cutoff is applied. Following this strategy with multiple iterations, signal with high fidelity is recovered. This is as described for a 1-D experiment and same principle is extended for a 2-D and a 3-D experiment.

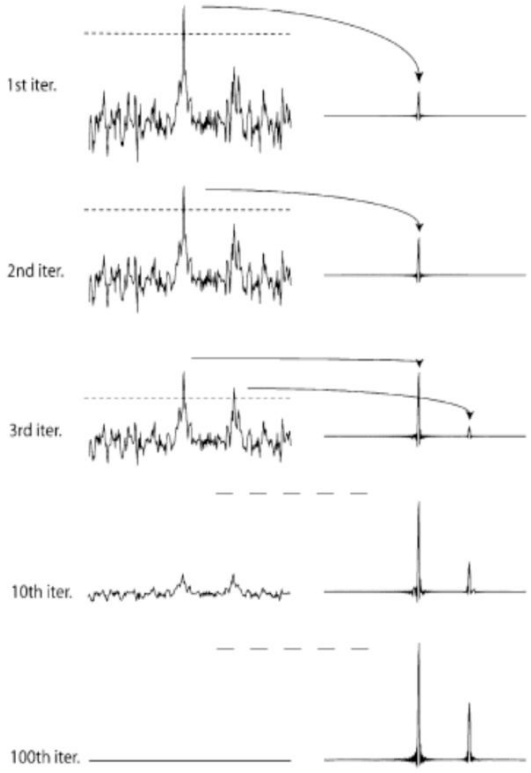

Figure 2.12: Pictorial illustration of the working principle of Iterative soft threshold used for reconstruction of non-uniform sampling NMR data sets [206].

3. Results

3.1 Role of N157 of subunit B of A-ATP synthase in nucleotide binding

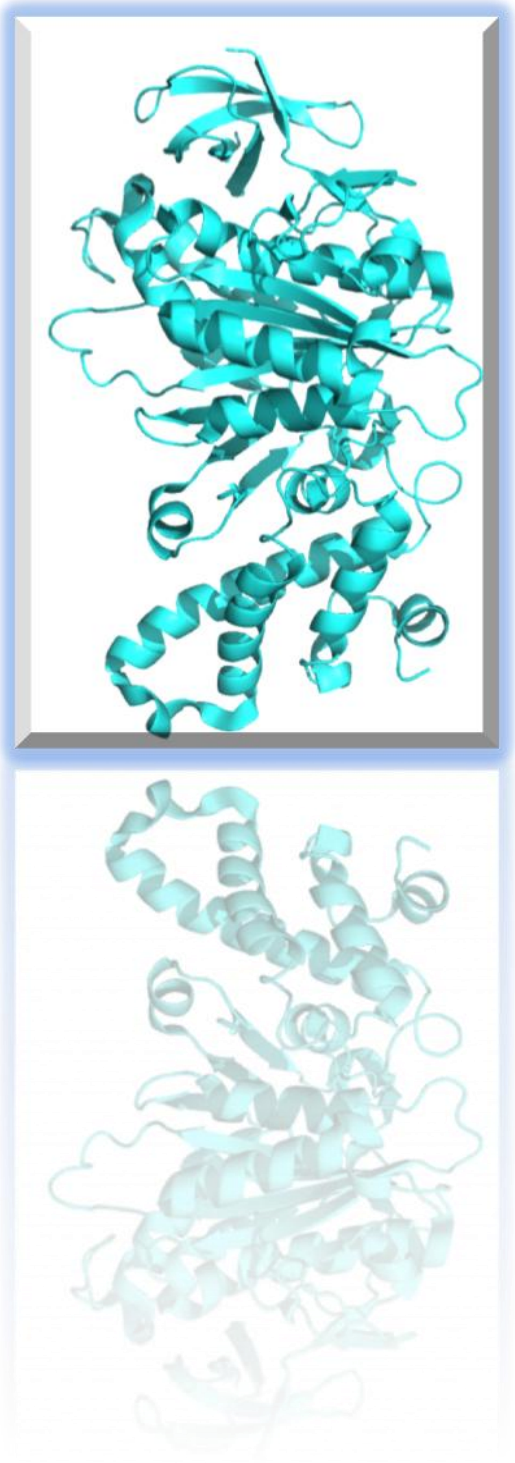

Role of N157 in A-ATP synthase subunit B in nucleotide binding

3.1.1 Introduction

The catalytic nucleotide-binding site in the subunit A of the A_1A_OATP synthases and V_1V_O ATPases possesses the consensus sequence GXXXXGKT(S), commonly referred to as the phosphate binding loop (P-loop), and is also present in the subunits α and β of F-ATP synthases [207, 208]. In subunit B of both A-ATP synthases and V-ATPases such P-loop sequence is not preserved at the equivalent position [52, 183]. The structure of subunit B from *Methanosarcina mazei* Gö1 of A-ATP synthase reveals a unique P-loop sequence ($_{150}$SASGLPHN$_{157}$), which is not conserved with respect to the P-loop sequence of related α subunits ($_{169}$GDRQTGKT$_{176}$) of F-ATP synthases [52]. Mutational studies in the P-loop residues K175 and T176 of subunit α of F-ATP synthases and residues N180 and T181 of subunit B of eukaryotic V-ATPases resulted in the loss of hydrolytic activity, implicating their role in nucleotide binding [185, 209]. To elucidate the role of P-loop amino acid residues in subunit B of A-ATP synthases from *M. mazei* Gö1 in nucleotide binding, mutants H156A, N157A were prepared and N157 was additionally mutated to threonine as it is the corresponding residue in the P-loop motif of the related subunit α of F-ATP synthases from *E. coli* [46]. As shown previously in figure 1.19, threonine residue of the P-loop interacts with the nucleotide by stabilising the Mg^{2+} ion. The main aim of this work is to determine the structure of the N157T mutant to get a better understanding of the relevance of the conserved asparagine residue in the formation and binding traits of the phosphate binding loop of non-catalytic nucleotide binding subunit B of A_1A_O ATP synthase.

3.1.2 Data collection and structure determination of subunit B N157T mutant of *M. mazei* Gö1 A_1A_O ATP synthase

The N157T mutant protein was prepared and crystallised by Dr. Vikram Tadwal [192]. The mutant was cloned using overlap extension polymerase chain reaction method with subunit B insert in pET-9d as a template. The positive clone was expressed as His_6-fusion protein in *E. coli* BL21 (DE3). The recombinant protein was purified using nickel-affinity chromatography and ion exchange chromatography. The N157T protein crystals were obtained by the method of hanging-drop vapour diffusion. Diffraction quality crystals were obtained for the N157T mutant, which diffracted to a resolution 1.7 Å. The crystal belongs to orthorhombic space group P_{212121}. The data collection statistics are shown in Table 3.1.1.

3.1.3 Crystallographic structure of subunit B mutant N157T of *M. mazei* Gö1 A_1A_O ATP synthase

I solved the structure of the P-loop mutant of subunit B from *M. mazei* Gö1, N157T, which diffracted up to a resolution of 1.7 Å [192]. For this mutant N157T, atomic coordinates and structure factors are available under accession code 3SSA (Protein Data Bank) [192]. Two molecules are seen in the asymmetric unit of the crystallised mutant protein. These are designated as chain A and B, and are orientated in a head to tail manner similar to the WT-B (PDB ID: 2C61) [52]. The overall structure of the P-loop mutant is similar to the structure of the WT-B consisting of three domains: an N-terminal β-barrel (residues 13-76), a central nucleotide binding α-β domain (residues 77-358) and a C-terminal α-helical bundle (residues 359-460) with the central nucleotide binding site containing the phosphate binding motif $_{150}$SASGLPHN$_{157}$ (Figure 3.1.1). The overall structure of the N157T mutant in subunit B of the *M. mazei* Gö1 A_1A_O ATP synthase has a cylindrical shape with approximate dimensions of 50 × 50 × 80 Å.

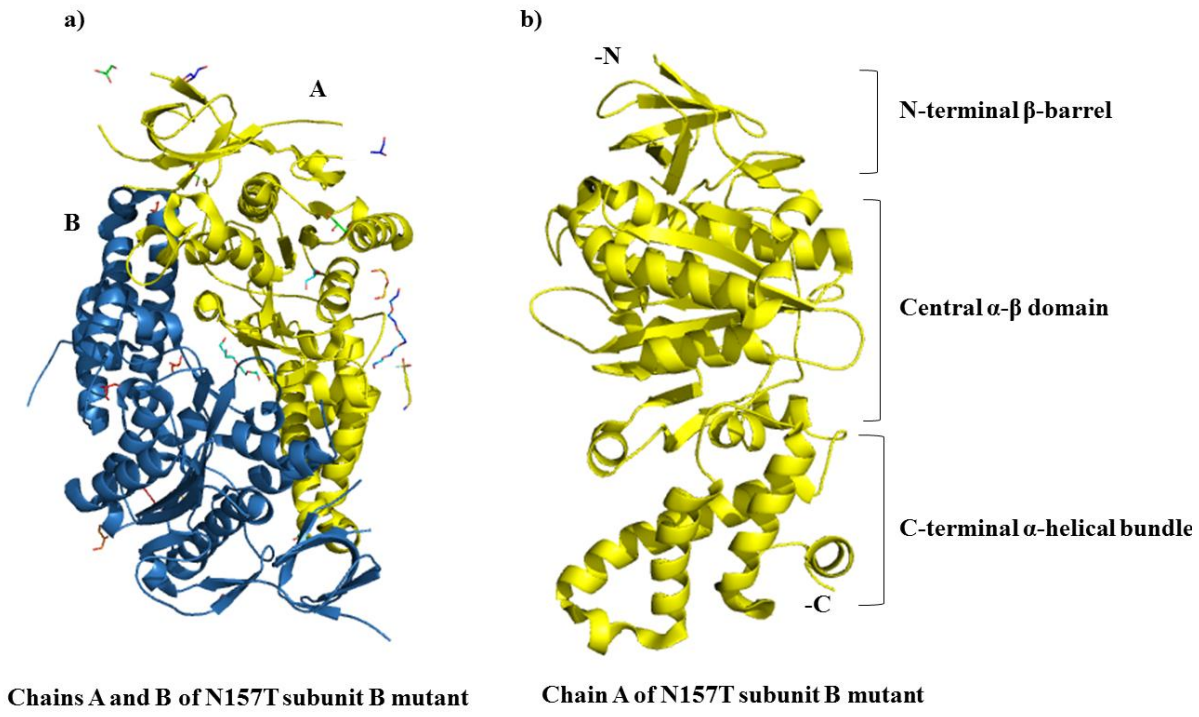

Figure 3.1.1: Crystal structure of N157T of subunit B of the *M. mazei* Gö1 A_1Ao ATP synthase. a) Shown in ribbon representation with head to tail orientation of two molecules in the asymmetric unit (yellow- chain A; blue - chain B). The additives such as glycerol, polyethylene glycol, triethylene glycol used for crystallization can also be visualized with stick representation. b) Chain A of N157T mutant showing the N-terminal β barrel, central α- β and the C-terminal α domain.

In the final refined model of the N157T mutant in subunit B of the *M. mazei* Gö1 A_1A_O ATP synthase, the densities are not visible for amino acid residues from 1-11, 61-69 and 457-460

in chain A, and 1-11, 58-68 and 260-270 in chain B. Despite the high resolution and very good electron density, the residue D125 in both chains A and B of N157A and N157T mutants and M115 of chain A of N157T mutant are found in the disallowed region. The final model comprised of 863 amino acid residues for both molecules (chains A and B) in the asymmetric unit for the subunit B N157T mutant. In addition, the structure contained a protease inhibitor Pefabloc^{SC}, chloride ions, and polyethylene glycol and glycerol molecules. A total of 1106 water molecules could be assigned for the N157T mutant. The N157T mutation in the P-loop ($_{150}$SASGLPHN$_{157}$) could be clearly visualised in the electron density map, fitting perfectly to the corresponding mutated residue (Figure 3.1.2).

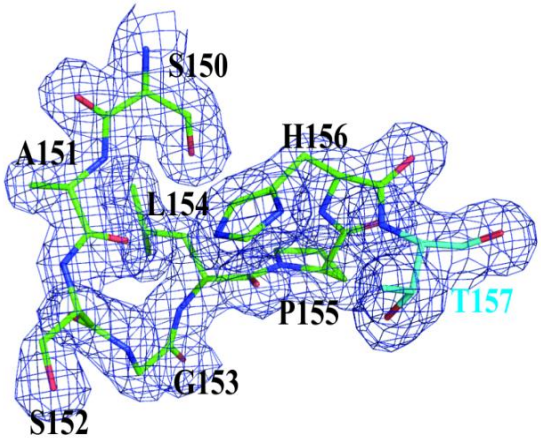

Figure 3.1.2: The $2F_o$-F_c electron density map contoured at 1.0σ (dark blue) showing the mutation at N157T in subunit B of the *M. mazei* Gö1 A_1A_O ATP synthase. The mutated residue is labelled in cyan colour**.**

3.1.4 Structural comparison of the mutant N157T with wild type subunit B

The overall mutant structure of N157T compares well with the WT-B (PDB ID: 2C61) yielding an *r.m.s.d* of 0.16 Å for 410 Cα atoms (Figure 3.1.3) [52]. Larger than average deviations are concentrated in the following regions for the mutant; viz. K33-G42, G93-P104, A113-L121, P147-E158, A182-A202, I302-Y338 and P437-K451. The segments K33-G42 and P437-K451 are highly flexible, causing larger deviations and these belong to the N- and C-terminal regions. The divergence in regions G93-P104 and A113-L121 are attributed to loop flexibility as these are a part of a long loop region connecting the N- and C-terminal domains to the central α-β domain, respectively.

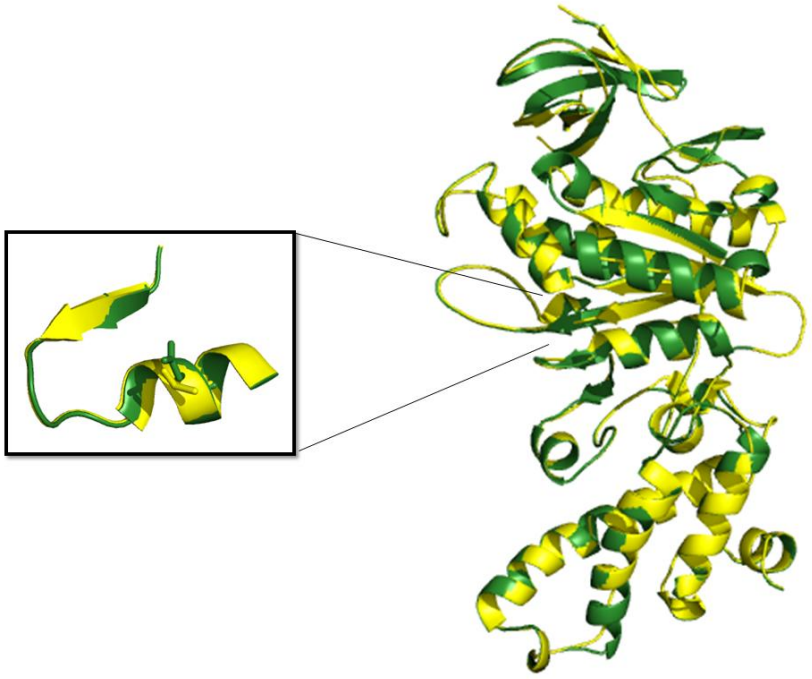

Figure 3.1.3: The superposition of chain A of N157T mutant (yellow) with chain A of subunit B-WT (green) (PDB ID: 2C61) [31]. The P-loop region is shown in the inset with the mutated residue in stick representation.

The region of importance is the P-loop containing region, P147-E158, and the region surrounding it, A182-A202 (the segment containing the $_{184}$GIT$_{186}$ loop, which is the homologues Walker B motif in the catalytic A subunit) and I302-Y338 (the segment adjoining the P-loop that contains the adenine binding pocket). Analysis of the P-loop residues ($_{150}$SASGLPHN$_{157}$) revealed that G153 is deviated more when compared to other residues in the mutant, with a maximum deviation of 0.39 Å. Even though the overall deviation in the P-loop region is negligible for the mutant, significant perturbations are observed in the side chain of residue S152. It displays a dual conformation, wherein one conformer orients opposite and the other takes up either perpendicular or similar orientation to the WT-B (Figure 3.1.4). The difference in the deviation of the residues could be attributed to the difference in the hydrogen bonding interaction in the P-loop residues (Table 3.1.2 and Figure 3.1.4). All of the backbone hydrogen bonding interactions that are found for WT-B are also preserved in the mutant structure.

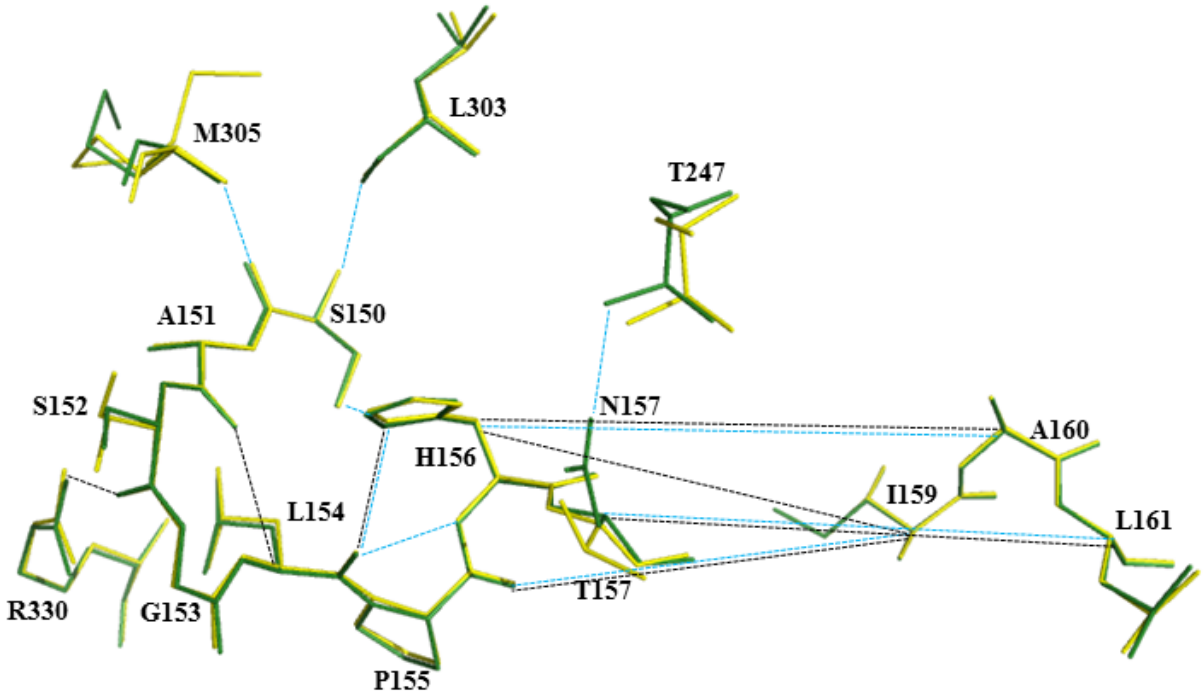

Figure 3.1.4: Structural overlap of subunit B –WT (green) with subunit B mutant N157T of the *M. mazei* Gö1 A_1A_O ATP synthase (yellow). The hydrogen bonding interactions for the P-loop residues are drawn in dotted line, with blue dotted lines indicating the hydrogen bonding interactions for the subunit B-WT and the black dotted lines for the subunit B mutant N157T.

In addition, two more backbone hydrogen bonding interactions are observed in the N157T mutant, one between the amino nitrogen of L154 and the carbonyl oxygen of A151 and the other between the carbonyl oxygen of H156 and the amino nitrogen of I159. Residue 156 shows bifurcated hydrogen bonding. Furthermore, this mutant also shows a main chain-side chain hydrogen bonding between the carbonyl oxygen of S152 and the terminal nitrogen of the guanidinium group in R330. The mutant does not show the weak main chain-side chain hydrogen bonding between the carbonyl oxygen atom of L154 and the imidazole carbon atom of H156. Additionally, because of the mutation, the side interactions for N157 are absent, but the side chain interaction between S150 and H156 is preserved. It can be noted that G153 does not have any hydrogen bonding interactions to the nearby residues, explaining its flexibility and deviation.

In comparison, the α subunit of the F-ATP synthase superimposes with WT-B with measured a r.m.s.d of 1.873 Å for 327 backbone Cα atoms [101]. Except for the arginine and glutamine residues in the middle of the P- loop in subunit α, other residues are located within the allowed deviation (Figure 3.1.5). Notably, lysine175 and threonine176 are positioned similar to the WT-B and N157T mutant, respectively.

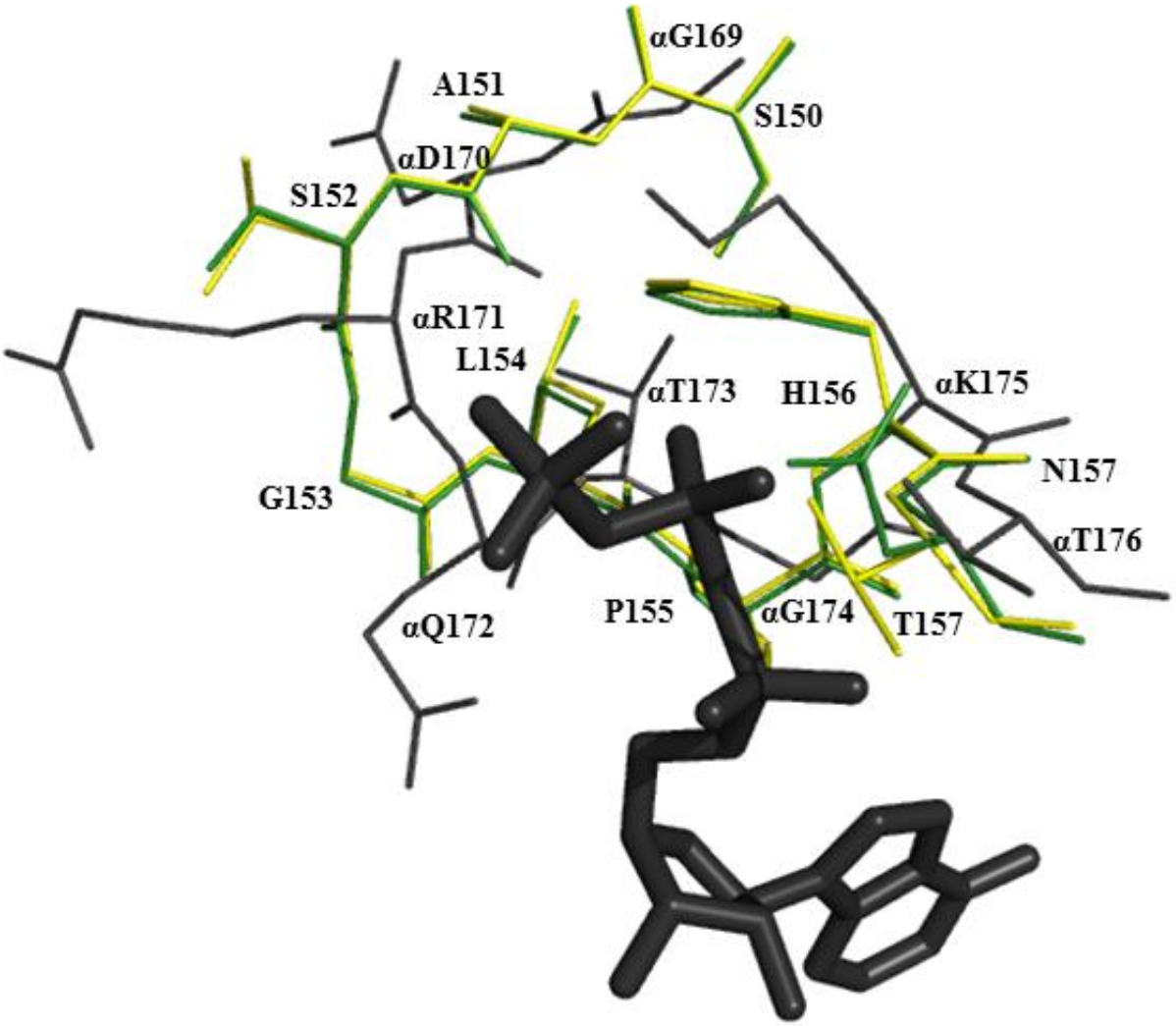

Figure 3.1.5: The P-loop region overlap of WT-B (green) with the N157T mutant protein (yellow) and with subunit α of the bovine F-ATP synthase (grey). The bound nucleotide is shown in grey stick representation.

Table 3.1.1: Crystallographic and refinement statistics of the N157T mutant of subunit B of *M. mazei* Gö1 A_1A_O ATP synthase [192].

	N157T
Data collection statistics	
Wavelength (Å)	1.0
Space group	$P2_12_12_1$
Unit cell parameters (Å)	
a (Å)	73.33
b (Å)	95.80
c (Å)	130.37
α=β=γ (˚)	90
Resolution range (Å)	30-1.7
Solvent content (%)	45.93
Number of unique reflections	101467
I/σ[a]	20.8 (3.2)
Completeness (%)	99.5 (98.1)
R merge[b] (%)	4.4 (28.4)
Multiplicity	7.8 (4.9)
Refinement statistics	
R-factor[c] (%)	14.6
R-free[d] (%)	19.3
Number of water molecules	1106
Number of Pefabloc molecules	1
Number of glycerol molecules	12
Number of PEG molecules	7
Number of Chloride atoms	3
Ramachandran statistics	
Most favoured (%)	92.1
Additionally allowed (%)	7.5
Generously (%)	0.0
Disallowed (%)	0.4
R.M.S. deviations	
Bond lengths (Å)	0.03
Bond angles (˚)	2.38
Mean atomic B values	
Overall	25.3
Wilson plot	18.9

[a] Values in parentheses refer to the corresponding values of the highest resolution shell.
[b] Rmerge = $\Sigma\Sigma_i I_h - I_{hi}| / \Sigma\Sigma_i I_h$, where I_h is the mean intensity for reflection h.
[c] R-factor = $\Sigma||F_O| - |F_C|| / \Sigma|F_O|$, where F_O and F_C are measured and calculated structure factors, respectively.
[d] R-free = $\Sigma||F_O| - |F_C| / \Sigma|F_O|$, calculated from 5% of the reflections selected randomly and omitted during refinement

Table 3.1.2: Hydrogen bonding interactions for the P-loop residues in WT-B and N157T mutant of subunit B of *M. mazei* Gö1 A_1A_O ATP synthase [192].

	WT-B	**N157T mutant -B**
S150	O…N/M305	O…N/M305
	N…O/L303	N…O/L303
	Oγ…$C\delta_2$/H156	Oγ…$C\delta_2$/H156
A151	-	O…N/L154
S152	-	O…NH_2/R330
G153	-	-
L154	O…N/H156	O…N/H156
	O…$C\delta_2$/H156	-
P155	O…N/I159	O…N/I159
H156	O…N/A160	O…N/A160
	-	O…N/I159
N157	O…N/L161	O…N/L161
	$O\delta_1$…$O\gamma_1$/T247	-

3.2 Insight into the structural and mechanistic traits of the C-terminus of subunit α of *M. tuberculosis* F-ATP synthase

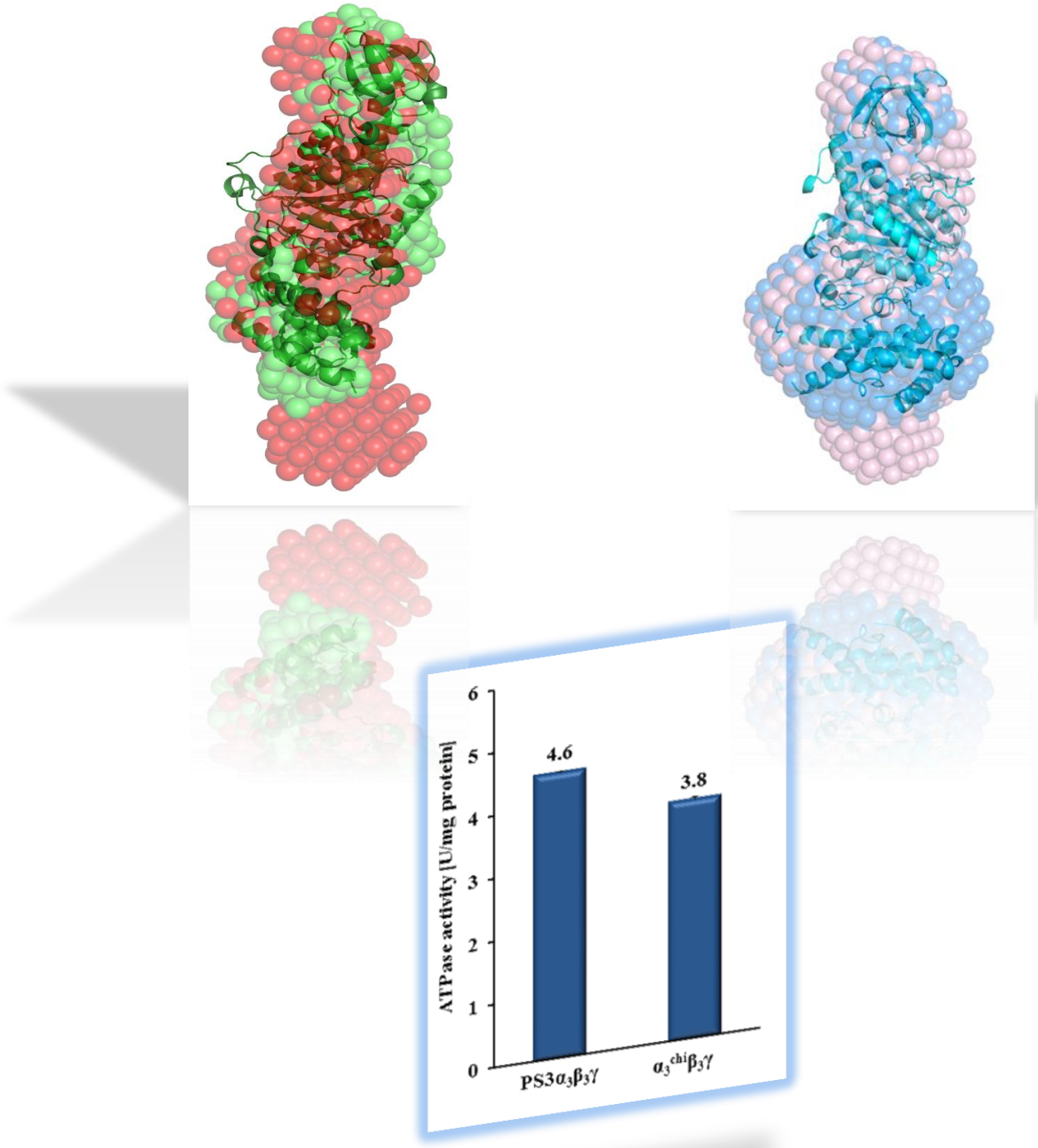

3.2.1. Introduction to subunit α of F-ATP synthase in *Mycobacterium tuberculosis*

Similar to A_3B_3 hexamer of A_1A_O ATP synthases, the head piece of the F_1F_O ATP synthase contains subunits α and β are arranged in an alternating fashion to form a hexamer ($\alpha_3\beta_3$) yielding a total of six nucleotide binding sites. Three of these sites belong to the catalytically active subunit β, homologous to subunit A in the A_1A_O ATP synthases. The equivalent position of subunit B of the A_1A_O ATP synthases is taken up by the nucleotide binding subunit α of F_1F_O ATP synthases. The nucleotide- binding sites of the three subunit α are believed to exchange nucleotides. Unlike the differentiation in the composition of the P-loop in subunits A and B, subunits α and β possess, the conserved glycine rich Walker A motif, which is the phosphate binding site. Subunit α is also capable of binding nucleotides and it relates very well to its A-ATP synthase counterpart i.e. the subunit B. However, unlike subunit B of A_1A_O ATP synthase, subunit *α* is not capable of binding ATP and ADP differently [210]. On similar lines, as the regulatory role of the subunit B and the importance of the P-loop residues were explored, efforts have also been invested to explore the structural and functional role of the homologous subunit in the F-ATP synthases, subunit α in *M. tuberculosis*.

The sequence comparison of subunit α from *Mycobacterium tuberculosis* (*Mt*) with other species of mycobacteria genus and species such as *E. coli*, *Bacillus* PS3 and bovine mitochondria (*Bos taurus*) highlighted an extra C-terminal tail loaded with charged residues (Figure 1.8). The sequence alignment across various species is shown in figure 1.8. Mainly considered are species for which the high resolution crystal structure is available, along with *E. faecalis*, a pathogen. Various species under the *Mycobacterium* genus, both pathogenic and non-pathogenic, have been included to highlight the residues that are conserved for this subunit. To explore the role of the C-terminus, a C-terminal truncated construct, *Mt*$\alpha_{1\text{-}513}$ was designed and compared with the wild type, *Mt*α for characterisation and interaction studies.

3.2.2 Cloning, expression and purification of *Mtα* and *Mtα*$_{1\text{-}513}$

Cloning for *Mt*α and *Mt*$\alpha_{1\text{-}513}$ was achieved using the PCR method by direct amplification from plasmid DNA coding for $\alpha_3\beta_3\gamma$ *M. tuberculosis* (synthesised from DNA 2.0, USA), using forward and reverse primers as described in section 2.2.6. The amplified products for both Δ*atp*A were digested with restriction enzymes, *Nco*I and *Sac*I and were ligated into the expression vector, pET9d(+)-His6 vector [211]. This vector containing the Δ*atp*A inserts were then transformed into *E. coli* BL21 (DE3) cells for production and grown on 30 µg/ml Kanamycin

containing LB-agar plates. Figure 3.2.1 (a) shows the amplification of both genes coding for *Mt*α and *Mt*α$_{1\text{-}513}$ using respective primers by polymerase chain reaction.

Successful production of the recombinant protein was achieved by the addition of IPTG to the liquid cultures. On checking the crude cell lysates for the total protein content, relevant bands for the proteins of interest were seen. Figure 3.2.1 (b) highlights the protein bands of right sizes seen for *Mt*α at 57 kDa and *Mt*α$_{1\text{-}513}$ at 54 kDa.

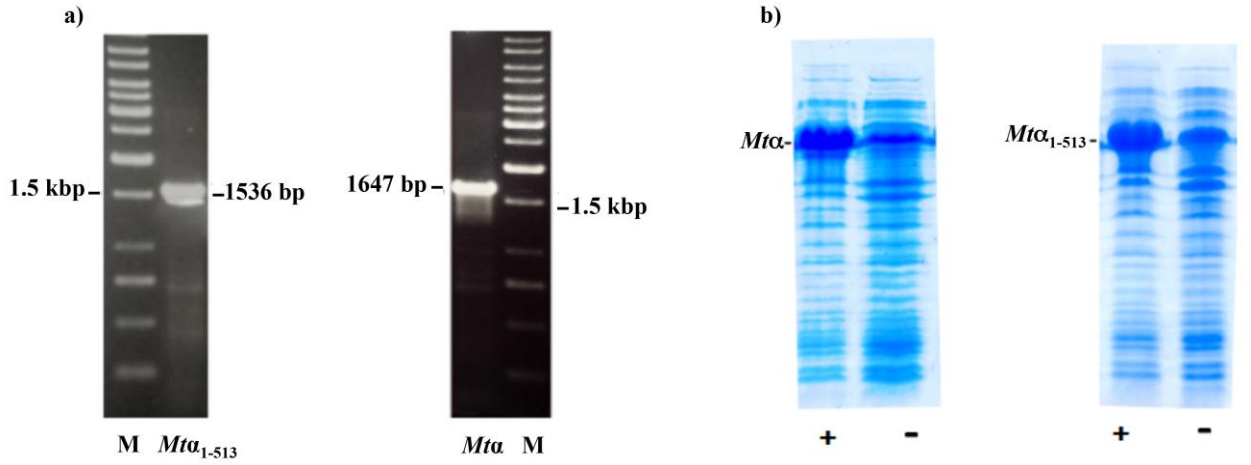

Figure 3.2.1: a) Agarose gels showing the PCR reaction products for *Mt*α and *Mt*α$_{1\text{-}513}$. b) SDS-PAGE gel showing induction test for *Mt*α and *Mt*α$_{1\text{-}513}$. The + and – signs indicate the presence and absence of IPTG, respectively.

Solubility of the proteins *Mt*α and *Mt*α$_{1\text{-}513}$ was checked for these strongly induced colonies and the protocol followed is given in section 2.2.7. From the SDS-PAGE gel shown in figure 3.2.2, the protein is soluble when the liquid cultures were grown at 15°C after induction with IPTG.

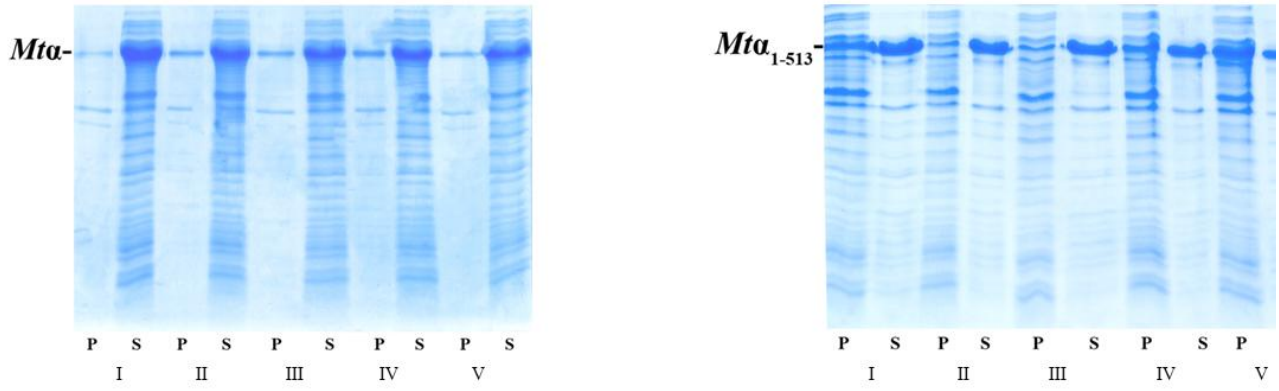

Figure 3.2.2: SDS-PAGE gel showing solubility test for *Mt*α and *Mt*α$_{1\text{-}513}$. P and S denote the pellet and the supernatant fractions, respectively for each of the buffer condition tested. Composition for buffers I-V are described in section 2.2.7.

Ni^{2+}-NTA Affinity chromatography was performed to bind the His- tagged recombinant protein for both *Mtα* and $Mt\alpha_{1\text{-}513}$, onto Ni^{2+} sepharose beads. These were subsequently eluted using a linear imidazole gradient. On verifying the fractions on an SDS-PAGE gel, fractions (75-250 mM Imidazole) were pooled together and were passed through an anion exchange column. The monomeric recombinant protein for *Mtα* and $Mt\alpha_{1\text{-}513}$ eluted with 200 mM and 220 mM NaCl, respectively. Buffer A (50 mM Tris-HCl, pH 8.5 and 10% glycerol) and B (50 mM Tris-HCl pH 8.5, 1 M NaCl and 10% glycerol) were used for this experiment. Fractions corresponding to the area under gray were pooled and the protein was concentrated using Centricon YM-30 (30 kDa molecular mass cutoff) spin concentrators (Millipore).

Gel filtration chromatography column using a Superdex 75 HR 10/30 column (GE Healthcare) was executed as a final step of purification. Buffer composing of 50 mM Tris-HCl (pH 7.5), 200 mM NaCl and 10% glycerol was used here. The protein fractions containing *Mtα* and $Mt\alpha_{1\text{-}513}$ were concentrated and subsequently applied onto a SDS gel to the check the purity and quantity of the recombinant protein (Figures 3.2.3 and 3.2.4).

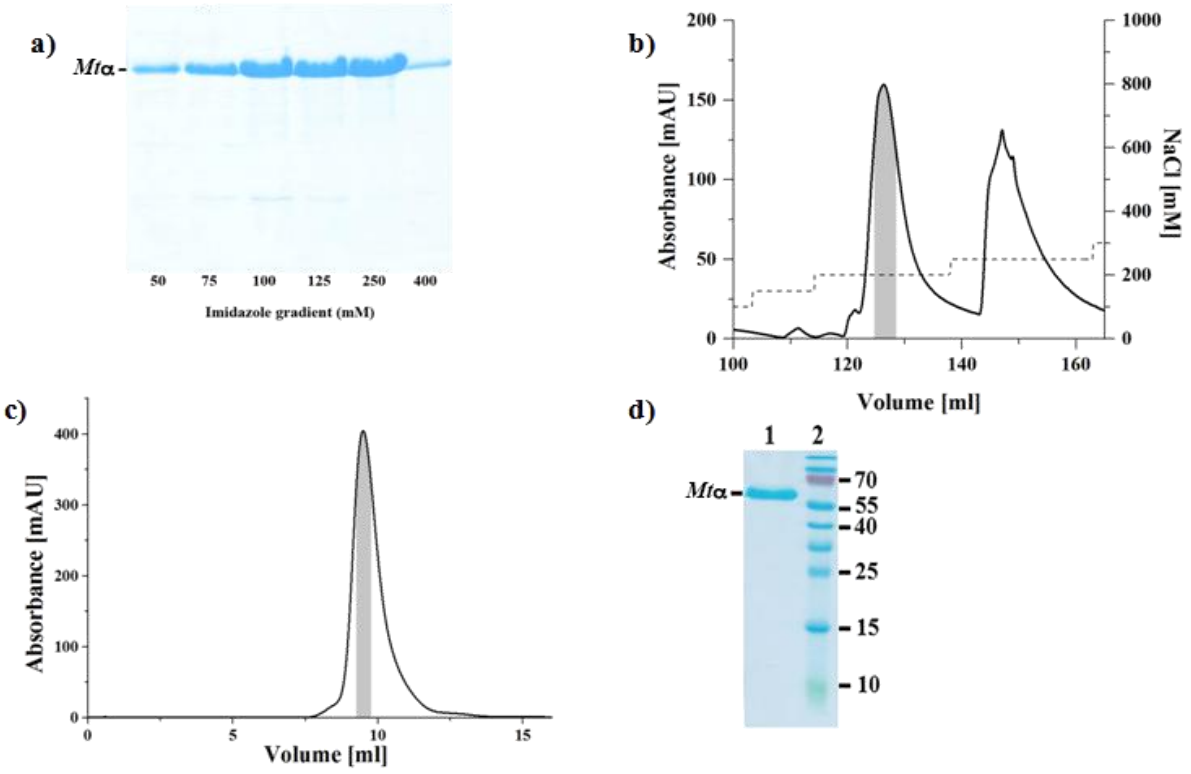

Figure 3.2.3: (a) Purification of recombinant *Mtα* protein using Ni^{2+}-NTA Affinity chromatography eluted in a linear Imidazole gradient with 50 mM Tris-HCl, pH 8.5, 200 mM NaCl and 10% glycerol. 20 µl of the protein samples were mixed with 5×SDS sample buffer and loaded on a 17% SDS-gel. (b) Purification of protein by a linear gradient of NaCl on an anion-exchange column (Resource Q (6 ml). 75-250 mM Imidazole fractions were pooled and applied at a constant flow rate of 2 ml/min. (c) Final step of purification using Superdex 75. (d) The final purified protein in lane 1, with the marker in lane 2.

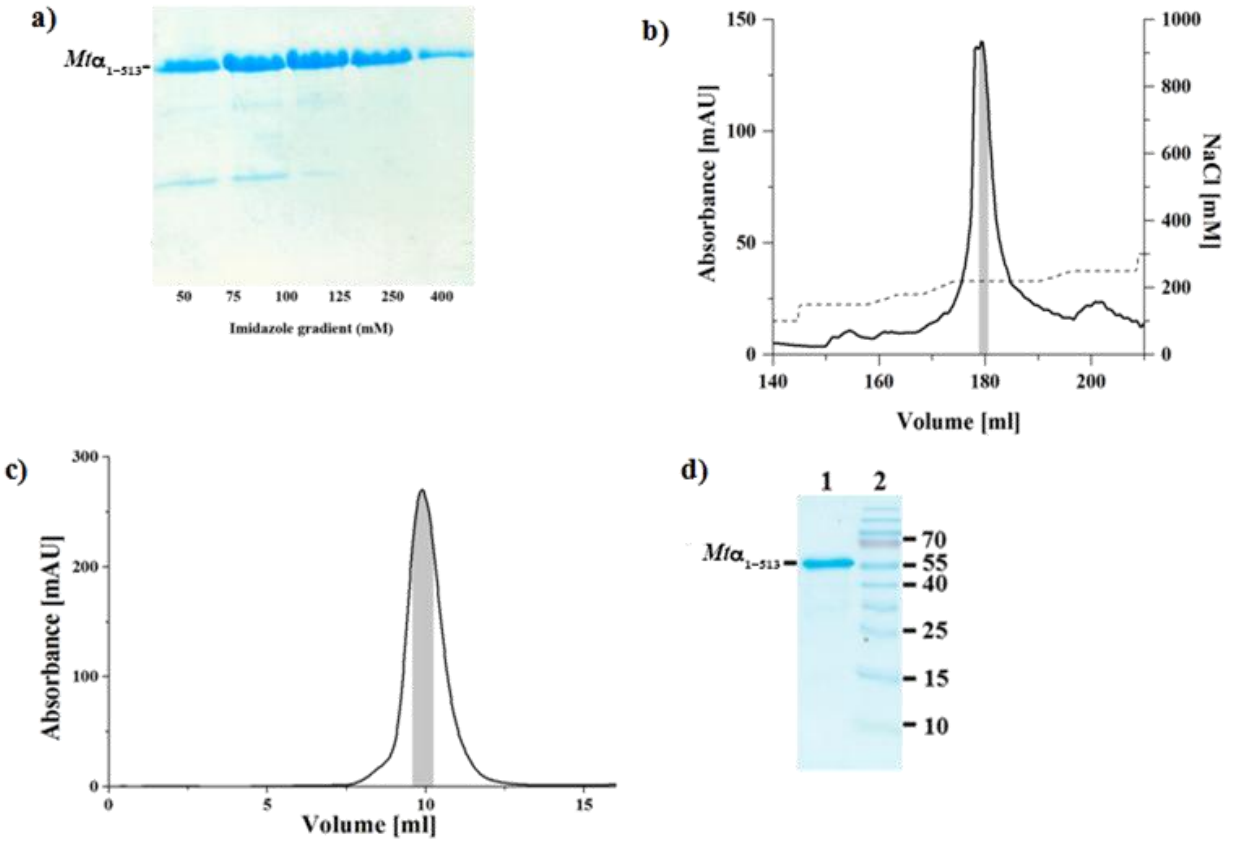

Figure 3.2.4: (a) Purification of recombinant $Mt\alpha_{1\text{-}513}$ protein using Ni^{2+}-NTA Affinity chromatography. (b) Purification of the protein by a linear gradient of NaCl on an anion-exchange column (Resource Q (6 ml). (c) Final step of purification using Superdex 75. (d) Final purified protein in lane 1, with the marker in lane 2.

3.2.3 Small angle X-ray scattering (SAXS) and data analysis

The pure protein for *Mt*α was concentrated to 2 mg/ml and SAXS measurements were performed as mentioned in section 2.2.8 by Dr. Neelagandan Kamaraiah. Preliminary SAXS measurements performed for $Mt\alpha_{1\text{-}513}$ revealed that the protein was not a monomer and the data set acquired indicated a mixture of oligomers. The experimental protocol followed for recording SAXS measurements for *Mt*α are as mentioned in section 2.2.8. Data were processed using ATSAS-package [212]. The final composite scattering curve for the SAXS pattern shows a well mono-dispersed protein as shown in figure 3.2.5. Good data quality and lack of aggregation were confirmed with the linearity of the Guinier plot at low angles. The radius of gyration (Rg) value of 34.31 ± 0.3 Å was deciphered from the Guinier Plots for *Mt*α. The distance distribution curve helped derive the D_{max} value of 110.3 ± 0.5 Å, indicating the dimension of elongation of the molecule. Also at low angles, the Kratky plot ($I(s)*s^2$ vs. s) showed a bell shaped form indicating a well folded protein (Figure 3.2.6). The normalized Kratky plot shown in figure 3.2.6 (c) is to

compare the flexibility of the *Mtα* protein (red) with that of lysozyme, which is used as a standard (blue).

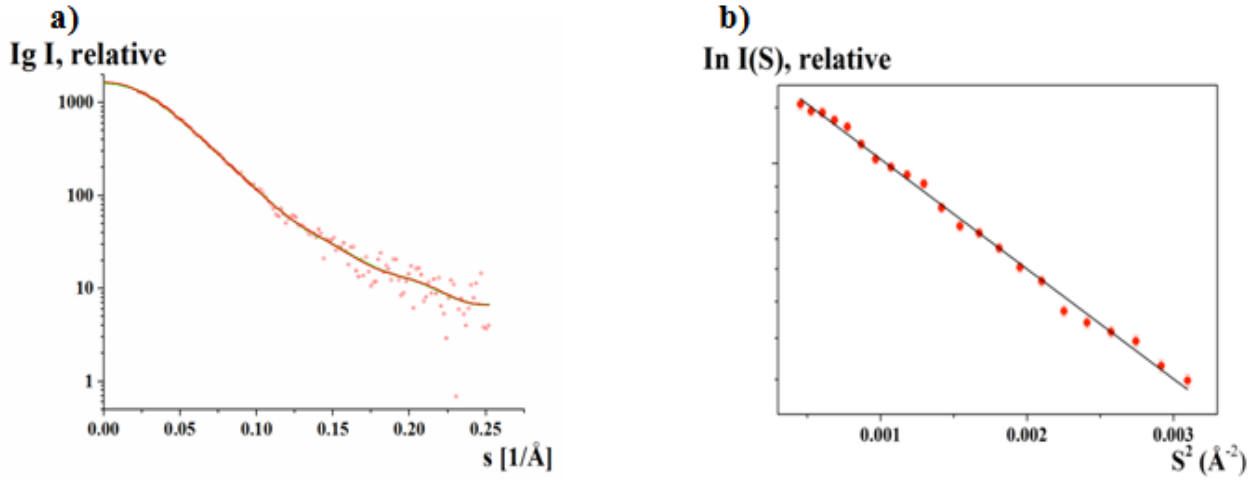

Figure 3.2.5: Solution X-ray scattering studies of *Mtα*. a) Forward scattering curve for *Mtα* 50 mM Tris-HCl, pH 7.5, 200 mM NaCl,10% glycerol with y-axis denoting the intensity and x-axis denoting the angle (s/q). b) Guinier plot of the protein displaying linearity at low angles.

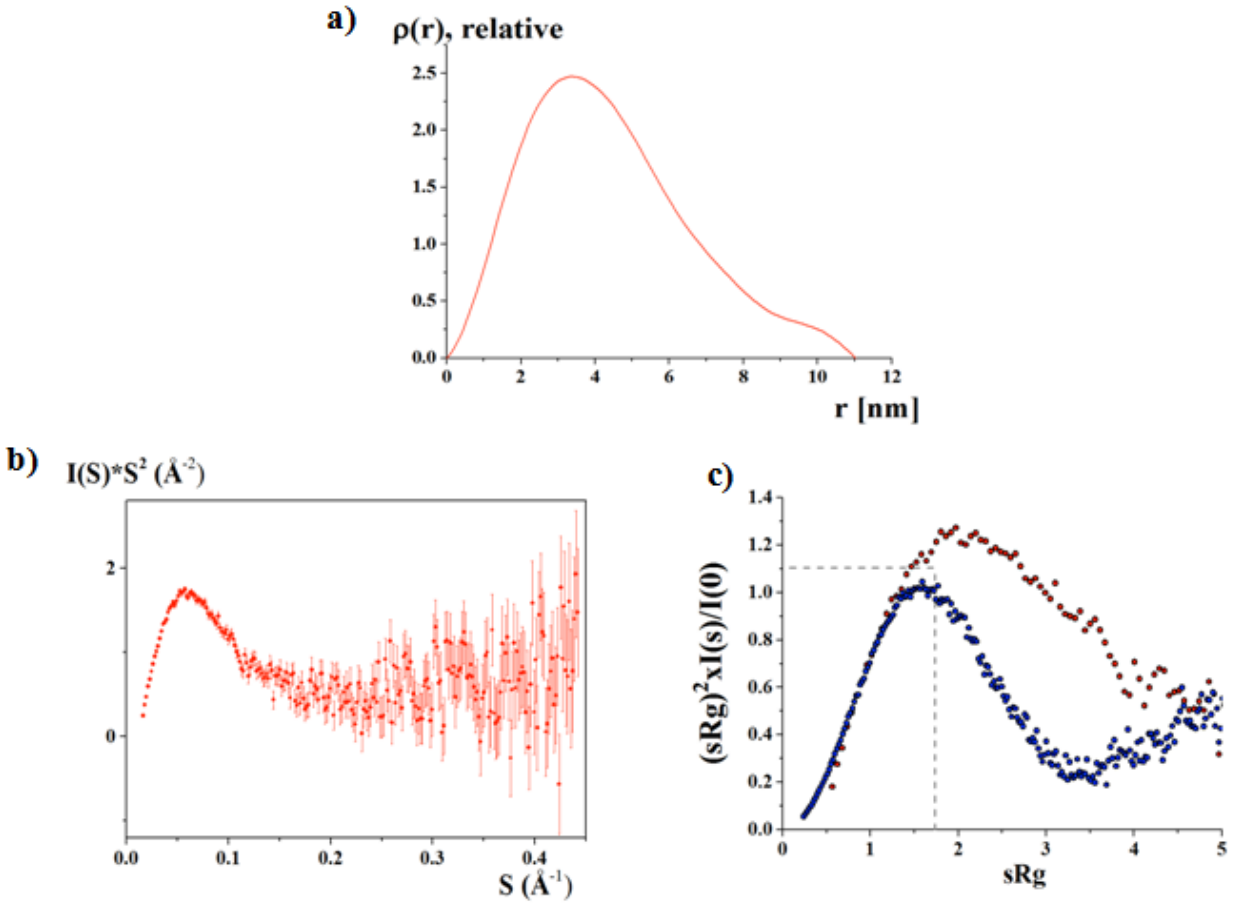

Figure 3.2.6: Solution X-ray scattering studies of *Mtα* (a) Distance distribution curve for *Mtα* at a concentration of 2 mg/ml. The elongated tail at higher 'r' value is indicative of an elongated particle in solution. (b) Kratky plot showing a bell shaped peak indicating a well-folded protein. (c) Normalized Kratky plot for understanding flexibility of protein, *Mtα* (red) in comparison with lysozyme used as the standard (blue).

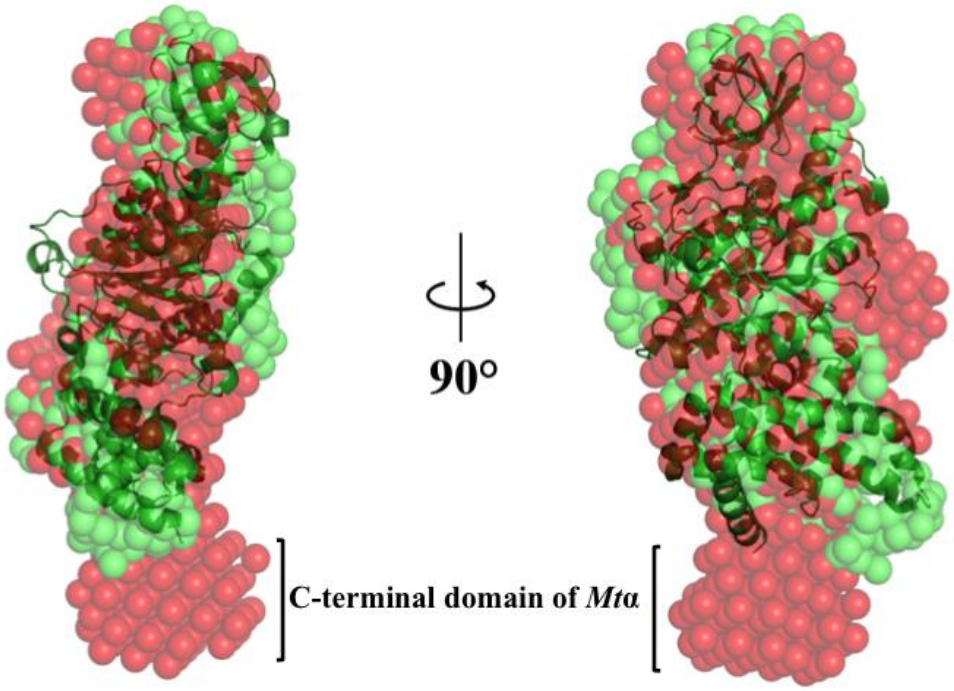

Figure 3.2.7: Superposition of DAMMIN model of *Mtα* (red spheres) onto a high resolution structure of *Ecα* (cartoon representation in green) (PDB ID: 1DS8). Also superimposed on the same high resolution structure of *Ecα* is DAMMIN model of *Ecα* (green spheres) highlighting the extended C-terminal domain of *Mtα* in solution. [179].

The quality of the solution shape obtained for *Mtα* is highly comparable to the solution structure of subunit α of *E. coli (Ecα*) determined in our laboratory by Dr. Vikram Tadwal [179]. Figure 3.2.7 shows the overlap of the crystallographic structure of *Ecα* (PDB: 1D8S) superimposed with the structure obtained from SAXS analysis, with *r.m.s.d* of 1.08. In solution, the total length for *Mtα* and *Ecα* measures to 96.6 ± 0.3 Å and 110.3 ± 0.5Å, respectively. This observation can be justified by the fact that *Mtα* is longer by 35 amino acids in its C-terminus, when compared to *Ecα*.

Fluorescence correlation spectroscopy was performed by Dr. Hendrik Sielaff to determine the binding affinity of the subunit *Mtα* with nucleotides. A binding constant, K_D of approximately 35 μM was determined with Mg-ATP.

3.2.4 Subunit *α* of *Bacillus* PS3 (PS3*α*) and chimeric *α* (α^{chi}) of *Bacillus* PS3 and *M. tuberculosis* F_1F_O ATP synthase

To further investigate the role played by the C-terminus of *Mtα*, this was fused with the subunit *α* of *Bacillus* PS3 to generate a chimeric *α* protein of *Bacillus* PS3 (residues 1-502) and *Mt* (515-549), α^{chi}. To serve as a control and for a comparative study, the native protein of subunit *α Bacillus* PS3, PS3*α* was also generated.

The clones encoding for PS3*α* and α^{chi} have been generated by Ms. Ankita Pan. The protein was expressed and purified with the help of Dr. Priya Raghunathan. The protocol for the protein purification for both proteins of PS3*α* and α^{chi} were similar to that of the *Mtα*, with Mono-Q column being used for anion exchange chromatography and as the final step of purification gel filtration chromatography was performed using S200 column HR 10/30 column (GE-Healthcare). The chromatograms for the anion exchange and gel filtration chromatography are shown in figures 3.2.8 and 3.2.9.

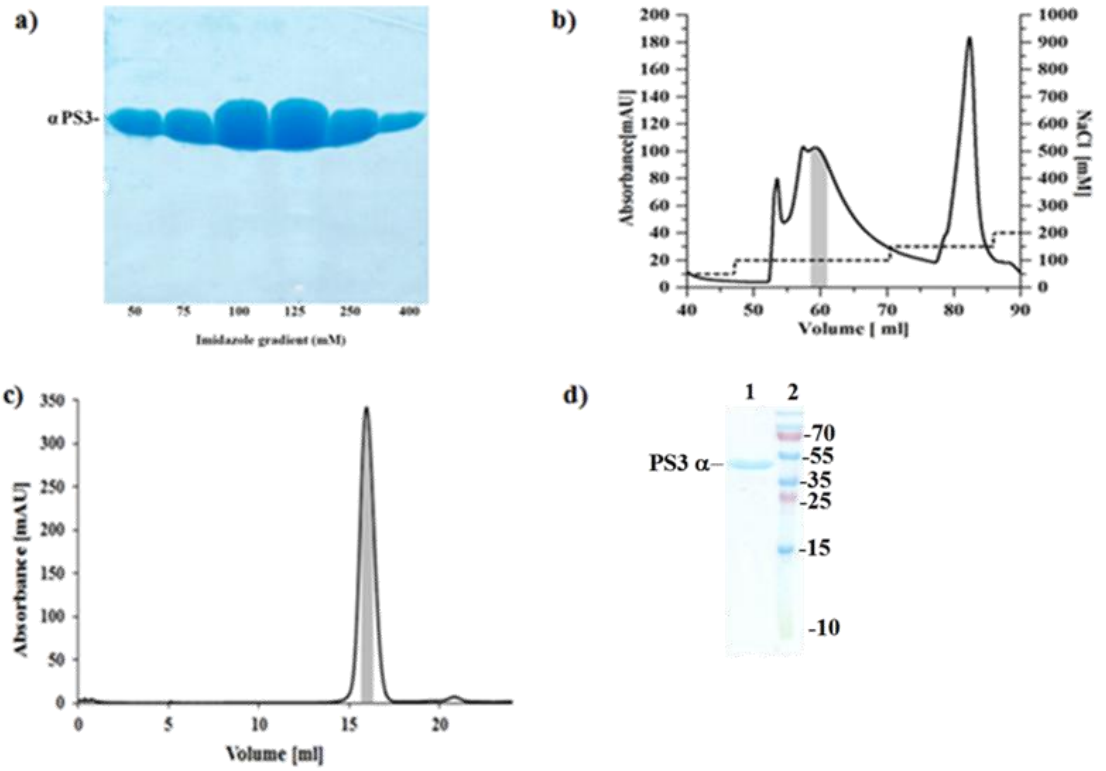

Figure 3.2.8: (a) Purification of recombinant PS3*α* using Ni^{2+}-NTA affinity chromatography. (b) Purification of the protein by a linear gradient of NaCl on an anion exchange column, Mono Q column (8 ml). (c) Final step of purification using Superdex 75. d) SDS-PAGE gel shows the final purified protein in lane 1, with the marker in lane 2.

Purified proteins for both PS3 α and α^{chi} of concentration ranging from 2.5 to 5 mg/ml were used for SAXS measurements, which were performed with the help of Dr. Malathy Sony in our laboratory. The data shown in the following section relates to that measured at the highest concentrations for both recombinant proteins.

The final composite scattering curve for both the proteins indicates well mono-dispersed samples (Figure 3.2.10). The Guinier plot at low angles is linear and shows no sign of aggregation. From Guinier approximation, *Rg* values of 27.98 ± 0.24 Å and 29.56 ± 0.32 Å were determined for PS3 α and α^{chi}, respectively. The distance distribution function, *p(r)* is shown in figure 3.3.11 and reveals a *Dmax* of 89.5 ± 10 Å and 102 ± 10 Å, indicating the greater length of the α^{chi} when compared to the PS3 α, given the addition of the extra C-terminal domain.

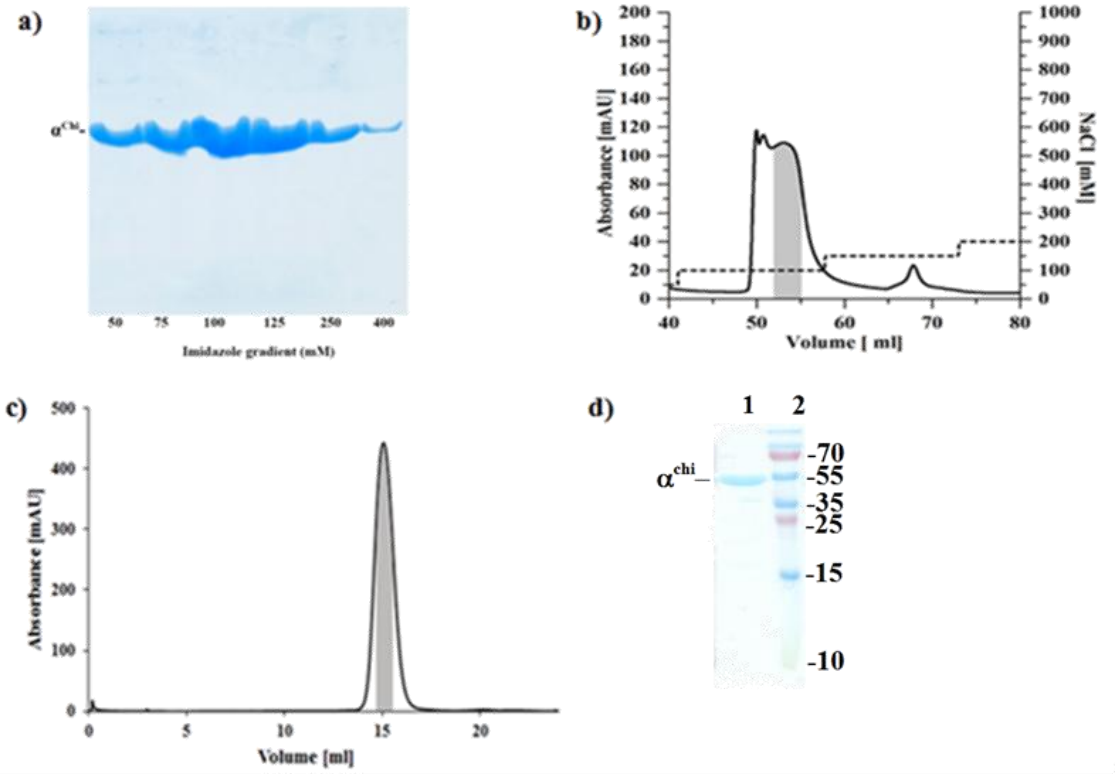

Figure 3.2.9: (a) Purification of recombinant α^{chi} protein using Ni^{2+}-NTA affinity (b) Anion exchange purification of the protein using Mono Q column (8 ml). (c) Final step of purification using Superdex 75. d) Final purified protein in lane 1, with the marker in lane 2.

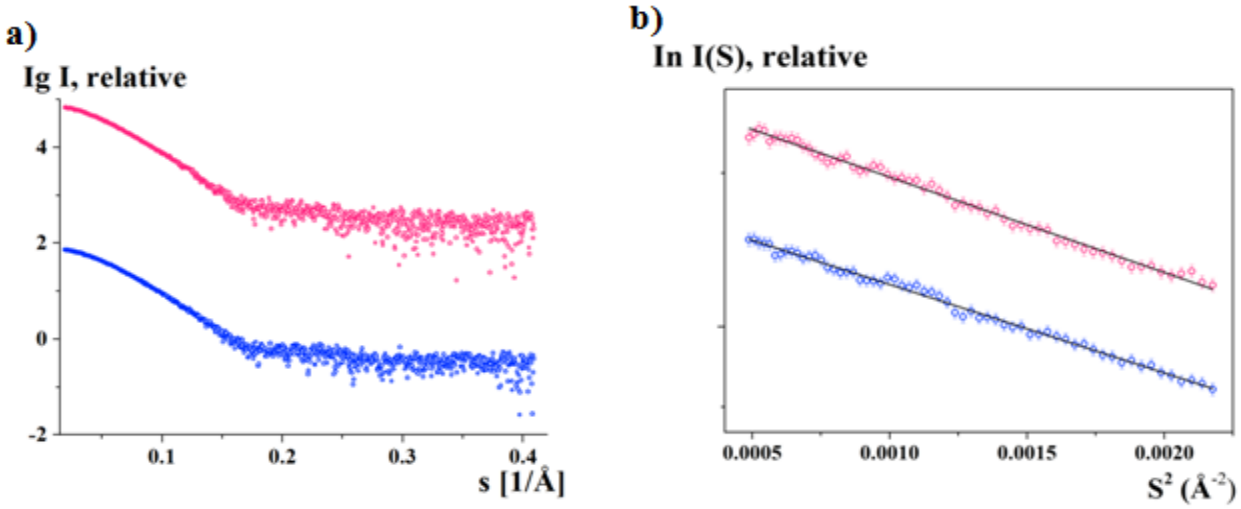

Figure 3.2.10: Solution X-ray scattering studies of PS3α and α^{chi}. a) Forward scattering curve for PS3α (blue) and α^{chi} (pink) recorded in buffer composed of 50 mM Tris-HCl, 200 mM NaCl, 10% glycerol. b) Guinier plot of protein displaying linearity at low angles. PS3α and α^{chi} are shown in blue and pink, respectively.

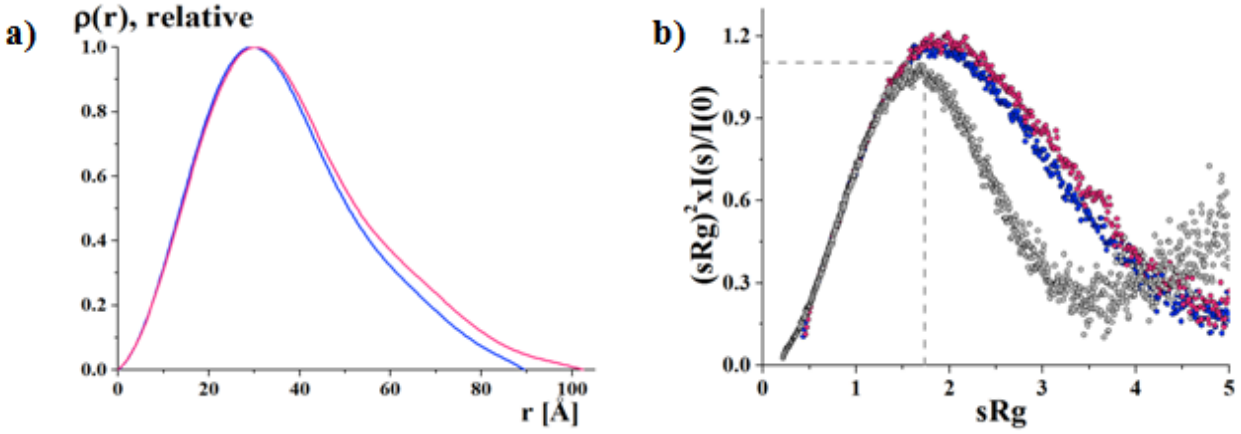

Figure 3.2.11: Solution X-ray scattering studies of PS3α and α^{chi}. a) Distance distribution curve for PS3α and α^{chi}. b) Normalised Kratky plot showing well folded protein for understanding flexibility of the protein. PS3α is shown in blue and α^{chi} is shown in pink colour and the measurement for the standard lysozyme is shown in grey.

The *ab initio* gross shapes were reconstructed using DAMMIF and fitted well to the experimental data in the entire scattering range with discrepancies of X^2 of 0.348 and 0.334 for PS3α and α^{chi}, respectively.

Superimposition of the shapes of PS3α and α^{chi} with the crystal structure of PS3α (PDB ID: 1SKY), indicated an extra domain of 15 Å x 22 Å resulting from the addition of 35 amino acids in the chimeric protein (Figure 3.2.12) [107].

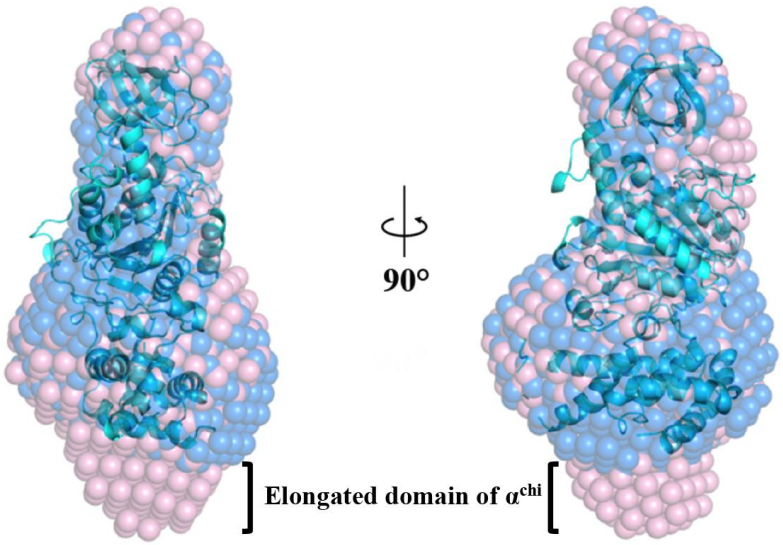

Figure 3.2.12: Superimposition of SAXS shapes PS3α, in blue and $\alpha^{chi,}$ in pink, with the crystal structure of PS3α (PDB ID: 1SKY) shown in cyan [107]. The elongated domain of the α^{chi} has been highlighted.

The statistics for the data collection and the scattering derived parameters for *Mt*α, PS3α and α^{chi} are listed in the Table 3.2.1.

Table 3.2.1: Data collection and scattering derived parameters for subunit *Mt*α, PS3α and α^{chi} using SAXS

Data collection parameters	***Mt*α**	**PS3α**	**α^{chi}**
Instrument (source & detector)	BRUKER NANOSTAR with MetalJet eXcillum VANTEC-2000		
Beam geometry	100 μm slit		
Wavelength (Å)	1.3414		
q range ($Å^{-1}$)	0.015-0.4		
Exposure time (min)	30 (6 frames x 5 min)		
Temperature (K)	288		
Concentration range (mg/ml)	2	2.5 – 5.0	2.5 – 5.0
Structural parameters*			
I(0) (cm^{-1}) [from P(r)]	1635 ± 13.8	80.18 ± 0.30	75.88 ± 0.47
R_g (Å) [from P(r)]	34.45 ± 0.33	28.18 ± 0.12	30.02 ± 0.23
I(0) (cm^{-1}) (from Guinier)	1640 ± 15.2	80.27 ± 0.49	75.78 ± 0.59
R_g (Å) (from Guinier)	34.30 ± 0.25	27.98 ± 0.24	29.56 ± 0.32
D_{max} (Å)	110.3 ± 10	89.5 ± 10	102.5 ± 10

Porod volume estimate ($Å^3$)	~113625	~79374	~88551
Dry volume calculated from sequence ($Å^3$)	~71734	~66050	~70660
Molecular mass determination (kDa)*			
Calculated monomeric MM from sequence	~59	~55	~58
MM from I(0)	50 ± 6	45 ± 6	46 ± 6
MM from Porod invariant	68 ± 6	48 ± 6	53 ± 6
MM from SAXS MoW	77 ± 6	56 ± 6	60 ± 6
MM from excluded volume	64 ± 6	53 ± 6	57 ± 6
Software employed			
Primary data reduction		BRUKER SAXS	
Data processing		PRIMUS	
Ab initio analysis	GASBOR	DAMMIF	DAMMIF
Validation and averaging		DAMAVER	
Computation of model intensities		CRYSOL	
Three-dimensional graphics representations		PyMOL	

3.2.5 Sub-complex of $\alpha^{chi}_3\beta_3\gamma$-hybrid protein of thermophilic *Bacillus* PS3 and *M. tuberculosis*

The C-terminus of subunit *α* of F-ATP synthase belonging to many species of *Mycobacterium* genus is unique with respect to sequence and composition and may have the potential to play a very important regulatory role. To probe into this aspect, a sub-complex of $\alpha_3\beta_3\gamma$ of *Bacillus* PS3 was engineered to accommodate 35 amino acids of the C-terminus of *Mtα* at the C-terminus end of (PS3) *α*. By far, $\alpha_3\beta_3\gamma$ complex of *Bacillus* PS3 is mechanistically the most well studied system and also structurally well understood, given the available crystal structure for $\alpha_3\beta_3$ for *Bacillus* PS3 (PDB code: 1SKY) and the $\alpha_3\beta_3\gamma\varepsilon$ for *Bacillus* $TA_2.A_1$ (PDB code: 2QE7) [107, 213]. These allowed to recreate a system, [(chimeric α_3) + $\beta_3\gamma$] referred to as $\alpha^{chi}_3\beta_3\gamma$, which can be used for comparative studies with native $\alpha_3\beta_3\gamma$ (manuscript in preparation).

Insertion of more than 30 nucleotides using oligo nucleotide synthesis is not a feasible task [214]. Hence mutagenesis to insert the C-terminus tail of the *Mtα* towards the rear part of the *PS3α* was achieved using Overlap extension-PCR. Using the strategy described in detail in section 2.2.9, products for the first step of three independent PCR reactions are as shown in figure 3.2.13 (a-c). Figure 3.2.13 (d) shows the final product obtained on overlap of the products generated in the previous step. This was executed using the overlap of products (a+d) and (c+f)

and using flanking primers to amplify in high yield. The labels for each of the products are defined by the primers used for the specific reactions as described in section 2.2.9.

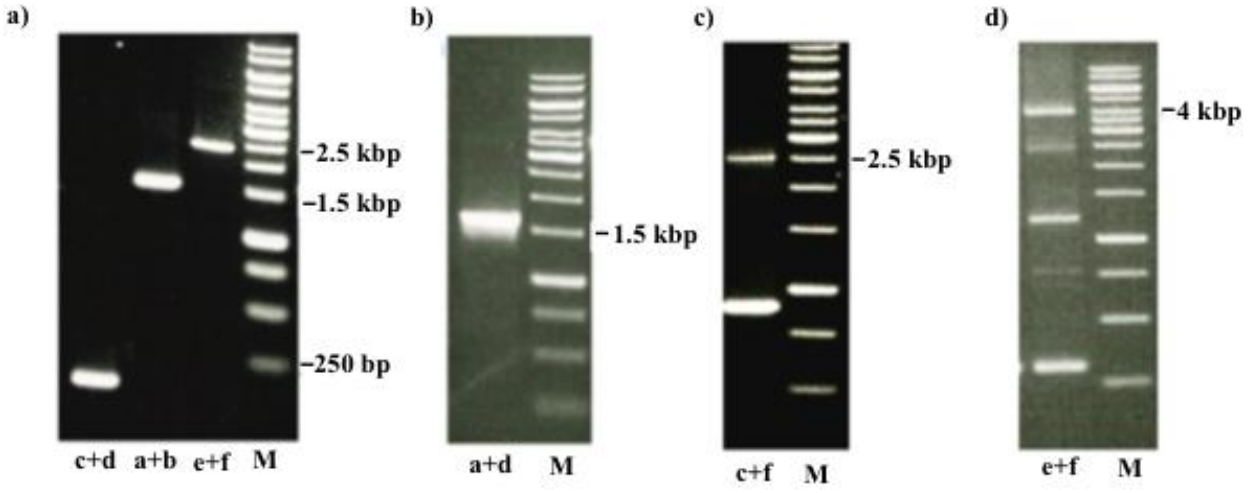

Figure 3.2.13: (a) PCR products for three independent reactions to generate (a+b); 122 bp, (c+d); 1.5 kbp and (e+f); 2.4 kbp. (b) PCR product for (a+d); 1.6 kbp, obtained on overlap PCR performed with (a+b) and (c+d). (c) Overlap PCR product for (c+f); 2.5 kbp, generated using (c+d) and (e+f). (d) Final PCR product of (a+f); 4.1 kbp, obtained via overlap extension using (a+d) and (e+f).

On restriction digestion of insert with *BamH*I and *Hind*III this was successfully ligated into similarly digested pET24b vector. The ligated product was transformed into *E. coli* DH5α strain for plasmid amplification. The positive clone was screened for and on sequence verification transformed into *E. coli* DK8 for protein expression.

In a Kanamycin enriched liquid culture of 2YT nutrient medium with this plasmid, protein expression was achieved with IPTG. The construct of $\alpha^{chi}{}_3\beta_3\gamma$ has a His_{10}-tag at the N-terminus of subunit β and the sub-complex was separated from other nonspecific proteins by Ni^{2+}-NTA affinity chromatography. A linear imidazole gradient was used to elute the bound protein and the fractions pooled were applied on the anion-exchange column (Resource-Q, 6ml). The $\alpha^{chi}{}_3\beta_3\gamma$ sub-complex bound to the column and eluted with 250 mM NaCl in the linear gradient.

$\alpha^{chi}{}_3\beta_3\gamma$ was concentrated using Centricon YM-100 (100 kDa molecular mass cutoff) spin concentrators (Millipore). A fraction of this sample (amounting to about 25 μg) was applied on the SDS-PAGE to check for purity and a representative gel is shown in the figure 3.2.14 (manuscript in preparation). The SDS-PAGE gel shows the bands of appropriate sizes seen for seen for α^{chi} (57.5 kDa), β (53 kDa), γ (27 kDa). As per the right stoichiometry, the purified protein appears in the proportion of $\alpha^{chi}{}_3\beta_3\gamma$. At the level of the Ni-NTA affinity chromatography the band for β is intense, given that the His-tag is present on the subunit β.

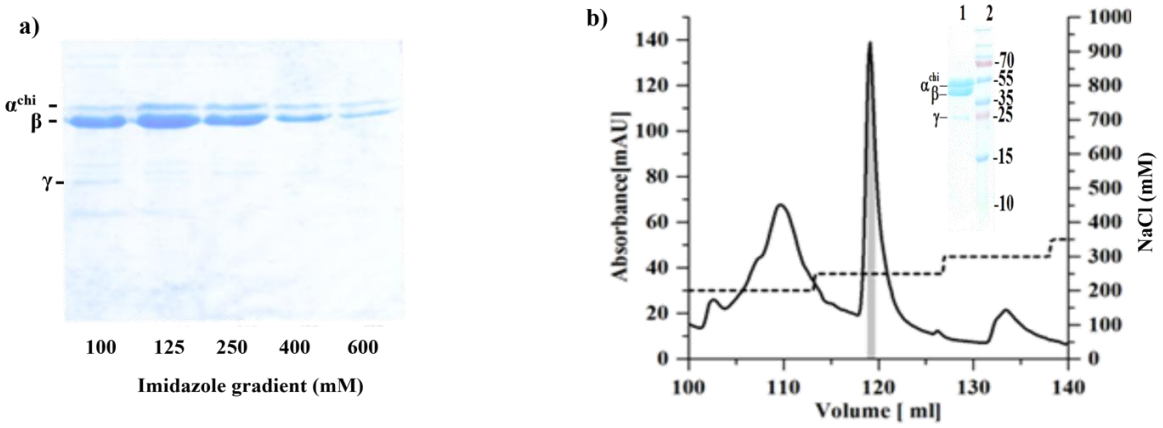

Figure 3.2.14: (a) Purification of recombinant protein $\alpha^{chi}{}_3\beta_3\gamma$ using Ni^{2+}-NTA affinity chromatography. (b) Purification of protein by a linear gradient of NaCl on anion exchange column, Res Q (6 ml). The inset shows the final purified protein in lane 1, with the marker in lane 2.

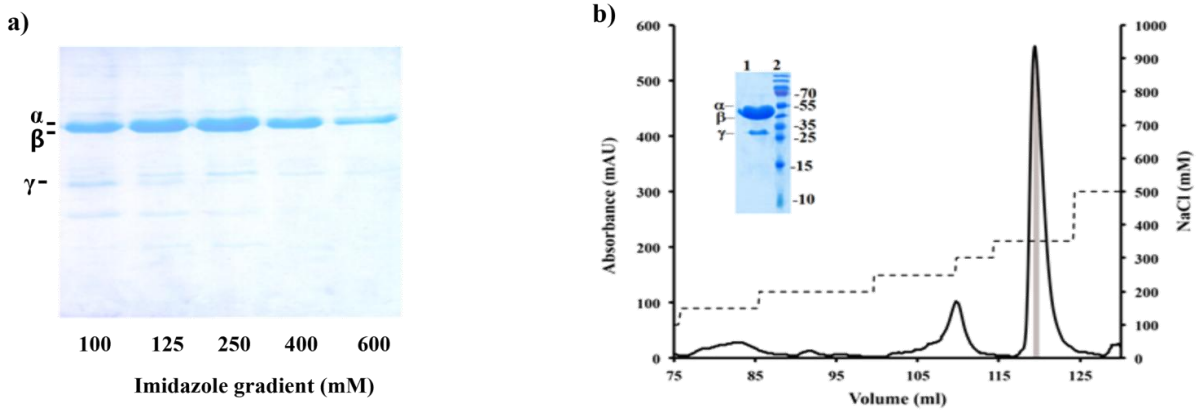

Figure 3.2.15: (a) Purification of recombinant protein PS3$\alpha_3\beta_3\gamma$ using Ni^{2+}-NTA Affinity chromatography eluted in a linear. (b) Anion exchange purification of protein using Res Q (6 ml). The inset shows the final purified protein in lane 1, with the marker in lane 2.

An identical protocol was used for the purification of PS3$\alpha_3\beta_3\gamma$ protein. The profile for the Ni^{2+}-NTA affinity chromatography and anion exchange chromatography is shown in figure 3.2.15. Comparing the SDS-PAGE analysis of both PS3$\alpha_3\beta_3\gamma$ and $\alpha^{chi}{}_3\beta_3\gamma$, it is evident that the subunit α^{chi} (57.5 kDa), which 3.5 kDa more than subunit PS3α (54 kDa) is better separated from the band of subunit PS3β (53 kDa). These samples were used to determine the activity of ATP hydrolysis using the NADH coupled assay as detailed in section 2.2.10.

Figure 3.2.16 shows the measurements for ATP hydrolytic activity of $\alpha^{chi}{}_3\beta_3\gamma$ made to investigate the role of the C-terminus of *Mt*α in the subcomplex, using PS3$\alpha_3\beta_3\gamma$ as control. From the specific activities measured by fitting the linear part of the slope for PS3$\alpha_3\beta_3\gamma$ and $\alpha^{chi}{}_3\beta_3\gamma$,

the specific activity for ATP hydrolysis is 4.6 U/mg of protein for PS3$\alpha_3\beta_3\gamma$ and 3.8 U/mg of protein for $\alpha^{chi}{}_3\beta_3\gamma$. Comparing these values, it is evident that there is a 17% drop for the ATPase activity of $\alpha^{chi}{}_3\beta_3\gamma$ complex. It is believed that the C-terminus of *Mt*α fused to the PS3α is responsible for reduction in hydrolytic activity (manuscript in preparation). This effect was verified by repeating the measurements six times to confirm the results.

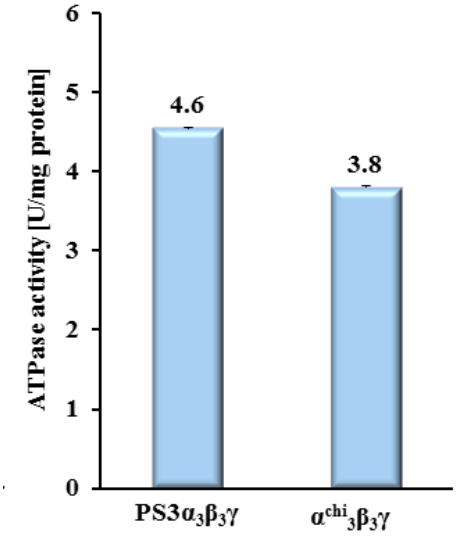

Figure 3.2.16: ATP hydrolysis measurement of PS3$\alpha_3\beta_3\gamma$ and $\alpha^{chi}{}_3\beta_3\gamma$.

3.2.6 Biotin labelling and single molecule rotation experiments for PS3$\alpha_3\beta_3\gamma$ and $\alpha^{chi}{}_3\beta_3\gamma$

With the ATP hydrolysis data obtained for the complexes PS3$\alpha_3\beta_3\gamma$ and $\alpha^{chi}{}_3\beta_3\gamma$, it was important to deepen the understanding of the mechanistic of their catalytic behaviour. Hence the single molecule rotation studies were performed after the purified protein complexes were biotinylated. The procedure used for biotin labelling and the rotation assay is as described in sections 2.2.11 and 2.2.12.

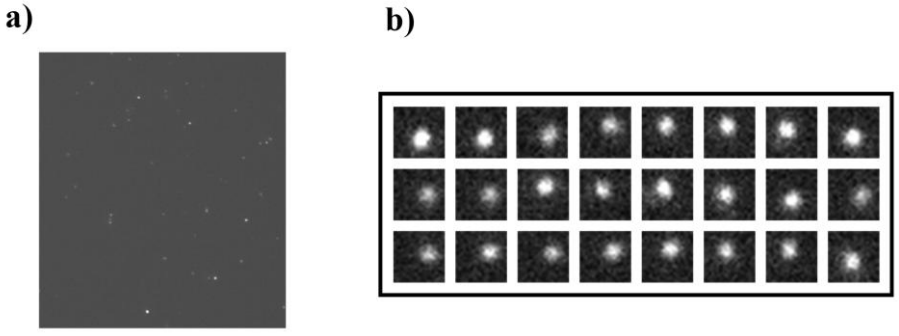

Figure 3.2.17: a) Visualization of laser excited quantum dots attached to the protein-bead complex under the inverted fluorescence microscope. b) Illustration of the rotation sequence of the protein-bead complex, at different time points.

These experiments were performed with Dr. Hendrik Sielaff and figure 3.2.17 illustrates the visualization of the quantum dots attached to protein-bead complexes (PS3$\alpha_3\beta_3\gamma$ and $\alpha^{chi}{}_3\beta_3\gamma$) excited using a 491 nm laser in a confocal microscope. On addition of 1 mM ATP, the hydrolytic activity of the protein complexes was recorded as continuous sinusoidal variations in their light intensities. Dr. Hendrik Sielaff performed the biophysical analysis of the data and it was seen that the angular velocity for the rotating single molecule of $\alpha^{chi}{}_3\beta_3\gamma$ was reduced by 19% in comparison to that of PS3$\alpha_3\beta_3\gamma$. This is in agreement with the ATP hydrolysis data that shows a reduced activity of 17 % for $\alpha^{chi}{}_3\beta_3\gamma$ when compared to that of the native PS3$\alpha_3\beta_3\gamma$ (manuscript in preparation). These results taken together strongly suggest a regulatory role for the C-terminus of the *Mt*α, which could be instrumental in causing the reduced ATP hydrolytic activity (manuscript in preparation).

3.3 Mechanistic and structural characterization of subunit ε of F_1F_O ATP synthase of *Mycobacterium tuberculosis*

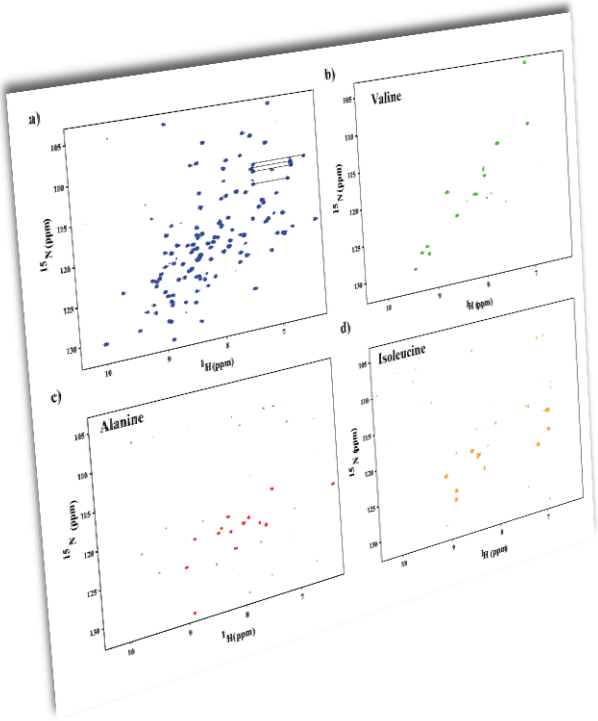

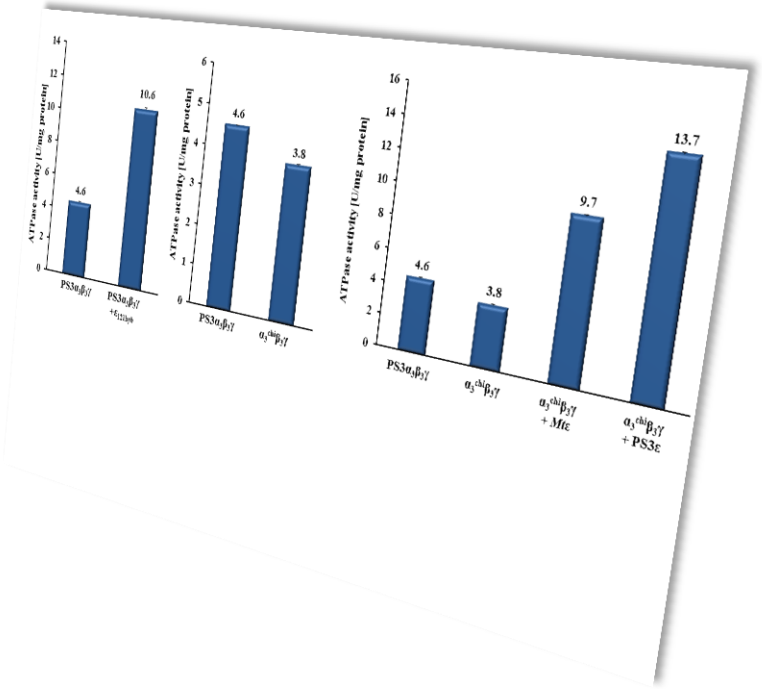

3.3.1 Introduction to subunit ε of F_1F_O ATP synthase from *M. tuberculosis*

The F-ATP synthase qualifies as a central enzyme in the bioenergetics of *Mycobacterium tuberculosis (Mt)*. Recent study in inverted membrane vesicles of *M. bovis*, a slow growing strain like *M. tuberculosis*, revealed that there is active ATP synthesis occurring [140]. It was also reported that there is neither hydrolysis taking place nor is ATP used as substrate to set up PMF and these were attributed to the inhibitory role of subunit ε [140]. However, treatment with methanol unmasked ATP hydrolysis due to disruption of hydrophobic interactions within the ATP synthase [140]. Upon PMF activation ADP inhibition was relieved and this allows the conformational switch of subunit ε to its non-inhibitory state [140]. Similarly, *M. tuberculosis* does not undergo ATP hydrolysis, to conserve the cellular ATP levels during the latent phase. Triggering ATP hydrolysis in the pathogen will lead to wasteful hydrolysis eventually resulting in cell death. Only recently, the high-resolution structure of the *c-ring* has been solved for the mycobacterial F-ATP synthase [41]. Investigating the structural details of the subunit ε will provide the basis for identifying drugs that would work as ATP hydrolysis activators that would target this intrinsic inhibitory subunit, which is unique to the bacterial F-ATP synthases without affecting the mitochondrial counterpart.

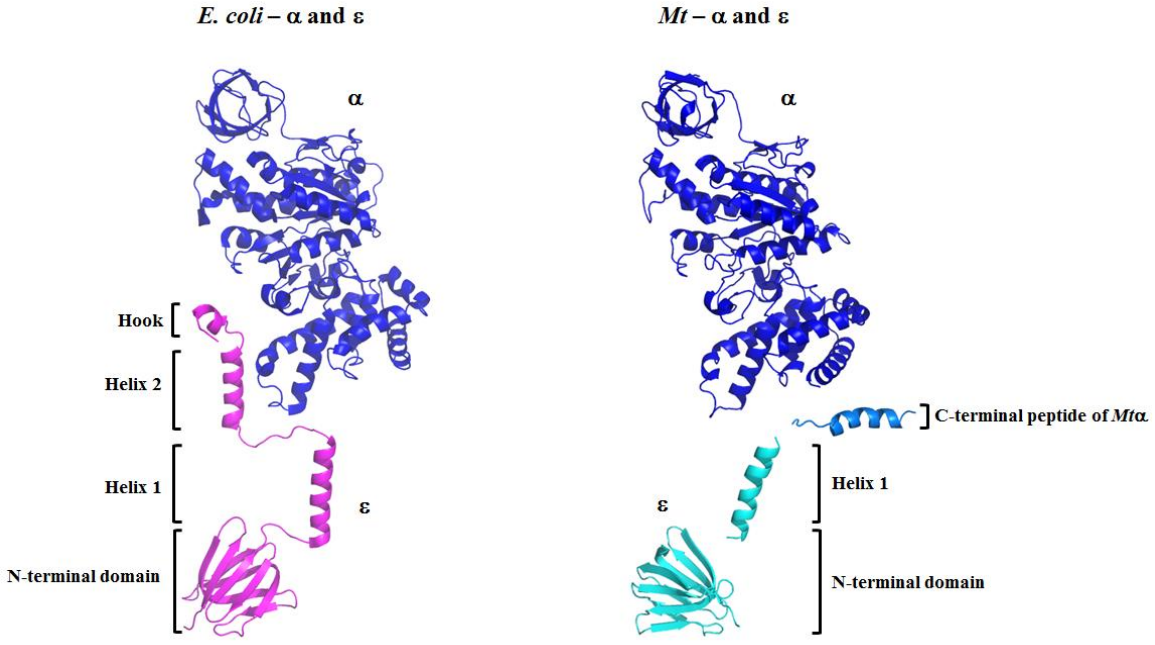

Figure 3.3.1: Cartoon representation of the subunits α and ε *E. coli* (left) and *M. tuberculosis* (*Mt*) (right). The arrangement of subunits α and ε for *E. coli* are based on crystal structure data. The models obtained for *M. tuberculosis* are superimposed on the arrangement for *E. coli* to get a comparative understanding.

Figure 3.3.1 shows the cartoon representation of the subunits α and ε as seen in the crystal structure of the F_1 complex of *E. coli* (PDB ID: 3OAA) [18]. The arrangement shown for *Mt*ε and *Mt*α is based on that of *E. coli* crystal structure. The model used for *Mt*α is explained in

the previous chapter and that for *Mt*ε has been obtained from previous work in our laboratory [130]. In comparison, *Mt*α is longer in sequence than the *Ec*α and *Mt*ε is shorter than *Ec*ε. It is evident from this illustration that the shorter length of the *Mt*ε is probably compensated for by the longer *Mt*α possibly to facilitate the interaction between the subunits during catalysis. To explore the feasible interactions, *Mt*ε is studied in complex with the mechanistically well understood PS3$\alpha_3\beta_3\gamma$ given the present difficulty in expressing *Mt*$\alpha_3\beta_3\gamma$ protein.

Subunit ε of *Ec* and *Bacillus* PS3 in their respective F_1-ATPase complex have been shown to bind ATP, as also seen with the individual subunit of *Bacillus subtilis* [127, 215, 216]. Subunit *Ec*ε and PS3ε are well studied systems, with their high resolution structures resolved (PDB ID: 1AQT and 2QE5 respectively). PS3ε with its native complex of $\alpha_3\beta_3\gamma$ is the most well studied mechanistically providing insight into its regulatory role as either an activator or inhibitor of ATP hydrolysis in an ATP concentration dependent manner. At high concentrations of ATP, PS3ε takes up a conformation that does not inhibit ATP hydrolysis, while at low ATP concentrations ATP hydrolysis is clearly inhibited [218]. However in the case of EF_1, subunit ε was observed to dissociate from complex $\alpha_3\beta_3\gamma$ during catalytic turnover. As a consequence of dissociation of ε from the complex, inhibition of ATP hydrolysis is relieved and leads to increase of hydrolytic activity, independent of the ATP concentration as observed for PS3ε [217]. Compared to PS3ε and *Ec*ε, the isolated subunit *Mt*ε is unable to bind ATP [81]. To serve as control in the process of investigating the mechanistic role of *Mt*ε, PS3ε and *Ec*ε were also cloned and prepared as described in the following section.

Sequence alignment of subunit ε from *Mt* and *Ec* clearly shows the difference in length (Figure 3.3.1) and earlier studies have revealed the C-terminal helix of the subunit ε is responsible for the inhibition of hydrolysis activity in the enzyme [129]. To further explore the role of the C-terminus and the effect it has on functionality of *Mt*ε, chimeric protein of *Mt*ε and *Ec*ε, *Mt*ε_{12hyb}, incorporating the very C-terminal residues of *Ec*ε in *Mt*ε was designed for an activity study. Also single amino acid truncated protein, *Mt*$\varepsilon_{1\text{-}120}$ was generated to yield a more stable form of the protein for *Mt*ε. The following section presents the data for the production of these various proteins *Mt*$\varepsilon_{1\text{-}120}$, *Mt*ε, *Mt*$\varepsilon_{12hyb}$, *Ec*ε, including PS3ε that served as control. These were reconstituted with PS3$\alpha_3\beta_3\gamma$ and ATP hydrolysis was studied. Additional interaction studies were performed with $\alpha^{chi}{}_3\beta_3\gamma$, which was prepared as described in section 3.2.5. $\alpha^{chi}{}_3\beta_3\gamma$ is composed of the PS3$\alpha_3\beta_3\gamma$ fused with very C-terminal residues of the *Mt*α, to yield chimeric alpha subunit in the complex. $\alpha^{chi}{}_3\beta_3\gamma$ complex offers the natural binding partner for PS3ε and also via the C-terminal residues of the *Mt*α it possibly provides the site for interaction with the

C-terminus of *Mt*ε. Hence both *Mt*ε and PS3ε were reconstituted with $\alpha^{chi}{}_3\beta_3\gamma$ and ATP hydrolysis study was performed.

3.3.2 Production and purification of subunit *Mt*ε and *Mt*ε$_{1-120}$ constructs from F_1F_O ATP synthase *M. tuberculosis*

*Mt*ε was earlier cloned and expressed as described in Biuković *et al* [81][81][81]. In order to investigate the specific interactions of the very C-terminus of *Mt*ε with PS3$\alpha_3\beta_3\gamma$, *Mt*ε$_{1-120}$ was generated by performing single amino acid truncation at the C-terminus to yield a stable protein. As described in the following section, 3.3.10, *Mt*ε$_{1-120}$ designed for mechanistic studies was found to be more suitable for structural studies also. Earlier attempts to use *Mt*ε for structural studies resulted in a relatively low quality 3D NMR data. Hence *Mt*ε$_{1-120}$ which yielded a better quality protein using a three step purification was used for NMR and crystallisation studies. The reason for improvement in protein quality of *Mt*ε$_{1-120}$ could be attributed to the removal of a terminal charged residue. The protocol for cloning and production of *Mt*ε$_{1-120}$ is described in sections 2.2.13 and 2.2.14. To induce the expression of recombinant proteins, IPTG supplement was added to the culture to achieve a final concentration of 1 mM. Figure 3.3.2 shows the representative gel for the constructs of *Mt*ε$_{1-120}$. SDS-PAGE of the produced recombinant proteins revealed prominent bands at 13 kDa for *Mt*ε$_{1-120}$ which were found in the crude lysates following IPTG induction (Figure 3.3.2 (a)). Solubility test was performed for the positively induced colonies for this construct as described in section 2.2.14. The SDS-PAGE gel showed that the construct yielded soluble proteins. Incubation temperature of 15°C was maintained for the liquid cultures of *Mt*ε$_{1-120}$ to obtain soluble protein (Figure 3.3.2 (b)).

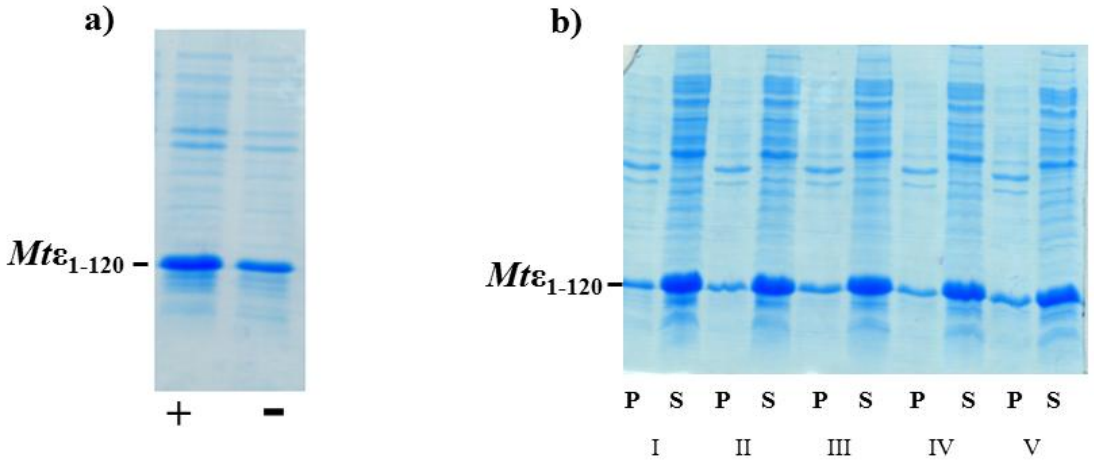

Figure 3.3.2: a) 17% SDS-PAGE showing the expression of recombinant subunit *Mt*ε$_{1-120}$. Induction of the protein was done by addition of IPTG to a final concentration of 1 mM. The + and - signs indicate the presence and absence of IPTG respectively. b) SDS-PAGE gel showing the solubility test for PS3ε, *and Ec*ε (P: Pellet & S: Supernatant). Composition for buffers I-V are described in section 2.2.14.

A purification protocol employing affinity chromatography and size exclusion chromatography was employed for *Mt*ε and *Mt*ε$_{1-120}$ to obtain protein of high purity for ATP hydrolysis studies. The recombinant protein ε constructs containing the His$_6$-tag were separated from the other contaminating proteins using a Ni^{2+}-NTA resin column and an imidazole gradient (10-400 mM) in buffer, consisting of 50 mM Tris-HCl (pH 8.5), 200 mM NaCl. Distinct bands of proteins were identified in the fractions 75-400 mM on a SDS gel (Figure 3.3.3 (a) *Mt*ε and (b) *Mt*ε$_{1-120}$). Imidazole was removed by gel filtration chromatography using a Superdex 75 HR 10/30 column (GE healthcare) and a buffer of 50 mM Tris-HCl (pH 8.5), 200 mM NaCl.

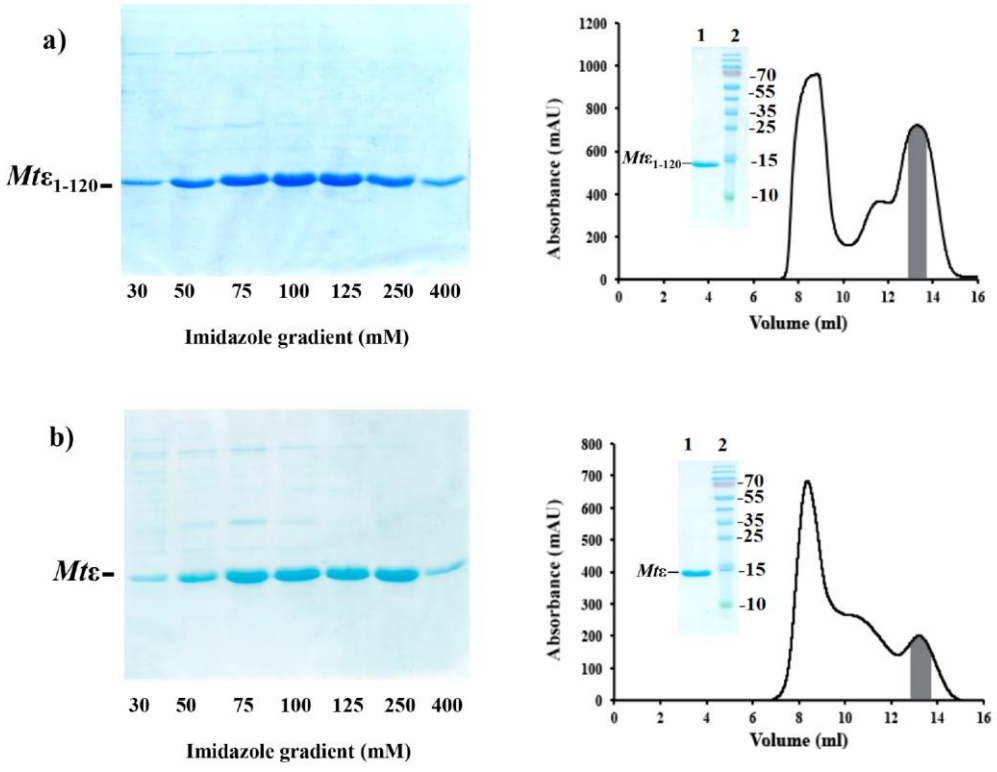

Figure 3.3.3: Purification of recombinant protein *Mt*ε and *Mt*ε$_{1-120}$ using Ni^{2+}-NTA affinity chromatography eluted in a linear Imidazole gradient with 50 mM Tris-HCl, pH 8.5, 200 mM NaCl and 10% glycerol. 20 µl of the protein samples were mixed with 5×SDS sample buffer and loaded on a 17% SDS-gel. Inset in the S75 profile shows the purified protein, with lane 1 indicating the protein of interest and lane 2 showing the protein marker.

3.3.3 Reconstitution of PS3$\alpha_3\beta_3\gamma$ with *Mt*ε and *Mt*ε$_{1-120}$ and ATP hydrolysis analysis using NADH coupled continuous assay.

An optimized protocol involving incubation with 1:5 molar excess of PS3$\alpha_3\beta_3\gamma$ protein and subunit ε constructs for 4 hours at 4°C was followed by the S200 gel filtration column run to isolate and purify the successfully bound complex. Subsequently, ATP hydrolysis activity

analysis was performed using NADH coupled assay and is as tabulated in the following section 2.2.10.

To probe into the interaction of *Mt*ε and *Mt*ε$_{1\text{-}120}$ with the catalytic headpiece, both of these purified proteins were reconstituted with PS3$\alpha_3\beta_3\gamma$ and the hydrolytic activity was detected. The gel filtration and SDS-PAGE gel profiles for these are shown in figure 3.3.4 with the ATP hydrolysis data presented in figure 3.3.5. In figure 3.3.4, the reconstituted complex with $\alpha_3\beta_3\gamma$ and individual subunits of *Mt*ε and *Mt*ε$_{1\text{-}120}$ is represented by cartoon illustration. The SDS-PAGE analysis shown as an inset is indicative of the successful complexation.

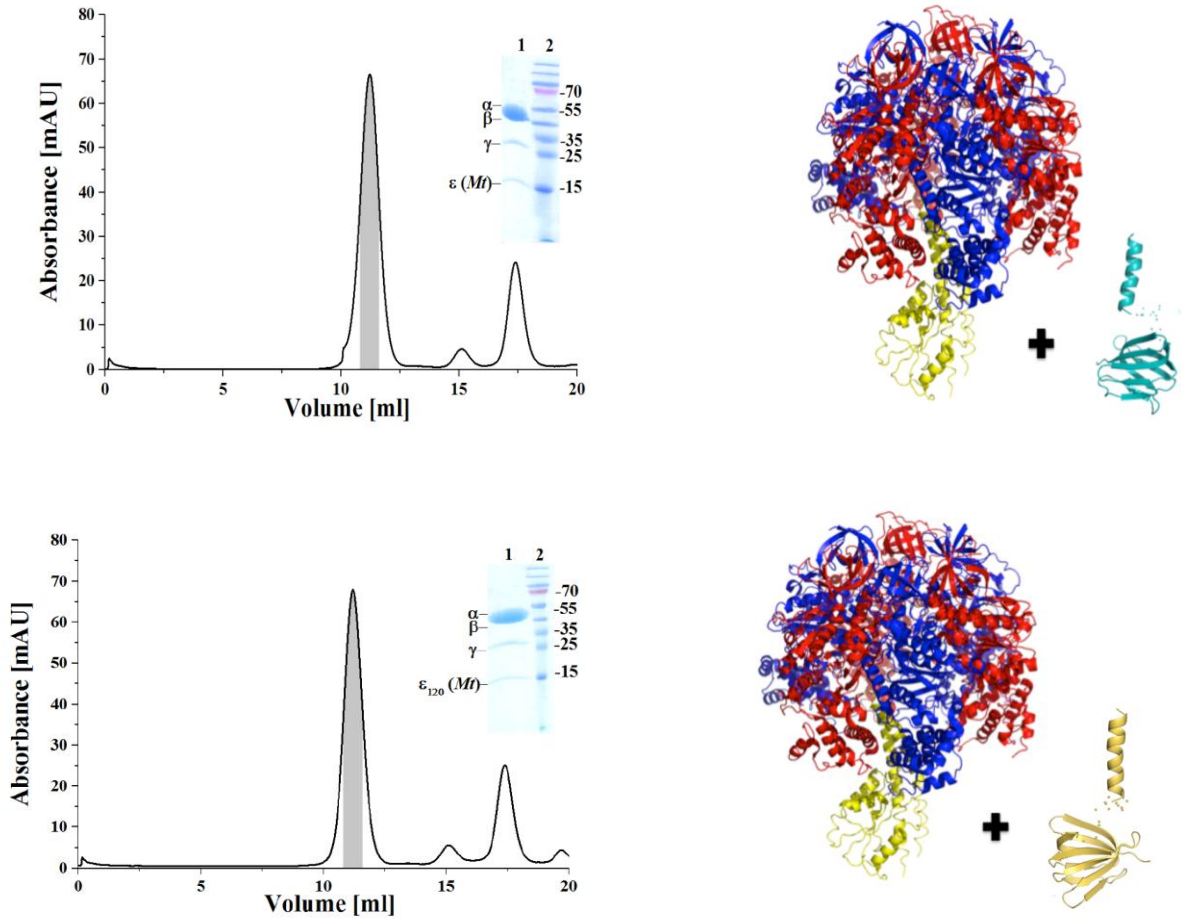

Figure 3.3.4: S200 gel filtration chromatography profile of reconstituted protein complexes of PS3$\alpha_3\beta_3\gamma$ + *Mt*ε, $\alpha_3\beta_3\gamma$ + *Mt*ε$_{1\text{-}120}$. Inset shows the 17% SDA-PAGE analysis of the reconstituted complex. Cartoon representation of the protein complexes with α (*blue*), β (*red*) and γ (*yellow*) in the $\alpha_3\beta_3\gamma$ complex and *Mt*ε- *teal*, *Mt*ε$_{1\text{-}120}$ -*orange* for individual subunits of ε (PDB ID: 1SKY, 2QE7 and 2LXS). Subunits *Mt*ε (teal) and *Mt*ε$_{1\text{-}120}$ (*orange*) are obtained from the models generated for N-terminal and the NMR structure for the C-terminal peptide (PDB ID: 2LX5). [81, 107, 213].

ATPase activity was measured for these reconstituted complexes and figure 3.3.5 shows these values tabulated. An averaged value of 4.6 U/mg protein was measured for PS3$\alpha_3\beta_3\gamma$ and values of 4.4 and 4.8 U/mg protein for PS3$\alpha_3\beta_3\gamma$ + *Mt*$\varepsilon_{1\text{-}120}$ and PS3$\alpha_3\beta_3\gamma$ + *Mt*ε, respectively. The complexes of PS3$\alpha_3\beta_3\gamma$ + *Mt*$\varepsilon_{1\text{-}120}$ and PS3$\alpha_3\beta_3\gamma$ + *Mt*ε showed readings comparable to that of the PS3$\alpha_3\beta_3\gamma$ complex, with PS3$\alpha_3\beta_3\gamma$ + *Mt*ε indicating a slight increase.

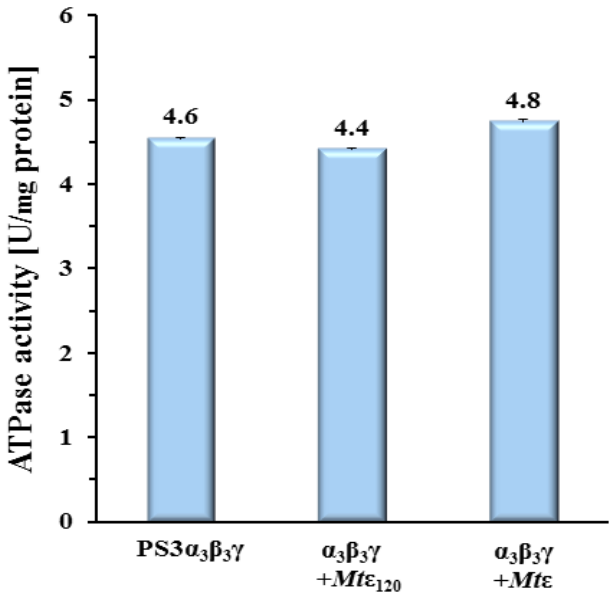

Figure 3.3.5: ATP hydrolysis specific activity calculated on performing the NADH coupled hydrolytic assay of $\alpha_3\beta_3\gamma$ of *Bacillus* PS3 with the recombinant protein, *Mt*ε and *Mt*$\varepsilon_{1\text{-}120}$.

3.3.4 Production and purification of PS3ε and *Ec*ε constructs of F_1F_O ATP synthase from *Bacillus* PS3 and *E. coli*.

To explore the interaction of PS3$\alpha_3\beta_3\gamma$ with *Ec*ε and PS3ε, the *atp*C gene encoding for subunit *Ec*ε was amplified using the primers mentioned in section 2.2.13 and using *E. coli* F-ATP synthase genomic DNA. For PS3ε, the DNA sequence coding for the subunit with restriction sites *Nco*I and *Sac*I was synthesised from DNA 2.0 (USA). The amplified products were digested with *Nco*I and *Sac*I restriction enzymes followed by the ligation with pET9d-His_6 vector [211].

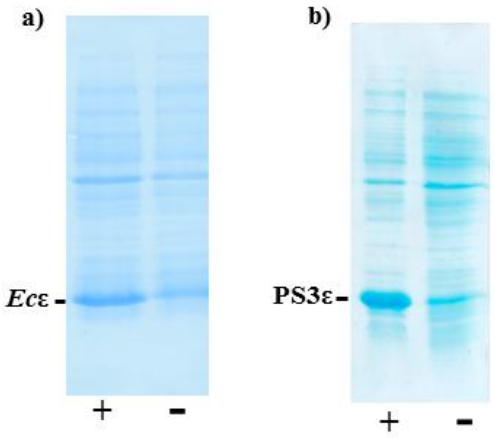

Figure 3.3.6: 17% SDS –PAGE showing the expression of recombinant subunit *Ec*ε and PS3ε proteins. Induction of the proteins was done by addition of IPTG to a final concentration of 1 mM. The + and - signs indicate the presence and absence of IPTG respectively.

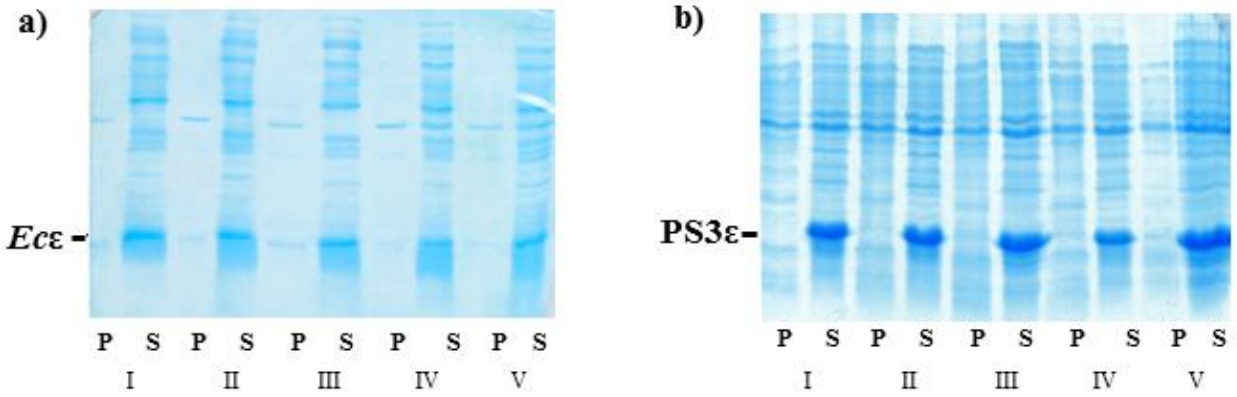

Figure 3.3.7: 17% SDS-PAGE gel showing the solubility test for PS3ε, *and Ec*ε (P: Pellet & S: Supernatant).

This vector containing the Δ*atpC* insert for each of the constructs was then transformed into *E. coli* BL21 (DE3) and grown on 30 µg/ml Kanamycin containing LB agar plates. Figure 3.3.6 indicates the induction test performed to check for expression of the protein. Solubility test was performed to find the suitable buffer for purification (Figure 3.3.7). The protocol for purification was identical to that followed for *Mt*ε and the protein was subjected to Ni^{2+}-NTA affinity chromatography and gel filtration chromatography to obtain the pure protein (Figure 3.3.8).

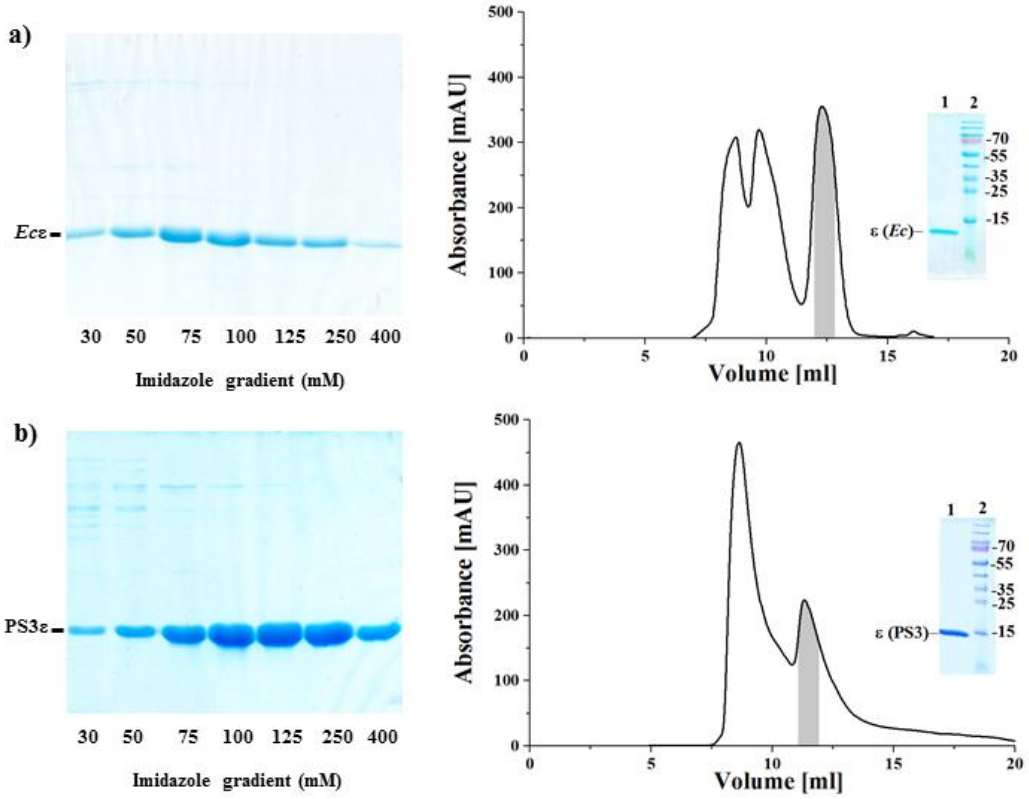

Figure 3.3.8: Purification of recombinant protein PS3ε and *Ec*ε using Ni^{2+}-NTA Affinity chromatography eluted in a linear Imidazole gradient with 50 mM Tris-HCl, pH 7.5, 200 mM NaCl and 10% glycerol. 20 µl of the protein samples were mixed with 5×SDS sample buffer and loaded on a 17% SDS-gel. Inset in the S75 profile shows the purified protein, with lane 1 indicating the protein of interest and lane 2 showing the protein marker.

3.3.5 Reconstitution of PS3$\alpha_3\beta_3\gamma$ with PS3ε and *Ec*ε and ATP hydrolysis analysis using NADH coupled continuous assay

A protocol identical to that of PS3$\alpha_3\beta_3\gamma$ with *Mt*ε was employed for reconstitution of PS3$\alpha_3\beta_3\gamma$ with PS3ε and *Ec*ε. Thus using the protein that was generated from the two-step purification protocol for the different constructs of subunit PS3ε and *Ec*ε. Reconstitution was set up with the PS3$\alpha_3\beta_3\gamma$ that was generated as described in section 2.2.9.

Figure 3.3.9 shows the profile for the S200 gel filtration chromatography after successful reconstitution for $\alpha_3\beta_3\gamma$ + *Ec*ε and $\alpha_3\beta_3\gamma$ + PS3ε. The reconstitution was also confirmed by applying the sample on a SDS-PAGE gel. The cartoon representation shown next to these profiles for each of the complexes are representative figures made with the available crystal structures or models generated for $\alpha_3\beta_3\gamma$ and the ε constructs.

The C-terminal of PS3ε and *Ec*ε are shown in the compact state wherein the two helices are in a hairpin fold and resting on the N-terminal. This is the expected orientation given the working concentration of 2 mM ATP used. However, for *Mt*ε, the C-terminus is expected to be a single

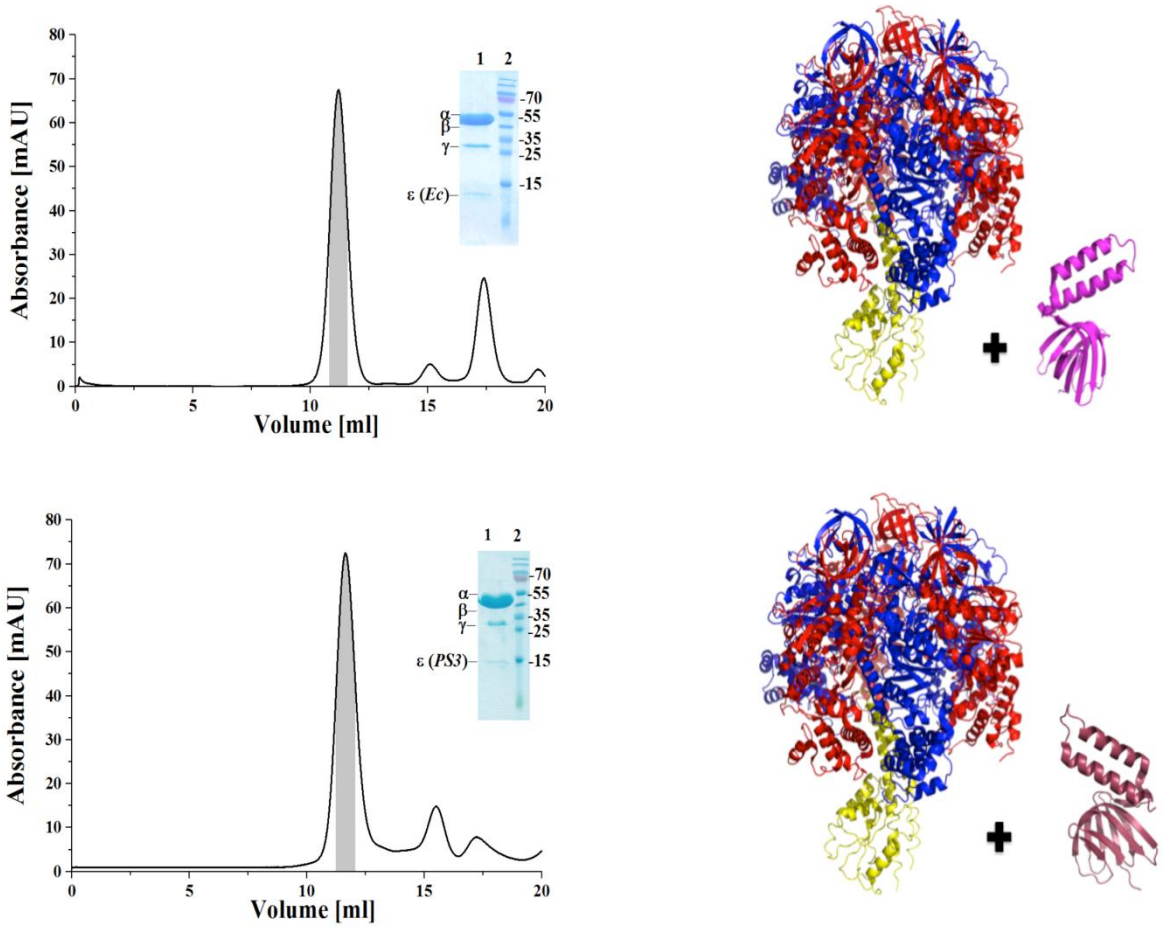

Figure 3.3.9: S200 gel filtration Chromatography profile of reconstituted protein complexes of $\alpha_3\beta_3\gamma$ + *Ec*ε and $\alpha_3\beta_3\gamma$ + PS3ε. 17% SDS-PAGE gel has been used for analysis. Cartoon representation is shown for the protein complexes with α (*blue*), β (*red*) and γ (*yellow*) in the $\alpha_3\beta_3\gamma$ complex and *Ec* ε - *magenta* and PS3ε - *deep salmon* for individual subunits of ε.

elongated helix, given the shortened length of the C-terminus. This is in agreement with the NMR structure obtained for the C-terminal peptide.

Figure 3.3.10 shows the ATP hydrolysis activity measured for these reconstituted complexes and PS3$\alpha_3\beta_3\gamma$ + PS3ε shows a high activity given that ATP binds to the ATP binding site in the subunit epsilon and retains the compact state at high concentrations of ATP. PS3$\alpha_3\beta_3\gamma$ + *Ec*ε also shows an increased activity, which is attributed to the dissociation of the ε from the complex, during catalytic turnover.

Figure 3.3.11 shows the ATPase activity measurements performed at lower concentration of ATP to understand the ATP concentration dependence of the specific activity. There is a reduction in the ATPase activity with decreasing concentrations of ATP.

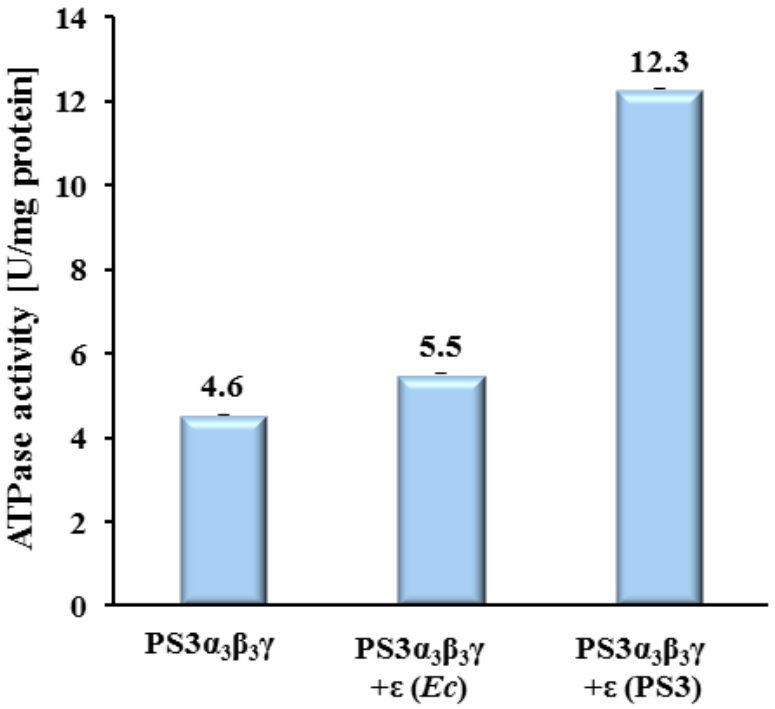

Figure 3.3.10: ATP hydrolysis specific activity calculated on performing the NADH coupled hydrolytic assay of $\alpha_3\beta_3\gamma$ of *Bacillus* PS3 with the recombinant protein, *Ec*ε and PS3ε.

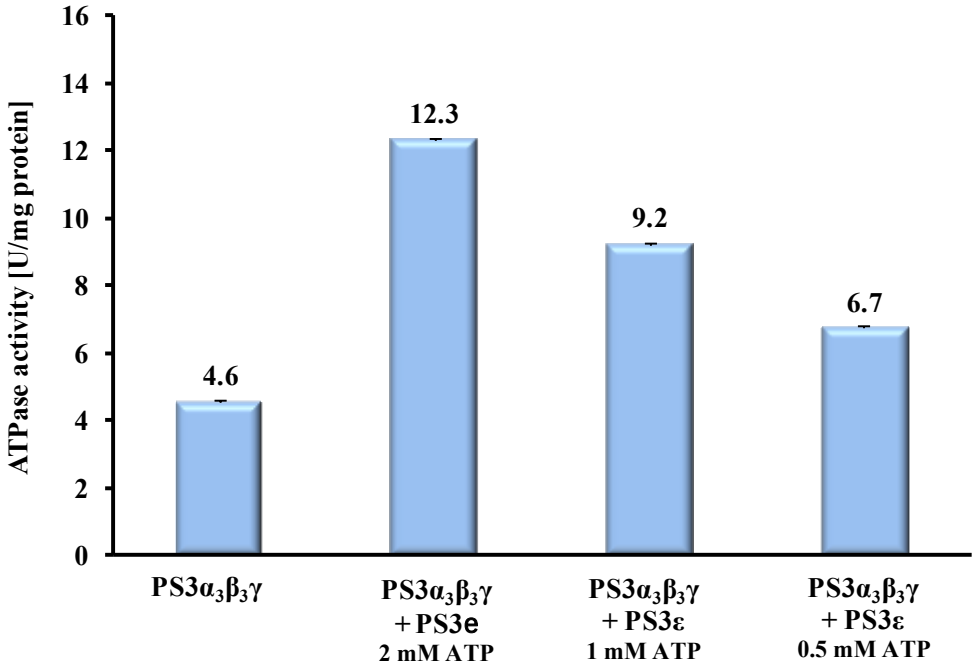

Figure 3.3.11: ATP hydrolysis specific activity calculated on performing the NADH coupled hydrolytic assay of $\alpha_3\beta_3\gamma$ of *Bacillus* PS3 with the recombinant protein PS3ε at different ATP concentrations.

3.3.6 Production and purification of subunit ε_{121hyb}, a hybrid construct from F_1F_O ATP synthase of *M. tuberculosis* and *E. coli*.

The importance of the hook like region of the C-terminus of *E. coli* ε F_1F_O ATP synthase has been well illustrated [18]. To extend the understanding of the role of the residues in the hook like region, $\varepsilon_{1\text{-}121hyb}$ was designed by elongating the C-terminus of subunit *Mt*ε with residues from subunit ε of *E. coli*. $\varepsilon_{1\text{-}121hyb}$ carries (1-121) residues of *Mt* and residues (136-138) of *Ec* to form a hybrid construct, *Mt*ε + C-terminal residues KAM of *Ec*ε, with a total length of 124 residues. The construct $\varepsilon_{1\text{-}121hyb}$ was cloned using PCR method by direct amplification from plasmid DNA of *M. tuberculosis* using forward and reverse primers. The methodology along with the primers used is described in section 2.2.13. Figure 3.3.12 shows the sequence alignment for the *Ec*ε and *Mt*ε and also the graphical illustration of the truncated constructs of *Mt*ε and the hybrid construct ε_{121hyb}.

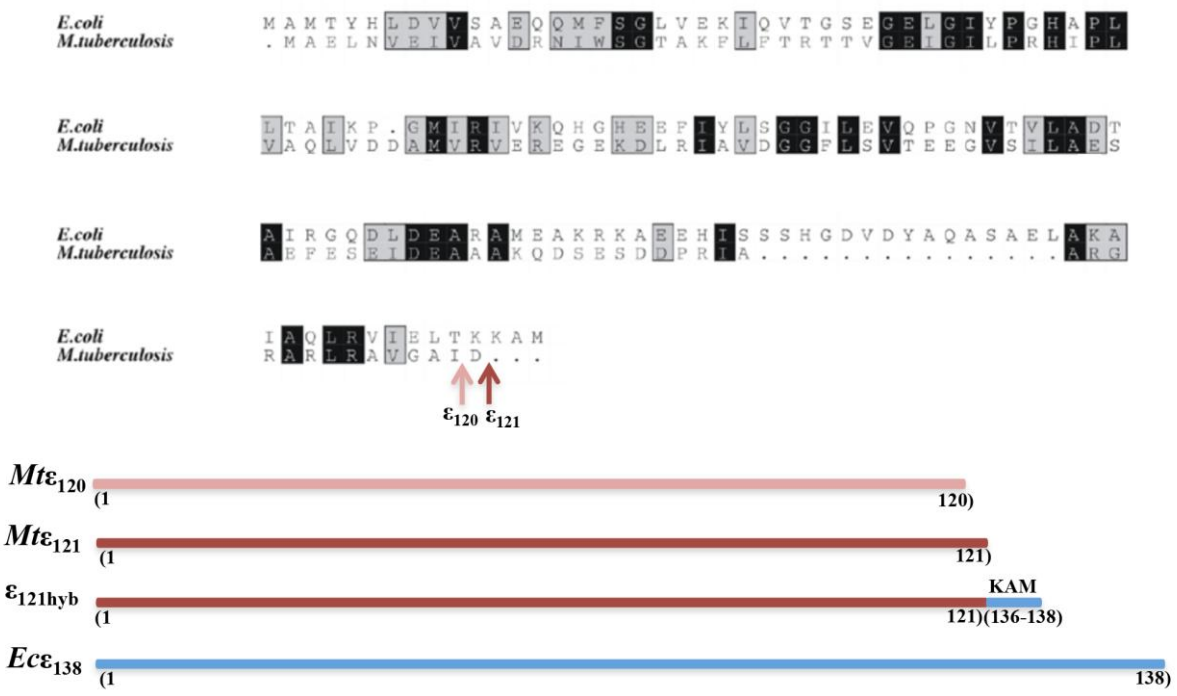

Figure 3.3.12: Sequence alignment of subunit epsilon from *E. coli* and *M. tuberculosis*. Cartoon representation of the truncated constructs of *Mt* ε and hybrid construct of *Ec*ε and *Mt*ε, ε_{121hyb} (red and blue), *Mt*ε_{120} (peach), *Mt*ε_{121} (red) and *Ec*ε (blue). The residue numbers are mentioned at the start and end of the length.

The induction and solubility tests performed for verification of protein expression and optimal buffer condition were performed and the representative gel for the SDS-PAGE analysis is shown in Figure 3.3.13.

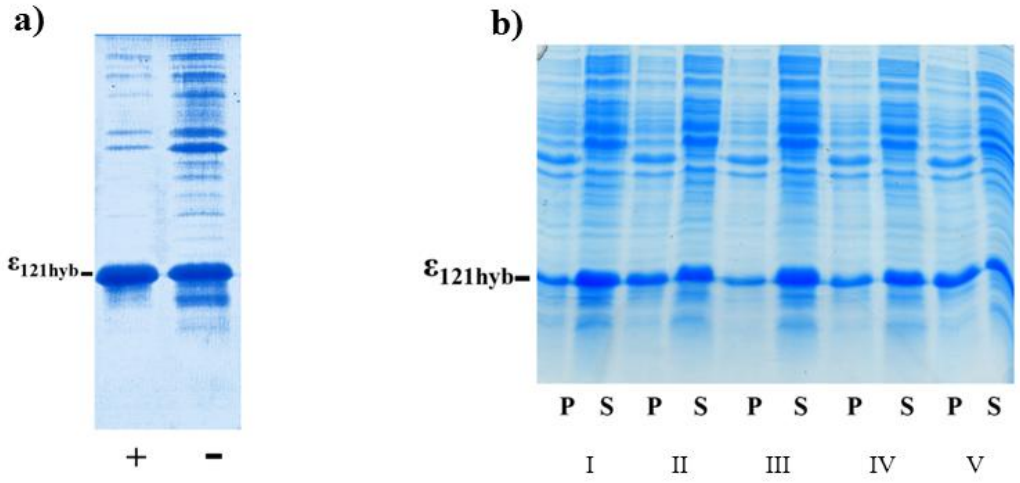

Figure 3.3.13: a) Induction test for protein expression of ε_{121hyb}. b) Solubility test for optimal buffer selection for ε_{121hyb}.

To obtain the pure protein for the hydrolysis assay, a two-step purification strategy was adopted involving Ni^{2+}-NTA affinity and gel filtration chromatography. ε_{121hyb} was prepared in the above mentioned manner and their SDS-PAGE gels along with their elution profiles are shown in figures 3.3.14. Buffer used in Ni^{2+}-NTA affinity and gel filtration chromatography was 50 mM Tris-HCl, pH 7.5, 200 mM NaCl and 10% glycerol.

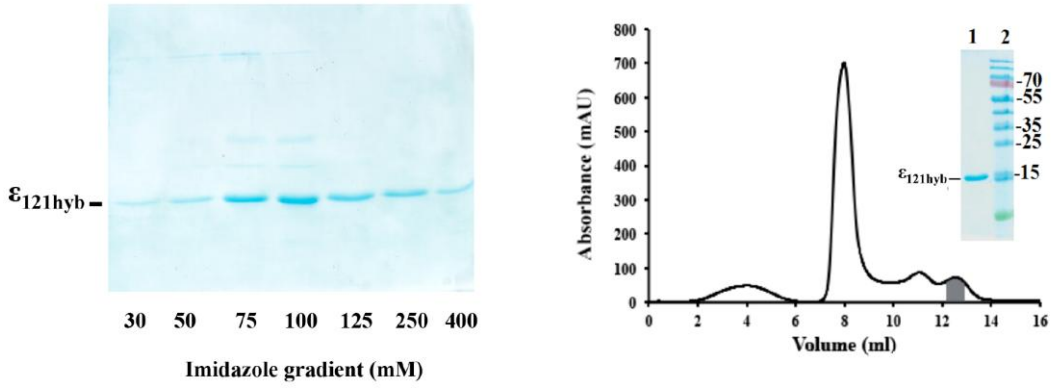

Figure 3.3.14: Purification of recombinant protein ε_{121hyb} using Ni^{2+}-NTA affinity chromatography eluted in a linear Imidazole gradient with 50 mM Tris-HCl, pH 8.5, 200 mM NaCl and 10% glycerol. 20 µl of the protein samples were mixed with 5×SDS sample buffer and loaded on a 17% SDS-gel. Inset in the S75 profile shows the purified protein, with lane 1 indicating the protein of interest and lane 2 showing the protein marker.

3.3.7 Reconstitution of PS3$\alpha_3\beta_3\gamma$ with ε_{121hyb} and ATP hydrolysis analysis using NADH coupled continuous assay

Successful reconstitution of PS3$\alpha_3\beta_3\gamma$ with ε_{121hyb} was achieved by following the established protocol. The pure protein obtained from the two-step purification protocol was used

for reconstitution as described in section 2.2.9. Figure 3.3.15 shows the successful complexation with the cartoon representation of the formed complex.

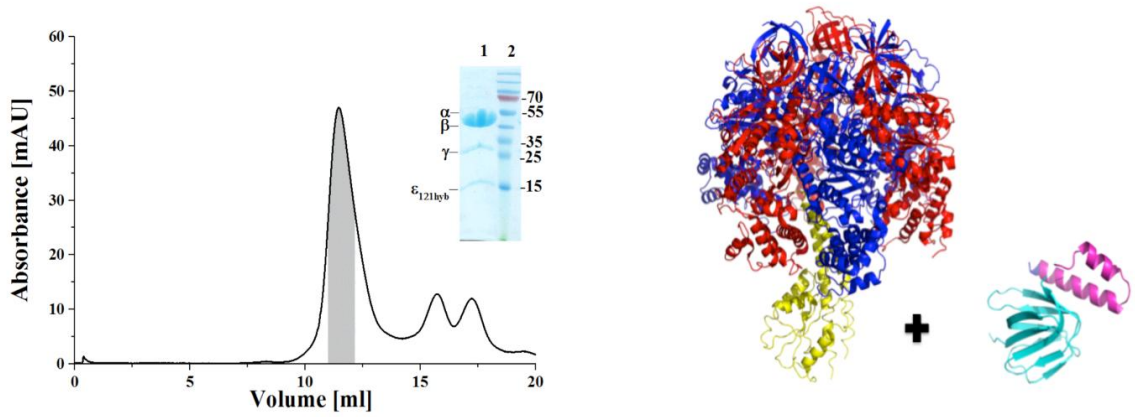

Figure 3.3.15: S200 gel filtration Chromatography profile of reconstituted protein complexes of $\alpha_3\beta_3\gamma$ + ε_{121hyb}. Cartoon representation of the protein complexes with α (*blue*), β (*red*) and γ (*yellow*) in the $\alpha_3\beta_3\gamma$ complex and *cyan and pink* for subunit ε_{121hyb}.

Figure 3.3.16 shows the ATPase activity measured. Interestingly, the $\alpha_3\beta_3\gamma$+ ε_{121hyb} complex showed an increased activity, which could be attributed to the extended length of the C-terminus with the addition of the residues from subunit ε (*Ec*). In figure 3.3.14, the model generated via I-TASSER shows the C-terminus to be in a compact state and is highlighted in pink with the terminal residues from *Ec* in blue.

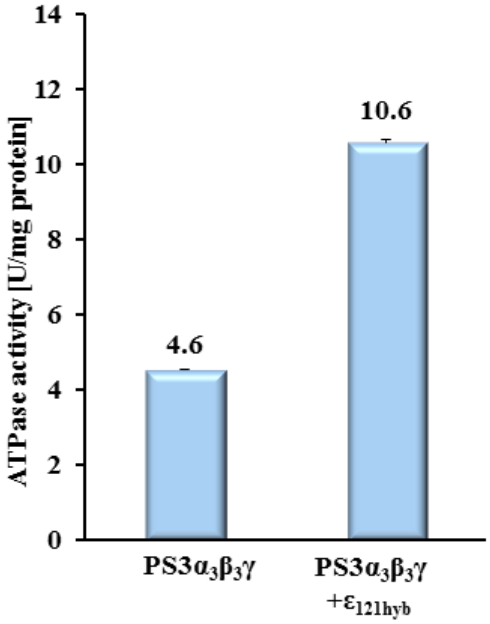

Figure 3.3.16: Specific ATPase activity calculated on performing the NADH coupled hydrolytic assay using 2 mM ATP for PS3$\alpha_3\beta_3\gamma$ with the recombinant protein ε_{121hyb}.

3.3.8 Reconstitution of $\alpha^{chi}_3\beta_3\gamma$ with *Mt*ε and PS3ε and ATP hydrolysis analysis using NADH coupled continuous assay

In figure 3.3.17, the model for $\alpha^{chi}_3\beta_3\gamma$ complex is shown with the C-terminus of the *Mt*α highlighted (light blue). To study the effects of the possible interaction between $\alpha^{chi}_3\beta_3\gamma$ (section 3.2.4) with *Mt*ε and PS3ε, reconstitution was performed to generate the complex for ATP hydrolysis activity studies. Both PS3ε and *Mt*ε complexed well and interestingly, showed high activity. Figure 3.3.18 show the profiles for the gel filtration reconstitution and SDS-PAGE analysis, along with the cartoon representation of the proteins $\alpha^{chi}_3\beta_3\gamma$ and PS3ε in deep salmon and *Mt*ε in teal colours.

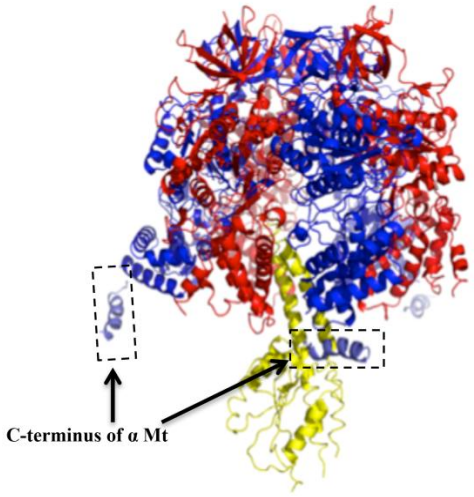

Figure 3.3.17: Cartoon representation of the protein complexes with α^{chi} (*blue*), β (*red*) and γ (*yellow*) in the $\alpha^{chi}_3\beta_3\gamma$ complex. The C-terminus of the *Mt*α of the α^{chi} is highlighted.

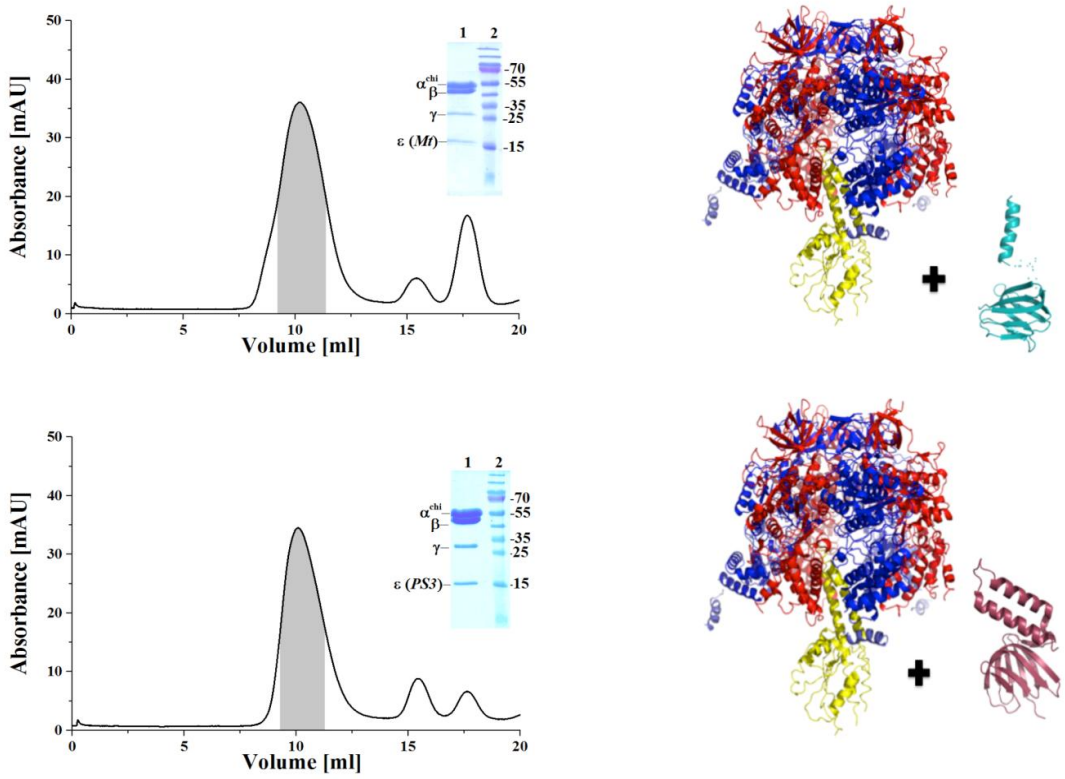

Figure 3.3.18: S200 gel filtration chromatography profile of reconstituted protein complexes of $\alpha^{chi}{}_3\beta_3\gamma$ + *Mt*ε and $\alpha^{chi}{}_3\beta_3\gamma$ + PS3ε. Cartoon representation of the protein complexes with α^{chi} (*blue*), β (*red*) and γ (*yellow*) in the $\alpha^{chi}{}_3\beta_3\gamma$ complex and *cyan* for *Mt*ε and *deep salmon* for subunit PS3ε.

In figure 3.3.19, $\alpha^{chi}{}_3\beta_3\gamma$ + PS3ε shows an activity of 13.7 U/mg protein, a similar increase in hydrolytic activity as was seen with $\alpha_3\beta_3\gamma$ + PS3ε. The increase in activity is plausible, given that specific interactions could arise between *Mt*ε and $\alpha^{chi}{}_3\beta_3\gamma$ as they could be natural binding or interacting partners. For $\alpha^{chi}{}_3\beta_3\gamma$ + *Mt*ε, an activity of 9.7 U/mg protein was observed. Further investigation is required to ascertain the nature of interaction and to confirm whether *Mt*ε undergoes any structural changes to allow this effect in the reconstituted complex of *Mt*ε and $\alpha^{chi}{}_3\beta_3\gamma$. Both these show a clear increase in activity and are in stark contrast when compared to the reduction seen in $\alpha^{chi}{}_3\beta_3\gamma$. This indicates a strong role played by the subunit ε in stimulating the ATPase activity.

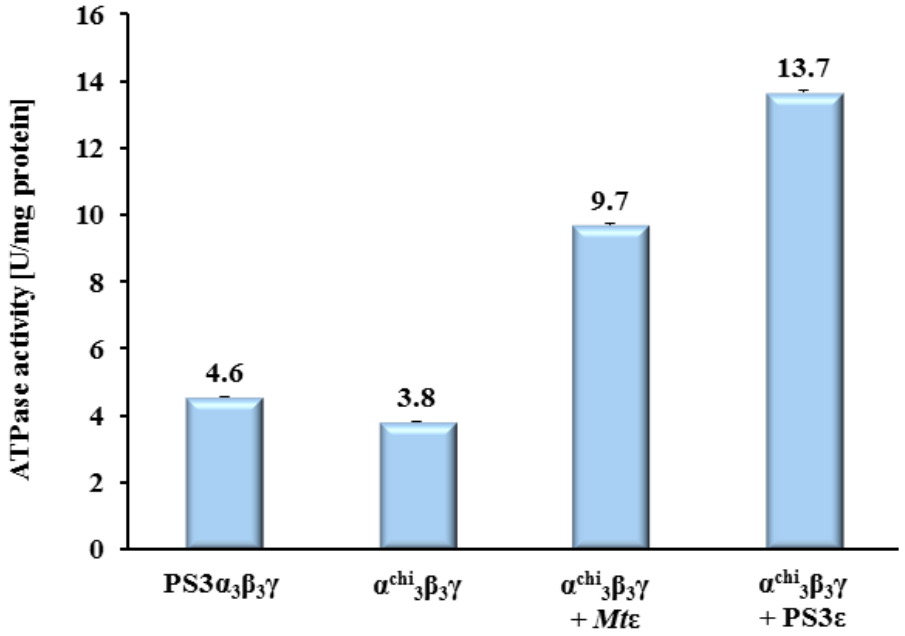

Figure 3.3.19: Specific activity calculated on performing the NADH coupled hydrolytic assay of $\alpha^{chi}{}_3\beta_3\gamma$ of with the recombinant protein, *Mt*ε and PS3ε.

3.3.9 ATP hydrolysis analysis using NADH coupled continuous assay for *Mm*A_3B_3D and *Mt*ε

To experiment with the possibility of assembly and activity, *Mt*ε was reconstituted with sub-complex A_3B_3D from *M. mazei* Gö1 (*Mm*). A_3B_3D has been tested and shown to be hydrolytically active and shows an increase in activity when reconstituted with subunit *Mm*F and *Sc*F (*Saccharomyces cerevisiae*), wherein F acts as a stimulator [218]. Subunit F of A-ATP synthases is the homologous subunit to the subunit ε in F-ATP synthases and forms a part of the central stalk. Although they share a high topographic identity, their functional roles are contrastingly different. Addition of subunit F to A_3B_3D-complex lead to stimulation and a similar reconstitution of subunit ε to A_3B_3D was performed to view a possible inhibitory effect.

Purified proteins of A_3B_3D and ε were incubated in molar ratios of 1:5 for 4 hours and were then passed through a gel filtration column to separate individual components and to collect the reconstituted sample. However, the profile of the size exclusion chromatography showed A_3B_3D and ε to elute separately (Figure 3.3.20). SDS-PAGE analysis of these fractions confirmed their elution as separate components on failure to assemble. The ATPase activity measurement performed also showed that the incubated sample of A_3B_3D+*Mt*ε had the same activity of 1.1 Unit/mg as that of A_3B_3D [219].

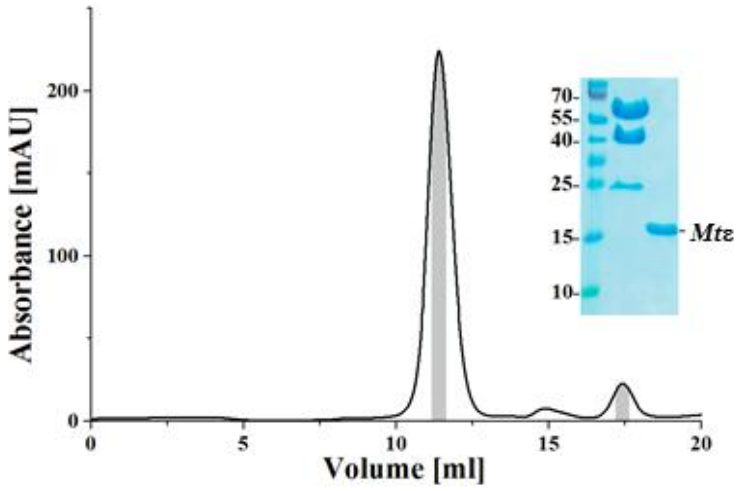

Figure 3.3.20: S200 gel filtration Chromatography profile of reconstituted protein complexes of *Mm* A_3B_3D + *Mt*ε. Inset shows the A_3B_3D protein in lane 1 and *Mt*ε in lane 2, eluted at 11 ml and 17 ml respectively.

3.3.10 Production and Purification of subunit *Mt*$\varepsilon_{1\text{-}120}$ F_1F_O ATP synthase *M. tuberculosis* for structural characterization.

Mt$\varepsilon_{1\text{-}120}$ was further subjected to a three step purification protocol to produce protein of higher purity for NMR and crystallisation studies. Optimising the purification protocol for *Mt*$\varepsilon_{1\text{-}120}$, 10% glycerol was included in the buffers used for purification to aid as a stabilising factor. Also an additional step of ion exchange chromatography was included before the size exclusion gel filtration chromatography step as described in section 2.3.3. This yielded the stable protein which was used for BCA and CD measurements and for ^{15}N-HSQC NMR studies.

The first step of purification for *Mt*$\varepsilon_{1\text{-}120}$ includes Ni^{2+}-NTA affinity chromatography as described for all the recombinant subunit ε constructs. The second step of purification involved the use of ion-exchange chromatography as described in section 2.3.3, to remove residual minor contaminants and imidazole. The protein was applied on the RESOURCE Q column (volume 6 ml, GE healthcare), which is a pre-packed high performance column for separating biomolecules by ion-exchange chromatography.

The pooled protein imidazole fractions were diluted appropriately in 50 mM Tris-HCl, pH 7.5, 10% glycerol buffer to yield a final NaCl concentration of 100 mM, thereby enabling efficient binding of the protein to the ion exchange column. The protein samples were filtered using syringe filters (0.45 µm pore size) prior to injection into the column. Column flow rate was kept at 2 ml/min. The monomeric recombinant protein of subunit *Mt*$\varepsilon_{1\text{-}120}$ does not bind to the column matrix and eluted in the flow through. However, the oligomer forms of *Mt*$\varepsilon_{1\text{-}120}$ together with impurities bind to the column. They were removed by using a linear gradient of

Buffer A (50 mM Tris-HCl, pH 7.5 and 10% glycerol) and B (50 mM Tris-HCl pH 7.5, 1 M NaCl and 10% glycerol). The flow through containing the protein was concentrated by using Centricon YM-3 (3 kDa molecular mass cutoff) spin concentrators (Millipore).

As a final step of purification, aliquots of 1 ml were applied on gel filtration chromatography column using a Superdex 75 HR 10/30 column (GE Healthcare) using buffer of 50 mM Tris-HCl (pH 7.5), 200 mM NaCl and 10% glycerol. The protein fractions containing *Mt*ε$_{1-120}$ were concentrated and subsequently applied onto a SDS gel to the check the purity and quantity of the recombinant protein.

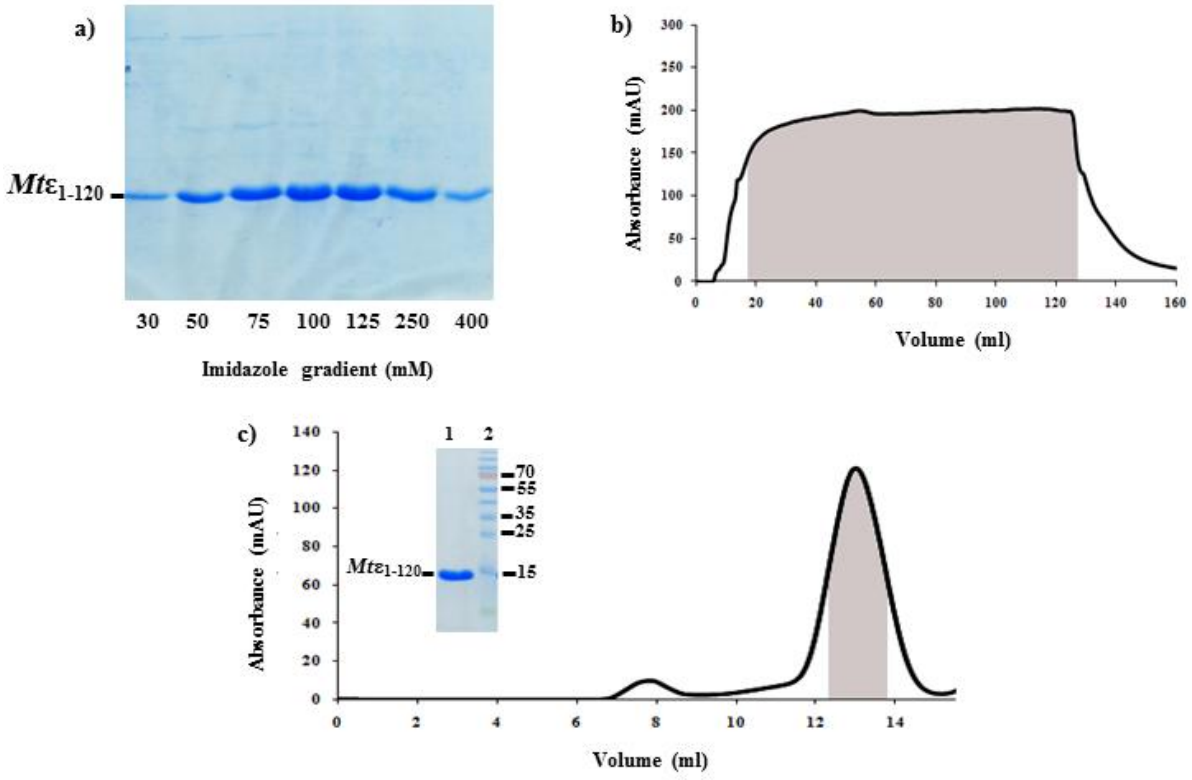

Figure 3.3.21: (a) Purification of recombinant *Mt*ε$_{1-120}$ protein using Ni^{2+}-NTA affinity chromatography eluted in a linear Imidazole gradient with 50 mM Tris-HCl, pH 7.5, 200 mM NaCl and 10 % glycerol. 20 µl of the protein samples were mixed with 5×SDS sample buffer and loaded on a 17% SDS-gel. (b) Purification of protein by a linear gradient of NaCl on anion exchange column (Resource Q (6 ml). 75-400 mM Imidazole fractions were pooled and applied at a constant flow rate of 2 ml/min. (c) Final step of purification using Superdex 75.

The concentration of the protein was determined by BCA method as described in section 2.3.4 and provided a value of 2 mg/ml.

3.3.11 Secondary structure content of *Mt*ε$_{1-120}$

Secondary structure content of *Mt*ε$_{1-120}$ was confirmed by CD spectroscopy, measured between 180-260 nm. At these wavelengths, the chromophore is the peptide bond and the signal arises when it is located in a regular, folded environment. α-helix, β-sheet and random coil

structures each give rise to a characteristic shape and magnitude of the CD spectrum. Like all spectroscopic techniques, the CD signal reflects an average of the entire molecular population.

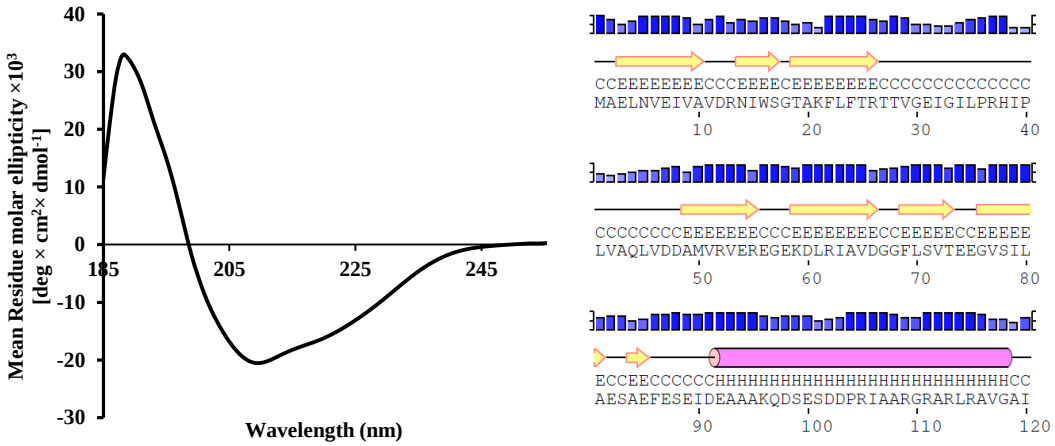

Figure 3.3.22: CD spectrum of *Mt*ε$_{1\text{-}120}$ measured at 2 mg/ml concentration at 20°C. Predicted secondary structure by online PSIPRED software, which uses position specific scoring matrices generated by PSI-BLAST for secondary structure calculation by a two stage neural network algorithm [220].

3.3.12 Crystallization of *Mt*ε$_{1\text{-}120}$ F_1F_O ATP synthase

Crystallization drops were set up for *Mt*ε$_{1\text{-}120}$ as described in section 2.2.17. Various Commercially available crystallization kits were used to set up drops in two different concentrations. The drops were monitored periodically to visualize any progress for crystal formation. It was observed that a few conditions showed microcrystalline precipitate, but no hits were obtained for the various conditions tested. A constant behaviour of the crystal drops noted was that immediate heavy precipitation was observed for conditions with pH in the range of 4 and 5. For pH 6 and 7, precipitation appeared in a few minutes from the time the drops were set up. The drops remained clear for buffers pH range of 8 and 9. This indicated that the protein seemed more stable and comfortable in higher pH range given a calculated pI of 4.58 for *Mt*ε$_{1\text{-}120}$.

Efforts were also directed to express *Mt*ε$_{120}$ in the *M. smegmatis* system as described in section 2.2.5 to obtain a stable protein. Although the cloning was successful, expression of the protein was very poor. Given that this proved to be extremely time consuming, this was effort abandoned. The doubling time for *M. smegmatis* cells are 3 hours and low temperature incubation for protein expression also extended the experimental time.

3.3.13 2D NMR Data acquisition of *Mt*$\varepsilon_{1\text{-}120}$ F_1F_O ATP synthase

Details on structure and the dynamics of proteins can be extracted with NMR spectroscopy. 2D heteronuclear single quantum correlation (HSQC) spectrum is the first in the set of experiments to be measured with an isotope-labelled protein, wherein nuclei apart from ^{1}H are referred to as heteronuclear. Theoretically one peak for each ^{1}H bound to a heteronucleus is observed as the heteronuclear single quantum correlation. With the exception of proline that lacks an amide-hydrogen due to the cyclic nature of its backbone, one signal is expected for each amino acid residue, in the ^{15}N-HSQC. Additional peaks are observed for amino acid residues with N- containing side chains such as tryptophan. Uniqueness of the signal pattern obtained for ^{15}N-HSQC spectrum is often cited as the fingerprint of a protein. The time required for acquisition for this experiment is very short and the analysis allows the user to understand if any problems are present with respect to sample homogeneity arising from multiple conformations. It also allows one to understand aspects related to protein stability and the feasibility of performing the other elaborate set of 3D experiments for specific peak assignment, as only 2D heteronuclear single quantum correlation is insufficient for the same purpose. The HSQC spectrum of *Mt*$\boldsymbol{\varepsilon_{1\text{-}120}}$ recorded at 298 K is the best dispersed and 111 peaks could be observed in the spectrum (Figure 3.2.23), which is about 90 % of the total number of residues.

However *Mt*$\varepsilon_{1\text{-}120}$ in this buffer condition could not be used for further NMR studies as the sample showed visible precipitation on day 2 after sample preparation. Acquisition of 3D NMR datasets requires the sample to be extremely stable and homogenous for over a week. To address the stability issue, the sample was prepared in other buffers and similarly 2D ^{15}N-HSQC spectrum was recorded to choose the best condition for performing the elaborate 3D NMR studies.

The buffer conditions tested are as detailed below.

- 50 mM Tris-HCl, pH 7.2, 200 mM NaCl, 10% glycerol.
- 50 mM Tris-HCl, pH 7.5, 200 mM NaCl, 10% glycerol.

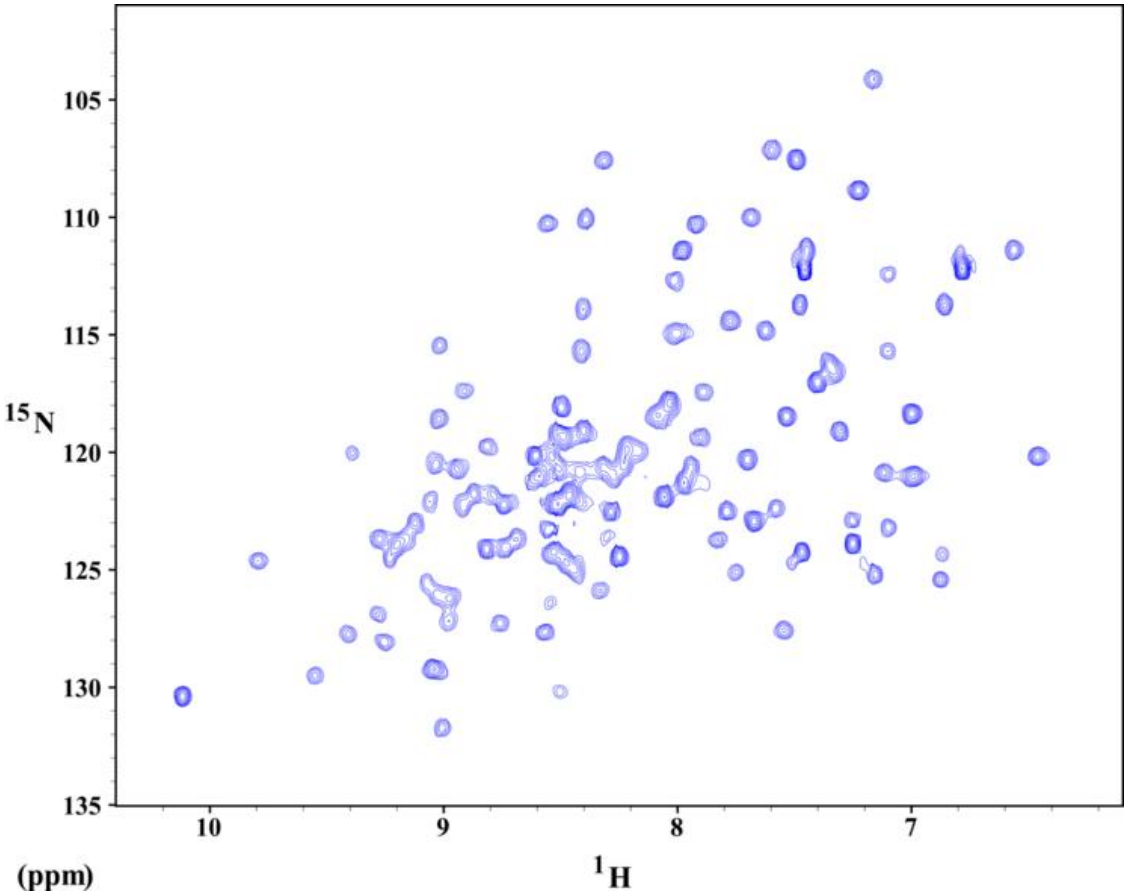

Figure 3.3.23: ^{15}N-^{1}H HSQC spectrum of the protein *Mt*ε$_{1\text{-}120}$ in 50 mM phosphate, pH 6.8, 200 mM NaCl, 10% glycerol recorded in a 600 MHz spectrometer at 298 K.

2D ^{15}N-HSQC experiments were recorded similarly and these showed a well dispersed spectrum with 106 and 102 peaks for buffers Tris pH 7.2 and Tris pH 7.5, respectively. The experiments were recorded over a period of three days to monitor the sample stability and are represented in figure 3.2.24. These conditions initially seemed promising as there was no visible precipitation on days 2 and 3, but the 2D ^{15}N-HSQC experiments performed on these subsequent days proved that there were some undesirable changes that were having with the sample although they looked clear. Appearance of extra peaks and drop in the intensity of peaks was clear evidence to the fact the sample was not as stable as desired.

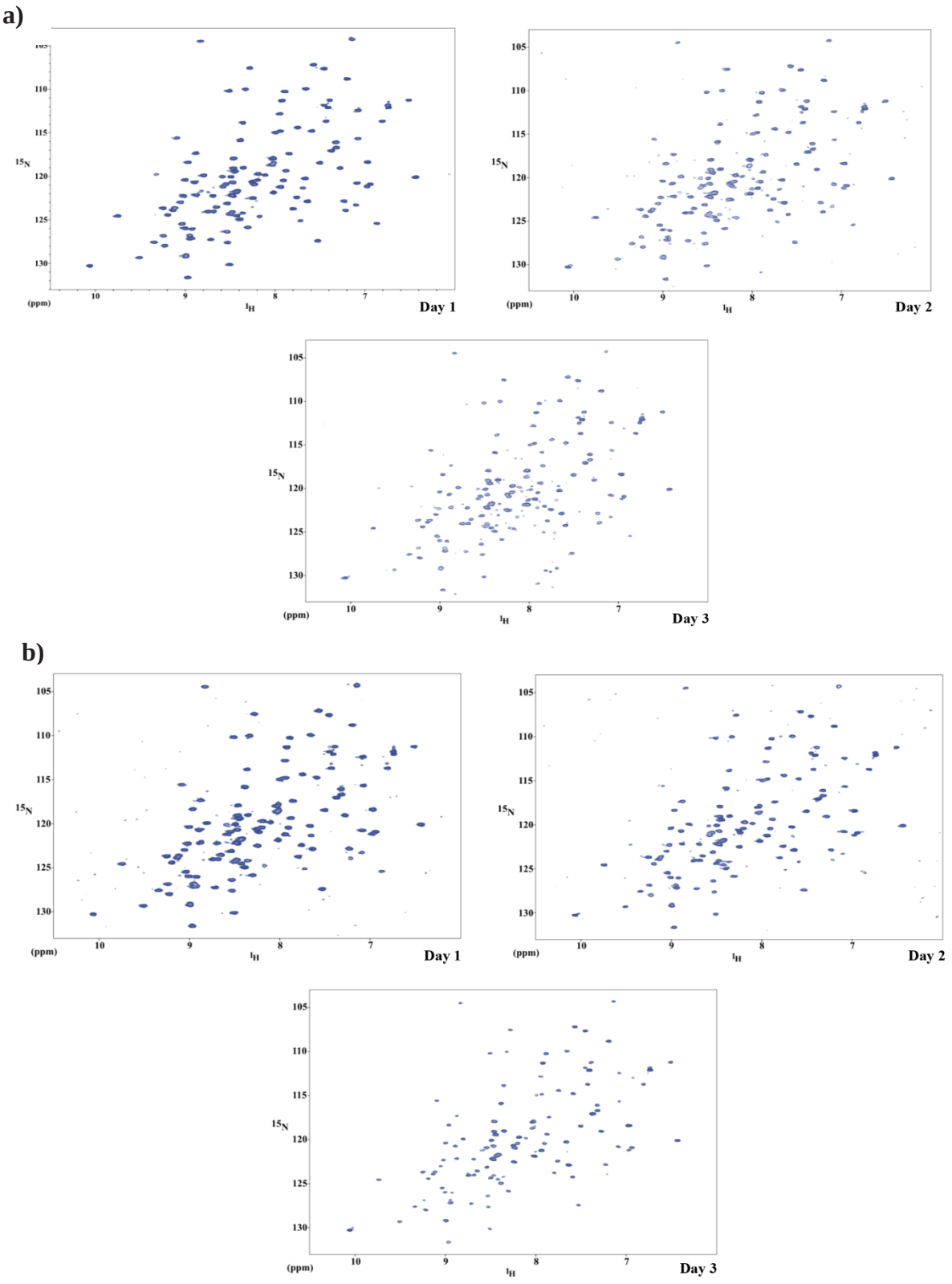

Figure 3.3.24: ^{15}N-^{1}H HSQC spectrum of the protein *Mt*$\varepsilon_{1\text{-}120}$ in a) 50 mM Tris, pH 7.2, 200 mM NaCl, 10% glycerol and b) 50 mM Tris, pH 7.5, 200 mM NaCl, 10% glycerol. The experiments were recorded in a 600 MHz spectrometer at 298 K, over 3 days. Comparison of the spectra shows considerable drop in intensity of peaks.

3.3.14 Thermofluor Stability Assay (TSA), buffer optimization for *Mt*$\varepsilon_{1\text{-}120}$ F_1F_O ATP synthase

A prerequisite for successful structure determination is to obtain good diffraction quality crystals or good quality NMR samples. This in turn requires the protein sample of interest to be soluble, homogenous and stable in the conditions required for the study. It is therefore obvious that improving these conditions will increase the success rate for the crystallization or NMR study of the protein of interest, which in this case is the $\varepsilon_{1\text{-}120}$. TSA was adopted in the direction to optimise the stability of this protein in the most appropriate buffer. TSA basically measures the change in fluorescence intensity of the protein on interacting with the dye (flurophore) which occurs with the protein melting with increasing temperature. This observation is based on the fact that a hydrophobic flurophore can bind to a protein when it moves from the folded to unfolded form due to increase in temperature. Ideally at low temperatures, the protein is properly folded and unable to interact with the thermofluor dye as no hydrophobic patches are exposed. This process of the protein melting with increasing temperature is recorded as a curve, wherein the RFU (Relative Fluorescence unit) is plotted against the temperature.

The Tm, melting temperature is deciphered from the same, by determining the inflection point of the curve. Inflection point is defined as the value of the second differential where the sign changes from positive to negative or vice versa. Buffer or solute conditions and components which cause the Tm to increase are believed to stabilise the protein better and further this stable protein will allow for better crystallization.

Figure 3.3.25 shows the graphs plotted for ε_{120} in different buffer conditions. Conditions with buffers pH 5.5 and pH 9.5 are shown to highlight the shift in the Tm values observed for a low and high pH range. Tm for buffer with cryoprotectant and salt has moved for 37°C to 44°C for pH 5.5 MES and pH 9.5 Glycine respectively. Also pH 6.5 K phosphate showed a tm value of 39°C and 8.5 Tris showed Tm of 41°C and these were the conditions used for NMR and crystallization respectively. Each curve in the following plot for the TSA study represents 4 different conditions, which are colour coded in the figure 3.2.27.

Condition 1: Buffer -B

Condition 2: Buffer -B+ Salt -S (150 mM NaCl)

Condition 3: Buffer -B+ Cryoprotectant -C (5 % glycerol)

Condition 4: Buffer-B+ Cryoprotectant -C (5 % glycerol)+ Salt-S (150 mM NaCl)

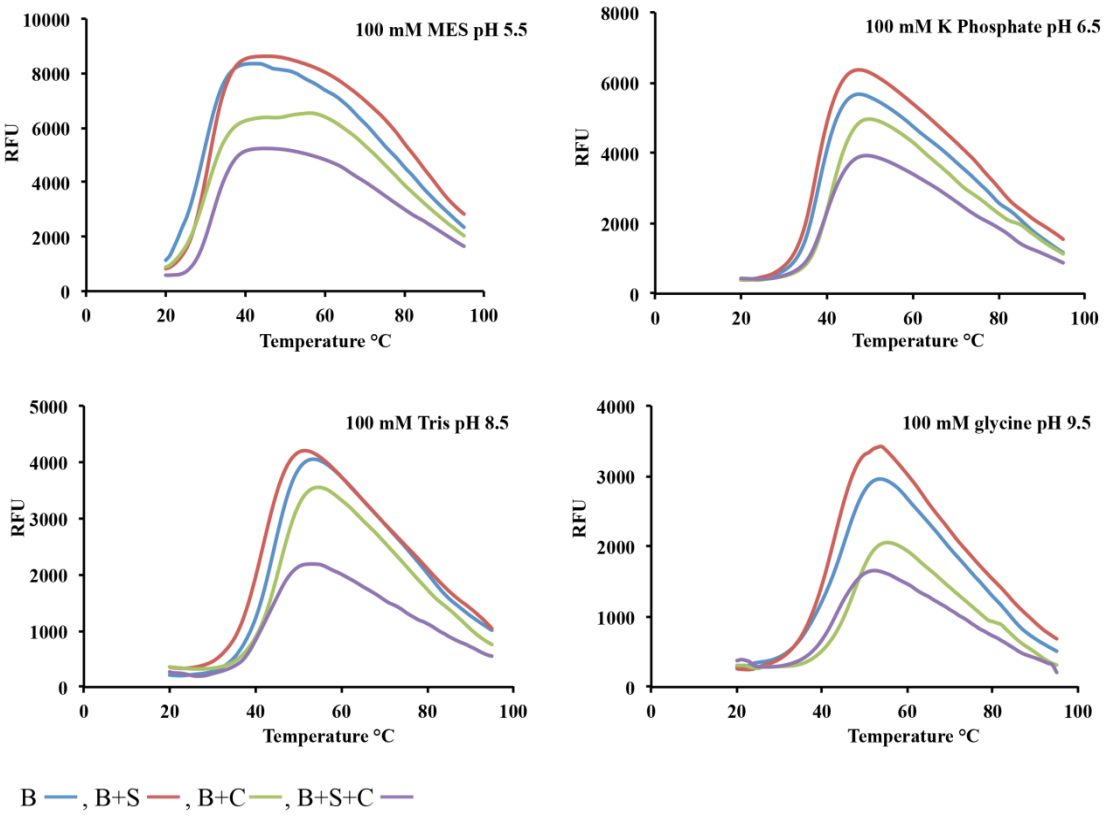

Figure 3.3.25: Plots to show the Thermofluor Stability assay shifts for ε_{120} in different Buffers

The condition with 100 mM Glycine pH 9.5 with 150 mM NaCl and 5% glycerol showed a Tm of 43°C which is higher than the conditions for 100 mM K Phosphate and 100 mM Tris which were conditions used for NMR and crystallization respectively. Hence it was decided these studies should be performed in this buffer condition which seemed to stabilise the protein better.

With respect to crystallization, crystal drops were set up with Wizard I and Crystal Screen I kits with similar conditions as described in previous crystallization attempts. Crystallization drops were examined over a period of time. Few conditions resulted in the formation of microcrystalline precipitate but unfortunately none of the conditions turned out to be promising for the generation of single crystals.

2D ^{15}N-HSQC was acquired in the same manner as previously described, anticipating a well dispersed spectrum. However the total number of peaks observed was lesser than that seen in the buffer of 50 mM phosphate pH 6.8, 200 mM NaCl, 10% glycerol, as only a total of 87 peaks were observable (Figure 3.3.26).

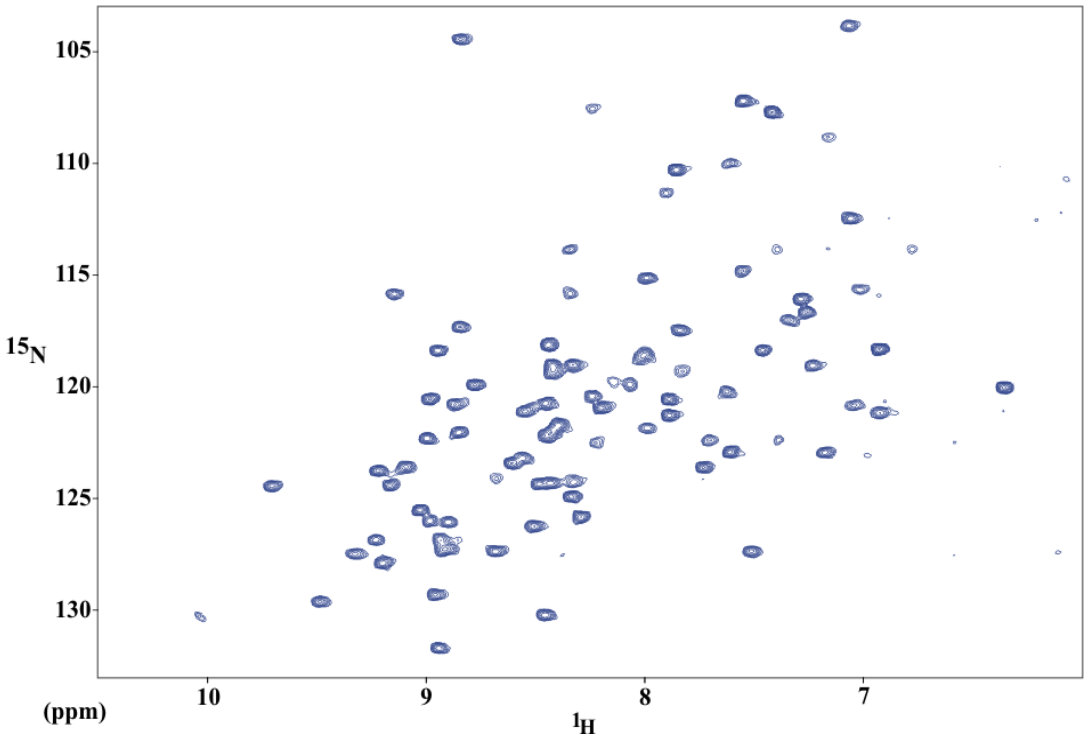

Figure 3.3.26: ^{15}N-^{1}H HSQC spectrum of the protein *Mt*ε$_{1\text{-}120}$ in 100 mM Glycine, pH 9.5, 150 mM NaCl, 5% glycerol.

3.3.15 NMR using Non Uniform Sampling for *Mt*ε$_{1\text{-}120}$ F_1F_O ATP synthase

Given the NMR 3D data sets that were acquired using Non uniform Sampling (NUS) as described in section 2.2.28, so far the backbone assignment for 53 amino acids has been possible (Figure 3.3.27) for *Mt*ε$_{1\text{-}120}$ expressed in BL21 GroEl-ES strain. The same protein when expressed in BL21 DE3 strain precipitated with the same buffer condition of 50 mM phosphate, pH 6.8, 200 mM NaCl, 10% glycerol, 5 mM EDTA. Extensive efforts were being made to acquire 3D data sets for HNCACB and HNCACO using NUS-NMR, which would help further assignments to be completed. However these experiments proved to be difficult given the poor quality of signals that were obtained.

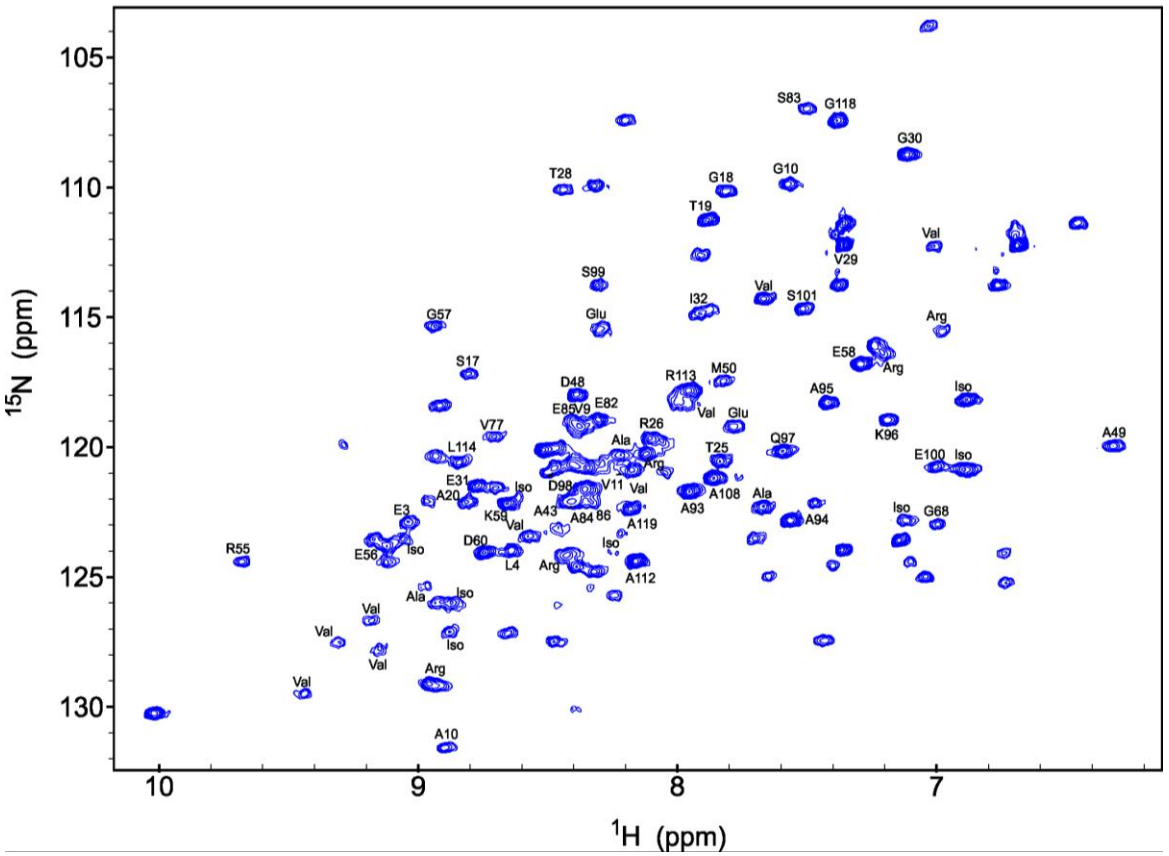

Figure 3.3.27: ^{15}N-^{1}H HSQC spectrum of the protein *Mt*ε$_{1\text{-}120}$ in 50 mM phosphate, pH 6.8, 200 mM NaCl, 10% glycerol recorded in a 700 MHz spectrometer at 298 K.

3.3.16 ^{15}N Single amino acid labelling of *Mt*ε$_{1\text{-}120}$ F_1F_O ATP synthase

To tackle this challenging protein, a novel technique was adopted to simplify the spectrum by selectively labelling certain amino acids. In this technique, free ^{15}N labelled amino acids were added to the minimal growth media prior to protein induction. ^{15}N labelled alanine, valine and isoleucine were used in separate growth cultures to obtain *Mt*ε$_{1\text{-}120}$ singly labelled protein. Traditional ^{15}N-^{1}H HSQC spectrum was recorded as described previously and the spectra are as illustrated in figure 3.3.28. In the figure, uniformly labelled ^{15}N-^{1}H HSQC is depicted to show the full spectrum and selectively labelled spectrum of valine (green), alanine (red) and isoleucine (orange) are shown. To complete the puzzle of identifying the specific residues, similar selective labelling will be performed for aspartic acid, glutamate and will also be performed to obtain a larger array of data that can be used in conjunction with 3D NMR data available on hand to assign more peaks.

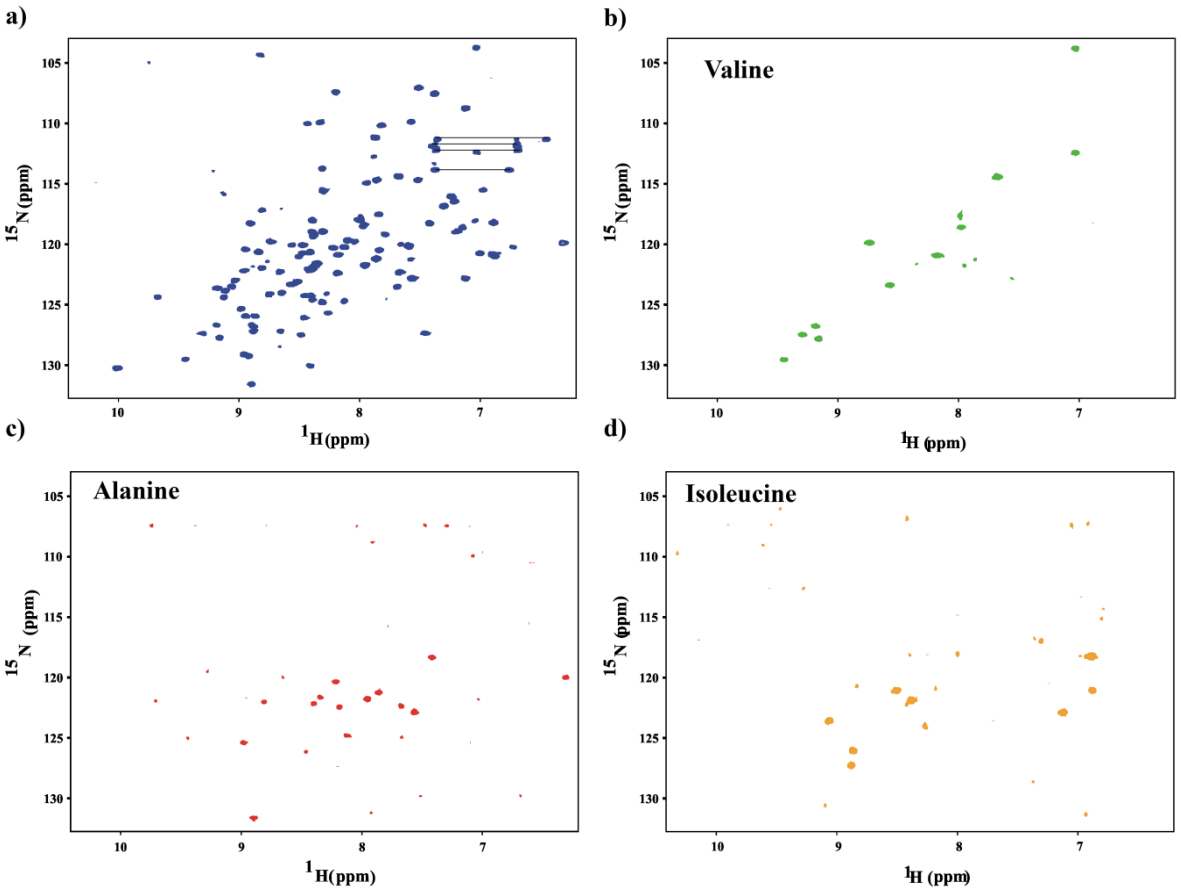

Figure 3.3.28: a) ^{15}N-^{1}H HSQC spectrum of uniformly ^{15}N isotope labeled *Mt*ε$_{\mathbf{1-120}}$ in 50 mM Tris-HCl, pH 7.5, 200 mM NaCl, 10% glycerol recorded in a 700 MHz spectrometer at 298 K. Single amino acid ^{15}N isotope labeled *Mt*ε$_{1-120}$ b) Valine, c) Alanine d) Isoleucine.

4. Discussion

4.1 Importance of the conserved asparagine residues in the phosphate-binding loop of the nucleotide binding subunit B of A_1A_O ATP synthases

Subunit B of *Methanosarcina mazei* Gö1 A-ATP synthase shows high topographic identity with its F-ATP counterpart, i.e., the subunit α [52]. However, the Glycine rich sequence $_{169}$GDRQTGKT$_{176}$ rendered as the Walker A motif conserved in both α and β subunits of F-ATP synthase is replaced with $_{150}$SASGLPHN$_{157}$ in the subunit B of A-ATP synthase. Interestingly, in F-ATP synthase, K175 and T176 are the only residues that interact with the nucleotide through their side chains and they are replaced by H156 and N157 in A-ATP synthase [100]. These residues (HN/KT) in both V-ATPases and F-ATP synthases, respectively are key residues with respect to catalysis as substitution experiments by mutagenesis show a significant suppression of hydrolytic activity accompanied by loss of proton translocation [185, 209].

A similar important role could be played by H156 and N157 and hence to probe further, H156A, N157A and N157T mutants were generated and the nucleotide binding traits were studied. Mutating H156 and N157 in the subunit B of *M. mazei* Gö1 A-ATP synthase to alanine showed better binding to the nucleotide analogue (ATP) in comparison to WT-B [192]. N157 was additionally mutated to threonine as described in section 3.1.1 and showed similar ATP binding to that of the WT-B (Table 4.1.1). The ability of the H156A and N157A mutants to bind the nucleotide (ATP) better is mainly acknowledged to the widening of the nucleotide binding region allowing for better access and binding of the nucleotide. This is a result of the replacement of the residues asparagine and histidine with bulky side chains by that of alanine.

Table 4.1.1: Binding of Mg-ATP ATTO-647N and Mg-ADP ATTO-647N to subunit B-WT and mutants H156A, N157A, N157T [192].

Protein	Mg-ATP ATTO-647N K_D [µM]	Mg-ADP ATTO-647N K_D [µM]
WT	27.4 ± 2.6	47.7 ± 2.6
H156A	13.0 ± 2.8	20.2 ± 2.8
N157A	13.7 ± 2.9	17.8 ± 2.8
N157T	27.4 ± 2.3	20.3 ± 2.3

Additionally, the hydrogen bonding interactions in the P-loop region might also play a crucial role. In the H156A and N157A mutant structures it can be noted that the absence of side

chain abolishes the hydrogen bonding interaction of side chain in the A156 and A157 and the binding region becomes wider. Additional interactions in H156A stabilize the P-loop at a proper position, enabling the stronger binding of the nucleotide. Earlier studies in subunit B of the V-ATPases have demonstrated a 30% quench in the ATP hydrolytic activity on mutation of H180 residue of the P-loop to Glycine and Cysteine. However, the activity was further suppressed to 50% with lysine substitution, given the larger side chain [185, 221].

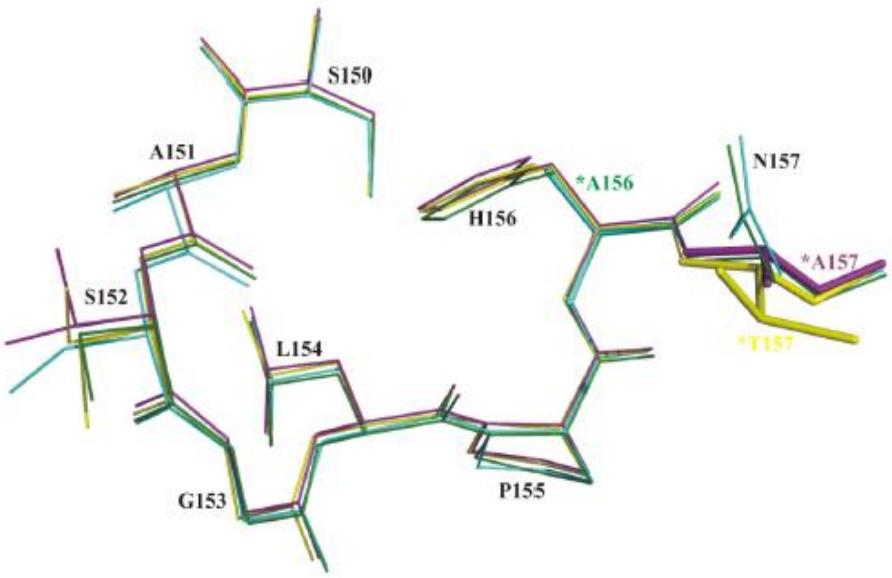

Figure 4.1: Overlap of the P-loop for WT-B (blue) and mutants H156A (green), N157A (purple) and N157T (yellow).

Such additional interactions are not observed in the N157A mutant and in spite of the presence of the bulkier H156 residue, it is weakly positioned in the binding region, because of the absence of main chain-side chain interaction of L154 and H156.

These contributions make the P-loop more flexible and hence would allow the widening of the binding pocket to accommodate the incoming nucleotide. Similar conformational change has also been observed for the V-ATPase, wherein the H180 of the P-loop orients its imidazole ring away from the binding pocket and hence resulting in the loss of interaction [221].

However, in the N157T mutant of the *M. mazei* Gö1 A-ATP synthase subunit B the side chain of T157 is oriented such as to abolish the hydrogen bond with T247, and the H156 is being held weakly, because of the absence of main chain-side chain interaction of L154 and H156 (Figure 4.2). Surprisingly the P-loop is stabilized by the additional interactions (between A151 and L154, A156 and I159 and S152 and R330) similar to the H156A mutant, which restricts the imidazole ring movement of H156, giving it similar binding affinity as that of the WT-B for Mg-ATP [192].

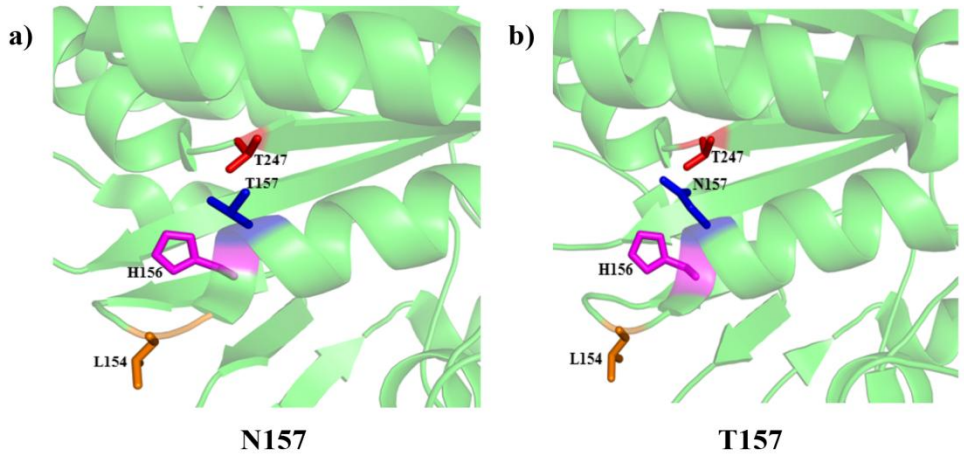

Figure 4.2: Cartoon representation of the P-loop highlighting the site of mutation and orientation of other important residues in the vicinity. (a) WT protein and (b) N157T mutant of subunit B A-ATP synthase.

The P-loop of subunit B of the A-ATP synthase has the ability to differentiate between nucleotides Mg-ATP and Mg-ADP [176]. The FCS experiments performed with these mutants proved the significance of the histidine and asparagine residues, as their ability to bind the nucleotides differently was lost. Former studies describe the K_D values of Mg-ATP ATTO-647N and Mg-ADP ATTO-647N to WT-B to be 22.0 ± 3.0 μM and 50.0 ± 3.0 μM, respectively [176]. The binding of the three mutants H156A, N157A and N157T to the ATP- and ADP analogous are similar, indicating that both P-loop residues are essential for ATP/ADP sensitivity. The ability to differentiate ATP/ADP binding capability seems to be unique only to subunit B of the A-ATP synthases and not seen in the subunit α of F-ATP synthase [179]. With the previously described specific inhibitory effect of subunit B, this feature adds on to qualify the nucleotide binding subunit B as a regulatory subunit [176, 210].

The mechanism of regulation and differential binding of nucleotides to subunit B can be explained with recent outcomes. Supportive evidence is offered from research work in F_1 ATPase, where it was shown that during ATP hydrolysis, Pi is released first followed by the release of ADP [222]. This sequential release of Pi and ADP is further supported in the mechanism proposed for the ADP inhibition of F_1. Mechanistically, Pi is released first from the catalytic site before ADP release during turnover, with the ADP stochastically and tightly entrapped in the catalytic site [114]. This understanding also leads to the hypothesis that binding of Pi to the catalytic site is required to facilitate the subsequent binding of ADP, thus favouring the enzyme to function in the synthesis mode. Comparatively in homologous A-ATP synthase, crystallographic structure shows vanadate (the phosphate analogue) binding to catalytic subunit

A. Binding of Vanadate first facilitates a conformational change in the nucleotide binding loop to allow preferential binding of ADP [166].

In the catalytic step of ATP synthesis, residues L347 and R349 of subunit B have been proposed to be involved in stabilisation of the penta-coordinated transition state catalytic step [176]. These subunit B residues play a supportive role in the catalytic events occurring in subunit A. Also the rendered sensitivity to the ATP/ADP binding at the A-B interface may thus play a role in the regulation of the catalytic process.

Given high ATP concentrations in the cell, ATP binding could be preferred by subunit B and given that the catalytic site has evolved with a strong Pi-holding site would work synergistically to cater to the demand for efficient ATP synthesis. Thus allowing archaea to deal with and adapt to their harsh environments and driving the motor enzyme to function primarily as A-ATP synthase.

4.2 Importance of P-loop residue K175 of *Mtα* F-ATP synthase in nucleotide binding

Of the six nucleotide binding sites of F_1, three of them can rapidly exchange the nucleotide with the medium, while the other three exchange at a slower rate and are referred to as the non-catalytic sites [223]. These sites are mainly located in the subunit α in F_1F_O ATP synthase and as mentioned earlier in the subunit B of the A_1A_OATP synthase.

These sites are perfectly capable of binding nucleotides, although nucleotide binding to these sites is not a prerequisite for ATP synthesis. As seen for the mitochondrial F_1, all the three non-catalytic sites can be occupied with ATP. The crystal structure shows AMP-PNP bound at all three α subunits [100]. Chloroplast F_1 also shows that ATP can occupy all three sites, while ADP is present only at 2 sites. The nucleotide occupancy was altered in chloroplasts with the coupling of F_1 to F_O. Mg^{2+} ions influence the nucleotide binding to the non-catalytic sites.

Mg-ADP inhibition is one of the inhibitory mechanisms occurring in the enzyme, wherein the Mg-ADP generated during hydrolysis is trapped at the catalytic sites leading to inactivation. The enzyme can be relieved of this reversible inhibition at the catalytic site by binding of ATP at its non-catalytic sites. Studies for a mutant lacking non-catalytic nucleotide binding site residues in *Bacillus* PS3 of $\alpha_3\beta_3\gamma$ sub complex provides strong evidence for this proposed role of the non-catalytic sites. A quadruple mutant K175A, T176A, D261A and D262A in the subunit α completely lacking the ability to bind ATP and ADP was shown to be incapable of releasing the entrapped inhibitory Mg-ADP from the catalytic sites. This led to all the enzyme molecules to fall into a Mg-ADP inhibited form rapidly during catalysis. The activity observed for the mutant

was similar to WT initially, but decayed rapidly to an inactivated form which could not be reversed even with the addition of ATP. This study clearly indicated that binding of nucleotide to non-catalytic site was essential for continuous hydrolysis in F_1-ATPase [224].

Subunit α is structurally attributed with a certain rigidity. This is clearly seen when comparing the subunit α from MF_1 with AMP-PNP bound at all three sites with that of the α3β3γ of thermophilic F_1-ATPase with empty sites. The structure of subunit α is very similar in both cases indicating no change caused by the nucleotide binding to the closed form. Contrastingly, the subunit β, carrying the catalytic site changes from open to closed form on nucleotide binding.

The subunit homologous to the B-subunit of A-ATP synthase is the subunit α in the F-ATP synthase. From the structures of subunit α that are currently available for *E. coli*, *Bacillus* PS3 and the Bovine mitochondria, it is possible to understand the overall structural features and similarities. Similar to the catalytic subunit β, this is also bestowed with the N-terminal β-sheet region, a central α-β domain containing the nucleotide binding phosphate loop and the C-terminus with the α-helices. Figure 4.3 shows the superimposition of the available 3D crystal structures for subunit α from *E. coli*, *Bacillus* PS3 and the Bovine mitochondria with the 3D model generated for the subunit α from *Mt*. Although the central domain is largely conserved, an interesting aspect in the model structure for *Mt*α lies in its very C-terminal tail. This stretch which is loaded with charged residues such as K, E and D is fairly highly conserved across the species in the *Mycobacterium* genus.

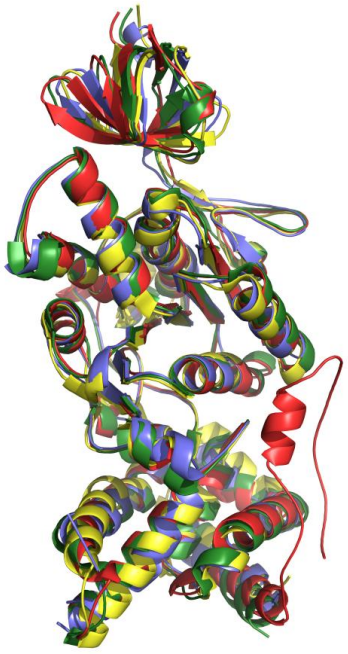

Figure 4.3: Superposition of structures for subunit α from *E. coli* (yellow), *Bacillus* PS3 (blue), bovine mitochondria (green) with the model generated for subunit *Mt*α (red) (PDB: 3OAA, 1SKY, 1H8E) [18, 101, 107].

Figure 1.8 shows the sequence alignment for different species for which the structures for these subunit α F-ATP synthase is available with those for *Mycobacterium* species. The sequence from *E. faecalis* has been included to consider another pathogen. From the comparison of both the sequence and structure, it is evident that this tail with charged residues is unique to the *Mycobacterium* genus and provides an interesting aspect for introspection.

Careful inspection of the sequence of the P-loop of subunit α revealed that, the Glycine rich sequence $_{169}$GDRQTGKT$_{176}$ is highly conserved across these diverse species except for the Q172, which is replaced by the K175 residue in the *Mycobacterium* genus (Figure 4.4).

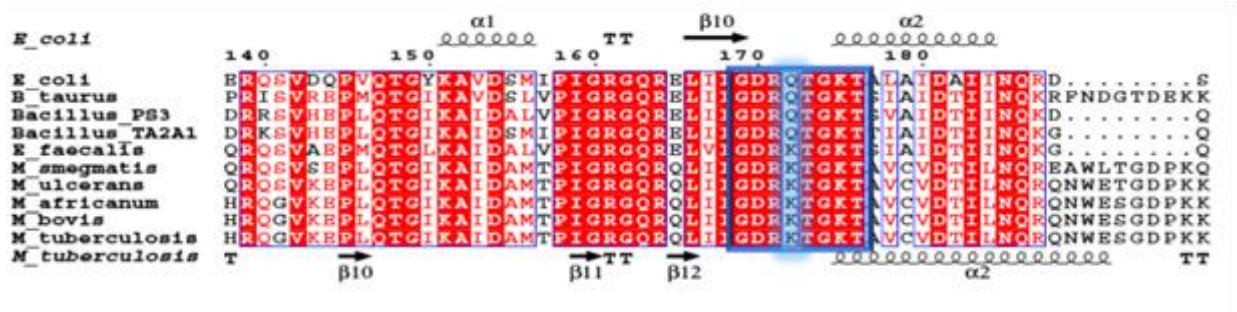

Figure 4.4: Sequence alignment of P-loop of subunit α F-ATP synthase from *E. coli*, *Bacillus* PS3, *Bacillus* TA2A1, Bovine mitochondria, *E. faecalis* with different species of *Mycobacterium* genus. The P-loop is highlighted in a box and conserved lysine residue of mycobacterial species is highlighted in blue.[118]

The Glutamine residue Q172, in subunit α has been described to be essential for nucleotide binding along with the βQ170 as these are the contact residues for stabilization at the α-β interface. This has been shown to be highly cardinal for cross talk between the two subunits [223]. Figure 4.5 shows the superimposition of the P-loop of subunit α from *Bacillus* TA2A1 (PDB ID: 2QE7) on the available nucleotide bound crystal structure of subunit α from *E. coli* (PDB ID: 3OAA). R.m.s.d of 0.874 was measured on the superimposition of the subunit α of *Ec* and *Bacillus* TA2A1. The nucleotide, AMP-PNP is an ATP analogue and is seen bound to the P-loop in the subunit α structure from *E. coli* (PDB ID: 3OAA). From this overlap, the residue Q172 is seen in two different rotamer states for *Ec* and *Bacillus* TA2A1, wherein the Q172 of *Bacillus* TA2A1 is in closer proximity to the nucleotide, measuring a distance of 3.1 Å when compared to that of 4.3 Å between Lysine 175 and the γ-phosphate of the nucleotide. Given that phylogenetically *Bacillus* TA2A1 is closely related to *Mt*, this was used as the comparison template. Replacement of Q172 by K175 in mycobacterial α could indicate that the lysine with its lengthier side chain can cause changes to the nucleotide binding cavity and/or be in closer proximity to the incoming nucleotide and hence affecting the binding.

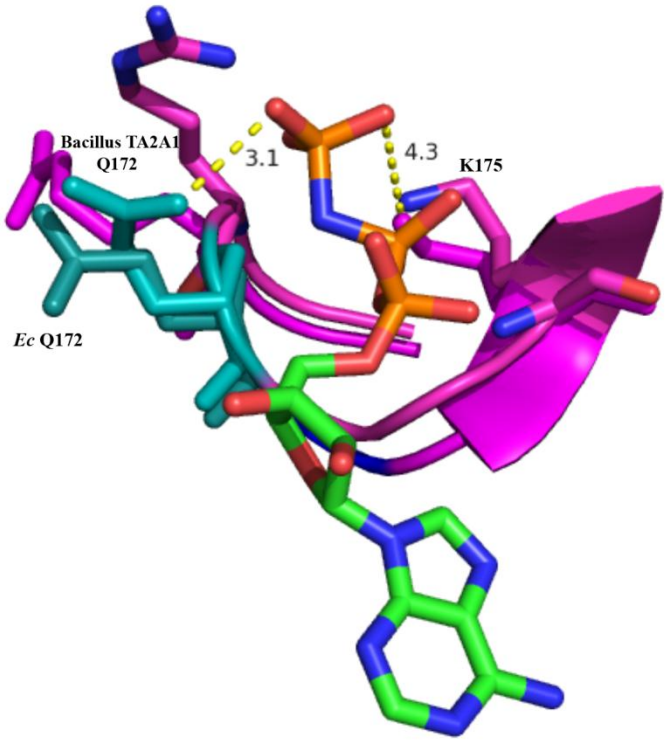

Figure 4.5: Superposition of P-loop structures for subunit α from *E. coli* (PDB: 3OAA) and *Bacillus* TA2A1 (PDB: 2QE7). The bound nucleotide (AMP-PNP) in the structure of *Ec* is shown in stick representation (PDB: 3OAA) [18, 213].

This glutamine being replaced by a lysine in the three dimensional mycobacterial α could possibly increase the stabilisation of nucleotide binding by formation of additional salt bridges. However, the FCS data acquired for ATP binding to *Mt*α show weaker binding of 35 μM when compared to that of *Ec*α at 1.6 μM (section) [179]. The reduced affinity for the nucleotide could be attributed to disruption of the nucleotide binding cavity resulting from steric clashes occurring due to two lysine residues present in close proximity. This line of thought can be verified only on obtaining the high resolution structural information of *Mt*α. But this is of high importance as binding of the nucleotide is influential for the cooperativity in the entire F_1F_O enzyme [223]. Also this could lead to strong Mg-ADP inhibition in the F_1 complex of *Mt*, as ATP binding to the noncatalytic sites is essential to relieve this form of inhibition. This could be another unique modification of the bacterium to allow the enzyme to control wasteful hydrolysis.

Although the subunit α is capable of binding the nucleotide and participates in catalysis by contributing to the interface for nucleotide binding. Unlike the homologous subunit B of the A-ATP synthases, this falls short in its ability to recognise the nucleotides differently. This inference is made from the fact that the binding constants obtained through FCS for *Ec*α are similar for ATP and ADP with 1.6 μM for ATP and 2.9 μM for ADP in *E. coli* [179].

4.3 Novel Insights into the C-terminal extension of *Mt*α

The unique stretch of 37 residues contributing to the extra 3.5 kDa of the C-terminus of *Mt*α offers an interesting platform to understand its structural and functional significance. To explore the role of this C-terminus, two constructs were designed. One which is the WT (*Mt*α) and the other which is the truncated (*Mt*$\alpha_{1\text{-}513}$), lacking the C-terminal tail. Efforts are focused to leverage all possible information on structural features and interaction studies. SAXS analyses of *Mt*α has provided information on the overall structure with the dimensions for the Rg and D_{max} indicating, a length of 110.3±10Å. *Ec*α measures a D_{max} of 96.6 ±10 Å (section 3.2.4). The extra length for *Mt*α is justified given that the C-terminus is larger by 37 residues.

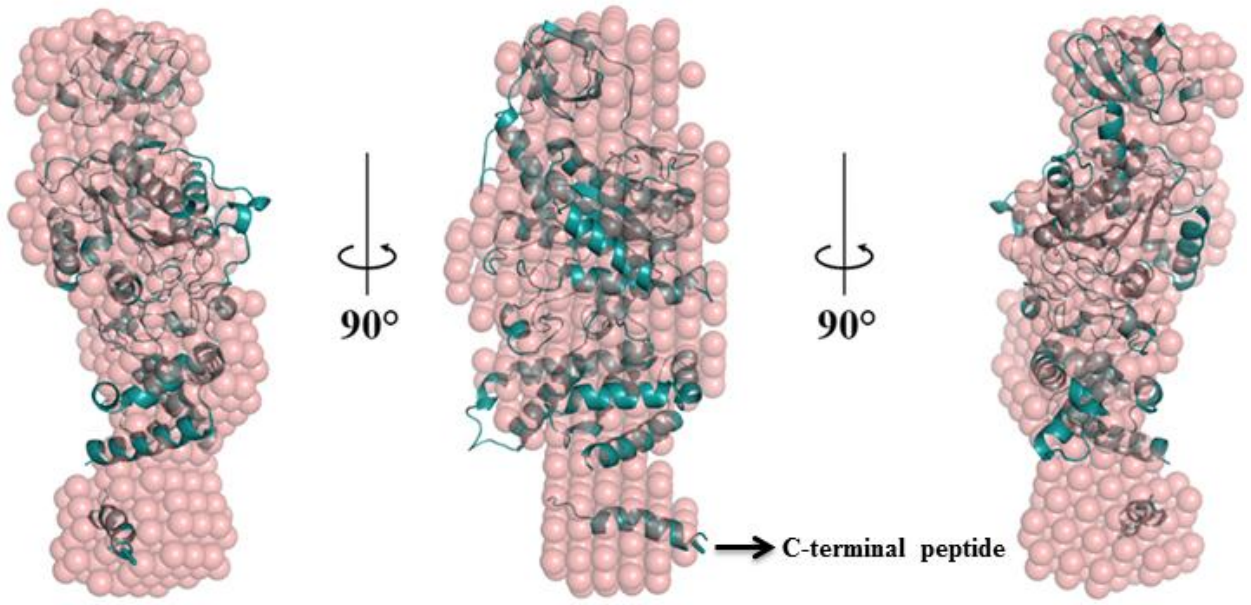

Figure 4.6: SAXS structure of the *Mt*α with fitting of model obtained from I-TASSER and C-terminal peptide structure obtained from NMR.

Fitting of the secondary structure into the SAXS data shows that residues 30 to 514 are accommodated well and does not include the very N-terminal region which is mostly random coiled and could be highly flexible. To explore the features of the C-terminus of *Mt*α, the peptide containing residues 521 to 540 was synthesised and the structure was elucidated using NMR by Dr. Priya Raghunathan from our lab (unpublished data). The secondary structure for this peptide has been fitted in the solution structure as shown in figure 4.6 and the orientation represented indicated towards possible interactions between the C-terminus of the subunit α with the C-terminus of the subunit ε.

This interaction is believed to be important as there could be a combinatorial effect of the longer C-terminus of subunit α with the shorter C-terminus of subunit ε leading to the strong inhibitory effect of hydrolysis seen in mycobacterial F-ATP synthases [140].

To understand the role of this C-terminus in ATP hydrolysis and synthesis, the WT and the Δα514-549 mutant of F-ATP synthase from *M. smegmatis* in inverted membrane vesicles were generated by Dr. Goran Biuković. Interestingly, the C-terminus deficient Δα514-549 mutant showed increased hydrolytic activity by 43%, while the ATP synthesis dropped by 31% when compared to that of the WT (unpublished data). These data are indicative of the important role of the C-terminus of subunit α in reducing the detectable levels of ATP hydrolysis seen in mycobacteria. This is in agreement to the energy requirements of the mycobacterial species that are functionally directed towards being ATP synthesizers rather than consumers.

To extend the study of the C-terminus of the *Mt*α, a chimeric protein (α^{chi}) of subunit α from *Bacillus* PS3 and *Mt* was generated. To serve as a control, the native protein of PS3α was used for determining the solution structure using SAXS. As described in section 3.2.4, the D_{max} for α^{chi} compares well with that of *Mt*α. The nucleotide affinity for both PS3α and α^{chi} showed comparable values indicating that the nucleotide binding was not affected given the addition of the 35 amino acids to the C-terminus.

To understand the role of the C-terminus of *Mt*α in terms of the activity of the enzyme, a unique complex of $\alpha_3\beta_3\gamma$ comprising the chimeric α was engineered to obtain $\alpha^{chi}{}_3\beta_3\gamma$ complex. PS3$\alpha_3\beta_3\gamma$ is the most widely studied F_1 enzyme unit structurally and mechanistically [213, 225-228]. This phylogenetically closely related system of *Mt* was chosen to serve as a control. The effect of the C-terminus of *Mt*α was studied in the complex of PS3$\alpha_3\beta_3\gamma$ to understand its role in catalytic activity. It was shown with ATP hydrolysis study for both $\alpha_3\beta_3\gamma$ and $\alpha^{chi}{}_3\beta_3\gamma$, that the C-terminus of the *Mt*α in $\alpha^{chi}{}_3\beta_3\gamma$ was responsible for suppression of the ATP hydrolysis. In comparison to the activity of PS3$\alpha_3\beta_3\gamma$, $\alpha^{chi}{}_3\beta_3\gamma$ showed a significant drop. This gives us insight into the important role played by this stretch of 35 amino acids that seems unique only to the Mycobacterial α F-ATP synthase.

To understand the interplay of the subunits in influencing catalytic activity, modelling studies have been employed based on the findings from the structural details available from *Ec*F_1 and MF_1 as detailed in the following section. Figure 4.7 shows the possible arrangement for the subunits α, β and ε in the *Ec*F_1 complex using available crystal structure. Subunit ε, the intrinsic inhibitor of the enzyme F_1F_O is shown to interact with the subunit β, blocking rotation in the direction of hydrolysis. Cross linking induced using water soluble carbodiimide has shown

interactions between residues E381 of subunit β and S108 of subunit ε in *E. coli* [229]. Cysteine mutation introduced at both these positions allowed for a disulphide bond to form confirming the close proximity of these two residues. The equivalent position to the E381 in subunit β is occupied by S411 in subunit α. The S108 residue in the subunit ε is also shown to form a disulphide bond to the S411in subunit α. With the double mutant αS411C, βE381C, high levels of α-β cross links were detected. This observation leads to the understanding that α and β may interact with each other. In support to these interactions subunit ε undergoes a simple relative movement [125] (Figure 4.7).

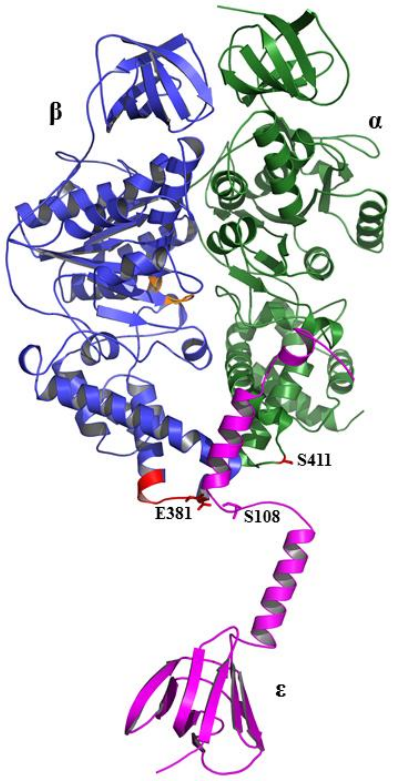

Figure 4.7: Structure for *Ec*F_1 showing only subunits α (green), β (blue) and ε (magenta) indicating the important residues in close proximity for interactions. In subunit β, the P-loop is highlighted in orange and the βDELSEED is highlighted in red (PDB accession code: 3OAA).

The C-terminus of subunit ε is believed to move in such a way that it interacts with the equivalent regions of either α or β subunit. Earlier studies suggest that these interactions of ε with α and β are nucleotide dependent. The linkage of ε through C108 to C381 of β subunit is predominantly with Mg^{2+}-ADP+Pi in the catalytic sites, whilst this is shifted to εC108 and αC411 in the presence of Mg^{2+}ATP (using Mg^{2+}AMP-PNP). This is in conjunction with studies performed previously on cryo electron microscope, which show a shift of the subunit ε by 20-25 Å between α and β subunits. For the α411C/ β381C/ε108C mutant, a high yield of cross linking of α to β subunits by $CuCl_2$ was observed, which requires the rotation of the C-terminal α helical

region of the α and/or β towards each other. As seen for the MF_1 structure, the arrangement for α_E is different in comparison to α_{DP} or $\alpha_{TP.}$ Also further for the modelling studies MF_1 is used as the template, given that the available crystal structure has been obtained with bound nucleotides [101].

The model for the three α^{chi} subunits, subunits γ and ε are shown in the figure 4.8 with the C-terminal domain of *Mt*α in α^{chi} highlighted. These have been generated by Dr. Malathy Sony based on the available SAXS data and peptide structure described previously.

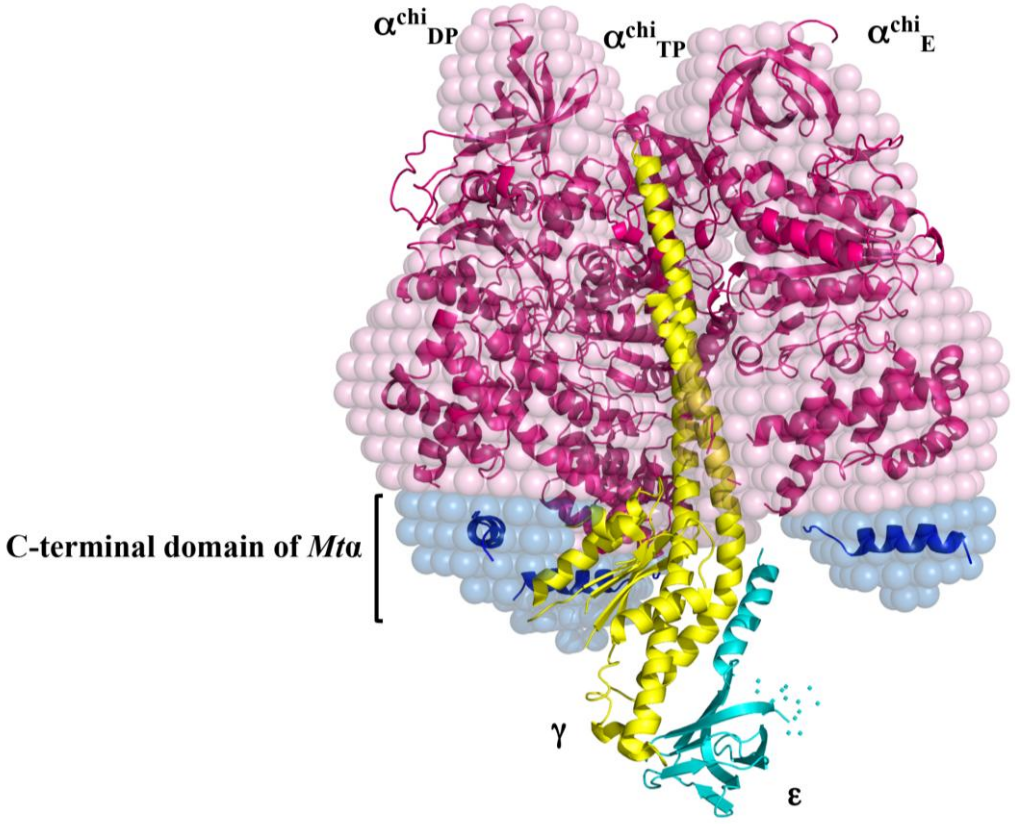

Figure 4.8: Assembled model for *Mt*F_1 showing only subunits α (red), γ (yellow) and ε (cyan). In subunit α, the C-terminal tail is highlighted in blue. For subunit ε, the extended C-terminus is represented using the peptide structure (cyan) available for residues 103-120 (PDB accession code: 2LXS). The template used is of bovine mitochondria (PDB accession code: 1H8E) [81, 101] .

Figure 4.9 (a) shows the specific site of interaction between the subunit α^{chi} and ε, wherein residues α^{chi}D518 and εA115 are in close proximity on a 160° rotation of the central stalk. With a 60° rotation of the central stalk, as seen in figure 4.9 (b), there are multiple sites of interaction in the DELSEED region of subunit α, between residues α^{chi}D401 and γK87, α^{chi}D401 and γK90 and C-terminal domain of $\alpha^{chi}{}_{DP}$ and γN95. These when considered cumulatively could act to interfere with the rotation process hence slow down the process.

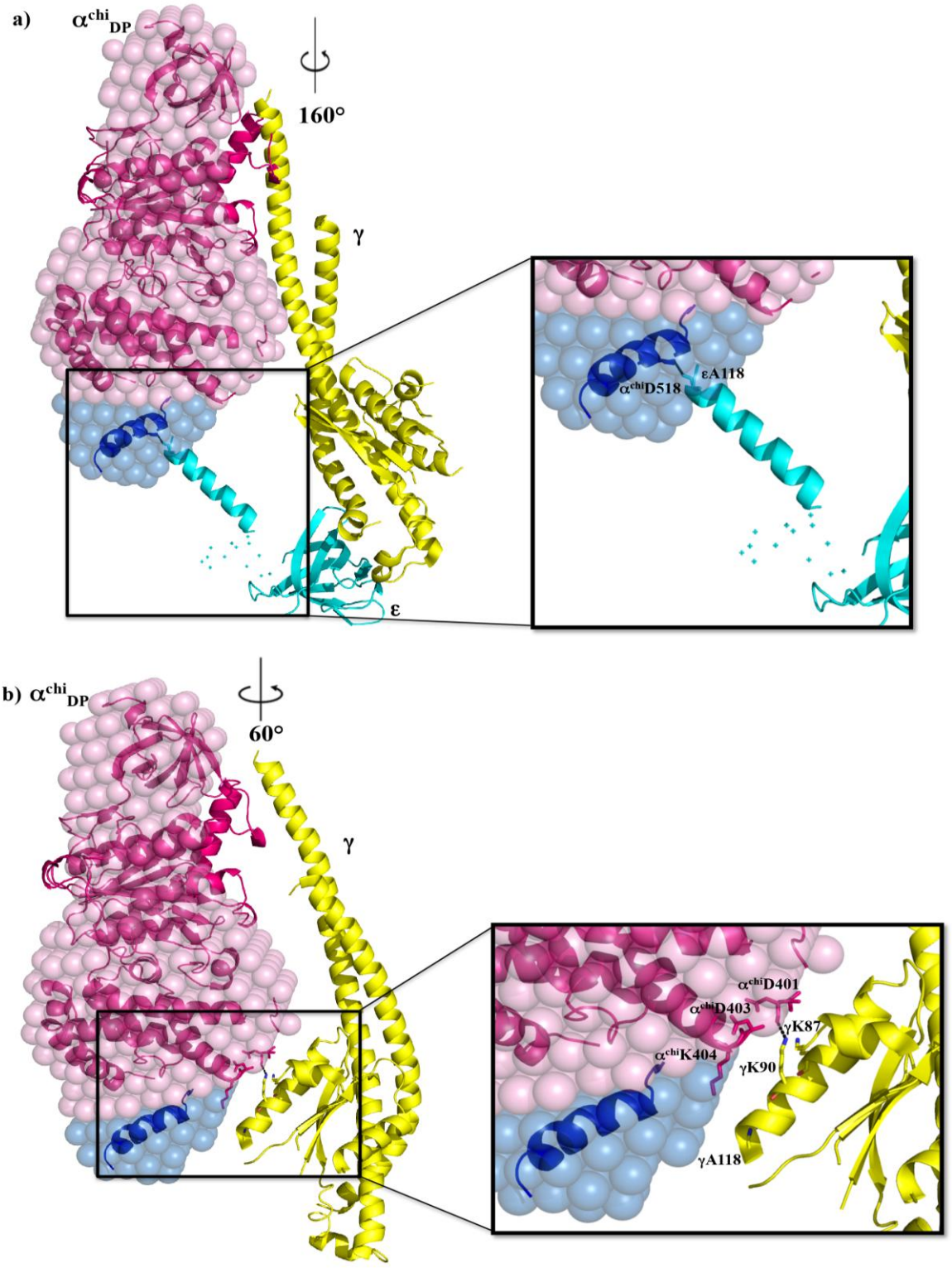

Figure 4.9: Specific interactions in the assembled model for *Mt*F_1 showing only subunits α (red), γ (yellow) and ε (cyan). a) The extended C-terminus of subunit ε represented as the peptide structure (cyan) is shown to interact with α^{chi} on 160° of the central stalk. b) Interaction of α^{chi}D401 and γK87 seen on 60° rotation of the central stalk (PDB accession codes: 2LXS and 1H8E) [87, 113].

Additional studies performed on the single molecule rotational analysis will provide deeper understanding of the behaviour of the motor enzyme and it will be of high importance to probe

into the duration of the binding dwells and catalytic dwell time and to see if the addition of approximately 3.5 kDa of protein in the $\alpha^{chi}{}_3\beta_3\gamma$ complex causes a drag in the rotational movement.

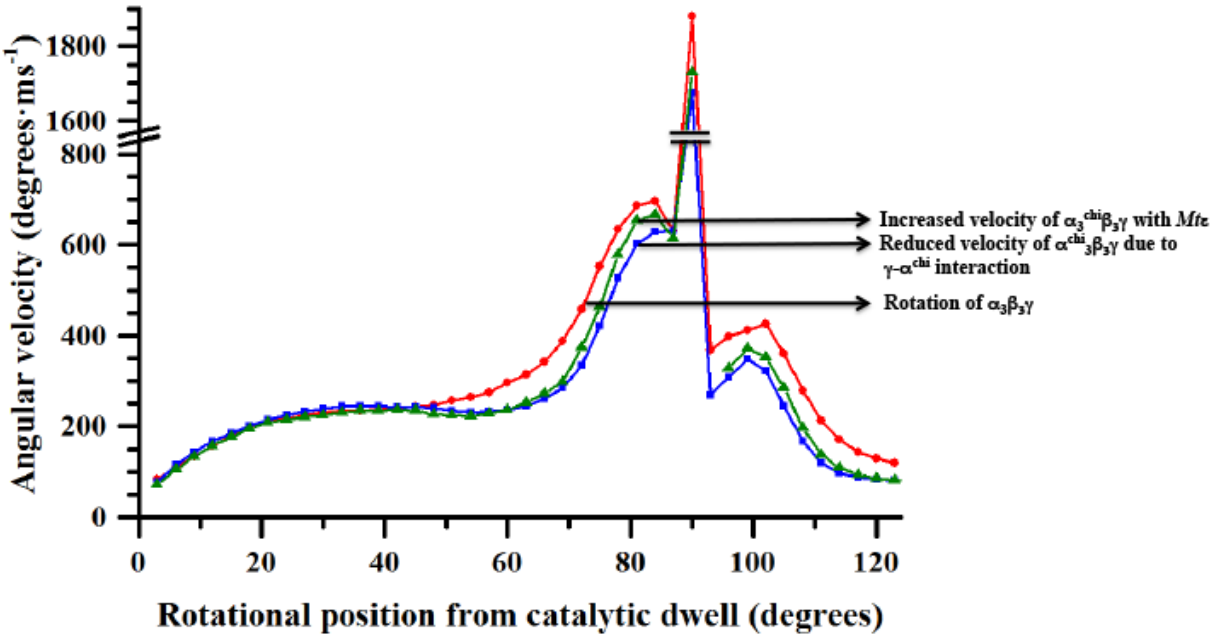

Figure 4.10: Angular velocity vs. rotational position plot between 2 catalytic dwells for $\alpha_3\beta_3\gamma$, $\alpha^{chi}{}_3\beta_3\gamma$ and $\alpha^{chi}{}_3\beta_3\gamma$+ *Mt*ε (Unpublished data).

Single molecule rotational studies were performed by Dr. Hendrik Sielaff at the laboratory of Dr. Wayne Frasch (Arizona State University) using gold nanorods of 40 x 76 nm dimension. As seen in figure 4.10, $\alpha^{chi}{}_3\beta_3\gamma$ shows reduced velocity with respect to the PS3$\alpha_3\beta_3\gamma$ as a result of the interaction between the α^{chi} and γ (unpublished data). On addition of *Mt*ε, $\alpha^{chi}{}_3\beta_3\gamma$ shows an increase in rotational angular velocity. This effect was not visualized with the experiments described in section 3.2.6, as the effect of the viscous drag of the 300 nm bead used was predominant. Figure 4.11 summarizes the mechanism proposed during ATP hydrolysis for $\alpha^{chi}{}_3\beta_3\gamma$. In both figures 4.10 and 4.11, the start position is indicated by the catalytic dwell and the ATP binding occurs during the ATP binding dwell. This is defined in the phase 1 that is indicated by a 50° rotation of the central γ subunit. Phase 2 is described by the rotation between 50°-120° during which catalysis occurs, leading to cleavage of ATP at the $\alpha^{chi}{}_{DP}$ and β_{DP}

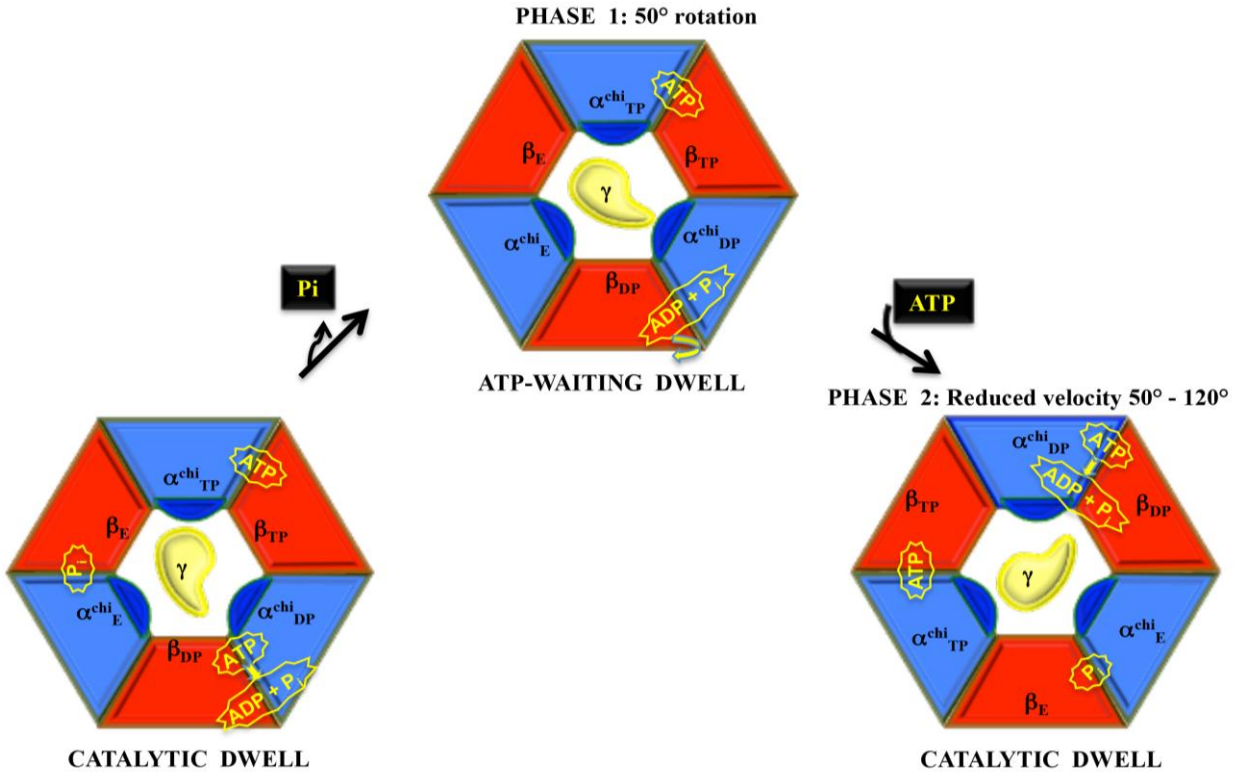

Figure 4.11: Schematic representation of the proposed ATP binding and catalysis events during the 120° rotation of subunit γ in $\alpha^{chi}{}_3\beta_3\gamma$ complex (Unpublished data).

interface. This phase is described as the power stroke and a reduction in rotational angular velocity has been visualised for the $\alpha^{chi}{}_3\beta_3\gamma$ in comparison to the $\alpha_3\beta_3\gamma$ complex. Also observed is the increase in angular velocity for the same phase on addition of *Mt*ε to $\alpha^{chi}{}_3\beta_3\gamma$, which could be a result of additional interaction between the native binding partners, *Mt*ε and *Mt*α.

4.4. Subunit ε of *Mycobacterium tuberculosis*

The ε-subunit is a coupling subunit and is rendered as an endogenous inhibitor in most F-ATP synthases. It is believed to undergo a drastic conformational change, with a non-inhibitory 'down' form and an inhibitory 'up' form (Figure 1.9) [18]. The C-terminal α-helix of the ε-subunit lies on the *c* ring (Fo domain) in the down-form, or it is lifted up to reach the bottom of an $(\alpha\beta)_3$ cylinder in the up-form. Electrostatic interactions between basic residues in the α-helix of the ϵ-subunit and acidic residues of the conserved 'DELSEED' region of the β-subunit seem to stabilize the association of the ε- and β-subunits, and the rotation is blocked, because the contact between the closed form of β and the γ axle is tight even without ε, leaving little space for the γε axle to get through. This blockage results in inhibition of ATPase activity. On the other

hand, anticlockwise rotation for ATP synthesis would be possible as β_{TP} will change to β_E leading to looser contact with the axle. The flexible property of the C-terminal helices will help it get through the relatively narrow space. Thus ATP-synthesis activity is maintained whereas ATP hydrolysis is blocked [1, 127].

Multiple sequence alignments of bacterial ε subunits show that particularly the second C-terminal α-helix displays high variability, both in length and in amino acid composition (Figure 1.10). This is consistent with the fact that some aerobic bacteria reveal stronger ε-inhibition on membranes than is observed in *E. coli* [230]. Since bacteria and especially pathogenic ones vary in their environmental and metabolic needs, the variation in the C-terminal sector may enable ε to adapt and fine tune its physiological role as an inhibitor to the differences in this bacterial ecology. In some bacteria the primary role of ATP synthase is not ATP synthesis, but maintenance of $\Delta\mu H^+$ at the expense of ATP hydrolysis, therefore a markedly different regulatory mechanism can be expected [9]. Like in the *Clostridium*, *Bacterioides* or *Bifidobacterium* genera, ε lacks the C-terminal α-helix. An interesting observation to be noted is that subunit epsilon is much shorter in anaerobic species of bacteria which predominantly function as ATP synthases such as *Cholorobium chlorochromati* (88 residues), *Bifidobacterium bifidum* (100 residues), *Bacteroides fragilis* (81 residues). As seen with the subunit ε of the *Mycobacterium* species, the predicted models reveal only one helix for the C-terminus, which could be due to the shortened length when compared to their *E. coli* or *Bacillus* counterparts. The extended length of the C-terminus allows them to form two helices with a loop and also helps them to switch between the extended and the retracted forms. The extended state of the ε subunit is seen in bacteria and chloroplasts [18]. Some bacteria like the thermophilic *Bacillus* PS3 possess an ATP binding motif, I(L)DXXRA in the C-terminus of subunit ε, which binds ATP and forms a folded conformation in solution as well as in the crystal [127]. However, there is no ATP binding seen in chloroplasts subunit ε [125].

Similarly subunit ε *of Mycobacterium tuberculosis* also does not bind ATP [81]. The C-terminus of ε in F-ATP synthases of slow- and fast-growing mycobacteria is responsible for blocking of ATP hydrolysis, preventing excess ATP consumption under low oxygen tensions [140]. These studies also demonstrated that suppression of hydrolytic activity appeared to be more pronounced in the slow-growing mycobacteria, reflecting an adaptation to environments with a low energy supply and/or decreased oxygen tension that is the conditions found in TB lesions in the lungs [141]. Mycobacteria require oxygen for growth; however they are capable to persist in a quiescent form under anaerobic conditions. Similar ATP hydrolysis inhibition

processes are reported for the obligate aerobic bacteria *Paracoccus denitrificans* and *Micrococcus luteus*, whose ATP synthases show variations in the inhibitory subunits, which are represented by the *Pd*ξ and the *Ml*δ subunit [136, 137, 231]. Based on the specificity of the C-terminal segment of *Mt*ε, and the variability of the C-termini of bacterial ε as well as the diversity of inhibitory proteins in F-ATP synthases described above, the C-terminal domain of *Mt*ε becomes a promising epitope for compounds to bind and to regulate the synthesis of the fuel ATP but also to stimulate ATP hydrolysis. An increase of ATP hydrolysis of the *Mt* F_1F_O ATP synthase would lead to depleted cellular ATP levels and would decrease the viability of the mycobacteria [140].

In contrast, the mitochondrial homolog of ε is believed to be non-inhibitory, with its CTD clamped in the compact ε_c state by a unique mitochondrial subunit. Instead, eukaryotes evolved a separate protein IF_1 to inhibit mitochondrial ATP synthases [16]. Despite their distinct origins there are broad similarities in the way the ε CTD and IF_1 interact with the catalytic F_1 core [18]. These distinct inhibitor proteins serve the same primary role, to block 'wasteful' ATP hydrolysis by F_1F_O ATP synthase under conditions when the PMF across the membrane is low or absent. In mitochondria, respiration and PMF decline markedly during cellular hypoxia, which occurs, for instance, during cardiac failure. Without PMF to drive ATP synthesis, F_1F_O begins to work in reverse, but acidification of the mitochondrial matrix transforms IF_1 into an active form that binds to and inhibits MF_1, minimizing wasteful ATP hydrolysis and the odds of cell death [17]. In plants, chloroplasts regularly lose PMF during long dark cycles, and inhibition by ε coordinates with a chloroplast-specific adaptation of γ to inactivate the ATP synthase in the dark [232]. Bacteria are more varied in their environmental and metabolic demands, and the physiological role of ε inhibition may be tuned to these differences in bacterial ecology; this is consistent with the variations in sequence and length of ε-helix2 between different types of bacteria [134] and with the fact that some aerobic bacteria show much stronger ε-inhibition on membranes than is observed with *E. coli* [129]. Some bacteria can neither respire nor photosynthesize, but require their F_1F_O to function as an ATPase-driven proton pump so as to maintain PMF, internal pH homeostasis or both [233].

It has been shown that in mycobacterial ATP synthases, generation of PMF by hydrolyzing ATP is not possible given that ATP hydrolysis mode is blocked [128]. ATP synthase essentially functions in the synthesis direction, most likely either to produce ATP, pH homeostasis, or for contributing to the NAD^+/NADH redox balance. Under low oxygen tension other membrane–protein complexes, nitrate reductase or fumarate reductase act in reverse to fulfill the task of PMF maintenance [70, 71].

To understand the mechanism of ATP hydrolysis blockage in mycobacteria, the effect of four different treatments reported to activate 'latent' ATP hydrolysis activity in bacteria has helped gain insight [140]. Cleavage of the inhibitory intrinsic subunit ε to activate ATP hydrolysis was achieved by limited trypsin proteolysis [129, 234]. Hydrophobic interactions within ATP synthase have been shown to be compromised on addition of methanol. [235]. Oxy-anions, for example sulfite aid in the removal of inhibitory ADP and uncoupling of ATP synthase function [236-238]. Relieving ADP inhibition and conformation switch of subunit ε to a non-inhibitory state is achieved via membrane energization [239].

A recent study on the subunit ε from the *E. coli* has shown that the C-terminus of this subunit containing the Loop2/Helix2 plays a pivotal role in inhibiting the F_1 activity of the enzyme [141]. Decrease in the rate of rotation and lengthening of the catalytic dwell in the inhibited state were observed. Residues S108 and Y114 have been identified as important for the inhibitory function. The epsilon in its extended state interacts with the α and β subunits in its extended conformation, thereby interfering with the smooth movement of the γ subunit [130]. Another study supporting this data is where the subunit ε did not inhibit the F_1 rotation when fused through its C-terminus to cytochrome b562, a globular protein [240].

Using the *E. coli* γ-ε as template, models were generated for *Mt*γ-ε the residues involved in polar interaction in subunits γ and ε are shown in the following figure 4.12. The polar contacts at the interface are highlighted in circles in the surface charge map and the inset shows the specific residues that may be interacting with each other.

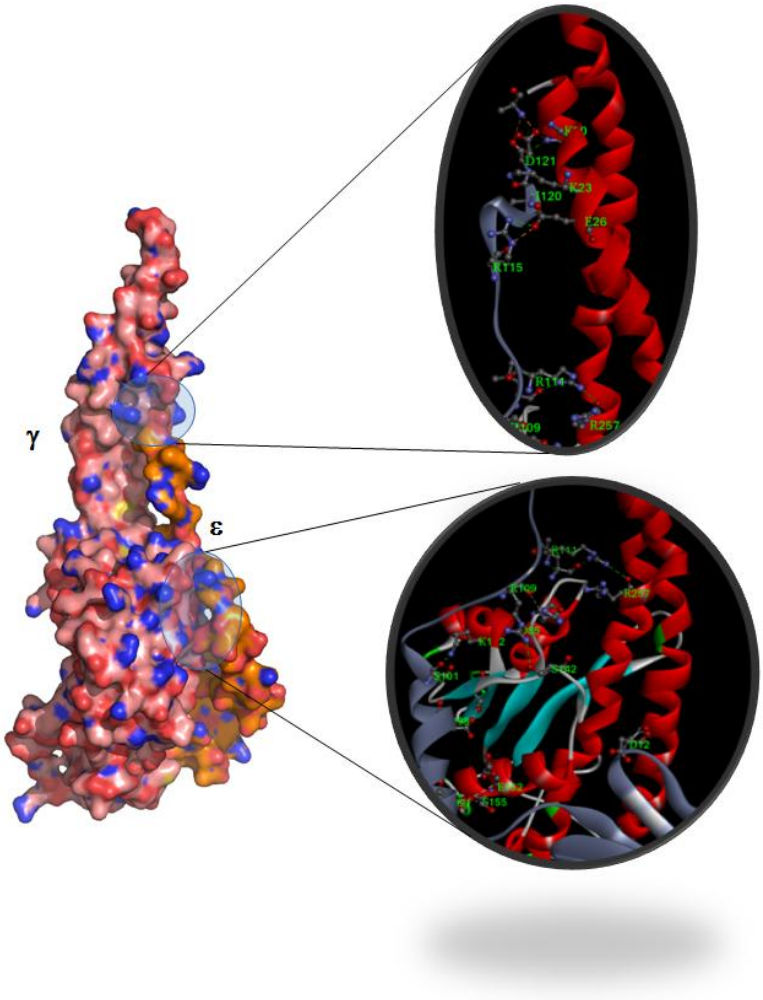

Figure 4.12: Surface charge representation of the *Mt*γ-ε interface using models generated for individual subunits. Regions highlighted in circles indicate the possible specific interactions in the coupling complex.

The following table shows the residues responsible for strong interactions observed for subunit ε and other subunits α, β and γ as seen in the crystal structure of *Bacillus* PS3 F_1 (TF_1) and *E. coli* F_1 (EF_1) [18, 107]. Residues in similar position for the *Mt*F_1 have been identified from sequence alignment.

Table 4.1.2: Interaction of residues of subunit ε with subunits α, β and γ in TF_1, EF_1 and *Mt*F_1

TF1	**EF_1**	***Mt*F_1**
TεQ107-TβE391 Affects catalysis and inhibition	EεS108-EβE381 Cross-linking between the two residues	*Mt*εA108-*Mt*βE381
TεD112-TαS400	EεD113-EαS411	*Mt*εR113-*Mt*αS411
TεD110-TγR85	EεD111-EγR84	*Mt*εR111-*Mt*γR83
TεF113-TγR85	EεY114-EγR84	*Mt*εR113-*Mt*γR83

The hydrolytic activity studies performed with the various mutants generated for both the native and chimeric protein of *M. tuberculosis* and *E. coli* give an indication towards the inhibitory/regulatory potential of this subunit that needs to be deciphered carefully. The study in this thesis reveals that, *Mt*ε on reconstitution with PS3$\alpha_3\beta_3\gamma$ shows a slight increase in ATP hydrolytic activity compared to PS3$\alpha_3\beta_3\gamma$ (section 3.3.3). Interestingly, with the extension of the C-terminus, as in with the ε_{121hyb} construct, the reconstituted complex of PS3$\alpha_3\beta_3\gamma$ + ε_{121hyb} seems to be perfectly capable of activating the hydrolytic activity (section 3.3.7). This indicates towards the role played by the length of the C-terminus, which could in turn influence the conformation adopted by the very C-terminus in the subunit ε, hence heavily influencing the functioning of the headpiece. Also the extension is believed to allow the subunit ε to better reach the essential residues of the C-terminus of the subunit α to necessitate interaction for activation. As seen in section 3.3.5, similar reconstitution of *PS3*ε and *Ec*ε confirmed the roles of activation played by these proteins, as already established [133, 228, 241, 242]. The assays described for these experiments have been performed at 25°C and with lower protein concentrations of 1µg/µl Also unlike the protocol described in this thesis, the sample was not applied on a gel filtration column prior to hydrolysis measurement.[241]. *Ec*ε has been shown to be capable of dissociating itself from the active complex hence causing the hydrolytic activity to increase [242]. The inhibitory effect of *PS3*ε has been reported at lower ATP concentrations and in physiologically relevant concentrations of >1 mM ATP, the TF_1 complex is believed to exist in an active form [241]. *Mt*ε differs from both *PS3*ε and *Ec*ε in its ability to bind ATP and makes for an additional interesting aspect to further probe.

As seen for the $\alpha^{chi}{}_3\beta_3\gamma$, the C-terminus of the *Mt*α has been shown to play an inhibitory role, but surprisingly is responsible for stimulating the hydrolytic activity on complexing with *Mt*ε. This experiment leads to a parallel line of thought to that observed with PS3$\alpha_3\beta_3\gamma$ + ε_{121hyb}. Wherein, the extended C-terminus of ε_{121hyb} allowed the otherwise shorter subunit of *Mt*ε to reach out to the C-terminus of PS3α. In this case the extension provided to PS3α, by generating α^{chi} in the complex, allows for the interaction between the native *Mt*ε and $\alpha^{chi}{}_3\beta_3\gamma$. This opens up the possibility of a strong interaction between the C-terminus of subunit α with that of subunit ε.

Insights into behavior of these proteins will allow us to understand the role played by the C-terminal segment of the *Mt*ε and *Mt*α and may present new drug targets, to design improved new leads with improved antibacterial activities.

Presently, only the low-resolution structural detail (SAXS) of subunit ε along with the NMR structure of the C-terminal peptide $\varepsilon_{103-120}$ is available for *Mt* [81]. The work in this thesis summarizes the attempts employed to obtain the high-resolution structure of subunit *Mt*ε_{1-120}.

Extensive efforts have been invested in crystallizing the protein. As mentioned in section 2.2.17 various commercially available crystallization kits were used. Micro-crystalline precipitate was formed in a select few cases. However most of the drops remained clear or a heavy precipitate was formed. The protein sample used for setting crystallization drops was monitored over time, to only shed light on the instability of the protein. These experiments only deepened the confirmation that the recombinant proteins from *M. tuberculosis* expressed in *E. coli* are not malleable for study via traditional techniques. Hence serious diverse efforts were directed towards stabilizing the protein to make it more amiable for further studies. The Thermofluor stability assay was performed to decipher a more stable buffer condition to select a better condition for both crystallization and NMR studies. Although the buffer condition with 50 mM Glycine pH 9.5 indicated to be the more favorable buffer for the protein, both crystallization and NMR studies did not deliver any promising results with this condition.

Another diverse approach which was attempted to express a stable protein of $Mt\varepsilon_{1\text{-}120}$ was by expressing the recombinant protein in *M. smegmatis*, a more closely related system to *M. tuberculosis* than is *E. coli*. A recent study on the mycobacterial ribosome reveals unique features with regard to structural diversity seen in bacterial ribosomes [243]. These unique features are believed to play a role in protein expression and folding and hence favoring the production of a stable soluble protein for *Mt* by circumventing the challenges posed by an *E. coli* expression system. However, this approach could not be adapted to completion as the level of protein expression was very poor and also given that the this is slow growing bacteria, the experimental procedures were time consuming and not very profitable.

Given that $Mt\varepsilon_{1\text{-}120}$ provided a good spectrum for the ^{15}N-^{1}H HSQC for 2D NMR, the challenge was more to keep the protein stable enough for a certain time period to allow for the more time consuming and elaborate 3D NMR experiments to be performed. A breakthrough solution to this situation was provided by the NUS technique, which only requires random sampling of the data set and hence shortening the acquisition time considerably. Also coupled to acquiring 3D NMR data using NUS, a more stable protein was expressed in *E. coli* BL21 GroEL-ES. This cell strain of *E. coli* BL21 carrying the GroEL-ES chaperone, stabilized the protein considerably, and allowed the collection of certain data sets. Currently backbone assignments for about 49 residues have been possible. However, with both the above-mentioned improvisations, the challenge continued to prevail. *E. coli* BL21 GroEL-ES only allowed the protein to be relatively more stable for a short period of an extra 24 hours and also the HNCACB and HNCACO acquired using NUS- NMR gave a weak signal intensity.

To further combat the struggle with assigning the peaks for the NMR experiment for *Mt*$\varepsilon_{1\text{-}120}$, selective ^{15}N amino acid labeling of the protein was performed and the 2D ^{15}N-HSQC spectrum was acquired. Currently, A, V, I, R, D and E specific labelled proteins have been prepared and their respective ^{15}N-HSQC spectrum have been acquired. This data in conjunction with the remaining 3D NMR data sets can be used to complete the assignment for rest of the residues to allow for structural elucidation. Since the completion of my experimental work, progress has been made and at present about 85 residues have been assigned.

5. Conclusions

5. Conclusions

The work in this thesis is mainly focussed on subunit B of A-ATP synthase of *Methanosarcina mazei* Gö1 and subunits α and ε of F-ATP synthase of *M. tuberculosis.* Although both these organisms are not closely related, they have developed their internal machinery to adapt to their harsh environmental conditions that they survive in and form interesting topics for study.

So far, subunit B of A-ATP synthase of *Methanosarcina mazei* Gö1 has been considered as a non-catalytic subunit [162]. However, recent studies have confirmed on its ability to bind nucleotides with different affinities for Mg-ATP and Mg-ADP and its role as a regulatory subunit [192]. Sequence comparison of subunit B with subunit α of F-ATP synthase reveals a different phosphate binding loop (P-loop) composed of residues $_{150}$SASGLPHN$_{157}$. To probe further into the role of the residues in the P-loop, specific mutants of residues H156 and N157 were generated. I have solved the structure for the N157T mutant of subunit B *Methanosarcina mazei* Gö1. Along with the other mutant structures, H156A and N156A of subunit B *Methanosarcina mazei* Gö1 and the binding studies performed using FCS, it was observed that the binding of the nucleotide to the alanine mutants was improved when compared to the WT and the N157T mutant. This was attributed to the widening of the binding pocket due to the substitution of smaller side chains of alanine. The mutants lost the ability to bind the nucleotides differentially displaying the importance of the Histidine and Asparagine in their respective positions in the P-loop of subunit B A-ATP synthase for recognition and binding of nucleotide.

The homologous subunit in F-ATP synthase is the subunit α, which unlike the subunit B binds the nucleotides with similar affinities. However, on sequence comparison, subunit α of *Mt* revealed a stretch of polar residues in it's C-terminal and is conserved only in the mycobacteria family. Study of the proteins of F-ATP synthase from *M. tuberculosis* are of utmost importance to understand the bioenergetics of the enzyme. Also no high resolution structural information is available from the F-ATP synthase of *M. tuberculosis*. I have cloned and expressed the protein for *Mt*α and the SAXS structure obtained shows the overall shape for the protein. *Mt*α binds ATP weakly when compared to PS3α and *Ec*α. This characteristic could be attributed to the composition of the P-loop which has deviated to $_{172}$GDRKTGKT$_{179}$ from otherwise conserved $_{169}$GDRQTGKT$_{176}$, as seen in *E. coli*, *Bacillus* PS3, *Bacillus* TA2A1, bovine mitochondria. To understand the role of the C-terminus of *Mt*α, a chimeric protein, α^{chi} was generated with subunit α of *M. tuberculosis* and *Bacillus* PS3. SAXS analysis confirmed the extra domain present due to the fusion of the C-terminus of *Mt*α to PS3α. The chimeric protein was incorporated into the

complex of PS3$\alpha_3\beta_3\gamma$, to generate $\alpha^{chi}{}_3\beta_3\gamma$ to investigate its role in ATP hydrolysis activity. For the first time, it was shown that the activity of $\alpha^{chi}{}_3\beta_3\gamma$ was reduced indicating inhibitory role of the C-terminus of *Mt*α.

Extensive studies on the subunit ε of *E. coli*, *Bacillus* PS3 have revealed the importance of this subunit for coupling F_1 to F_O and also its role in the regulation of ATP hydrolysis. Their role as an inhibitor/ stimulator of ATP hydrolysis is attributed to the different conformations, subunit ε can adopt based on the ATP concentration, and is well supported with the high resolution structures. However, for *Mtε,* structural information is available only on the SAXS structure and the C-terminal peptide obtained via NMR. My work in this thesis has been focussed on generating a stable protein to perform both crystallization and NMR studies. Working along this line of thought, various strategies were used. Thermofluor stability assay was performed to optimise the buffer condition. Expression of the recombinant protein in *M. smegmatis* host cell showed very low levels of protein expression. With recent advancements in NMR, NUS and selective amino acid labelling techniques were employed to acquire 3D NMR data sets, with this long term stability challenged protein. This has helped us assign close to 50 % of the total peaks as of now and is promising for further assignments. Mechanistic characterisation of *Mt*ε was possible with the various constructs of both native and chimeric proteins that were generated. These, on reconstitution with PS3$\alpha_3\beta_3\gamma$ have given insights into the behaviour of complex formation and the effect on ATP hydrolysis, indicating that the length of $Mt\varepsilon_{hybrid}$ was influential in causing the stimulatory effect. The otherwise inhibited complex of $\alpha^{chi}{}_3\beta_3\gamma$, also showed increase in its ATP hydrolytic activity indicating the possible interactions between the C-terminus of *Mt*α and *Mt*ε. Recent studies from our laboratory, on the inverted vesicles of *M. smegmatis* revealed detectable hydrolysis activity, altering the understanding that mycobacterial ATP synthase is capable of performing ATP hydrolysis.

6. References

References

1. Yoshida, M., E. Muneyuki, and T. Hisabori, *ATP synthase--a marvellous rotary engine of the cell.* Nat. Rev. Mol. Cell Biol., 2001. **2**(9): p. 669-77.
2. Grüber, G., et al., *Structure-function relationships of A-, F- and V-ATPases.* J. Exp. Biol., 2001. **204**(Pt 15): p. 2597-605.
3. Müller, V., C. Ruppert, and T. Lemker, *Structure and function of the A1A0-ATPases from methanogenic Archaea.* J. Bioenerg. Biomembr., 1999. **31**(1): p. 15-27.
4. Hilario, E. and J.P. Gogarten, *The prokaryote-to-eukaryote transition reflected in the evolution of the V/F/A-ATPase catalytic and proteolipid subunits.* J. Mol. Evol., 1998. **46**(6): p. 703-15.
5. Muench, S.P., J. Trinick, and M.A. Harrison, *Structural divergence of the rotary ATPases.* Q. Rev. Biophys., 2011. **44**(3): p. 311-56.
6. Forgac, M., *Vacuolar ATPases: rotary proton pumps in physiology and pathophysiology.* Nat. Rev. Mol. Cell Biol., 2007. **8**(11): p. 917-29.
7. Mayer, F. and V. Müller, *Adaptations of anaerobic archaea to life under extreme energy limitation.* FEMS Microbiol. Rev., 2014. **38**(3): p. 449-72.
8. Adams, M.W., *Biochemical diversity among sulfur-dependent, hyperthermophilic microorganisms.* FEMS Microbiol. Rev., 1994. **15**(2-3): p. 261-77.
9. Feniouk, B.A., www.atpsynthase.info.
10. Boyer, P.D., *The ATP synthase--a splendid molecular machine.* Annu. Rev. Biochem., 1997. **66**: p. 717-49.
11. Nicholls, D.G., *The influence of respiration and ATP hydrolysis on the proton-electrochemical gradient across the inner membrane of rat-liver mitochondria as determined by ion distribution.* Eur. J. Biochem., 1974. **50**(1): p. 305-15.
12. Scott, I.D. and D.G. Nicholls, *Energy transduction in intact synaptosomes. Influence of plasma-membrane depolarization on the respiration and membrane potential of internal mitochondria determined in situ.* Biochem. J., 1980. **186**(1): p. 21-33.
13. St-Pierre, J., M.D. Brand, and R.G. Boutilier, *Mitochondria as ATP consumers: cellular treason in anoxia.* Proc. Natl. Acad. Sci. U S A, 2000. **97**(15): p. 8670-4.
14. Cabezon, E., et al., *Homologous and heterologous inhibitory effects of ATPase inhibitor proteins on F-ATPases.* J. Biol. Chem., 2002. **277**(44): p. 41334-41.
15. Pullman, M.E. and G.C. Monroy, *A Naturally occuring inhibitor of mitochondrial Adenosine Triphosphate.* J. Biol. Chem., 1963. **238**: p. 3762-9.
16. Campanella, M., et al., *IF_1: setting the pace of the F_1F_O-ATP synthase.* Trends Biochem. Sci., 2009. **34**(7): p. 343-50.
17. Gledhill, J.R., et al., *How the regulatory protein, IF(1), inhibits F(1)-ATPase from bovine mitochondria.* Proc. Natl. Acad. Sci. U S A, 2007. **104**(40): p. 15671-6.
18. Cingolani, G. and T.M. Duncan, *Structure of the ATP synthase catalytic complex (F_1) from Escherichia coli in an autoinhibited conformation.* Nat. Struct. Mol. Biol., 2011. **18**(6): p. 701-7.
19. von Ballmoos, C., G.M. Cook, and P. Dimroth, *Unique rotary ATP synthase and its biological diversity.* Annu Rev Biophys, 2008. **37**: p. 43-64.
20. Dimroth, P., C. von Ballmoos, and T. Meier, *Catalytic and mechanical cycles in F-ATP synthases. Fourth in the Cycles Review Series.* EMBO Rep., 2006. **7**(3): p. 276-82.
21. Meier, T., et al., *Structure of the rotor ring of F-Type Na+-ATPase from Ilyobacter tartaricus.* Science, 2005. **308**(5722): p. 659-62.
22. Wieczorek, H., *The insect V-ATPase, a plasma membrane proton pump energizing secondary active transport: molecular analysis of electrogenic potassium transport in the tobacco hornworm midgut.* J. Exp. Biol., 1992. **172**: p. 335-43.

23. Hirata, T., et al., *Regulation and reversibility of vacuolar H(+)-ATPase.* J. Biol. Chem., 2000. **275**(1): p. 386-9.
24. Müller, V. and G. Grüber, *ATP synthases: structure, function and evolution of unique energy converters.* Cell Mol. Life Sci., 2003. **60**(3): p. 474-94.
25. Hochstein, L.I. and H. Stan-Lotter, *Purification and properties of an ATPase from Sulfolobus solfataricus.* Arch. Biochem. Biophys., 1992. **295**(1): p. 153-60.
26. Inatomi, K., *Characterization and purification of the membrane-bound ATPase of the archaebacterium Methanosarcina barkeri.* J. Bacteriol., 1986. **167**(3): p. 837-41.
27. Pisa, K.Y., et al., *A sodium ion-dependent A1AO ATP synthase from the hyperthermophilic archaeon Pyrococcus furiosus.* FEBS J., 2007. **274**(15): p. 3928-38.
28. Coskun, U., et al., *Three-dimensional organization of the archaeal A_1-ATPase from Methanosarcina mazei Gö1*. J. Biol. Chem., 2004. **279**(21): p. 22759-64.
29. Lingl, A., et al., *Isolation of a complete A1AO ATP synthase comprising nine subunits from the hyperthermophile Methanococcus jannaschii.* Extremophiles, 2003. **7**(3): p. 249-57.
30. Pisa, K.Y., et al., *The coupling ion in the methanoarchaeal ATP synthases: H(+) vs. Na(+) in the A(1)A(o) ATP synthase from the archaeon Methanosarcina mazei Go1*. FEMS Microbiol Lett., 2007. **277**(1): p. 56-63.
31. McMillan, D.G., et al., *A1Ao-ATP synthase of Methanobrevibacter ruminantium couples sodium ions for ATP synthesis under physiological conditions.* J. Biol. Chem., 2011. **286**(46): p. 39882-92.
32. Schlegel, K. and V. Müller, *Evolution of Na(+) and H(+) bioenergetics in methanogenic archaea.* Biochem Soc Trans, 2013. **41**(1): p. 421-6.
33. Stewart, A.G., et al., *Rotary ATPases: models, machine elements and technical specifications.* Bioarchitecture, 2013. **3**(1): p. 2-12.
34. Ackerman, S.H. and A. Tzagoloff, *Function, structure, and biogenesis of mitochondrial ATP synthase.* Prog. Nucleic Acid Res. Mol. Biol., 2005. **80**: p. 95-133.
35. DeLano, W.L., *The PyMOL Molecular Graphics System* 2002, http://www.pymol.org DeLano Scientific, Palo Alto, CA, USA
36. Berman, H.M., et al., *The Protein Data Bank.* Nucleic Acids Res., 2000. **28**(1): p. 235-42.
37. Wilkens, S., et al., *Structural characterization of the interaction of the delta and alpha subunits of the Escherichia coli F1F0-ATP synthase by NMR spectroscopy.* Biochemistry, 2005. **44**(35): p. 11786-94.
38. Dickson, V.K., et al., *On the structure of the stator of the mitochondrial ATP synthase.* Embo J., 2006. **25**(12): p. 2911-8.
39. Priya, R., et al., *Solution structure, determined by nuclear magnetic resonance, of the b30-82 domain of subunit b of Escherichia coli F_1F_O ATP synthase.* J. Bacteriol., 2009. **191**(24): p. 7538-44.
40. Dmitriev, O., et al., *Structure of the membrane domain of subunit b of the Escherichia coli F0F1 ATP synthase.* J. Biol. Chem., 1999. **274**(22): p. 15598-604.
41. Preiss, L., et al., *Structure of the mycobacterial ATP synthase Fo rotor ring in complex with the anti-TB drug bedaquiline*. Vol. 1. 2015.
42. Lu, P., H. Lill, and D. Bald, *ATP synthase in mycobacteria: special features and implications for a function as drug target.* Biochim. Biophys. Acta., 2014. **1837**(7): p. 1208-18.
43. Grüber, G. and V. Marshansky, *New insights into structure-function relationships between archeal ATP synthase (A_1A_0) and vacuolar type ATPase (V_1V_0).* Bioessays, 2008. **30**(11-12): p. 1096-109.
44. Grüber, G., et al., *ATP synthases from archaea: the beauty of a molecular motor.* Biochim. Biophys. Acta., 2014. **1837**(6): p. 940-52.

45. Balakrishna, A.M., C. Hunke, and G. Grüber, *The structure of subunit E of the Pyrococcus horikoshii OT3 A-ATP synthase gives insight into the elasticity of the peripheral stalk.* J. Mol. Biol., 2012. **420**(3): p. 155-63.
46. Kumar, A., et al., *Nucleotide binding states of subunit A of the A-ATP synthase and the implication of P-loop switch in evolution.* J. Mol. Biol., 2010. **396**(2): p. 301-20.
47. Murata, T., et al., *Structure of the rotor of the V-Type Na+-ATPase from Enterococcus hirae.* Science, 2005. **308**(5722): p. 654-9.
48. Gayen, S., et al., *NMR solution structure of subunit F of the methanogenic A_1A_O adenosine triphosphate synthase and its interaction with the nucleotide-binding subunit B.* Biochemistry, 2007. **46**(42): p. 11684-94.
49. Iwata, M., et al., *Crystal structure of a central stalk subunit C and reversible association/dissociation of vacuole-type ATPase.* Proc. Natl. Acad. Sci. U S A, 2004. **101**(1): p. 59-64.
50. Saijo, S., et al., *Crystal structure of the central axis DF complex of the prokaryotic V-ATPase.* Proc. Natl. Acad. Sci. U S A, 2011. **108**(50): p. 19955-60.
51. Lee, L.K., et al., *The structure of the peripheral stalk of Thermus thermophilus H+-ATPase/synthase.* Nat. Struct. Mol. Biol., 2010. **17**(3): p. 373-8.
52. Schafer, I.B., et al., *Crystal structure of the archaeal A_1A_O ATP synthase subunit B from Methanosarcina mazei Gö1: Implications of nucleotide-binding differences in the major A_1A_O subunits A and B.* J. Mol. Biol., 2006. **358**(3): p. 725-40.
53. Collins, C.H., J.M. Grange, and M.D. Yates, *Mycobacteria in water.* J. Appl. Bacteriol., 1984. **57**(2): p. 193-211.
54. organisation, W.H., *Global tuberculosis Report, 2014.*
55. Daffe, M. and P. Draper, *The envelope layers of mycobacteria with reference to their pathogenicity.* Adv. Microb. Physiol., 1998. **39**: p. 131-203.
56. Cole, S.T., et al., *Deciphering the biology of Mycobacterium tuberculosis from the complete genome sequence.* Nature, 1998. **393**(6685): p. 537-44.
57. Pandey, A.K. and C.M. Sassetti, *Mycobacterial persistence requires the utilization of host cholesterol.* Proc. Natl. Acad. Sci. U S A, 2008. **105**(11): p. 4376-80.
58. Cook, G.M., et al., *Physiology of mycobacteria.* Adv. Microb. Physiol., 2009. **55**: p. 81-182, 318-9.
59. Barry, C.E., 3rd, et al., *The spectrum of latent tuberculosis: rethinking the biology and intervention strategies.* Nat. Rev. Microbiol., 2009. **7**(12): p. 845-55.
60. Kumar, A., et al., *Redox homeostasis in mycobacteria: the key to tuberculosis control?* Expert Rev. Mol. Med., 2011. **13**: p. e39.
61. Russell, D.G., *Who puts the tubercle in tuberculosis?* Nat. Rev. Microbiol., 2007. **5**(1): p. 39-47.
62. Gengenbacher, M., et al., *Nutrient-starved, non-replicating Mycobacterium tuberculosis requires respiration, ATP synthase and isocitrate lyase for maintenance of ATP homeostasis and viability.* Microbiology, 2010. **156**(Pt 1): p. 81-7.
63. Leistikow, R.L., et al., *The Mycobacterium tuberculosis DosR regulon assists in metabolic homeostasis and enables rapid recovery from nonrespiring dormancy.* J. Bacteriol., 2010. **192**(6): p. 1662-70.
64. Rao, S.P., et al., *The protonmotive force is required for maintaining ATP homeostasis and viability of hypoxic, nonreplicating Mycobacterium tuberculosis.* Proc. Natl. Acad. Sci. U S A, 2008. **105**(33): p. 11945-50.
65. Schnappinger, D., et al., *Transcriptional Adaptation of Mycobacterium tuberculosis within Macrophages: Insights into the Phagosomal Environment.* J Exp Med, 2003. **198**(5): p. 693-704.

66. Shi, L., et al., *Changes in energy metabolism of Mycobacterium tuberculosis in mouse lung and under in vitro conditions affecting aerobic respiration.* Proc Natl Acad Sci U S A, 2005. **102**(43): p. 15629-34.
67. Garton, N.J., et al., *Cytological and transcript analyses reveal fat and lazy persister-like bacilli in tuberculous sputum.* PLoS Med., 2008. **5**(4): p. e75.
68. Saviola, B., *Mycobacterium tuberculosis Adaptation to Survival in a Human Host*. Tuberculosis - Current Issues in Diagnosis and Management2013.
69. Koul, A., et al., *Diarylquinolines are bactericidal for dormant mycobacteria as a result of disturbed ATP homeostasis.* J. Biol. Chem., 2008. **283**(37): p. 25273-80.
70. Schnorpfeil, M., et al., *Generation of a proton potential by succinate dehydrogenase of Bacillus subtilis functioning as a fumarate reductase.* Eur. J. Biochem., 2001. **268**(10): p. 3069-74.
71. Wayne, L.G. and C.D. Sohaskey, *Nonreplicating persistence of mycobacterium tuberculosis.* Annu Rev Microbiol, 2001. **55**: p. 139-63.
72. Cox, R.A. and G.M. Cook, *Growth regulation in the mycobacterial cell.* Curr Mol Med, 2007. **7**(3): p. 231-45.
73. Hartman, T., et al., *Succinate dehydrogenase is the regulator of respiration in Mycobacterium tuberculosis.* PLoS Pathog, 2014. **10**(11): p. e1004510.
74. MacMicking, J.D., G.A. Taylor, and J.D. McKinney, *Immune control of tuberculosis by IFN-gamma-inducible LRG-47.* Science, 2003. **302**(5645): p. 654-9.
75. Ehrt, S. and D. Schnappinger, *Mycobacterial survival strategies in the phagosome: defence against host stresses.* Cell Microbiol., 2009. **11**(8): p. 1170-8.
76. Stewart, A.G., et al., *The dynamic stator stalk of rotary ATPases.* Nat. Commun., 2012. **3**: p. 687.
77. Segala, E., et al., *New mutations in the mycobacterial ATP synthase: new insights into the binding of the diarylquinoline TMC207 to the ATP synthase C-ring structure.* Antimicrob. Agents. Chemother., 2012. **56**(5): p. 2326-34.
78. Haagsma, A.C., et al., *Probing the interaction of the diarylquinoline TMC207 with its target mycobacterial ATP synthase.* PLoS One, 2011. **6**(8): p. e23575.
79. de Jonge, M.R., et al., *A computational model of the inhibition of Mycobacterium tuberculosis ATPase by a new drug candidate R207910.* Proteins, 2007. **67**(4): p. 971-80.
80. Upadhayaya, R.S., et al., *Design, synthesis, biological evaluation and molecular modelling studies of novel quinoline derivatives against Mycobacterium tuberculosis.* Bioorg Med Chem, 2009. **17**(7): p. 2830-41.
81. Biukovic, G., et al., *Variations of subunit ε of the Mycobacterium tuberculosis F_1F_O ATP synthase and a novel model for mechanism of action of the tuberculosis drug TMC207.* Antimicrob. Agents. Chemother., 2013. **57**(1): p. 168-76.
82. Priya, R., et al., *Solution structure of subunit gamma (gamma(1-204)) of the Mycobacterium tuberculosis F-ATP synthase and the unique loop of gamma(165-178), representing a novel TB drug target.* J. Bioenerg. Biomembr., 2013. **45**(1-2): p. 121-9.
83. Steed, P.R. and R.H. Fillingame, *Residues in the Polar Loop of Subunit c in Escherichia coli ATP Synthase Function in Gating Proton Transport to the Cytoplasm.* The Journal of Biological Chemistry, 2014. **289**(4): p. 2127-2138.
84. Cook, G.M. and A. Heikal, *Bridging the gap between a TB drug and its target.* Sci Transl Med, 2012. **4**(150): p. 150fs33.
85. Neres, J., et al., *Structural basis for benzothiazinone-mediated killing of Mycobacterium tuberculosis.* Sci Transl Med, 2012. **4**(150): p. 150ra121.
86. Ibrahim, M., et al., *Synergistic activity of R207910 combined with pyrazinamide against murine tuberculosis.* Antimicrob Agents Chemother, 2007. **51**(3): p. 1011-5.

87. Lounis, N., et al., *Combinations of R207910 with drugs used to treat multidrug-resistant tuberculosis have the potential to shorten treatment duration.* Antimicrob Agents Chemother, 2006. **50**(11): p. 3543-7.
88. Hards, K., et al., *Bactericidal mode of action of bedaquiline.* J Antimicrob Chemother, 2015.
89. Singh, S., et al., *Novel, potent, orally bioavailable and selective mycobacterial ATP synthase inhibitors that demonstrated activity against both replicating and non-replicating M. tuberculosis.* Bioorg Med Chem, 2015. **23**(4): p. 742-52.
90. Cole, S.T., et al., *Massive gene decay in the leprosy bacillus.* Nature, 2001. **409**(6823): p. 1007-11.
91. Russell, D.G., *Trp'ing tuberculosis.* Cell, 2013. **155**(6): p. 1209-10.
92. Zhang, Y.J., et al., *Tryptophan biosynthesis protects mycobacteria from CD4 T-cell-mediated killing.* Cell, 2013. **155**(6): p. 1296-308.
93. Via, L.E., et al., *Effects of cytokines on mycobacterial phagosome maturation.* J. Cell Sci., 1998. **111 (Pt 7)**: p. 897-905.
94. Fisher, M.A., B.B. Plikaytis, and T.M. Shinnick, *Microarray analysis of the Mycobacterium tuberculosis transcriptional response to the acidic conditions found in phagosomes.* J. Bacteriol., 2002. **184**(14): p. 4025-32.
95. Park, H.D., et al., *Rv3133c/dosR is a transcription factor that mediates the hypoxic response of Mycobacterium tuberculosis.* Mol. Microbiol., 2003. **48**(3): p. 833-43.
96. Kumar, A., et al., *Mycobacterium tuberculosis DosS is a redox sensor and DosT is a hypoxia sensor.* Proc. Natl. Acad. Sci. U S A, 2007. **104**(28): p. 11568-73.
97. Florczyk, M.A., et al., *A family of acr-coregulated Mycobacterium tuberculosis genes shares a common DNA motif and requires Rv3133c (dosR or devR) for expression.* Infect Immun., 2003. **71**(9): p. 5332-43.
98. Vasudeva-Rao, H.M. and K.A. McDonough, *Expression of the Mycobacterium tuberculosis acr-coregulated genes from the DevR (DosR) regulon is controlled by multiple levels of regulation.* Infect Immun., 2008. **76**(6): p. 2478-89.
99. Bowler, M.W., et al., *Ground state structure of F_1-ATPase from bovine heart mitochondria at 1.9 A resolution.* J. Biol. Chem., 2007. **282**(19): p. 14238-42.
100. Abrahams, J.P., et al., *Structure at 2.8 A resolution of F_1-ATPase from bovine heart mitochondria.* Nature, 1994. **370**(6491): p. 621-8.
101. Menz, R.I., J.E. Walker, and A.G. Leslie, *Structure of bovine mitochondrial F(1)-ATPase with nucleotide bound to all three catalytic sites: implications for the mechanism of rotary catalysis.* Cell, 2001. **106**(3): p. 331-41.
102. Bowler, M.W., et al., *How azide inhibits ATP hydrolysis by the F-ATPases.* Proc. Natl. Acad. Sci. U S A, 2006. **103**(23): p. 8646-9.
103. Kabaleeswaran, V., et al., *Novel features of the rotary catalytic mechanism revealed in the structure of yeast F1 ATPase.* Embo J., 2006. **25**(22): p. 5433-42.
104. Rees, D.M., et al., *Structural evidence of a new catalytic intermediate in the pathway of ATP hydrolysis by F1-ATPase from bovine heart mitochondria.* Proc. Natl. Acad. Sci. U S A, 2012. **109**(28): p. 11139-43.
105. Junge, W., *Protons, proteins and ATP*. Photosynth. Res., 2004. **80**(1-3): p. 197-221.
106. von Ballmoos, C., A. Wiedenmann, and P. Dimroth, *Essentials for ATP synthesis by F1F0 ATP synthases.* Annu. Rev. Biochem., 2009. **78**: p. 649-72.
107. Shirakihara, Y., et al., *The crystal structure of the nucleotide-free alpha 3 beta 3 subcomplex of F1-ATPase from the thermophilic Bacillus PS3 is a symmetric trimer.* Structure, 1997. **5**(6): p. 825-36.

108. Weber, J., et al., *Tryptophan fluorescence provides a direct probe of nucleotide binding in the noncatalytic sites of Escherichia coli F1-ATPase.* J. Biol. Chem., 1994. **269**(15): p. 11261-8.
109. Abbott, M.S., J.J. Czarnecki, and B.R. Selman, *Localization of the high-affinity binding site for ATP on the membrane-bound chloroplast ATP synthase.* J. Biol. Chem., 1984. **259**(19): p. 12271-8.
110. Weber, J. and A.E. Senior, *Location and properties of pyrophosphate-binding sites in Escherichia coli F1-ATPase.* J. Biol. Chem., 1995. **270**(21): p. 12653-8.
111. Ono, S., et al., *Origin of apparent negative cooperativity of F(1)-ATPase.* Biochim. Biophys. Acta., 2003. **1607**(1): p. 35-44.
112. Matsui, T., et al., *Catalytic activity of the alpha3beta3gamma complex of F1-ATPase without noncatalytic nucleotide binding site.* J. Biol. Chem., 1997. **272**(13): p. 8215-21.
113. Dou, C., et al., *ADP-fluoroaluminate complexes are formed cooperatively at two catalytic sites of wild-type and mutant alpha3beta3gamma subcomplexes of the F1-ATPase from the thermophilic Bacillus PS3.* Biochemistry, 1997. **36**(12): p. 3719-27.
114. Feniouk, B.A., T. Suzuki, and M. Yoshida, *Regulatory interplay between proton motive force, ADP, phosphate, and subunit epsilon in bacterial ATP synthase.* J. Biol. Chem., 2007. **282**(1): p. 764-72.
115. Aggeler, R. and R.A. Capaldi, *Nucleotide-dependent movement of the epsilon subunit between alpha and beta subunits in the Escherichia coli F_1F_O-type ATPase.* J. Biol. Chem., 1996. **271**(23): p. 13888-91.
116. Aggeler, R., G. Grüber, and R.A. Capaldi, *Trapping of conformations of the Escherichia coli F_1 ATPase by disulfide bond formation. A state of the enzyme with all three catalytic sites of equal and low affinity for nucleotides.* FEBS Lett., 1998. **426**(1): p. 37-40.
117. Kishikawa, J., et al., *Molecular basis of ADP inhibition of vacuolar (V)-type ATPase/synthase.* J. Biol. Chem., 2014. **289**(1): p. 403-12.
118. Gouet, P., et al., *ESPript: analysis of multiple sequence alignments in PostScript.* Bioinformatics, 1999. **15**(4): p. 305-8.
119. Arntzen, C.J., *Inhibition of photophosphorylation by tentoxin, a cyclic tetrapeptide.* Biochim. Biophys. Acta., 1972. **283**(3): p. 539-42.
120. Steele, J.A., et al., *Chloroplast coupling factor 1: A species-specific receptor for tentoxin.* Proc. Natl. Acad. Sci. U S A, 1976. **73**(7): p. 2245-8.
121. Steele, J.A., et al., *Tentoxin. An uncompetitive inhibitor of lettuce chloroplast coupling factor 1.* Biochim. Biophys. Acta., 1978. **501**(1): p. 72-82.
122. Tucker, W.C., et al., *Role of the ATP synthase alpha-subunit in conferring sensitivity to tentoxin.* Biochemistry, 2001. **40**(25): p. 7542-8.
123. Avni, A., et al., *Tentoxin sensitivity of chloroplasts determined by codon 83 of beta subunit of proton-ATPase.* Science, 1992. **257**(5074): p. 1245-7.
124. Hu, D., et al., *Catalytic properties and sensitivity to tentoxin of Chlamydomonas reinhardtii ATP synthases changed in codon 83 of atpB by site-directed mutagenesis.* J. Biol. Chem., 1997. **272**(9): p. 5457-63.
125. Uhlin, U., G.B. Cox, and J.M. Guss, *Crystal structure of the epsilon subunit of the proton-translocating ATP synthase from Escherichia coli.* Structure, 1997. **5**(9): p. 1219-30.
126. Wilkens, S. and R.A. Capaldi, *Solution structure of the epsilon subunit of the F1-ATPase from Escherichia coli and interactions of this subunit with beta subunits in the complex.* J. Biol. Chem., 1998. **273**(41): p. 26645-51.
127. Yagi, H., et al., *Structures of the thermophilic F1-ATPase epsilon subunit suggesting ATP-regulated arm motion of its C-terminal domain in F1.* Proc. Natl. Acad. Sci. U S A, 2007. **104**(27): p. 11233-8.

128. Yagi, H., et al., *Structural and functional analysis of the intrinsic inhibitor subunit epsilon of F1-ATPase from photosynthetic organisms.* Biochem. J., 2010. **425**(1): p. 85-94.
129. Keis, S., et al., *Inhibition of ATP hydrolysis by thermoalkaliphilic F1Fo-ATP synthase is controlled by the C terminus of the epsilon subunit.* J. Bacteriol., 2006. **188**(11): p. 3796-804.
130. Nakanishi-Matsui, M., et al., *Inhibition of F1-ATPase Rotational Catalysis by the Carboxyl-terminal Domain of the ϵ Subunit.* J. Biol. Chem, 2014. **289**(44): p. 30822-30831.
131. Mizumoto, J., et al., *epsilon subunit of Bacillus subtilis F1-ATPase relieves MgADP inhibition.* PLoS One, 2013. **8**(8): p. e73888.
132. Oka, H., et al., *Elastic rotation of Escherichia coli F(O)F(1) having epsilon subunit fused with cytochrome b(562) or flavodoxin reductase.* Biochem. Biophys. Res. Commun., 2014. **446**(4): p. 889-93.
133. Kato, S., M. Yoshida, and Y. Kato-Yamada, *Role of the epsilon subunit of thermophilic F1-ATPase as a sensor for ATP.* J. Biol. Chem., 2007. **282**(52): p. 37618-23.
134. Feniouk, B.A., T. Suzuki, and M. Yoshida, *The role of subunit epsilon in the catalysis and regulation of FOF1-ATP synthase.* Biochim. Biophys. Acta., 2006. **1757**(5-6): p. 326-38.
135. Rodriguez, A.D., S.D. Dunn, and L. Konermann, *ATP-induced dimerization of the F0F1 epsilon subunit from Bacillus PS3: a hydrogen exchange-mass spectrometry study.* Biochemistry, 2014. **53**(24): p. 4072-80.
136. Grüber, G., J. Godovac-Zimmermann, and T. Nawroth, *ATP synthesis and hydrolysis of the ATP-synthase from Micrococcus luteus regulated by an inhibitor subunit and membrane energization.* Biochim. Biophys. Acta., 1994. **1186**(1-2): p. 43-51.
137. Morales-Rios, E., et al., *A novel 11-kDa inhibitory subunit in the F1FO ATP synthase of Paracoccus denitrificans and related alpha-proteobacteria.* Faseb J., 2010. **24**(2): p. 599-608.
138. Lu, J., et al., *An ATPase inhibitory peptide with antibacterial and ion current effects.* Biochem. Biophys. Res. Commun., 2014. **446**(2): p. 519-22.
139. Gledhill, J.R. and J.E. Walker, *Inhibitors of the catalytic domain of mitochondrial ATP synthase.* Biochem Soc Trans, 2006. **34**(Pt 5): p. 989-92.
140. Haagsma, A.C., et al., *ATP synthase in slow- and fast-growing mycobacteria is active in ATP synthesis and blocked in ATP hydrolysis direction.* FEMS Microbiol Lett., 2010. **313**(1): p. 68-74.
141. Via, L.E., et al., *Tuberculous granulomas are hypoxic in guinea pigs, rabbits, and nonhuman primates.* Infect Immun., 2008. **76**(6): p. 2333-40.
142. Miller, T.L. and M.J. Wolin, *Enumeration of Methanobrevibacter smithii in human feces.* Arch Microbiol, 1982. **131**(1): p. 14-8.
143. Robertson, D.E., et al., *Occurrence of beta-glutamate, a novel osmolyte, in marine methanogenic bacteria.* Appl. Environ. Microbiol., 1990. **56**(5): p. 1504-8.
144. Kulik, E.M., et al., *Identification of archaeal rDNA from subgingival dental plaque by PCR amplification and sequence analysis.* FEMS Microbiol Lett., 2001. **196**(2): p. 129-33.
145. Stetter, K.O., *History of discovery of the first hyperthermophiles.* Extremophiles, 2006. **10**(5): p. 357-62.
146. Fiala, G., et al., *Staphylothermus marinus sp. nov. Represents a Novel Genus of Extremely Thermophilic Submarine Heterotrophic Archaebacteria Growing up to 98 °C.* Systematic and Applied Microbiology, 1986. **8**(1–2): p. 106-113.

147. Stetter, K.O., H. Konig, and E. Stackebrandt, *Pyrodictium gen. nov., a New Genus of Submarine Disc-Shaped Sulphur Reducing Archaebacteria Growing Optimally at 105 degrees C.* Syst. Appl. Microbiol., 1983. **4**(4): p. 535-51.
148. Zillig, W., et al., *Hyperthermus butylicus, a hyperthermophilic sulfur-reducing archaebacterium that ferments peptides.* J. Bacteriol., 1990. **172**(7): p. 3959-65.
149. Kurr, M., et al., *Methanopyrus kandleri, gen. and sp. nov. represents a novel group of hyperthermophilic methanogens, growing at 110°C.* Archives of Microbiology, 1991. **156**(4): p. 239-247.
150. Blochl, E., et al., *Pyrolobus fumarii, gen. and sp. nov., represents a novel group of archaea, extending the upper temperature limit for life to 113 degrees C.* Extremophiles, 1997. **1**(1): p. 14-21.
151. Deppenmeier, U. and V. Müller, *Life close to the thermodynamic limit: how methanogenic archaea conserve energy.* Results Probl. Cell Differ., 2008. **45**: p. 123-52.
152. Gottschalk, G. and R.K. Thauer, *The Na(+)-translocating methyltransferase complex from methanogenic archaea.* Biochim. Biophys. Acta., 2001. **1505**(1): p. 28-36.
153. Müller, V., C. Winner, and G. Gottschalk, *Electron-transport-driven sodium extrusion during methanogenesis from formaldehyde and molecular hydrogen by Methanosarcina barkeri.* Eur. J. Biochem., 1988. **178**(2): p. 519-25.
154. Schonheit, P. and D.B. Beimborn, *ATP synthesis in Methanobacterium thermoautotrophicum coupled to CH4 formation from H2 and CO2 in the apparent absence of an electrochemical proton potential across the cytoplasmic membrane.* Eur. J. Biochem., 1985. **148**(3): p. 545-50.
155. Thauer, R.K., et al., *Methanogenic archaea: ecologically relevant differences in energy conservation.* Nat. Rev. Microbiol., 2008. **6**(8): p. 579-91.
156. Mayer, F., et al., *A c subunit with four transmembrane helices and one ion (Na+)-binding site in an archaeal ATP synthase: implications for c ring function and structure.* J. Biol. Chem., 2012. **287**(47): p. 39327-37.
157. Deppenmeier, U., *Redox-driven proton translocation in methanogenic Archaea.* Cell Mol. Life Sci., 2002. **59**(9): p. 1513-33.
158. Hedderich, R., *Energy-converting [NiFe] hydrogenases from archaea and extremophiles: ancestors of complex I.* J. Bioenerg. Biomembr., 2004. **36**(1): p. 65-75.
159. Biegel, E. and V. Müller, *A Na^+-translocating pyrophosphatase in the acetogenic bacterium Acetobacterium woodii.* J. Biol. Chem., 2011. **286**(8): p. 6080-4.
160. Müller, V., *An exceptional variability in the motor of archael A1A0 ATPases: from multimeric to monomeric rotors comprising 6-13 ion binding sites.* J. Bioenerg. Biomembr., 2004. **36**(1): p. 115-25.
161. van de Vossenberg, J.L., et al., *Ion permeability of the cytoplasmic membrane limits the maximum growth temperature of bacteria and archaea.* Mol. Microbiol., 1995. **18**(5): p. 925-32.
162. Schafer, G., M. Engelhard, and V. Müller, *Bioenergetics of the Archaea.* Microbiol. Mol. Biol. Rev., 1999. **63**(3): p. 570-620.
163. Coskun, U., et al., *Structure and subunit arrangement of the A-type ATP synthase complex from the archaeon Methanococcus jannaschii visualized by electron microscopy.* J. Biol. Chem., 2004. **279**(37): p. 38644-8.
164. Maegawa, Y., et al., *Structure of the catalytic nucleotide-binding subunit A of A-type ATP synthase from Pyrococcus horikoshii reveals a novel domain related to the peripheral stalk.* Acta. Crystallogr. D. Biol. Crystallogr., 2006. **62**(Pt 5): p. 483-8.
165. Arai, S., et al., *Rotation mechanism of Enterococcus hirae V_1-ATPase based on asymmetric crystal structures.* Nature, 2013. **493**(7434): p. 703-7.

166. Manimekalai, M.S., et al., *The transition-like state and Pi entrance into the catalytic a subunit of the biological engine A-ATP synthase.* J. Mol. Biol., 2011. **408**(4): p. 736-54.
167. Kumar, A., et al., *The critical roles of residues P235 and F236 of subunit A of the motor protein A-ATP synthase in P-loop formation and nucleotide binding.* J. Mol. Biol., 2010. **401**(5): p. 892-905.
168. Chen, C., et al., *Mitochondrial ATP synthase. Crystal structure of the catalytic F_1 unit in a vanadate-induced transition-like state and implications for mechanism.* J. Biol. Chem., 2006. **281**(19): p. 13777-83.
169. Smith, C.A. and I. Rayment, *X-ray structure of the magnesium(II).ADP.vanadate complex of the Dictyostelium discoideum myosin motor domain to 1.9 A resolution.* Biochemistry, 1996. **35**(17): p. 5404-17.
170. Grüber, G., et al., *Structural Insights into the A_1 ATPase from the archaeon, Methanosarcina mazei Gö1.* Biochemistry, 2001. **40**(7): p. 1890-6.
171. Maher, M.J., et al., *Crystal structure of A3B3 complex of V-ATPase from Thermus thermophilus.* Embo J., 2009. **28**(23): p. 3771-9.
172. Coskun, U., et al., *Cross-talk in the A_1-ATPase from Methanosarcina mazei Gö1 due to nucleotide binding.* J. Biol. Chem., 2002. **277**(19): p. 17327-33.
173. Schafer, I., et al., *Structural and functional analysis of the coupling subunit F in solution and topological arrangement of the stalk domains of the methanogenic A_1A_O ATP synthase.* J. Bioenerg. Biomembr., 2006. **38**(2): p. 83-92.
174. Srinivasan, S., et al., *Crystal structure of the cytoplasmic N-terminal domain of subunit I, a homolog of subunit a, of V-ATPase.* J. Mol. Biol., 2011. **412**(1): p. 14-21.
175. Balakrishna, A.M., C. Hunke, and G. Gruber, *The structure of subunit E of the Pyrococcus horikoshii OT3 A-ATP synthase gives insight into the elasticity of the peripheral stalk.* J Mol Biol, 2012. **420**(3): p. 155-63.
176. Kumar, A., et al., *Spectroscopic and crystallographic studies of the mutant R416W give insight into the nucleotide binding traits of subunit B of the A_1A_O ATP synthase.* Proteins, 2009. **75**(4): p. 807-19.
177. Kumar, A., M.S. Manimekalai, and G. Grüber, *Structure of the nucleotide-binding subunit B of the energy producer A_1A_O ATP synthase in complex with adenosine diphosphate.* Acta. Crystallogr. D. Biol. Crystallogr., 2008. **64**(Pt 11): p. 1110-5.
178. Manimekalai, M.S., et al., *A second transient position of ATP on its trail to the nucleotide-binding site of subunit B of the motor protein A_1A_O ATP synthase.* J. Struct. Biol., 2009. **166**(1): p. 38-45.
179. Hunke, C., et al., *The effect of NBD-Cl in nucleotide-binding of the major subunit alpha and B of the motor proteins F_1F_O ATP synthase and A_1A_O ATP synthase.* J. Bioenerg. Biomembr., 2010. **42**(1): p. 1-10.
180. Inatomi, K., et al., *Amino acid sequence of the alpha and beta subunits of Methanosarcina barkeri ATPase deduced from cloned genes. Similarity to subunits of eukaryotic vacuolar and F0F1-ATPases.* J. Biol. Chem., 1989. **264**(19): p. 10954-9.
181. Puopolo, K., et al., *Differential expression of the "B" subunit of the vacuolar H(+)-ATPase in bovine tissues.* J. Biol. Chem., 1992. **267**(6): p. 3696-706.
182. Iwabe, N., et al., *Evolutionary relationship of archaebacteria, eubacteria, and eukaryotes inferred from phylogenetic trees of duplicated genes.* Proc. Natl. Acad. Sci. U S A, 1989. **86**(23): p. 9355-9.
183. Olendzenski, L., et al., *Horizontal transfer of archaeal genes into the deinococcaceae: detection by molecular and computer-based approaches.* J. Mol. Evol., 2000. **51**(6): p. 587-99.
184. Laskowski, R.A. and M.B. Swindells, *LigPlot+: multiple ligand-protein interaction diagrams for drug discovery.* J. Chem. Inf. Model, 2011. **51**(10): p. 2778-86.

185. Liu, Q., et al., *Site-directed mutagenesis of the yeast V-ATPase B subunit (Vma2p).* J. Biol. Chem., 1996. **271**(4): p. 2018-22.
186. Otwinowski, Z. and W. Minor, *Processing of X-ray diffraction data collected in oscillation mode,* 1997, Elsevier. p. 307-326.
187. McCoy, A.J., et al., *Phaser crystallographic software.* J. Appl. Crystallogr., 2007. **40**(Pt 4): p. 658-674.
188. Murshudov, G.N., A.A. Vagin, and E.J. Dodson, *Refinement of macromolecular structures by the maximum-likelihood method.* Acta Crystallogr D Biol Crystallogr, 1997. **53**(Pt 3): p. 240-55.
189. Emsley, P. and K. Cowtan, *Coot: model-building tools for molecular graphics.* Acta Crystallogr D Biol Crystallogr, 2004. **60**(Pt 12 Pt 1): p. 2126-32.
190. Laskowski, R.A., et al., *PROCHECK: a program to check the stereochemical quality of protein structures.* Journal of Applied Crystallography, 1993. **26**(2): p. 283-291.
191. Krissinel, E. and K. Henrick, *Secondary-structure matching (SSM), a new tool for fast protein structure alignment in three dimensions.* Acta Crystallogr D Biol Crystallogr, 2004. **60**(Pt 12 Pt 1): p. 2256-68.
192. Tadwal, V.S., et al., *Relevance of the conserved histidine and asparagine residues in the phosphate-binding loop of the nucleotide binding subunit B of A_1A_O ATP synthases.* J. Struct. Biol., 2012. **180**(3): p. 509-18.
193. Grüber, G., et al., *Expression, purification, and characterization of subunit E, an essential subunit of the vacuolar ATPase.* Biochem. Biophys. Res. Commun., 2002. **298**(3): p. 383-391.
194. Svergun, D.I., et al., *A model of the quaternary structure of the Escherichia coli F_1 ATPase from X-ray solution scattering and evidence for structural changes in the delta subunit during ATP hydrolysis.* Biophys. J., 1998. **75**(5): p. 2212-9.
195. Kozin, M.B. and D.I. Svergun, *Automated matching of high- and low-resolution structural models.* J. Appl. Crystallogr., 2001. **34**(1): p. 33-41.
196. Volkov, V.V. and D.I. Svergun, *Uniqueness of ab initio shape determination in small-angle scattering.* J. Appl. Crystallogr., 2003. **36**(3 Part 1): p. 860-864.
197. Montemagno, C. and G. Bachand, *Constructing nanomechanical devices powered by biomolecular motors.* Nanotechnology, 1999. **10**(3): p. 225.
198. Ho, S.N., et al., *Site-directed mutagenesis by overlap extension using the polymerase chain reaction.* Gene, 1989. **77**(1): p. 51-9.
199. Laemmli, U.K., *Cleavage of structural proteins during the assembly of the head of bacteriophage T4.* Nature, 1970. **227**(5259): p. 680-5.
200. Manavalan, P. and W.C. Johnson, *Variable selection method improves the prediction of protein secondary structure from circular dichroism spectra.* Anal. Biochem., 1987. **167**(1): p. 76-85.
201. Sreerama, N. and R.W. Woody, *A self-consistent method for the analysis of protein secondary structure from circular dichroism.* Anal. Biochem., 1993. **209**(1): p. 32-44.
202. Provencher, S.W., *A constrained regularization method for inverting data represented by linear algebraic or integral equations.* Comp. Phys. Comm., 1982. **27**(3): p. 213-227.
203. Andrade, M.A., et al., *Evaluation of secondary structure of proteins from UV circular dichroism spectra using an unsupervised learning neural network.* Protein Eng. Des. Sel., 1993. **6**(4): p. 383-390.
204. Deléage, G. and C. Geourjon, *An interactive graphic program for calculating the secondary structure content of proteins from circular dichroism spectrum,* 1993, Oxford University Press.
205. Böhm, G., R. Muhr, and R. Jaenicke, *Quantitative analysis of protein far UV circular dichroism spectra by neural networks.* Protein Eng., 1992. **5**(3): p. 191-195.

206. Hyberts, S.G., et al., *Application of iterative soft thresholding for fast reconstruction of NMR data non-uniformly sampled with multidimensional Poisson Gap scheduling.* J. Biomol. NMR, 2012. **52**(4): p. 315-27.
207. Walker, J.E., et al., *Distantly related sequences in the alpha- and beta-subunits of ATP synthase, myosin, kinases and other ATP-requiring enzymes and a common nucleotide binding fold.* Embo J., 1982. **1**(8): p. 945-51.
208. Saraste, M., P.R. Sibbald, and A. Wittinghofer, *The P-loop--a common motif in ATP- and GTP-binding proteins.* Trends Biochem. Sci., 1990. **15**(11): p. 430-4.
209. Jounouchi, M., M. Maeda, and M. Futai, *The alpha subunit of ATP synthase (F0F1): the Lys-175 and Thr-176 residues in the conserved sequence (Gly-X-X-X-Gly-Lys-Thr/Ser) are located in the domain required for stable subunit-subunit interaction.* J. Biochem., 1993. **114**(2): p. 171-6.
210. Hunke, C., et al., *Binding of subunit E into the A-B interface of the A_1A_O ATP synthase.* Biochim. Biophys. Acta., 2011. **1808**(9): p. 2111-8.
211. Grüber, G., et al., *Expression, purification, and characterization of subunit E, an essential subunit of the vacuolar ATPase.* Biochem. Biophys. Res. Commun., 2002. **298**(3): p. 383-91.
212. Petoukhov, M.V. and D.I. Svergun, *Analysis of X-ray and neutron scattering from biomacromolecular solutions.* Curr Opin Struct Biol, 2007. **17**(5): p. 562-71.
213. Stocker, A., et al., *The structural basis for unidirectional rotation of thermoalkaliphilic F1-ATPase.* Structure, 2007. **15**(8): p. 904-14.
214. Lee, J., et al., *Versatile PCR-mediated insertion or deletion mutagenesis.* Biotechniques, 2004. **36**(3): p. 398-400.
215. Kato-Yamada, Y. and M. Yoshida, *Isolated epsilon subunit of thermophilic F1-ATPase binds ATP*. J. Biol. Chem., 2003. **278**(38): p. 36013-6.
216. Kato-Yamada, Y., *Isolated epsilon subunit of Bacillus subtilis F1-ATPase binds ATP*. FEBS Lett., 2005. **579**(30): p. 6875-8.
217. Sternweis, P.C. and J.B. Smith, *Characterization of the inhibitory (epsilon) subunit of the proton-translocating adenosine triphosphatase from Escherichia coli.* Biochemistry, 1980. **19**(3): p. 526-31.
218. Singh, D., et al., *The roles and dynamics of subunits D and F of M. mazei Gö1 A_1 A_O ATP synthase*, 2015.
219. Singh, D., et al., *The stimulating role of subunit F in ATPase activity inside the A1-complex of the Methanosarcina mazei Gö1 A1AO ATP synthase.* Biochimica et Biophysica Acta (BBA) - Bioenergetics, 2016. **1857**(2): p. 177-187.
220. McGuffin, L.J., K. Bryson, and D.T. Jones, *The PSIPRED protein structure prediction server*. Bioinformatics, 2000. **16**(4): p. 404-5.
221. Vasilyeva, E., et al., *Cysteine scanning mutagenesis of the noncatalytic nucleotide binding site of the yeast V-ATPase.* J. Biol. Chem., 2000. **275**(1): p. 255-60.
222. Watanabe, R., R. Iino, and H. Noji, *Phosphate release in F1-ATPase catalytic cycle follows ADP release.* Nat. Chem. Biol., 2010. **6**(11): p. 814-20.
223. Falson, P., et al., *Structural insight into the cooperativity between catalytic and noncatalytic sites of F1-ATPase.* Biochim. Biophys. Acta., 2004. **1658**(1-2): p. 133-40.
224. Bald, D., et al., *ATP synthesis by F_OF_1-ATP synthase independent of noncatalytic nucleotide binding sites and insensitive to azide inhibition.* J. Biol. Chem., 1998. **273**(2): p. 865-70.
225. Noji, H., et al., *Direct observation of the rotation of F1-ATPase.* Nature, 1997. **386**(6622): p. 299-302.
226. Yasuda, R., et al., *F1-ATPase is a highly efficient molecular motor that rotates with discrete 120 degree steps.* Cell, 1998. **93**(7): p. 1117-24.

227. Yasuda, R., et al., *Resolution of distinct rotational substeps by submillisecond kinetic analysis of F1-ATPase.* Nature, 2001. **410**(6831): p. 898-904.
228. Tsumuraya, M., et al., *Effect of epsilon subunit on the rotation of thermophilic Bacillus F1-ATPase.* FEBS Lett., 2009. **583**(7): p. 1121-6.
229. Dallmann, H.G., T.G. Flynn, and S.D. Dunn, *Determination of the 1-ethyl-3-[(3-dimethylamino)propyl]-carbodiimide- induced cross-link between the beta and epsilon subunits of Escherichia coli F1-ATPase.* J. Biol. Chem., 1992. **267**(26): p. 18953-60.
230. Iino, R., et al., *Mechanism of inhibition by C-terminal alpha-helices of the epsilon subunit of Escherichia coli FoF1-ATP synthase.* J. Biol. Chem., 2009. **284**(26): p. 17457-64.
231. Zharova, T.V. and A.D. Vinogradov, *Energy-dependent transformation of F0.F1-ATPase in Paracoccus denitrificans plasma membranes.* J. Biol. Chem., 2004. **279**(13): p. 12319-24.
232. Richter, M.L., *Gamma-epsilon Interactions Regulate the Chloroplast ATP Synthase.* Photosynth. Res., 2004. **79**(3): p. 319-29.
233. Slonczewski, J.L., et al., *Cytoplasmic pH measurement and homeostasis in bacteria and archaea.* Adv Microb Physiol, 2009. **55**: p. 1-79, 317.
234. Bogin, E., T. Higashi, and A.F. Brodie, *The effect of trypsin and heat treatment on oxidative phosphorylation in Mycobacterium phlei.* Biochem. Biophys. Res. Commun., 1970. **41**(4): p. 995-1001.
235. Hisabori, T., et al., *The regulatory functions of the gamma and epsilon subunits from chloroplast CF1 are transferred to the core complex, alpha3beta3, from thermophilic bacterial F1.* Eur. J. Biochem., 1997. **247**(3): p. 1158-65.
236. Bakels, R.H., et al., *The effect of sulfite on the ATP hydrolysis and synthesis activity of membrane-bound H^+-ATP synthase from various species.* Biochem. Biophys. Res. Commun., 1994. **201**(2): p. 487-92.
237. Cappellini, P., et al., *Sulfite stimulates the ATP hydrolysis activity of but not proton translocation by the ATP synthase of Rhodobacter capsulatus and interferes with its activation by delta muH$^+$.* Eur. J. Biochem., 1997. **248**(2): p. 496-506.
238. Pacheco-Moises, F., et al., *Sulfite inhibits the F1F0-ATP synthase and activates the F1F0-ATPase of Paracoccus denitrificans.* J. Bioenerg. Biomembr., 2002. **34**(4): p. 269-78.
239. Suzuki, T., et al., *F0F1-ATPase/synthase is geared to the synthesis mode by conformational rearrangement of epsilon subunit in response to proton motive force and ADP/ATP balance.* J. Biol. Chem., 2003. **278**(47): p. 46840-6.
240. Nakanishi-Matsui, M., et al., *Stochastic high-speed rotation of Escherichia coli ATP synthase F1 sector: the epsilon subunit-sensitive rotation.* J. Biol. Chem., 2006. **281**(7): p. 4126-31.
241. Kato, Y., et al., *Thermophilic F1-ATPase is activated without dissociation of an endogenous inhibitor, epsilon subunit.* J. Biol. Chem., 1997. **272**(40): p. 24906-12.
242. Smith, J.B. and P.C. Sternweis, *Purification of membrane attachment and inhibitory subunits of the proton translocating adenosine triphosphatase from Escherichia coli.* Biochemistry, 1977. **16**(2): p. 306-11.
243. Shasmal, M. and J. Sengupta, *Structural Diversity in Bacterial Ribosomes: Mycobacterial 70S Ribosome Structure Reveals Novel Features.* PLoS One, 2012. **7**(2): p. e31742.

List of Author's publication

Tadwal, V.S., **Sundararaman, L.**, Manimekalai, M. S. S., Hunke, C., Grüber, G (2012). *Relevance of the conserved histidine and asparagine residues in the phosphate-binding loop of the nucleotide binding subunit B of A_1A_O ATP synthases*. J. Struct. Biol, 180(3): 509-18.

Singh, D., Sielaff, H., **Sundararaman, L.,** Bhushan, S., Grüber, G (2016). *The stimulating role of subunit F in ATPase activity inside the A1-complex of the Methanosarcina mazei Gö1 A1AO ATP synthase*. Biochimica et Biophysica Acta (BBA) - Bioenergetics 1857(2): 177-187.

Ragunathan, P[#]., Sielaff, H[#]., **Sundararaman, L[#].**, Biuković, G., Manimekalai, M. S. S., Singh, D., Kundu, S., Wohland, T., Frasch, W., Dick, T and Grüber, G (2016). *The uniqueness of subunit α of mycobacterial F-ATP synthases: An evolutionary variant for niche adaptation.* Nat. Commun. (under revision).

Conference attendance

18th European Bioenergetics Conference (EBEC), Lisbon, Portugal from 9th – 14th July. 2014

Posters and Abstracts

18th European Bioenergetics Conference (EBEC), Lisbon, Portugal from 9th – 14th July. 2014
Title: "*Subunit ε of Mycobacterium tuberculosis* F-ATP synthases is critical in ATPase inhibition". Biochim. Biophys. Acta **1837**: e1–e129

Awards

Nanyang research scholarship (2011-2015)